PRODUCTION AND CHARACTERIZATION OF Ti-6Al-4V SAMPLES MANUFACTURED BY HIGH-POWER LASER POWDER BED FUSION

NKUTWANE WASHINGTON MAKOANA

Thesis submitted in fulfilment of the requirements for the degree

DOCTOR of ENGINEERING:
MECHANICAL ENGINEERING

in the

Department of Mechanical and Mechatronic Engineering
Faculty of Engineering, Built Environment and Information Technology

at the

Central University of Technology

Promoter: Prof. I. Yadroitsev

Co-promoters: Dr. I. Yadroitsava, Dr. L. Tshabalala and Prof. S. Pityana

BLOEMFONTEIN
October 2022

DECLARATION OF INDEPENDENT WORK

DECLARATION WITH REGARD TO

INDEPENDENT WORK

I, NKUTWANE WASHINGTON MAKOANA, identity number _____ and student number _____, do hereby declare that this research project submitted to Central University of Technology, Free State, for the Doctor of Engineering in Mechanical Engineering, is my own independent work; and complies with the Code of Academic Integrity, as well as other relevant policies, procedures, rules and regulations of Central University of Technology, Free State; and has not been submitted before to any institution by myself of any other person in fulfilment (or partial fulfilment) of the requirements for the attainment of any qualification.

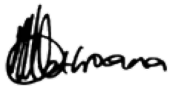

_____ 25-Jul-2023

SIGNATURE OF STUDENT **DATE**

ACKNOWLEDGEMENTS

There are so many people I would like to thank. I am so grateful for the time these people have given me to produce this thesis and finish my doctorate. Firstly, I must thank my supervisors at Central University of Technology, **Prof. Igor Yadroitsev** and **Prof. Ina Yadroitsava**, as well as my colleagues and co-supervisors at the Council for Scientific and Industrial Research, **Prof. Sisa Pityana** and **Dr. Lerato Tshabalala**, for their help and support throughout this process. They have been reliable supervisors who gave me the freedom to do things in my own order and supported and guided me to see important things in research. I want to sincerely thank all of them for the innumerable opportunities they offered beyond the domain of my doctorate, which enriched me both personally and professionally.

Secondly, I must thank the people who provided access to some of the characterization facilities, as this thesis would never have been completed without their support. I wish to express my warm and sincere thanks to **Prof. Anton du Plessis and Ms. Moufhe Tshalanganda** from Stellenbosch University for their assistance with the scanning and analysis of my results obtained using X-ray computed tomography. My sincere thanks to **Dr. Dreyer Bernard** and **Dr. Viera Wagener** from Nelson Mandela University for their technical assistance with residual stress measurements using X-ray diffraction. To **Dr. Dean Kouprianoff** at Central University of Technology, Centre for Rapid Prototyping and Manufacturing, thank you very much for your assistance with manufacturing my samples on the EOS machine; much appreciated. To **Mr. Stephen Masete** from the Council for Scientific and Industrial Research, MSM Material Testing Laboratory, thank you very much for your time and assistance with testing my samples. I wish to acknowledge the **South African Research Chairs Initiative** of the National Research Foundation of South Africa (Grant №. 97994) and the **Collaborative Program in Additive Manufacturing** of the Department of Science and Innovation (Contract № CSIR-NLC-CPAM-150MOA-CUT-01 and CSIR-NLC-CPAM-HLHC21X) for the financial support to carry out my research. I would also like to thank all the members of the Council for Scientific and Industrial Research, Laser-Enabled Manufacturing research group. It is their kind help and support that has made my study possible.

Finally, I would like to express my gratitude to my family and friends. Without their tremendous understanding and encouragement over the past few years, it would be impossible for me to complete my study. Above all, I would like to praise and thank God, the Almighty, who has granted me countless blessings, knowledge, and strength throughout my doctoral journey and life thus far. Amen!

EXECUTIVE SUMMARY

The use of high-powered lasers in laser powder bed fusion (LPBF) presents an opportunity to improve productivity without significantly increasing equipment costs. Instead of using a multi-beam system, a single laser equipped with a larger beam spot size can increase the melting volume, thus allowing the melting of a large area of powder to reduce the scanning time, which in turn increases the build rate. However, random porosity, poor surface quality, high residual stresses, and inconsistent mechanical properties are some of the challenges in LPBF, and this can be made worse by the increased intensity at the processing zone when the laser power is increased without increasing the beam spot size. The purpose of this study was to investigate the manufacturability of Ti-6Al-4V alloy using high laser powers at an enlarged beam spot size and shorter interaction times to improve productivity. This study has demonstrated the feasibility of improving productivity by using high laser power and shorter interaction time to gain a high build rate. It was shown that almost fully dense test coupons could be manufactured at a build rate of 18 mm^3/s, exhibiting low top surface roughness and residual stress below the yield strength, while the microstructure exhibited coarser prior-beta grains in the as-built condition. The vertical surface roughness of the parts manufactured using high-power was found to be higher due to the presence of partially melted powder particles attached to the surface. Surface finishing by centrifugal barrel finishing was investigated to improve the surface quality, and it was shown that the surface roughness could be reduced by 90%, with some small cavities remaining on the surface. The application of HIPing improved tensile properties and fatigue strength. However, the presence of localized near-surface and interlayer defects drastically affected the fatigue strength. These defects are believed to be related to powder delivery and contouring deficiencies. The key contributions in this study further enrich the scientific knowledge regarding LPBF process development and improvement of build rate and highlight some of the challenges that may arise, especially for researchers and machine developers wishing to improve the build rates of their machines by using high powers from a single laser source.

TABLE OF CONTENTS

LIST OF FIGURES

LIST OF TABLES

LIST OF PUBLICATIONS

1. L. Mugwagwa, I. Yadroitsava**, N.W. Makoana**, I. Yadroitsev. Residual stress in laser powder bed fusion. In: Fundamentals of Laser Powder Bed Fusion of Metals, ed. by I. Yadroitsev, I.Yadroitsava, A. du Plessis, E. MacDonald. 1st Edition, Elsevier, 2021, pp. 245-276. DOI:10.1016/B978-0-12-824090-8.00014-7

2. M. Khomenko, **N.W. Makoana,** S.L. Pityana, F. Mirzade, 2021. Coupled heat transfer, fluid flow and solidification kinetics for laser additive manufacturing applications. Journal of Manufacturing Processes, 67, pp. 611-618. DOI: 10.1016/j.jmapro.2021.05.019

3. **N.W. Makoana**, I. Yadroitsava, I. Yadroitsev, A. du Plessis, L. Tshabalala, S. Pityana, 2021. Residual stress, porosity and surface roughness for laser powder bed fusion manufactured Ti-6Al-4V at high laser powers. In: proc. "Rapid Product Development Association of South Africa - Robotics and Mechatronics - Pattern Recognition Association of South Africa (RAPDASA-RobMech-PRASA" conference, CSIR, 3-5 November 2021, Publisher: IEEE, paper #11.

4. **N.W. Makoana**, I. Yadroitsava, L. Tshabalala, I. Mathoho, S. Pityana, I. Yadroitsev, 2022. Post-processing of Ti-6Al-4V manufactured using high power laser powder bed fusion, Transactions on Additive Manufacturing Meets Medicine, 4 (1), p. 653. DOI: 10.18416/AMMM.2022.2209653.

LIST OF ABBREVIATIONS

2D - Two-dimensional

3D - Three-dimensional

AFM - Abrasive flow machining

AM - Additive manufacturing

ASTM - American society for testing and materials

bcc - body centered cubic

CAD - Computer-aided design

CBF - Centrifugal barrel finishing

CPAM - Collaborative program in additive manufacturing

CSIR - Council for scientific and industrial research

CT - Computed tomography

CV - Coefficient of variance

DED - Direct energy deposition

DSI - Department of science and innovation

EBSD - Electron backscatter diffraction

EDX - Energy dispersive X-ray

EOS - Electro Optical Systems GmbH

ET - Electromagnetic testing

HCF - High cycle fatigue

hcp - hexagonal close-packed

HIP - Hot isostatic pressing

HT - Heat treatment

IR - Infrared radiation

ISO - International organization for standardization

LCF - Low cycle fatigue

LOF - Lack of fusion

LPBF - Laser powder bed fusion

ND - Neutron Diffraction

NLC - National laser center

PRASA - Pattern recognition association of South Africa

RAPDASA - Rapid product development association of South Africa

RobMech - Robotics and mechatronics

SARChi - South African research chairs initiative

SD - Standard deviation

SEM - Scanning electron microscope

SLM - Selective laser melting

SLPS - Solidus liquid phase sintering

SLS - Selective laser sintering

TEM - Transmission electron microscope

UNSM - Ultrasonic nanocrystal surface modification

USP - Ultrasonic Shot Peening

UT - Ultrasonic testing

UTS - Ultimate tensile strength

wt% - weight percent

XCT - X-ray computed tomography

XRD - X-ray Diffraction

YS - Yield strength

LIST OF SYMBOLS

ΔK - Range of stress intensity factor

$\Delta\sigma$ - Stress range

a - Crack length

a_c - Critical crack length

d - Inter-planer spacing

d_0 - Strain free inter-planar spacing

$d'_{10,50,90}$ - 10th, 50th and 90th percentile particle diameter

d_ψ - Inter-planar spacing of planes at an angle Ψ to the surface

K_{IC} - Critical stress intensity factor

K_t - Stress concentration factor

m, c - Material coefficients obtained experimentally

n - An integer

N - Number of load cycles

N_i - Number of crack initiation load cycles

N_p - Number of crack propagation load cycles

$Ø_s$ - Laser beam spot diameter

R - Stress ratio

$S_{1\{hkl\}}$, $½S_{2\{hkl\}}$ - X-ray elastic constant of the family of plane {hkl}

α - Hexagonal close packed phase in titanium and titanium alloys

α' - Hexagonal close packed martensitic phase in titanium and titanium alloys

α2 - Hexagonal close packed intermetallic phase in titanium and titanium alloys

β - Body centered cubic phase in titanium and titanium alloys

ε - Strain

$\varepsilon_{\Phi\psi}$ - Strain measured in the direction of measurement defined by the angles phi, psi

θ - Angular position of the diffraction lines according to Bragg's Law

λ - Wavelength

σ_a - Stress amplitude

σ_m - Mean stress

σ_{max} - Maximum stress

σ_{min} - Minimum stress

Φ (phi) - Angle between a fixed direction in the plane of the sample and projection in that plane of the normal of the sample and the normal of the diffracting plane

χ (Chi - Angle of rotation in the plane normal to that containing omega and 2-theta about the axis of the incident beam

Ψ (psi) - Angle between the normal of the sample and the normal of the diffracting plane

ω (omega) - Angular rotation about a reference point

Chapter 1 Introduction

1.1 Background and motivation

The use of additive manufacturing (AM) platforms is gaining popularity in the manufacturing sector worldwide due to their attractive benefits over traditional manufacturing techniques. In metal laser-based powder bed fusion (LPBF), also known as selective laser melting (SLM), a high-powered laser beam is used to melt metal powder particles to build 3D structures. The procedure begins with creating a 3D CAD model of the component, which is then divided into 2D layer models and fed into the AM machine. The powder is delivered to the building platform using a scraper followed by a laser beam that can scan the powder layer. The build platform is then lowered by one layer after each successful scan, and the procedure is repeated until the entire build is complete (see Figure 1.1). Complex shape parts and lattice structures were manufactured successfully and are used in aircraft, automotive, dental, medical, and other hi-tech industries. The high mechanical load capacity of the components is comparable with conventional techniques.

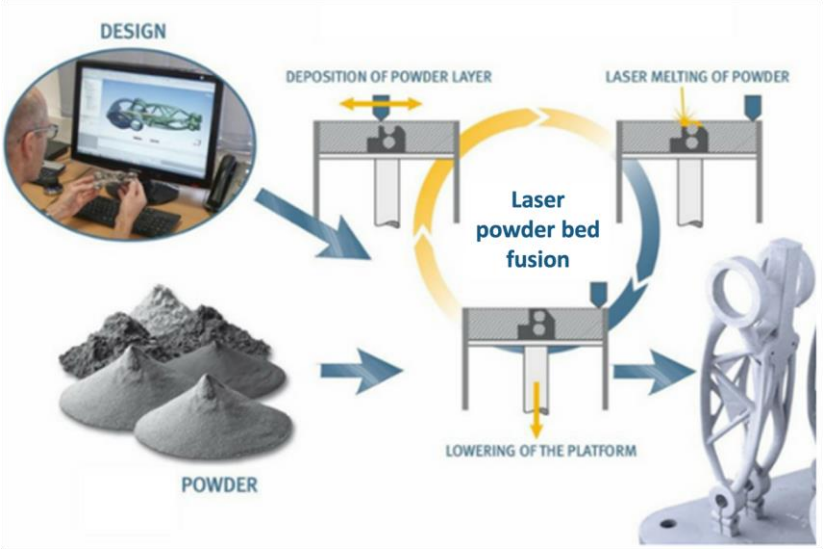

Figure 1.1: LPBF schematic.

The cost of equipment is decreasing and becoming simpler to use, increasing its use in both commercial and consumer markets. This has also expanded the scope for the application of AM technology. Figure 1.2 shows the use of AM within specific industrial areas, the most popular of which are end-use parts and functional prototypes. End-use parts are intended for use in the final stage of product development, where the industry has recently expanded the most.

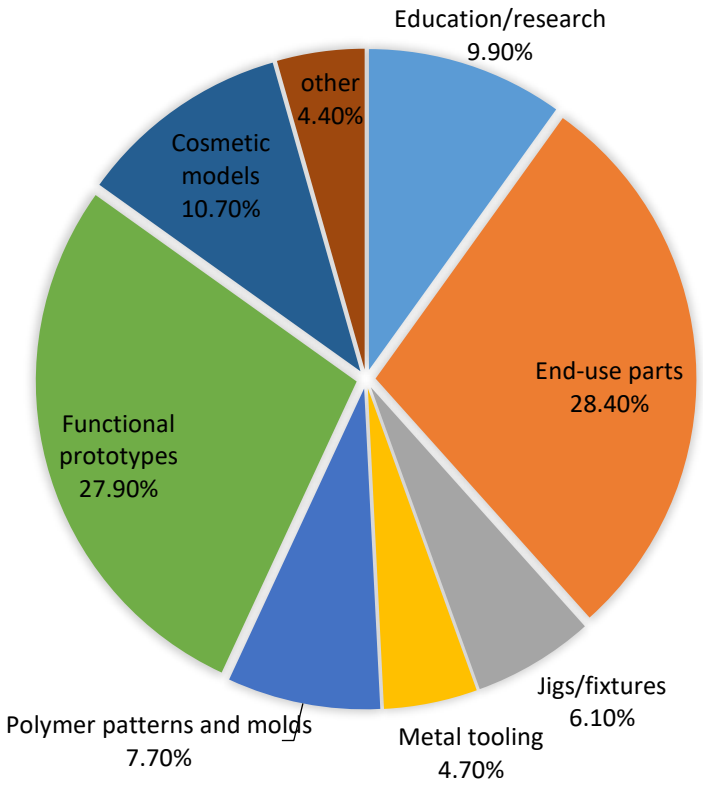

Figure 1.2: How consumers use the parts built on Metal and Polymer AM systems [1].

Notwithstanding the attractive benefits of LPBF, several challenges remain to overcome. Affordability and wide adoption of this technology are limited by the speed of part manufacturing, the volumetric size of the equipment, and, therefore, the maximum part size that can be manufactured. Most of the systems available on the world market use one fibre laser of 200 W to 1 kW capacity to selectively fuse the powder bed layer. The build chamber is filled with inert gas to prevent oxidation. The power of the laser source,

scan speed, hatch distance between the tracks, and the thickness of the deposited powder layer are the main processing parameters [2], [3]. A layer thickness of 20–100 μm can be used depending on the material and process parameters. Many of the LPBF systems have low build rates of 5–20 cm^3/hr, and the maximum part size that can be produced (build volume) was limited to 250 x 250 x 325 mm^3 which increases part cost and limits its use only for small and medium-sized parts [4]. In recent years, machine manufacturers and researchers worldwide have focused on expanding the capabilities of their machines by increasing the build rates and build volumes.

SLM Solution from Germany launched the first machine (SLM500 HL) in 2012, which uses double-beam technology to increase the build rate up to 35 cm^3/hr and has a build volume of 500 x 350 x 300 mm^3. This machine uses two sets of lasers, each set with two lasers (400 W and 1000 W). This means four lasers scan the powder layer simultaneously. The following year in 2013, EOS from Germany also launched the EOSINT M400 machine, which has a build volume of 400 x 400 x 400 mm^3 and uses a 1 kW fibre laser to increase the build rate. In 2015, Concept Laser and Fraunhofer Institute for Laser Technology launched the biggest commercial AM machine for metals (X line 2000R) which also uses double-beam technology to increase the build rate up to 120 cm^3/hr and has a build volume of 800 x 400 x 500 mm^3. Details of the process capabilities in terms of build volumes, build rates, and scan speeds of some LPBF machine models are given in Table 1.1. It is important to note that these machines use multi-beam technology, which can significantly increase the cost of the LPBF system.

The Council for Scientific and Industrial Research (CSIR), together with the Department of Science and Innovation and Aerosud (Pty) Ltd., jointly developed a large-build AM envelope called Aeroswift. The machine is equipped with a single laser operating at a laser power of up to 5 kW and has a variable beam size allowing for higher parameter regimes. Additionally, the typical layer thickness is between 50–150 μm which is different from the commonly employed 50–75 μm layer thickness used by commercial LPBF systems. Due to the large scale of the system, it is difficult to process different materials because of the high risk of cross-contamination, and as such, the system is used to only process titanium. A smaller version, called Hummingbird, was also developed in-house

to carry out experimental development work and exploration of different materials, see Figure 1.3. This system was used in this research.

Table 1.1: Some of the largest commercial LPBF machine models per manufacturer

Manufacturer	**Model**	**Energy source**	**Build volume (mm^3)**	**Max build rate (cm^3/hr)**
EOS	EOS M400-4	4 x 400 W fibre lasers operating independently	400 x 400 x 400	up to 100
FARSOON	FS421M	500 W (dual laser optional)	420 x 420 x 420	NA
SLM Solution	SLM 500HL	2 x 400 W lasers & 2 x 1000 W lasers (optional)	500 x 280 x 325	up to 70
ReaLizer	SLM 300*i*	400 W–1000 W fibre laser	300 x 300 x 300	NA
SLM Solution	SLM 800	4 x 400 or 4 x 700W fibre lasers	500 x 280 x 365	up to 171
Concept Laser	X Line 2000R	2 x 1 kW fibre laser	800 x 400 x 500	up to 120
Renishaw	RenAM 500Q	4 x 500 W lasers operating independently	250 x 250 x 350	up to 150

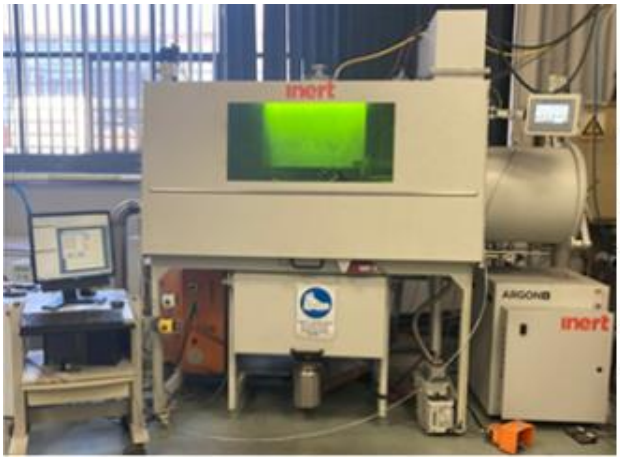

Description	Specification
Energy source	5 kW fibre laser
Max build volume	Ø 270 mm x H 400 m
Operating environment	Argon atmosphere
Layer thickness	50 µm

Figure 1.3: Photo and specification of the Hummingbird machine.

1.2 Problem statement

The actual production of AM parts is slow, with parts taking as much as one week or longer to produce, depending on the size and complexity. The cost of acquiring a multi-beam LPBF system with higher build rates can be a limitation for organizations with low capital investment. Thus, a low-cost LPBF system capable of manufacturing large complex parts at higher build rates is a viable alternative. However, random porosity, poor surface quality, high residual stresses, and anisotropy in mechanical properties are other factors that hinder the widespread adoption of LPBF technology as the end manufacturing technique, especially in highly regulated industries such as aerospace.

1.3 Research aim and objectives

The aim of this study is to investigate the peculiarities of LPBF of Ti-6Al-4V using high laser powers and high scanning speed in pursuit of high build rates. The specific research objectives are:

i. To identify the process parameter window for low porosity and high build rate.

ii. To characterize the surface roughness, residual stresses, and microstructure.

iii. To investigate the effect of post-processing on the surface roughness and mechanical properties.

1.4 Brief overview of methodology

This research focuses on understanding the implications of using high laser powers and high scanning speeds on LPBF of Ti-6Al-4V and the effects on the response variables, namely porosity, surface roughness, residual stresses, microstructure, and mechanical properties. The flow chart below shows a brief overview of the research methodology followed in this study.

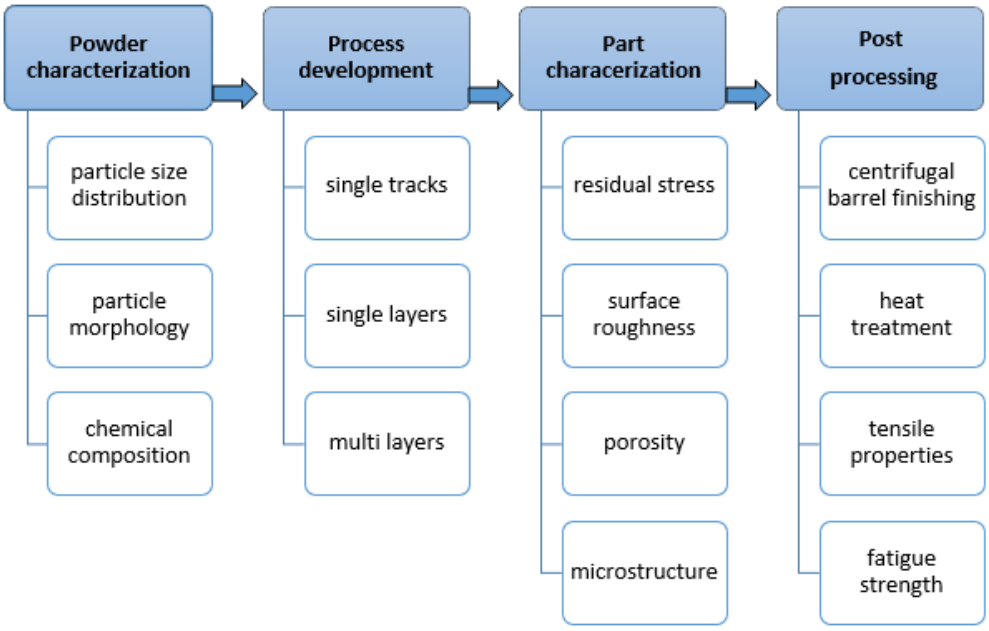

Figure 1.4: Flow chart of the research methodology adopted.

1.5 Dissertation outline

The introduction is the first of the seven chapters of this thesis. This chapter presents the context and motivation, the purpose and goals of the research, and a quick summary of the research methodology. Following is how the remaining chapters are arranged:

- Chapter 2 features an extensive literature review of additive manufacturing in the following broad categories:
  - Metal AM processes
  - Characteristics of LPBF products
  - Material characterization techniques
  - Post-processing of LPBF and mechanical properties
- Chapter 3 – Material and methods
- Chapter 4 – Process development for high-power LPBF of Ti-6Al-4V
- Chapter 5 – Comparison of Ti-6Al-4V samples manufactured using high- and low-PBF systems
- Chapter 6 – Effects of post-processing operations on the surface quality and mechanical properties
- Chapter 7 – Conclusions and future outlook.

Chapter 2
Literature review

2.1 Metal additive manufacturing

AM techniques can be classified based on the state of the starting materials (i.e. solid, liquid, powder); according to the type of material processed (i.e. polymer, metal, ceramics, paper, cement, etc.); or according to the different mechanisms of 3D manufacturing as illustrated in Figure 2.1, The current AM technology for the manufacture of metallic parts usually employs three main processes: Selective Laser Sintering (SLS), or partial sintering, Laser Powder Bed Fusion (LPBF), and Direct Energy Deposition (DED).

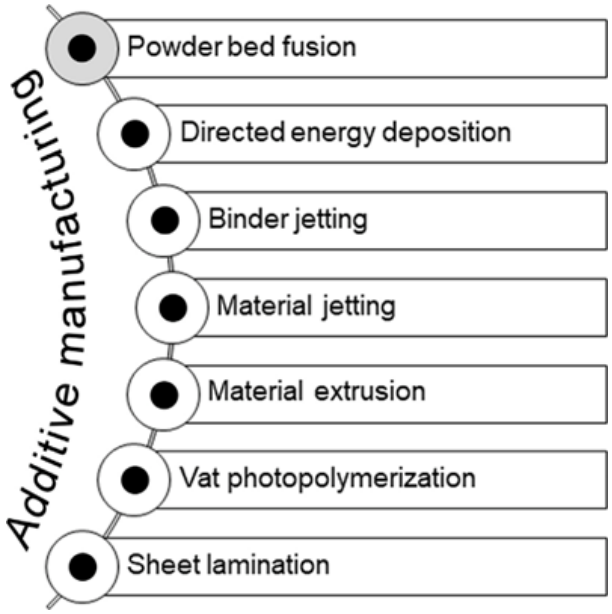

Figure 2.1 AM process categories according to ISO/ASTM 52900:2015 [5].

2.1.1 Selective laser sintering

Selective Laser Sintering (SLS) is based on a liquid-phase sintering (LPS) mechanism involving a partial melting of the powder [6]. A high-melting-point metallic component serves as the structural metal in the multi-component powder combination. A small number of additives, such as a fluxing agent or deoxidizer, are introduced together with a low-melting-point metallic component that acts as the binder [7]. The working SLS

temperature is carefully adjusted between these two melting temperatures by modifying laser-processing settings. Densification of the solid/liquid system happens because of solid particle rearrangement under the impact of capillary forces placed on them by the wetting liquid [2], [8]. Pre-alloyed powder displays a mushy zone, where liquid and solid phases coexist during the melting/solidification process, in contrast to pure metals with a congruent melting point (Figure 2.2). The temperature must be in the mushy zone for optimized parameters to create a semi-solid structure. The metallurgical mechanism for the solidus liquid phase sintering (SLPS) of pre-alloyed powder is provided by this method. To attain adequate mechanical properties, post-processing procedures such as furnace post-sintering [9], hot isostatic pressing (HIP) [10] , or secondary infiltration with a low-melting-point material [11] are typically required.

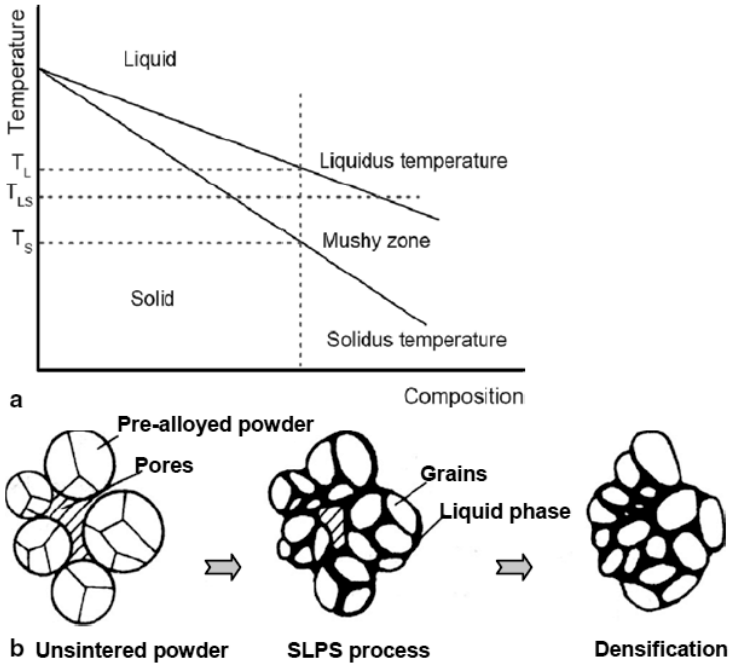

Figure 2.2: An idealized phase diagram for a pre-alloyed binary metal system (a), Schematic illustration of SLPS densification of pre-alloyed powder (b) [12].

2.1.2 Direct energy deposition

Direct Energy Deposition (DED) follows the same general AM principle, but powder delivery changes from spreading the powder over the baseplate to coaxial powder feeding (Figure 2.3). The powder delivery system comprises a powder feeder uniquely built to

distribute powder into a gas delivery system via the nozzles. In the middle of the nozzle array, a high-energy laser beam is supplied along the z-axis and focused by a lens near the workpiece. A computer-controlled drive system moves the workpiece in the X-Y direction to create the appropriate cross-sectional shape. Consecutive layers are deposited additively, resulting in a three-dimensional component [13], [14]. DED technology is used to build new components, repair worn-out surfaces, and apply wear and corrosion-resistant coating to surfaces [15]-[17].

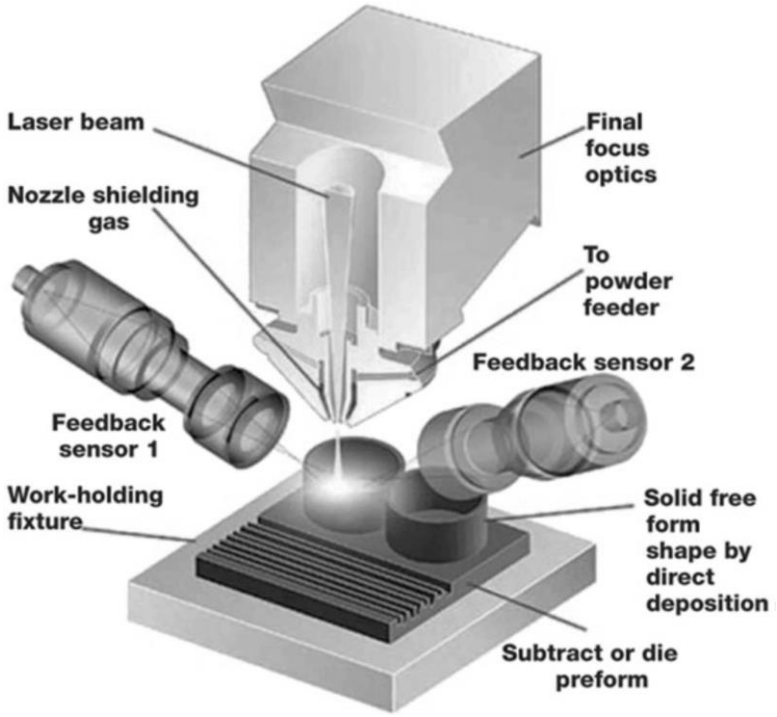

Figure 2.3: Schematic of the DED system [15].

2.1.3 Laser powder bed fusion

Laser powder bed fusion (LPBF), formerly known as selective laser melting, was developed from SLS, driven by the need to produce fully dense parts with mechanical properties comparable to those of bulk materials and to minimize post-processing cycles. The full melting of the powder particles occurs rather than the sintering or partial melting that characterizes SLS. Therefore, LPBF produces denser components than SLS. LPBF shares the same processing apparatus and procedure with SLS. The process begins with the creation of a 3D CAD model of the component. The model is then divided into 2D

layers and loaded into the machine. A scraper or recoating blade moving over the powder bed delivers the new powder layer, which is then scanned by the laser beam. When the laser beam has finished scanning the layer, the baseplate is dropped by one layer, and a fresh powder layer is placed on top of the previously formed layer. This process is repeated until the component is completed (Figure 2.4).

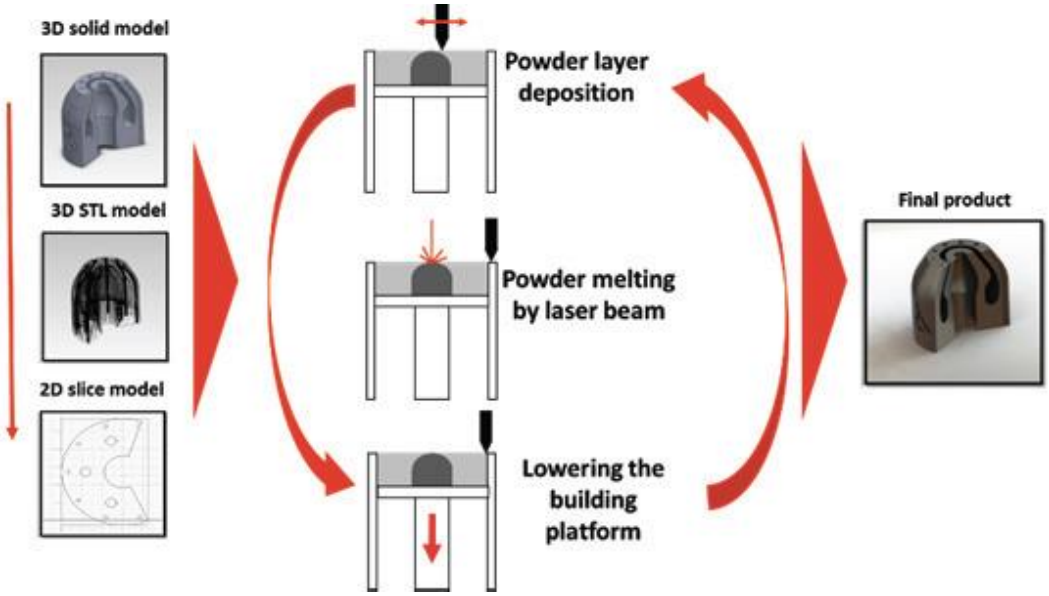

Figure 2.4: Schematic diagram of the LPBF process [18].

During scanning, electromagnetic waves carried by laser radiation deliver energy to the powder material. The scanning speed and spot size of the laser beam affect how long the laser beam interacts with the powder. As a result, the properties of the material, laser power, scanning speed, spot size, and process parameters all affect how well scanning works [19]-[21]. These parameters are either predetermined or customizable. The controls over the heating, melting, and solidification processes are programmable. Predetermined parameters are also a part of the process, although they cannot be changed while scanning is taking place. The energy input, powder layer thickness, and scan strategy all affect the final properties of an LPBF component, including geometry and mechanical properties [3], [7], [22]. Figure 2.5 shows the effects of several geometric, laser, and material properties on energy input. It should be emphasized that most of these variables interact and depend on one another.

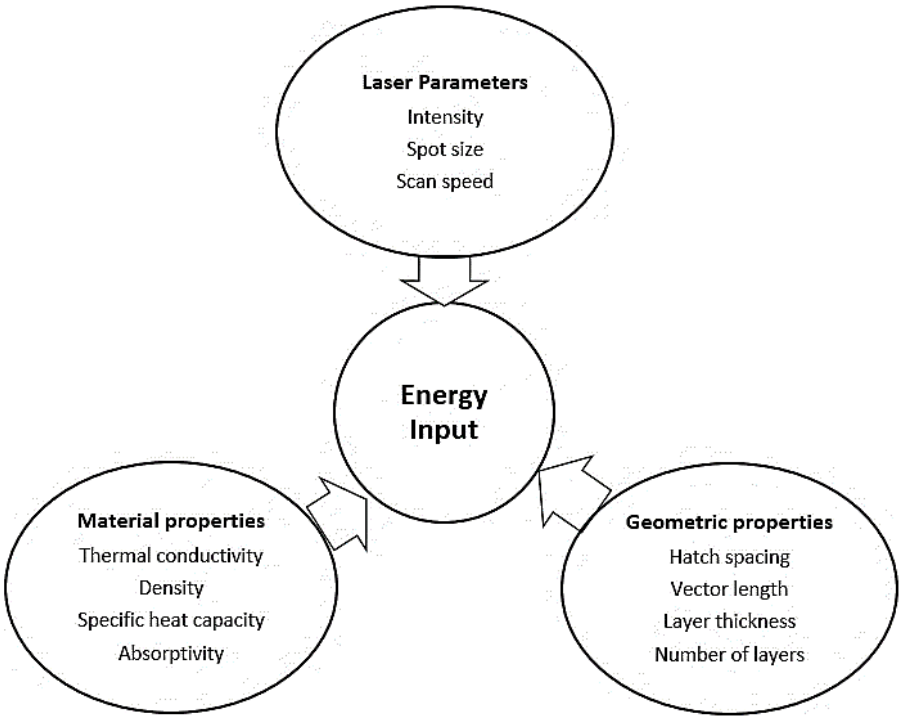

Figure 2.5: The interaction of laser, material, and geometric parameters on energy input.

Some researchers indicate that the manufacture of a fully dense material involves a combination of the four major process parameters, as given in Equation 2.1 [3], [23], [24]. Other procedures, such as thorough LPBF parameter analysis, are essential to control the quality of the final product [25].

$$E_d = \frac{P}{v\text{x}h\text{x}l} \qquad (2.1)$$

Ed – Total energy input per melted track volume ($J{\cdot}mm^{-3}$)
P – Power of the laser (W)
v – Laser beam scan speed ($mm{\cdot}s^{-1}$)
h – Hatch spacing (mm)
l – Thickness of the layer deposited (mm)

2.2 Physical phenomena in LPBF

The primary function of LPBF is to scan a laser beam over the surface of a thin powder layer. A sequence of powder particles is heated by the beam, melting the material and

creating a dynamic molten pool. This process is complex and influenced by the material's chemistry, optical, thermal, and rheological characteristics. Examples of the main phenomena that occur during single-track melting are shown in Figure 2.6, that are heavily material-dependent and influenced by a material's chemistry and its optical, thermal, and rheological characteristics. The following are examples of the main phenomena that occur during single-track melting.

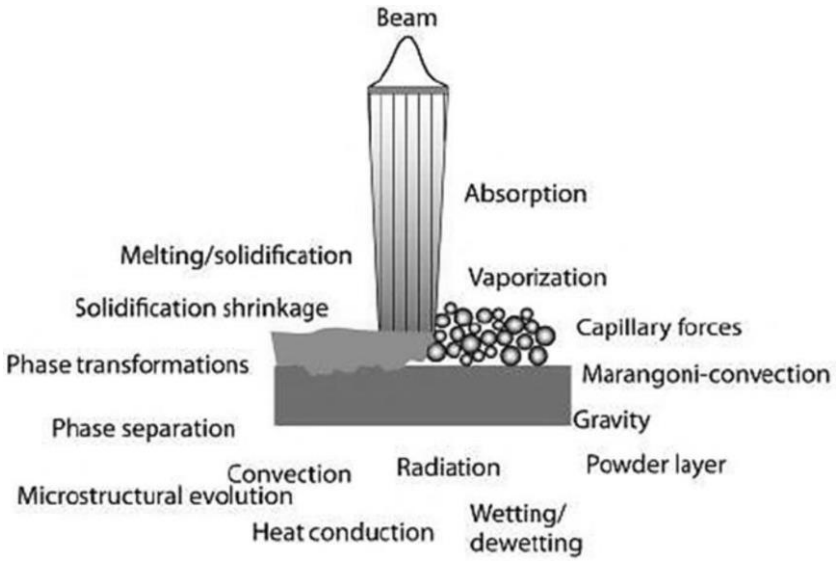

Figure 2.6: Physical phenomena taking place during LPBF (based on [26]).

2.2.1 Melting

LPBF is a process that transforms solid powder grains into liquid phase before cooling and solidification [27]. To ensure bonding, the entire material region exposed to the laser beam is melted to a depth larger than the layer thickness. This technique is highly successful at generating well-bonded, high-density structures [28]-[29].

2.2.2 Vaporization

The temperature of the powder grains soon increases over the melting point when the laser beam interacts with the powder that has been deposited. Controlling the maximum temperature reached could occasionally be difficult and ambiguous. If the temperature rises over the material's melting point, it evaporates rapidly [30].

2.2.3 Marangoni effect

The Marangoni effect is the fluid flow behaviour generated by differences in temperature in molten material. It is important because it influences the geometrical features of the melt pool. The surface tension temperature coefficient and the Prandtl number are two important factors in Marangoni convection. A positive surface tension temperature coefficient causes the liquid to be pulled to the centre of the top surface before sinking . As temperature rises, surface tension decreases, resulting in a narrow melt pool that can enable deeper penetration, thus providing a deeper bond in the case of LPBF. Most alloys and pure metals have a negative surface tension temperature coefficient, which may be changed to a positive value by adding certain elements. The Prandtl number specifies the kind of heat flow [31].

2.2.4 Plateau-Rayleigh instability

Plateau-Rayleigh instability is the behaviour of a liquid cylinder and the conditions under which it separates into droplets. Surface tension is mostly responsible for this phenomenon, which is often observed in LPBF due to the use of a laser to create a dynamic molten pool (see Figure 2.7). Temperature gradients in LPBF are strong, resulting in Marangoni effects. Plateau-Rayleigh instabilities are further impacted by the liquid's internal and surface motion [32].

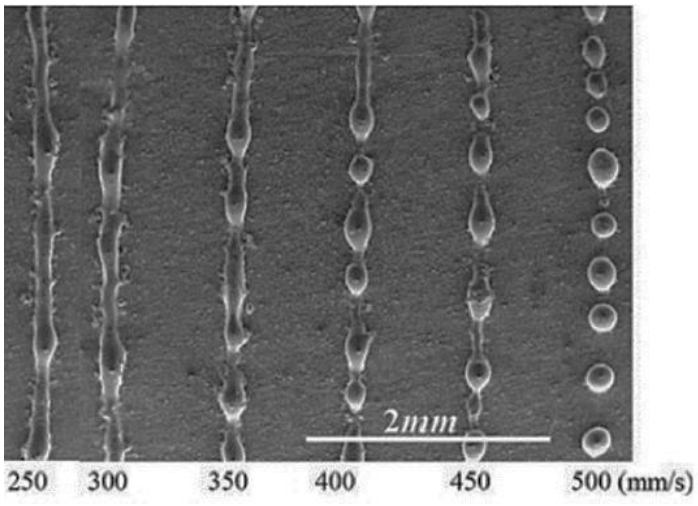

Figure 2.7: Example of Plateau-Rayleigh instabilities and balling effect in LPBF [33].

2.2.5 Wetting

Wetting is the ability of a liquid to retain contact with a solid surface due to intermolecular interactions [23]. The contact angle between the liquid and the surface with which it makes contact determines the degree of wetting. It is the most significant occurrence in LPBF because it involves the full melting of material in successive layers that must bond to allow proper consolidation. High-temperature oxidation can adversely influence wetting, so it is important to use inert gas or vacuum to impose a low-oxygen-content environment and give enough laser energy to re-melt portion of the prior layer [26], [27], [34], [35]. Increased scanning speed causes unfavorable wetting, flowing, spreading, and balling effects (see Figure 2.8).

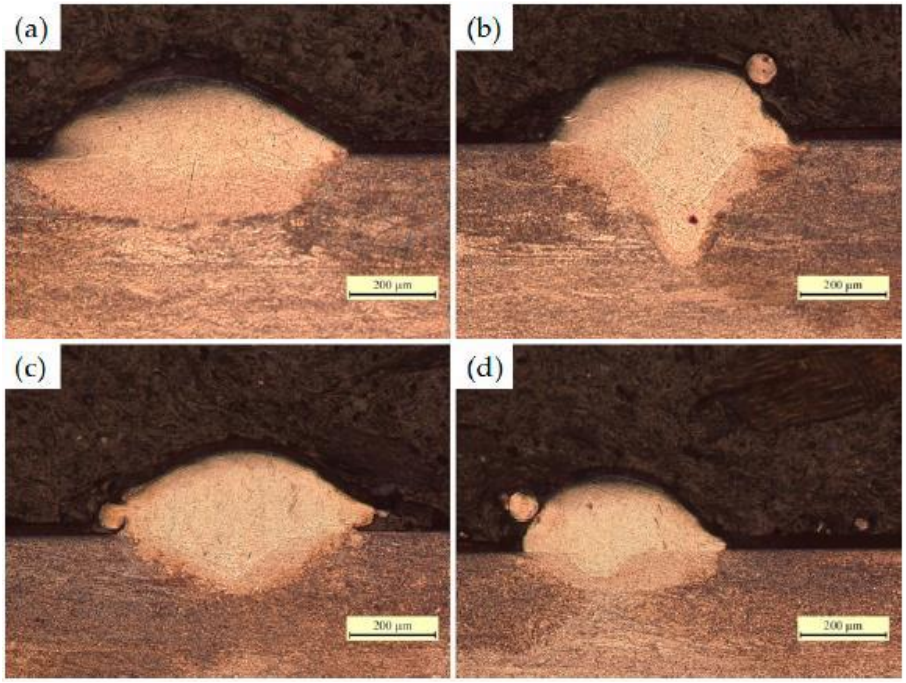

Figure 2.8: Optical micrographs of Ti-6Al-4V single tracks showing wetting of molten pool to the baseplate as the scanning speed increased (P = 400 W, l = 200 µm). (a) 80 mm/s, (b) 120 mm/s, (c) 160 mm/s, (d) 200 mm/s [36].

2.3 General characteristics of LPBF parts

The layer-by-layer approach, along with rapid heating by a laser followed by rapid solidification, characterizes the LPBF process. As such, the characteristics of products manufactured by LPBF are different from what is achievable with conventional

manufacturing processes. Properly understanding these characteristic features is important to avoid problems with material processing.

2.3.1 Porosity

The first and possibly most crucial consideration is the achievable density following LPBF. The goal is normally to achieve 100% density. This aim, however, is difficult to meet because there is no mechanical pressure, as in molding operations, and LPBF is solely defined by temperature effects, gravity, and capillary forces during manufacture. Furthermore, gas bubbles can become entrapped in the material during the LPBF process for various reasons, including a reduction in the solubility of dissolved components in the melt pool during solidification [36]. Many previous studies have focused on achieving almost entirely dense LPBF components [2], [37]-[40]. Despite these, little residual porosity is usually present in finished parts. The main sources of porosity during LPBF are insufficient melting, entrapment of gas, and balling [2], [41]-[42]. Figure 2.9 shows the type of pores commonly observed in LPBF. Porosity in LPBF can be controlled through the optimization of scanning parameters and environmental processing conditions. Usually, post-processing treatment such as HIPing is applied to improve the density of LPBF parts [43]-[46].

Internal flaws can also form stochastically because of irregular spreading and packing of powder and process by-products like spatter particles [48]. Spatters can have varied formation mechanisms and, as a result, different sizes, morphologies, and temperatures upon ejection, affecting their detectability [49]-[51]. Unlike systematic flows, the incidence and distribution of stochastic flaws cannot, in principle, be anticipated, as their formation is not driven by user-defined parameters. Their distribution is irregular, as illustrated in Figure 2.10, which shows cross-sections of samples produced at invariable processing conditions.

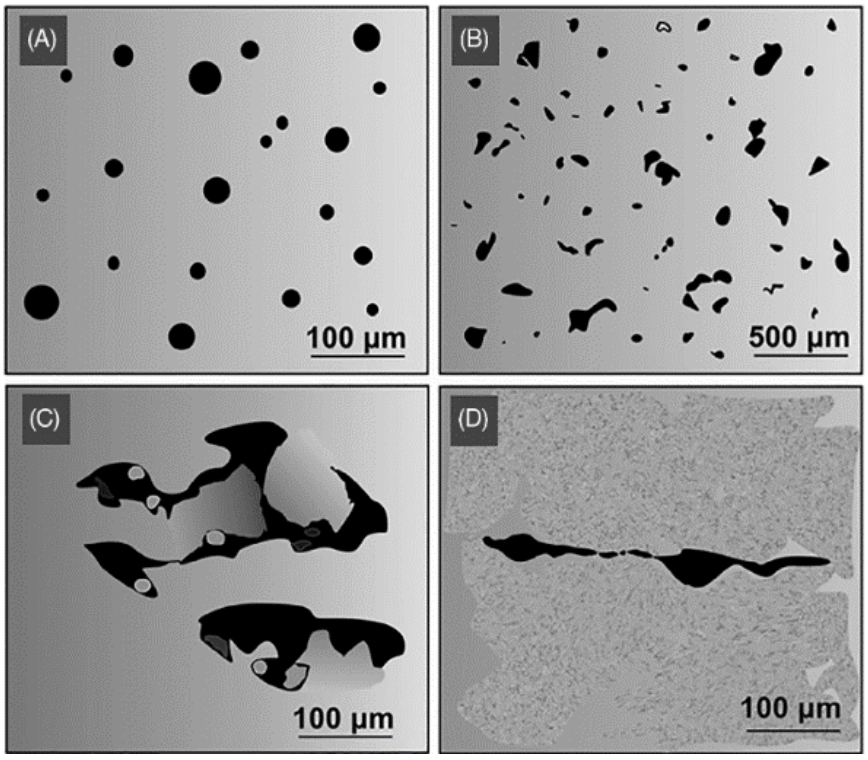

Figure 2.9: Pore types in LPBF parts: (a) entrapped gas porosity; (b) partial melting-induced porosity; (c) lack of fusion with unmelted particles inside large irregular pores; and (d) cracks [47].

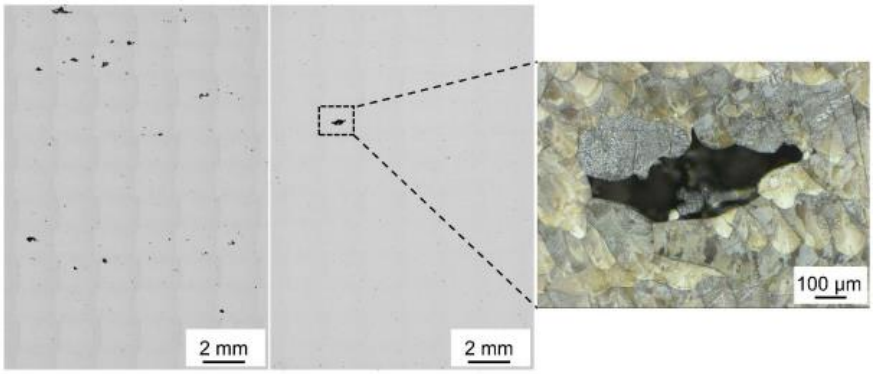

Figure 2.10: Cross-sectional views of a specimen containing stochastic flaws [52].

2.3.2 Surface roughness

Surface quality is not only a fundamental concern for users but also an important factor in completing the component during production. The achievable surface quality, particularly roughness, of LPBF components is regarded as one of the key challenges of the process and has been the topic of much research [43], [53]-[55]. Figure 2.11 shows examples of the surface topography of an LPBF part obtained in the as-built condition.

The surface roughness is dependent on numerous factors, such as the reliability of the machine, the quality of powder material, and, most importantly, the optimization of the process parameters [43], [56]-[57]. Surface roughness is a source of crack initiation that promotes fatigue failure to occur. Additionally, a rough surface, usually caused by balling, results in the entrapment of gases when a successive layer is added, leading to the formation of porosity [56]. Thus, correct parameter optimization for the required material can result in less balling and better surface quality for LPBF components. LPBF is also sensitive to poor surface roughness and sagging on geometrical elements with low surface angles, and its overall orientation relative to the build platform is critical. Problematic locations usually include holes, fillets, and unsupported overhangs [58]. Surface polishing techniques can result in satisfactory finishing; however, inaccessible internal voids or cavities are challenging for the currently available surface treatment techniques.

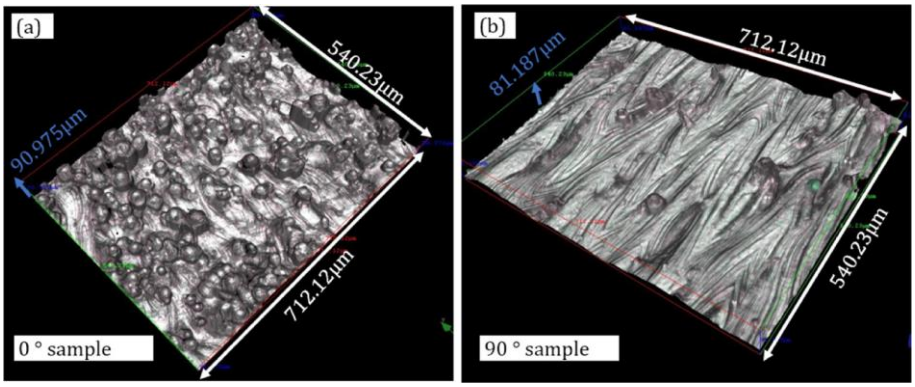

Figure 2.11: Example of representative surface topography of as-built LPBF part. (a) side view, (b) top view [57].

2.3.3 Residual stresses

The formation of high internal residual stresses because of continuous heating and cooling of successive layers of powder during building is a serious issue with components made using the LPBF process. The LPBF process generates fast heating and cooling effects and high-temperature gradients inside the structure. As a result, the overall microstructural characteristics created by the LPBF process differ from those acquired by conventional manufacturing, and these complicated thermal effects enhance the formation of residual stresses. If residual stresses are not recognized and accounted for in the design process, they can be a major factor in the subsequent failure of a component

in service, particularly one subjected to alternating loadings [59]-[62]. Unmanaged residual stresses have the direct effect of producing failure during manufacturing (see Figure 2.12). LPBF parts typically require extra support structures to prevent build failure. Support structures restrain the component during building to prevent curling, deformation, and collisions with the powder re-coating blade. High residual stresses lead the material to break and fracture in severe circumstances, allowing the component to deform freely and collide with the re-coating process once more. Other problematic post-build residual stress artifacts include deformation, higher susceptibility to fracture development, and worse fatigue performance. Because bending is feasible within the build plate, some component deformation and residual stress buildup are unavoidable even with sturdy thick supports. More post-processing is required to remove residual stresses by heat treatment to stress-relieve the component or by HIPing [63].

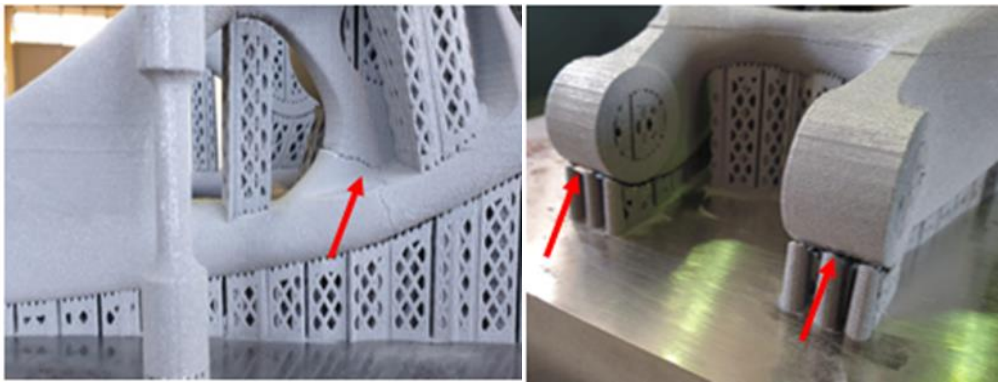

Figure 2.12: Cracking and delamination in Ti-6Al-4V component caused by the build-up of residual stress.

2.3.4 Microstructures

Due to the line and layer-wise building pattern used in LPBF, the microstructure of an LPBF part may differ in various views (see Figure 2.13). Columnar grain structure dominates, with high amounts of grain orientation. Subsequent heating and cooling cycles of the material may cause axial variation of grains and phases [26], [36], [64]. The resultant microstructure depends on the starting powder material, employed temperatures, and building strategy [36], [65]. Each powder undergoes several phase changes in a short time, and these changes determine the eventual microstructure. The anisotropic microstructure leads to the anisotropy of mechanical properties [6], [64], [66]-[67]. Post-

heat-treatment processes, such as recrystallization annealing, are often applied to LPBF parts to tailor/refine the structure [68]-[69].

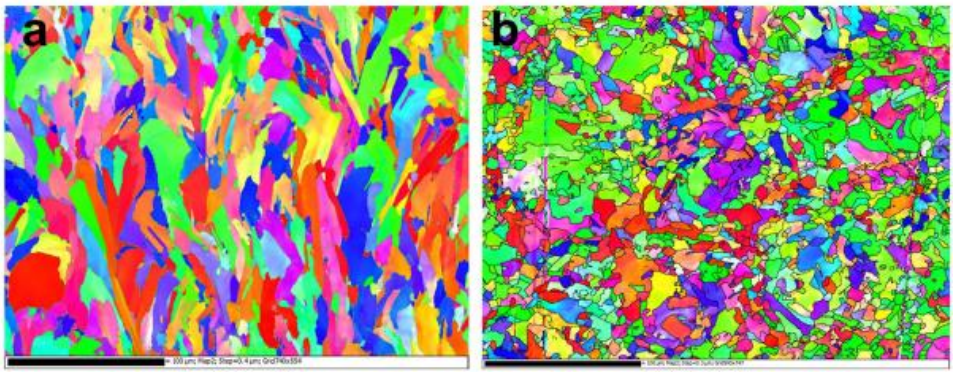

Figure 2.13: EBSD maps (inverse pole figure: blue is 111, green is 101 and red is 001) taken from as-built 316L prepared using SLM on an EOS280 using factory-recommended print settings: (a) the build direction is vertical, and (b) the plane of the image is perpendicular to the build direction [71].

2.3.5 Mechanical properties

The most common tests used to compare additively manufactured components to traditionally manufactured materials are tensile tests to determine yield strength (YS), ultimate strength (UTS), and elongation (i.e. cast and wrought). The mechanical properties depend not only on the material composition but also on the microstructure obtained, and the presence of defects in the final parts is determined by the process parameters and manufacturing strategy [36]. Porosity, residual stress, test specimen orientation, and thermal history are particularly important factors that affect the mechanical properties of LPBF components. Generally, LPBF can produce parts with mechanical properties that compare well with conventional manufacturing methods apart from ductility, which is lower in most LPBF-manufactured parts [36], [65], [70]-[73]. Some authors have reported ductility higher than 10%, achieved through process optimization or by manipulation of process parameters to obtain martensite decomposition during the process [74]-[75]. The dynamic properties such as fracture toughness and fatigue limit are also important and have received attention from various authors [75]-[80]. The fracture toughness was found to be dependent on the build orientation of the specimen and the orientation of the crack growth [44], [81]. Studies on high-cycle-fatigue life and limit for

LPBF parts have produced a wide range of contradictory results; however, the fatigue properties for as-built parts are worse than heat-treated or HIPed parts.

2.4 Post treatments of LPBF parts

2.4.1 Stress relieving

Stress-relief heat treatment is a thermal post-processing method used to minimize interlocked stresses in the part. It involves recovery at elevated temperatures where atomic diffusion increases and atoms in regions of high stresses can move [82]. This movement of atoms relieves internal strain energy, which relieves internal stresses. The part is heated to a temperature high enough to allow atomic mobility but remains short in time to avoid recrystallization and growth. Appropriate treatment can relieve up to 70-90% of stresses introduced during the manufacturing process [65], [84], [85], [86].

2.4.2 Annealing

Annealing is a process used to transform the microstructure of a material to remove the texture resulting from the manufacturing process. It involves heating the material above its recrystallization temperature for an appropriate time and then cooling it. Columnar-orientated grains, usually formed in LPBF, are replaced by a new set of grains that nucleate and grow until the original grains have been entirely replaced (see Figure 2.14). The three stages of the annealing process are recovery, recrystallization, and grain growth. Recovery occurs at low temperatures, followed by recrystallization, followed by grain growth if the time is prolonged [87]-[90].

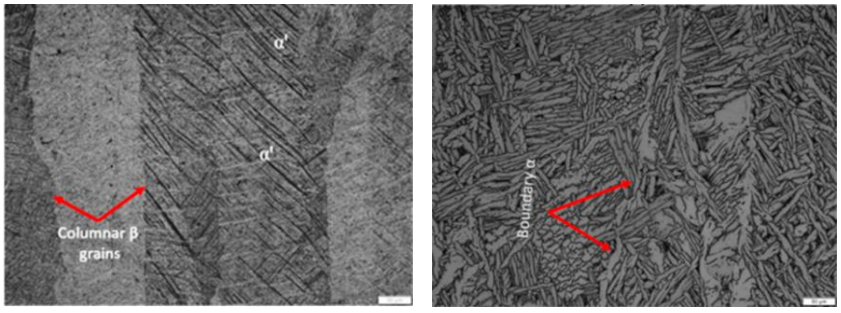

Figure 2.14: Typical LPBF Ti-6Al-4V microstructures before (left) and after annealing (right) [91] .

2.4.3 Hot isostatic pressing

Hot isostatic pressing (HIP) is a process used to reduce internal porosity and increase density by subjecting the material to elevated temperature and isostatic gas pressure, mostly argon, in a high-pressure vessel. It has been demonstrated to enhance ductility and reduce strength, and to increase fatigue life of Ti-6Al-4V LPBF specimens by reducing the defect population and altering the microstructure around defects [91], [93]-[96]. The selection of pressure, temperature, and time is dependent on the desired material properties, the component geometry, and acceptable manufacturing costs. Most LPBF parts are treated by HIP to close pores and internal cracks (see Figure 2.15).

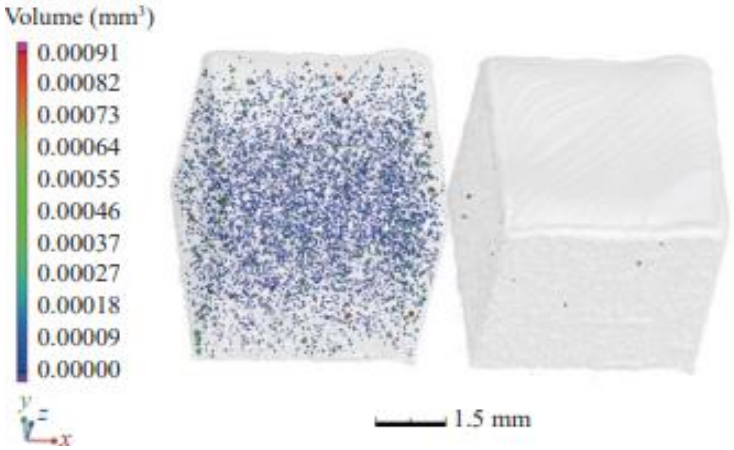

Figure 2.15: Micro-CT images of a Ti-6Al-4V sample before and after HIP [97].

2.4.4 Surface finishing

The inherent surface roughness of LPBF parts is usually unacceptable for some applications. Techniques such as abrasive blasting, barrel finishing, laser polishing, and electropolishing can improve surface roughness, but it is difficult to solve unilaterally. Two aspects of the problem require attention: the polishing of internal surfaces and developing a single process to solve all defect-related post-processing concerns. Chemical-abrasive flow polishing and abrasive flow machining have been used to finish interior surfaces [96], while ultrasonic surface treatments such as ultrasonic shot peening and ultrasonic nanocrystal surface modification have partially solved defect issues [99], [100]. Surface roughness is known to reduce fatigue life, and for AM components to be considered for use in dynamic environments, the surface finish must be held in equal

regard as in conventional manufacturing. The fatigue performance of AM Ti-6Al-4V parts has been shown to be reduced by up to 80% in conventionally manufactured Ti-6Al-4V parts, with the fatigue-life-limiting factors being firstly surface finish and secondly porosity imperfections [102].

2.5 Defect detection methods in LPBF

2.5.1 In-situ methods

In-situ monitoring methods for LPBF have been explored to detect defects during the manufacturing process. Popular approaches include thermographic and visual methods, but other strategies have also been studied. Much of the early work has utilized an in-line camera-based set-up to transmit electromagnetic radiation from the melt pool through the scan head, and a semi-transparent mirror is used to transmit an image to a high-speed camera and a photodiode as illustrated in Figure 2.16a. Closed-loop feedback can be used to stabilize the melt pool and keep temperatures within a predefined window [103]-[112].

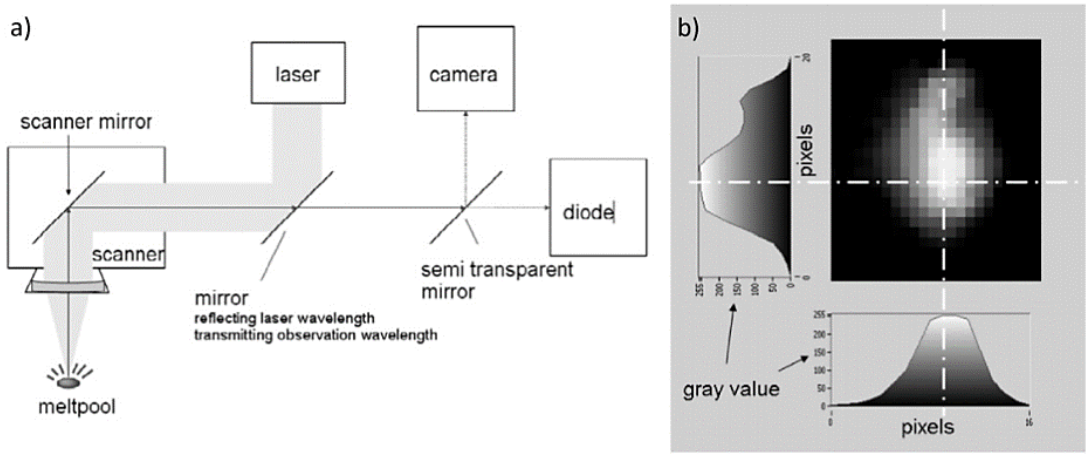

Figure 2.16: Schematic diagram showing the optical set-up to measure the intensity at the processing zone (a) and output example from the camera system (b) [107].

Although pyrometry-based systems have been demonstrated to create usable pictures of the melt pool region, there are no instances of pyrometry being utilized for closed-loop inspection due to the restricted data collection rate of pyrometers. Infrared (IR) cameras provide an alternative non-contact thermal measurement with a higher capture rate and

improved precision [112]-[113]. Figure 2.17 shows actual defect detection and three-dimensional reconstruction results obtained by the mapping method.

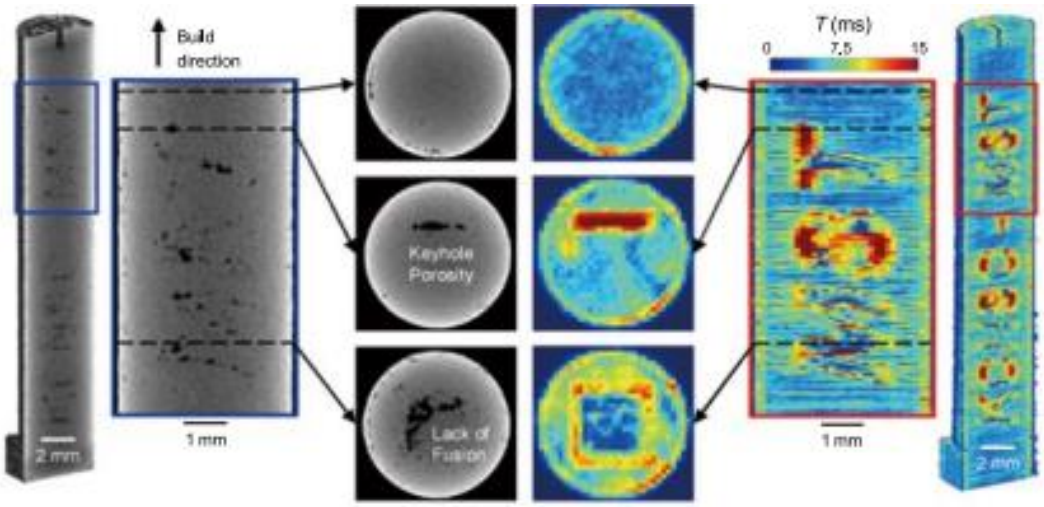

Figure 2.17: Example of comparison between actual defect detection results and 3D reconstruction results obtained by the mapping method [115].

High-speed cameras can be used to detect errors and material discontinuities on the powder bed [103], [106], [115]- [116]. Figure 2.18 shows an example set-up where multiple light sources were used to provide enough illumination, and imperfections were caused by a damaged recoater blade. Table 2.1 summarizes the image analysis methods applied in the LPBF process, many which are based on classical image processing algorithms and machine learning models. High-semantic-level image analysis approaches based on intelligent deep neural networks have previously been employed for in-situ monitoring of the LPBF process with satisfactory results [117].

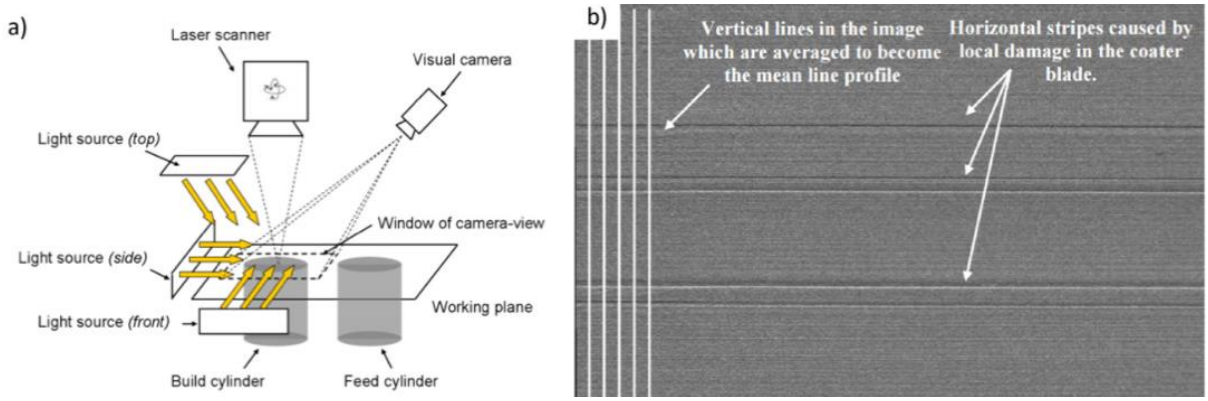

Figure 2.18: The basis of a visual inspection system (a) and a picture of a deposited layer (b) [114].

Table 2.1: Image analysis methods often employed in in-situ monitoring of the LPBF process [118]

Brief description	**Semantic level of image analysis**		
	Low	Medium	High
Typical algorithms	Image processing	Image processing + machine learning	Deep learning
Comments	Extract the basic features of images manually, such as brightness, geometry, and texture	Extract the basic features of images manually and recognize the defects automatically	Extract the basic features of images automatically and recognize the defects automatically
	Qualitative analysis	Quantitative analysis	Automatic, accurate and quantitative analysis

Acoustic monitoring has been envisaged as a potential monitoring technology for LPBF, but to date, there have been few published studies of this monitoring approach applied to the LPBF process [119], [120].

2.5.2 Ex-situ methods

Common non-destructive methods used to detect defects after LPBF manufacturing include ultrasonic testing (UT), X-ray computed tomography (X-ray CT), and electromagnetic testing (ET) to characterize LPBF builds with an emphasis placed on material properties. UT can be used to detect discontinuities in the part, and it is sensitive to any microstructural changes, which can be used to predict the mechanical properties of the part [40]. The UT technique is also being explored to gain insight into microstructure variations throughout the printed part by utilizing grain scattering techniques [120]. Figure 2.19 illustrates the variation in the longitudinal wave attenuation coefficient measured at various locations on a Ti-6Al-4V sample manufactured by LPBF.

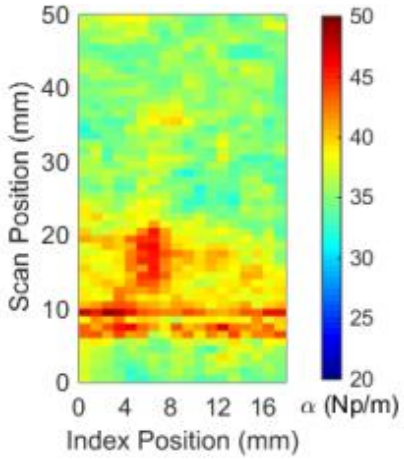

Figure 2.19: C-scan map ultrasonic attenuation of an AM Ti-6Al-4V part with the build direction along the scanning direction [122].

X-ray CT is a widely used technique in LPBF for detecting porosity and other flaws, such as cracking and dimensional deviations. It is based on the voxel size, the detector's sensitiveness to X-rays, and the direction of the flaws [123]-[128]. However, it cannot identify flaws when there is an attenuation that is too weak. Nevertheless, many researchers believe X-ray CT is a powerful instrument for the non-destructive testing of AM parts. Figure 2.20 illustrates an X-ray CT analysis in a Ti-6Al-4V test sample manufactured by LPBF.

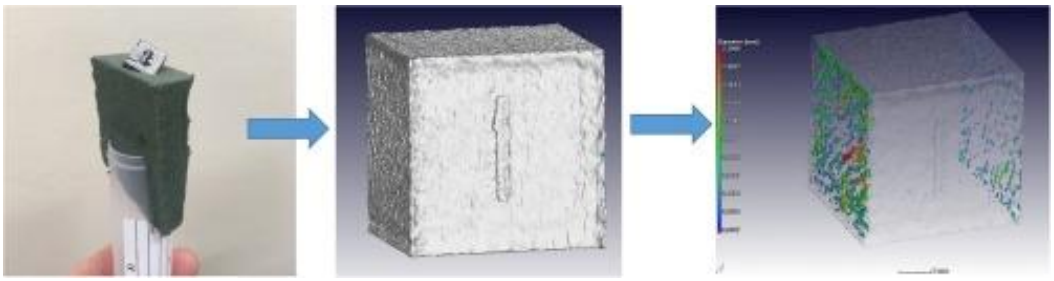

Figure 2.20: X-ray CT scanning procedure [128].

Electromagnetic testing techniques such as eddy current, microwaves, and magnetic resonance imaging can be used to detect surface and subsurface flaws in conductive parts by inducing electric currents or magnetic fields inside a part and measuring the electromagnetic response. Todorov et al. [129] used ET methods to investigate the electromagnetic properties of LPBF materials, including Inconel 625, duplex stainless steel 2205, and carbon steel 4140. However, the LPBF parts' surface finish and material

properties (conductivity) influence the success of these inspection techniques. Table 2.2 summarizes the various techniques that can be used for quality evaluation or in-service checking of LPBF parts.

Table 2.2: Example of non-destructive techniques that can be used to detect defects [130].

Methods	***Structure***	***Cracks, pores, voids***	***Mechanical properties***	***Geometric accuracy***	***Surface roughness***	***Residual stress***
Ultrasonic	Y	S, I	Y	Y	N	Y
Eddy current	Y	S	N	N	N	N
Radiographic	Y	S, I	N	S, I	S, I	N
Magnetic	Y	S	N	N	N	Y
Liquid/dye penetration	N	S	N	N	S	N
Acoustic	Y	Y	Y	Y	Y	Y
Thermography	N	Y	N	N	N	N

N – not applicable, S – surface sensitive, I – internal or through thickness, Y – applicable.

2.6 Residual stress measurement by diffraction methods

X-ray and neutron diffraction methods are used to measure residual stresses in LPBF parts. They use electromagnetic radiation to determine the distance between atomic planes in crystalline or polycrystalline materials. The radiation is absorbed and then reradiated with the same frequency, resulting in significant emissions at some orientations and low emissions at others. The angles at which the strong emissions occur are described by Bragg's equation:

$$n\lambda = 2d \sin\theta \qquad (2.2)$$

where n is an integer, λ is the wavelength of the electromagnetic radiation, d is the distance between the diffracting planes (inter-atomic lattice spacing), and θ is the angle at which X-rays contact the surface of the crystal, illustrated in Figure 2.21. A range of angles is scanned for stress measurements using X-ray and neutron diffraction, and the angle at which the most intense radiation is recorded is determined as the Bragg angle.

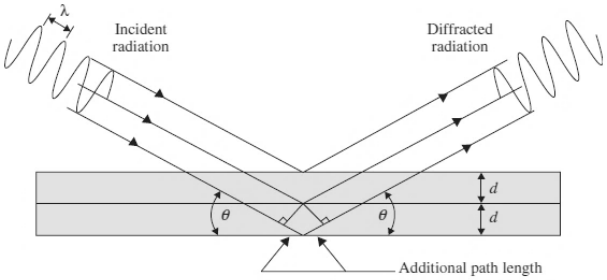

Figure 2.21: Diffraction of radiation within a crystal structure: d= distance between lattice planes, θ = half Bragg angle, and λ = radiation wavelength [131].

The position of the peaks is governed by the radiation wavelength and the material's inter-planar spacing. Peak positions can be changed by adjusting either of these. Thus, using a constant radiation wavelength and comparing the peak positions of strain-free and strained materials, it is feasible to calculate the lattice strain existing in a material [131]-[134]. The general strain equation for diffraction methods is as follows:

$$\varepsilon_{\psi} = \frac{d_{\Phi\psi} - d_0}{d_0} \qquad (2.3)$$

where ε_{ψ} is the strain in the direction defined by angle ψ, $d_{\Phi\psi}$ is the inter-planar spacing in the direction defined by angles Φand ψ, and d_0 is the strain-free inter-planar spacing. The $\sin^2 \psi$ method, commonly used with XRD, is used to convert the measured strain to stress.

2.6.1 X-ray diffraction

The most commonly utilized X-ray wavelengths for stress measurements are incapable of penetrating deep into most materials. Typically, X-rays from a specific anode or target of an X-ray tube, such as copper, chromium, or iron, are employed. X-ray penetration is typically in the order of 0.025 mm and is regarded as a surface stress assessment method in most cases. XRD can resolve type I and type II stresses depending on the grain size of the material being examined. The resolution of XRD stress measurements is influenced by the detector used and the Bragg peak chosen [131]-[135]. With position-sensitive detectors and a high Bragg angle larger than 120°, lattice measurements on the scale of 1e-6 Å are possible [133]. This results in a stress resolution of approximately 1MPa in Ti-6Al-4V [134]. Even though X-rays only offer stress assessments to a depth of about

0.025 mm, non-contact X-ray diffraction methods are currently the only non-destructive approaches for detecting residual surface stresses. Because of the technique's modest penetration depth, the recorded stress state is often considered in-plane stress. As a result, all stresses perpendicular to the surface are assumed to be zero.

2.6.2 Synchrotron X-ray

This approach, like the standard XRD method, employs X-rays; however, the X-rays are considerably more intense and of much greater energy, and because of their high energy, they penetrate significantly deeper into materials, on the order of millimetres. The strain measurement is based on Bragg's equation, but the Bragg angle is occasionally maintained constant. The stress state on the irradiated region cannot be assessed under plane stress and must be considered in three dimensions, so the strain is calculated by subtracting the unstressed lattice parameter from the stress value. This uncertainty in the unstressed lattice parameter is a significant source of inaccuracy in synchrotron diffraction residual stress measurement [130], [134].

2.6.3 Neutron diffraction

Neutron diffraction (ND) is a diffraction method that uses penetrating radiation and interacts directly with the nucleus of the atom. It has a spatial resolution of less than one millimetre and can quantify elastic strains generated by residual stresses across the volume of components of thickness ranging from 0.1 to 1.5 metres. It measures the Bragg angle of scattered radiation, which is proportional to the distance between crystallographic planes. However, the precision of ND approaches requires exact knowledge of the unstressed lattice spacing of the measure crystallographic planes, which is difficult to quantify due to the elemental composition and the lattice spacing varies greatly within an alloy component. Additionally, the component must be transported near a neutron source, each strain measurement takes several minutes to an hour, and the measurements are expensive [130], [134]-[138].

2.7 Ti-6Al-4V alloy

Among the family of titanium alloys, Ti-6Al-4V has 4 wt% vanadium and 6 wt% aluminum, which are added to stabilize the α and β phases, respectively. The microstructure of the alloy is mainly made up of 90 wt% hcp phase stable at room temperature, with the balance being the metastable bcc β. The amounts of these phases may vary depending on the type of heat treatment applied and the cooling rate, and the microstructure may contain primary or globular α, grain boundary α, acicular martensite α', basketweave and Widmanstätten structures [139]-[142]. Aluminium is added to increase the strength of the alloy by solution strengthening, while vanadium improves the room temperature ductility by obtaining balanced mechanical properties from both α and β phases. The Ti-6Al-4V ELI version of this alloy contains extra-low interstitial elements such as oxygen, nitrogen, carbon, and hydrogen, with high fracture toughness values and excellent damage properties [141], [143]-[144]. However, this alloy can be used up to temperatures of about 300°C due to low creep properties.

The solidification of this alloy can be traced with the ternary phase diagram shown in Figure 2.22. Under slow cooling conditions from the β transus temperature, the β phase primarily transforms to globular α. When cooled rapidly, the β phase is transformed into acicular α plates emerging from β grain boundaries to form a classical Widmanstätten structure in castings. It must be noted that depending on processing conditions, this alloy can also form metastable phases (α' and α'') and the intermetallic phase α_2. Figure 2.23 shows the typical microstructure observed in Ti-6Al-4V.

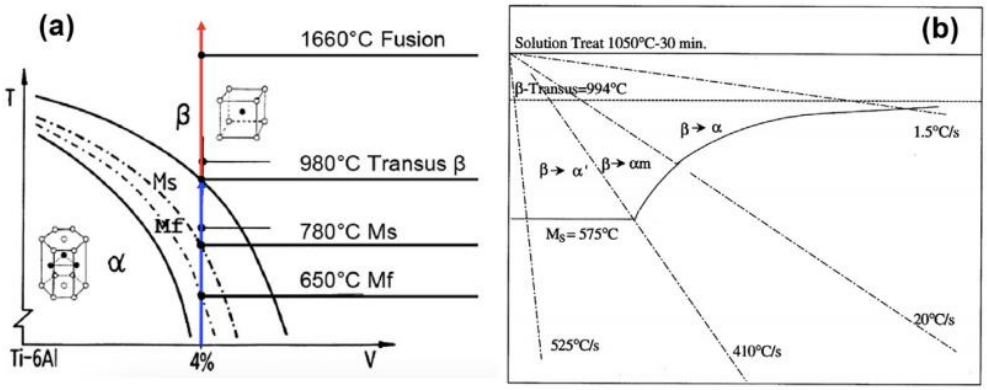

Figure 2.22: Phase diagram [144] (a) and continuous cooling curve of Ti-6Al-4V (b) [145].

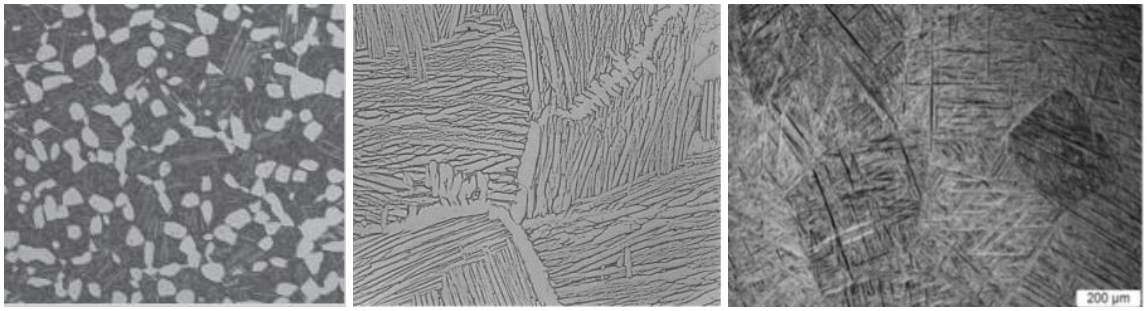

Figure 2.23: Classical Ti-6Al-4V microstructures showing bi-modal (a), Widmanstätten (b), and acicular martensite (c) [146].

The microstructural features that affect the mechanical properties of Ti-6Al-4V are the β-grain size, α-colony size, the thickness of grain boundary α and lamellar α, the size and shape of the primary α grains, the volume fraction of α and β, and tempered martensite. In lamellar α+β alloys, the most important factor that affects the mechanical properties is the α-colony size. Decreasing the α-colony size has the effect of improving the yield strength, ductility, crack propagation, and nucleation resistance. On the contrary, macro-crack propagation resistance and fracture toughness are improved by a larger α-colony size because of increased crack roughness and crack closure phenomena [146]. The α-colony size primarily depends on the cooling rate from the β-phase region and prior β grain. Interstitial elements such as oxygen can decrease ductility through age hardening by promoting the precipitation of coherent Ti_3Al particles, also known as the α_2 intermetallic phase. The chemical composition and mechanical properties of cast wrought and LPBF Ti-6Al-4V are shown in ASTM standards presented in Tables 2.3 and 2.4.

Table 2.3: ASTM standard requirement for chemical composition of cast and wrought Ti-6Al-4V alloy [147]-[149]

Element	**Chemical composition (wt. %)**		
	ASTM F1108-14 (cast)	**ASTM F136-13 (wrought)**	**ASTM F2924-14 (LPBF)**
Al	5.50 – 6.75	5.50 – 6.50	5.50 – 6.75
V	3.50 – 4.50	3.50 – 4.50	3.50 – 4.50

Fe	≤ 0.30	≤ 0.25	≤ 0.30
O	≤ 0.20	≤ 0.13	≤ 0.20
C	≤ 0.1	≤ 0.08	≤ 0.08
N	≤ 0.05	≤ 0.05	≤ 0.05
H	≤ 0.015	≤ 0.015	≤ 0.015
Titanium	Balance	Balance	Balance

Table 2.4: Minimum tensile properties of cast and wrought Ti-6Al-4V alloy [147]-[149]

Standard	**YS (MPa)**	**UTS (MPa)**	**Elongation (%)**
ASTM F1108-14	758	860	8
ASTM F136-13	795	860	10
ASTM F2924-14	825	895	6

2.8 Fatigue phenomenon

According to the ASTM E11050, fatigue can be defined as "the process of progressive localized permanent structural change occurring in a material subjected to conditions that produce fluctuating stresses and strains at some point or points and that may culminate in cracks or complete fracture after a sufficient number of fluctuations". The fatigue process usually takes place following three stages, namely (i) crack initiation, (ii) crack propagation, and (iii) sudden fracture of a material (see Figure 2.24). All these stages determine the material's fatigue life (N_f), which is the total number of load cycles required to initiate or nucleate a crack (N_i) and the number of load cycles to propagate the crack until the material fails (N_p). The loads applied are of a sinusoidal form, either between maximum and minimum tensile stresses or between maximum and minimum compressive stresses.

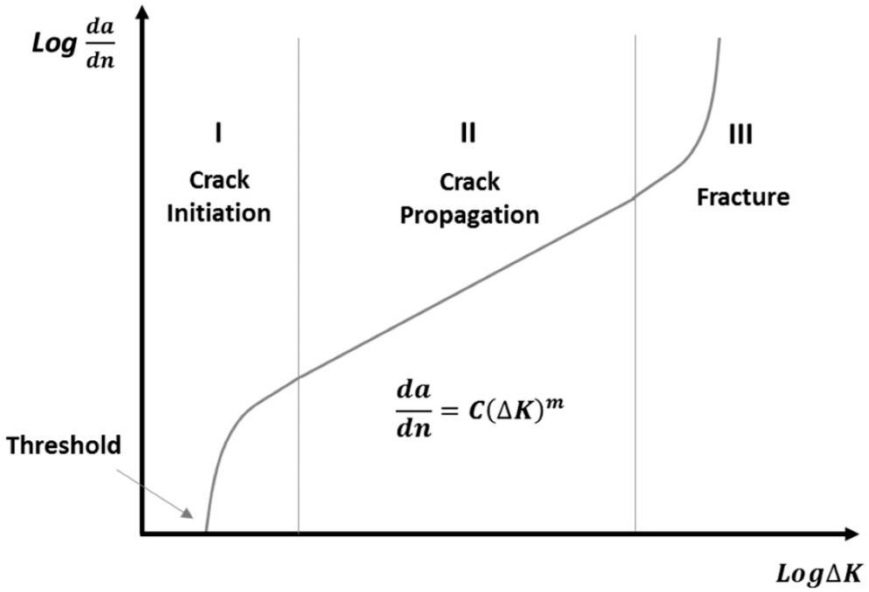

Figure 2.24: Fatigue crack propagation stages [150].

2.8.1 Crack initiation

Crack initiation occurs at stress amplitudes below the yield strength of a material whereby cyclic slip, Figure 2.25, occurs at a microscopic level involving only a few grains. It normally occurs at the surface since the material is less constrained than the inside. As shown in Figure 2.25, slip occurs in the plane of maximum shear stress (45°C) in ductile materials. Due to shear strain at the surface, the cyclic stresses cause dislocations to accumulate and slip bands to develop. A micro-crack is then nucleated, which may continue to grow under further cyclic loading. This stage is critical because it accounts for most of the fatigue life and is extremely reliant on the material's strength and surface quality.

Geometrical design and manufacturing discontinuities, including holes, keyways, notches, and changes in diameter, can also result in stress concentration areas on the surface. The stress concentration sites in LPBF Ti-6Al-4V may also come from process-induced micropores whose stress intensities during tension-tension loading are increased by the presence of tensile residual stresses on the surface. The number of stress cycles needed to create localized plastic deformation at all stress concentration locations decreases with an increase in the stress concentration factor (K_t), which lowers the number of cycles needed to start a crack. Where a crack develops from slip cracking, the

crack initiation site is characterized by facets similar to cleavages in flawless specimens (see Figure 2.26).

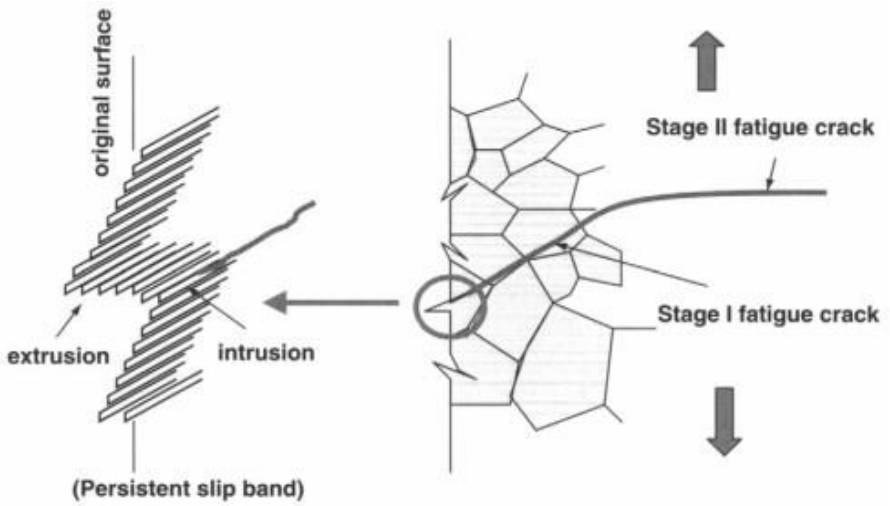

Figure 2.25: Stages of fatigue damage process by formation of slip bands and a crack along a slip plane [150].

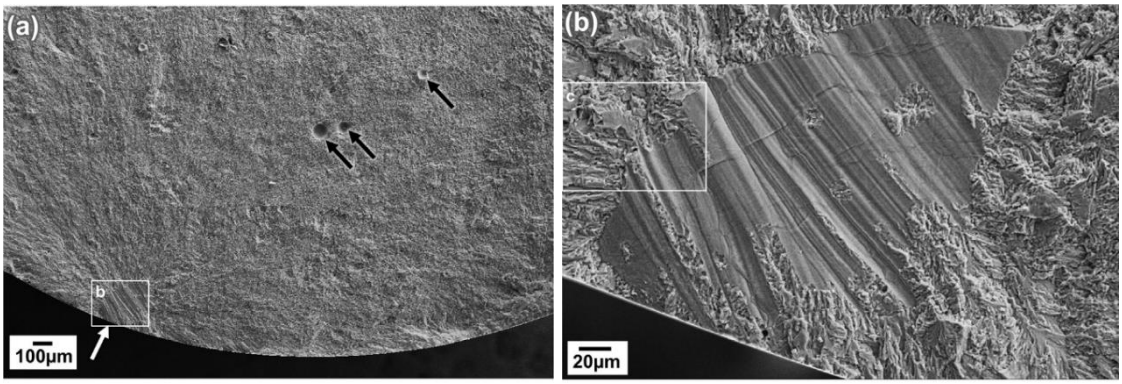

Figure 2.26: Example of crack initiation site caused by lack of fusion defect [151].

2.8.2 Crack propagation

This region makes up most of the fracture surface, and the crack often spreads in a trans-granular manner along the grain boundaries, generating a ragged, zigzag path. As the crack reaches this stage, the stress field at the crack tip has grown sufficiently to become dominant, and the fracture's general direction of development has turned perpendicular to the main loading direction. As a result, microstructural characteristics like phase and

grain size become crucial in terms of the resistance to crack growth at this stage. The crack propagation rate is significantly determined by the magnitude of the alternating load stresses rather than the mean stress and microstructure, and the surface condition has no bearing on this. Striations marks, which are crack arrests, perpendicular to the direction of crack propagation are usually observed on the fracture surface, as shown in Figure 2.27. The distance between each new set of striations is determined by the alternating stress magnitude. The gap widens as the alternating stress intensity increases. The following Paris equation, where C and m are both material constants, and ΔK is the change in stress intensity factor, describes the relationship between the alternating stress and fatigue crack growth rate.

$$\frac{da}{dN} = C(\Delta K)^m \qquad (2.4)$$

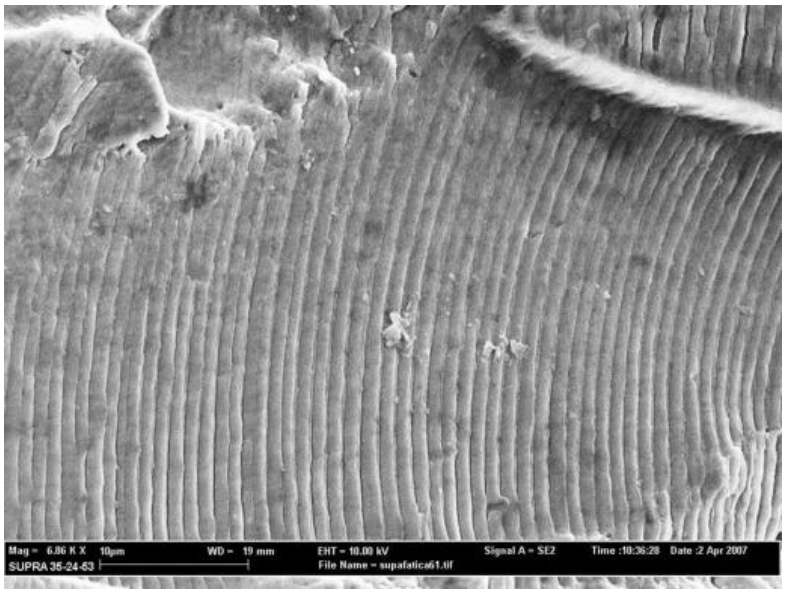

Figure 2.27: Example of striation marks observed on the fracture surface [152].

2.8.3 Final fracture

This stage begins when the crack has developed to the point that the amount of force remaining on the material causes stresses to exceed the material's ultimate tensile strength, which causes an abrupt fracture. The applied load and critical length (a_c) of the crack at the beginning of this stage define a material's fracture toughness (K_{IC}). Figure 2.28 illustrates the ultimate fracture shear surface, which has cleavage at 45° angle.

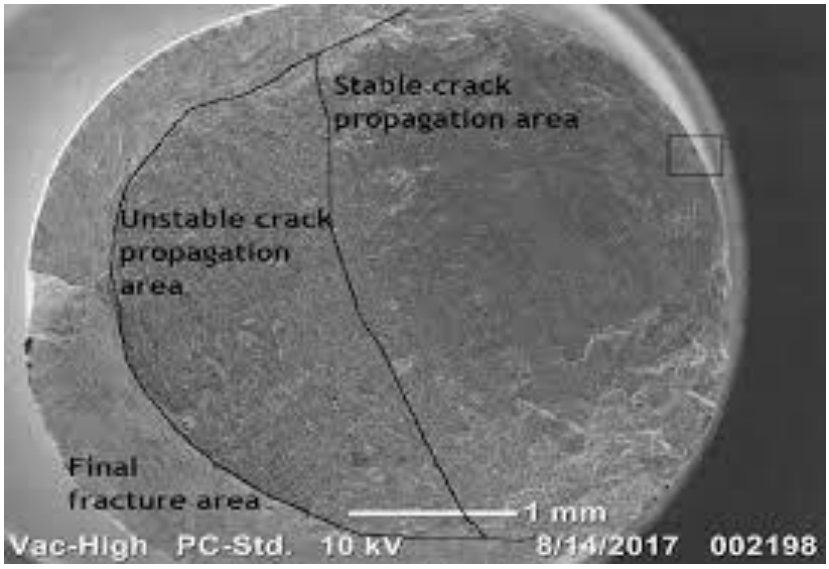

Figure 2.28: Fracture surface showing different stages of crack propagation [153].

2.8.4 Fatigue stress

Since fatigue damage is driven by stress fluctuations rather than maximal stress, the stress amplitude σa (or range Δσ) and the mean stress σm are the essential aspects of fatigue assessment (see Figure 2.29). The difference between the minimum and maximum stress in a cycle is used to calculate the stress range. The stress range or amplitude can be calculated using nominal or local stresses. Furthermore, other directional stress components or principal stresses might be employed. With so many options, it is important to describe in text or by utilizing subscripts to which specific stress, range, or amplitude they correspond. Stress amplitudes are usually used for machine components and stress ranges for weld components. In practice, the mean stress is typically linked to the stress amplitude so that as the amplitude increases, so does the mean stress. This condition can be stated using a constant stress ratio (R). Figure 2.30 shows the most applied stress ratios in fatigue testing. Positive stress ratios (R) for the compression-compression and tension-tension cyclic load regimes fall between 0 and 1. The R value is smaller than zero when tension-compression takes place.

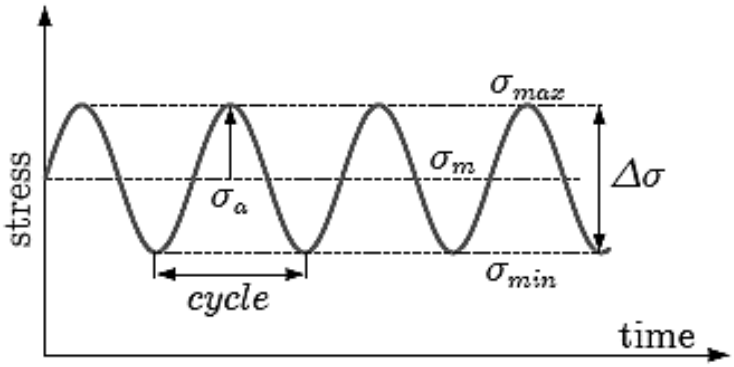

Figure 2.29: Example of fatigue stress profile for repeated stress cycling.

$$\sigma_a = \frac{\sigma_{max} - \sigma_{min}}{2} \quad (2.5)$$

$$\Delta\sigma = \sigma_{max} - \sigma_{min} = 2\sigma_a \quad (2.6)$$

$$\sigma_m = \frac{\sigma_{max} + \sigma_{min}}{2} \quad (2.7)$$

$$R = \frac{\sigma_{min}}{\sigma_{max}} = \frac{\sigma_m - \sigma_a}{\sigma_m + \sigma_a} \quad (2.8)$$

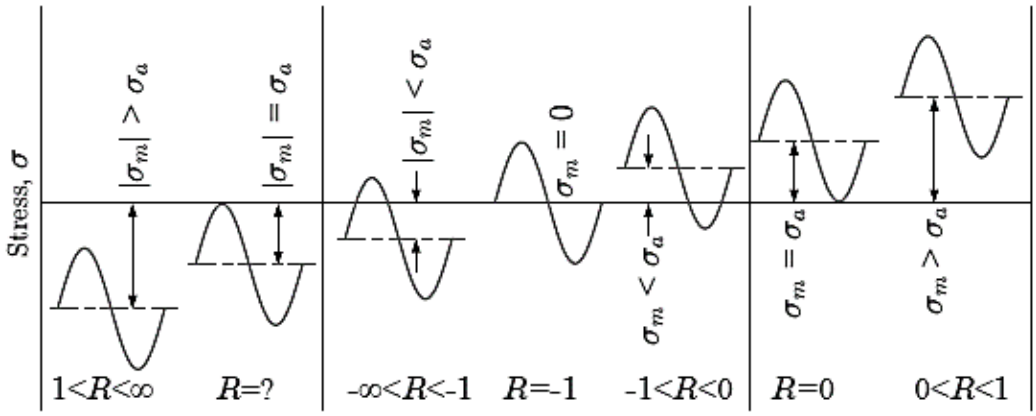

Figure 2.30: Types of fatigue stress loading conditions.

The fatigue strength for high-cycle fatigue is often expressed using an S-N curve as illustrated in Figure 2.31. The S-N curve is commonly derived using an axial fatigue test machine, in which each sample is subjected to a constant load amplitude at a specified frequency. Cyclic loading is applied to the specimens until they fracture or run out. Upon testing of the specimens, the corresponding values of σ_{max} or σ_a and number of cycles

(N), represented as $log_{10}N$ are plotted to give a semi-log S-N curve. The number of cycles that determine the run-out criteria can vary (e.g., 10^5-10^8) depending on the intended application. To allow comparison of the results obtained, the specified R ratio and frequency must be the same for all specimens for a series of tests.

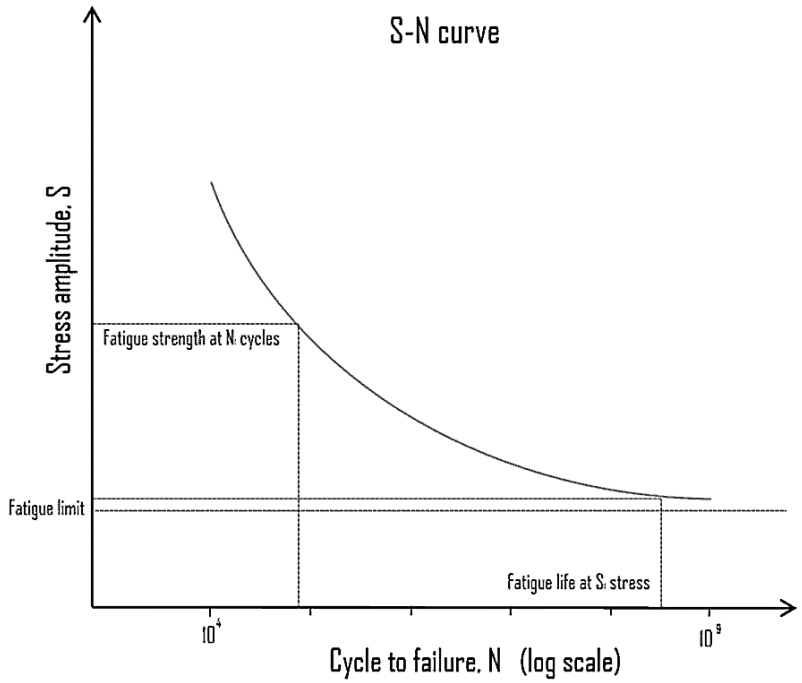

Figure 2.31: Typical S-N curve and fatigue life determination.

2.9 LPBF of Ti6-Al-4V

2.9.1 Microstructure evolution

In LPBF, solidification takes place quickly due to large thermal gradients. As such, the developed microstructure is dominated by metastable α' phase inside columnar prior-beta grains, which appear as continuous multi-layered structures, as depicted in Figure 2.32a. The average width of the prior-beta grains is directly associated with the scan track width or hatch distance and can also be affected by the laser energy density [154]-[157]. The columnar grains grow epitaxially by a remelting and nucleation process on top of previously solidified layers [158]. Many studies have been carried out to reconstruct the previous structures and texture using electron backscatter diffraction (EBSD) to understand the growth mechanism of the prior-beta grains based on the Burgers orientation relationship.

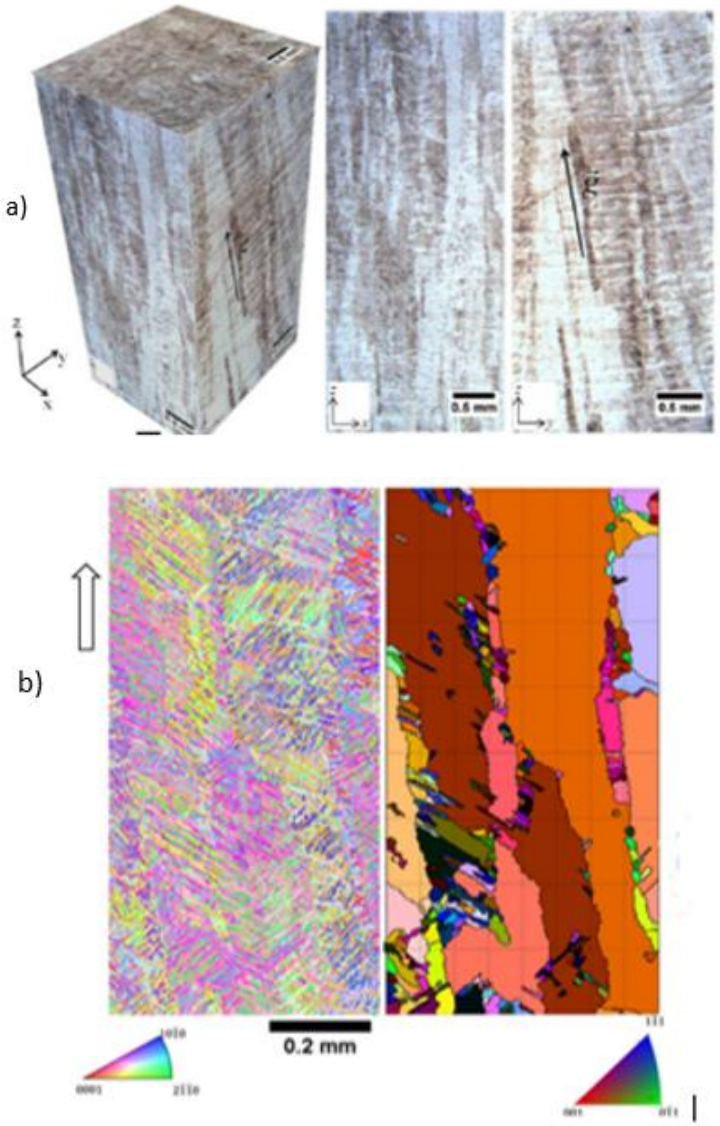

Figure 2.32: Typical columnar grains (a) and prior-beta reconstruction by EBSD (b) [154].

A solid <001> fibre texture with a longitudinal axis of prior β grains, b, parallel to the building direction, has been reported in many studies [159], [160]. This is because the direction of heat flow in LPBF is perpendicular to and toward the substrate, caused by a downward conductive and outward convective heat flow. The scanning strategy has also been shown to influence the microstructure texture. Simonelli et al. [155] noted columnar grains that grew at an inclined angle of around 20° to the z-axis when using a rotating scanning strategy. Wavy grain boundaries were also observed by Zhang et al. [159], and this was attributed to changes in scanning vectors.

Because of the track-by-track and layer-by-layer manufacturing method, the α'-grain size has been found to increase with the input energy density [154]-[155], [159]. Coarsening of the grains occurs because of multiple thermal cycles in the overlapped zones. The low thermal conductivity of Ti-6Al-4V of about 7 W/m·K at room temperature also leads to heat accumulation with increased numbers of layer, which result in higher temperature and a slower cooling rate at the upper zone of the manufactured part [159]. The morphology of α' can be detected easily by light microscopy and scanning, as depicted in Figure 2.33.

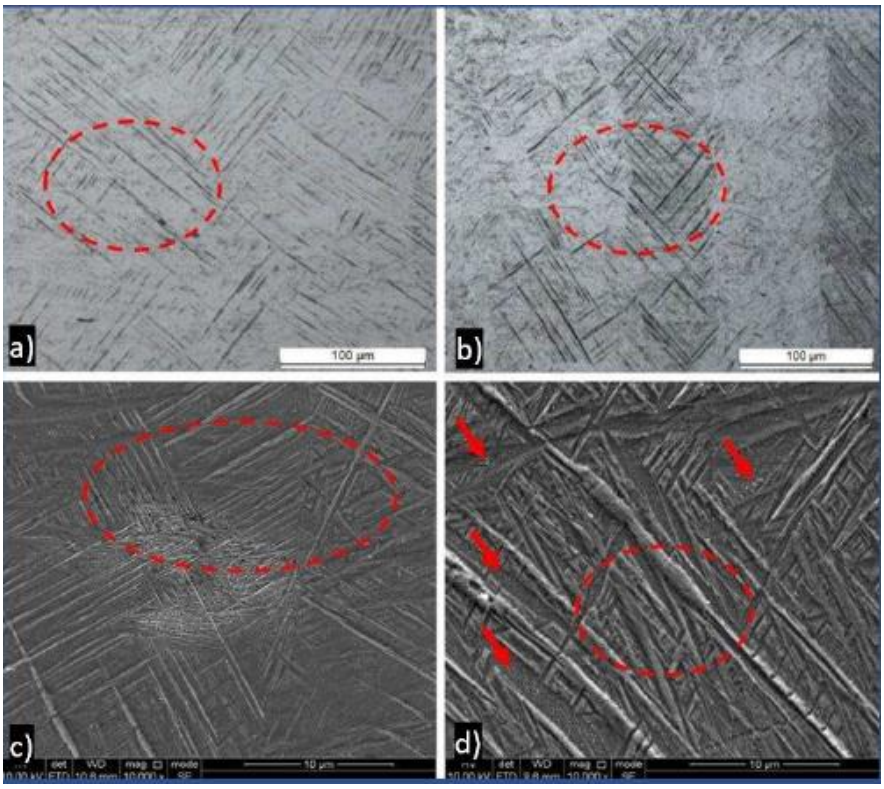

Figure 2.33: Optical micrographs showing acicular martensite in Ti-6Al-4V (a, b) and the corresponding SEM micrographs (c, d) [162].

A few studies found that a small amount of the β phase can be present in the specimens fabricated at either high laser powers or short hatch distances [96]. The laser power and shorter hatch distance increase the in-process temperatures and the time at high temperatures during intrinsic thermal cycling. The α_2 precipitates in the as-built condition have also been reported based on TEM and XRD analysis, and it was believed to have

formed due to thermal cycling just below the α_2 solvus temperature. The formation of this phase can be suppressed by careful control of Al and O in the alloy and low concentration of O in the chamber during the printing process [161]. Figure 2.34 shows the superlattice reflection of α_2 formed in the α lamella.

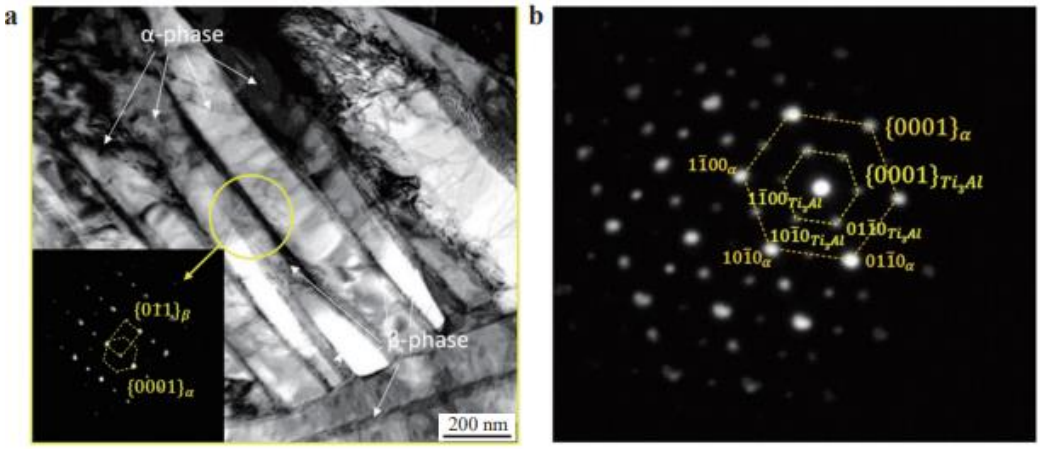

Figure 2.34: TEM used to detect β and α_2 phase in the as-built LPBF Ti-6Al-4V. (a) TEM bright field view of Ti-6Al-4V sample with α+β microstructure at the middle height (Z~5 mm) of a Ti-6Al-4V sample. (b) Ordered α_2 selected area diffraction (SAD) pattern within α plate [96].

The effect of preheating the substrate, mainly to mitigate residual stress development, on the microstructure was also investigated, and it was found that the decomposition of α' commences at a low temperature of 400 °C [161]. β phase was also observed in the as-built condition when the substrate was preheated to 200 °C in conjunction with a smaller hatch distance of 40 μm [162]. Preheating at 500 °C resulted in partial decomposition of the α' phase, which improved the elongation to about 10% [161]-[162]. However, Ali et al. [162] found that high temperature preheating at 550 °C led to significant oxidation since titanium has a high affinity to oxygen at high temperatures. High oxygen content will cause embrittlement and deteriorate powder recyclability. In addition, high-temperature preheating is energy intensive and can account for 40% of the total energy consumed [163]. Other in-situ methods, such as manipulation of the beam focal offset distance [164] and interlayer time [165] have been applied to promote α' decomposition.

2.9.2 Heat treatment response and tensile properties

The advantage to Ti-6Al-4V alloy is that it is heat treatable, and various properties can be obtained for specific application needs. Standard heat treatments for this alloy can be classified into four categories: *stress relief, annealing, solution treatment and aging, and hot isostatic pressing*. Heat treatment is usually carried out under a protective environment (argon or vacuum) to prevent oxidation when the temperature is raised to above 427 °C. Heat treatment under an oxygen environment will lead to the formation of a brittle phase denoted as alpha case, resulting in low ductility and fatigue performance [166].

Stress-relieving heat treatment is generally carried out to relieve residual stresses that develop during the printing process to avoid post-cracking or distortion. The heat treatment is carried out in temperatures between 450–650 °C while the parts are still attached to the baseplate and supports, followed by air or furnace cooling. The holding time is dependent on the temperature; see Figure 2.35. The α_2 solvus temperature is about 550 °C for Ti-6Al-4V; therefore, the treatment temperature should be chosen carefully on whether α_2 is ideal for application, especially if the parts are to be used after stress relieving [166].

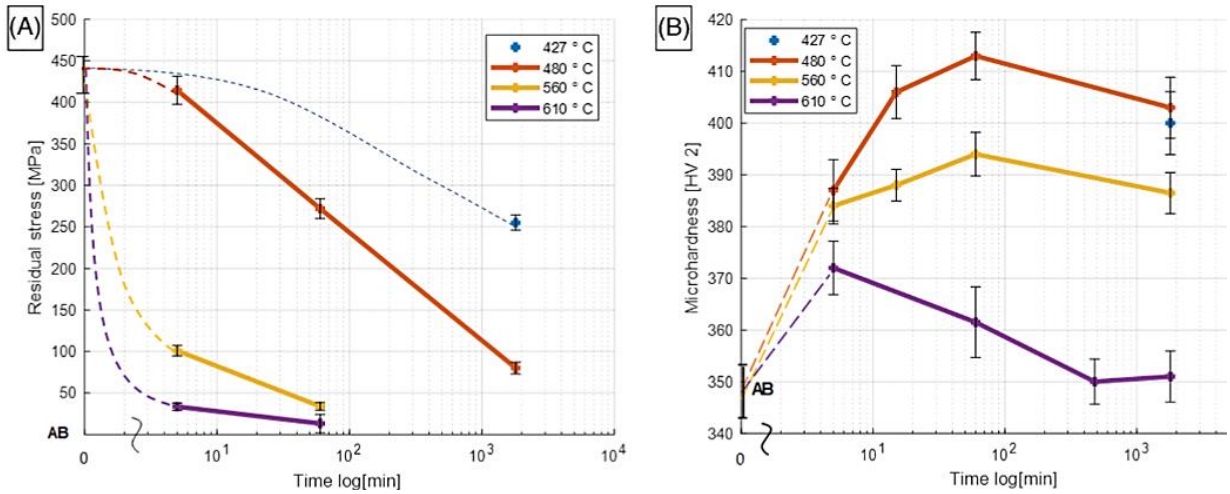

Figure 2.35: Magnitude of residual stress and microhardness for stress-relieved samples as a function of time [166].

Annealing/recrystallization heat treatments are applied to Ti-6Al-4V to transform the brittle metastable α' phase found in the as-built condition to an equilibrium α+β microstructure. Previous studies have shown these heat treatments can be applied at a

temperature range of 750–950 °C to effectively facilitate the decomposition of the α' phase and improve the ductility, toughness, thermal stability, and creep resistance [87], [166]. Heat treatment above the β transus temperature coarsens the prior β-grains, and the β grains lose the columnar morphology, as shown in Figure 2.36.

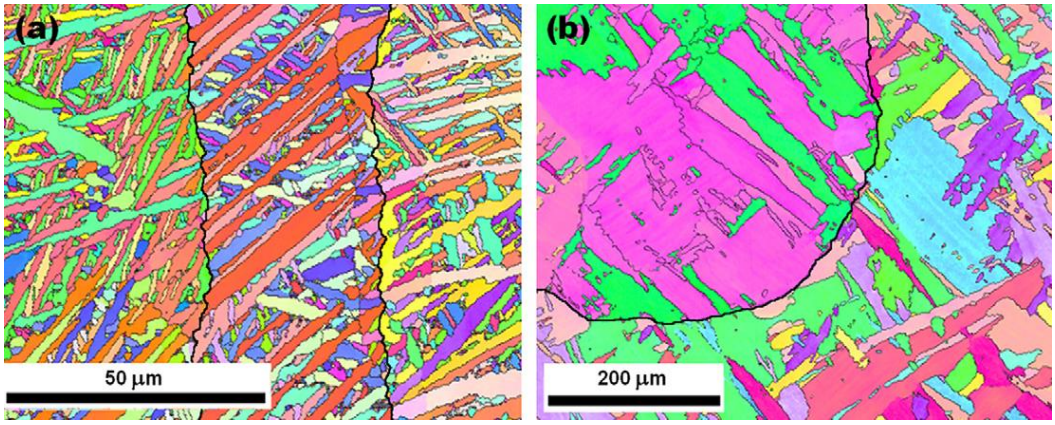

Figure 2.36: Effect of heat-treatment temperature on microstructure. [a] EBSD orientation map of post-process heat treated at sub-transus 850 °C/2h/FC84. [b] EBSD orientation map of post-process heat treated at super-transus 1020 °C/0.5h followed by sub-transus 730 °C/2h/AC [88].

Because of the wide range of annealing temperatures, numerous microstructures with varying sizes, volume fractions, and morphologies of distinct phases are achievable. A list of established annealing heat treatments and typical microstructures formed is presented in Table 2.5.

Table 2.5: Summary of annealing heat treatments for alpha-beta alloys [168]

Heat treatment designation	**Heat treatment**	**Microstructure**
Duplex anneal	Solution treat at 50–75 °C below T_β, air cool, and age for 2–8 h at 540–675 °C	Primary α, plus Widmanstatten α-β regions
Beta anneal	Solution treat at 15 °C above T_β, air cool, and stabilize at 650–760 °C for 2 h	Widmanstatten α-β colony microstructure
Recrystallization anneal	925 °C for 4 h, cool at 50°C/h to 760 °C, air cool	Equiaxed α with β at grain boundary triple points
Mill anneal	α-β hot work plus anneal at 705 °C for 30 min to several hours and air cool	Incompletely recrystallized α with a small volume fraction of small β particles

Solution treatment and aging is carried out to obtain maximum strength by increasing the volume fraction of the β phase. The procedure involves heating slightly below or above the β transus temperature. Treatment carried out below the β transus has yielded high strengths and adequate ductility. When the temperature is raised above the β transus, excellent strengths are obtained at the expense of ductility [167]-[168]. The heat-treatment procedure involves solution treating, quenching, and aging at temperatures ranging from 480–595 °C. *Hot isostatic pressing (HIP)* is primarily applied to reduce porosity and improve the fatigue strength of Ti-6Al-4V. One drawback of HIP is the longer holding time, which has been shown to coarsen the microstructure and slightly reduce the overall tensile strength. However, the benefit of better fatigue strength far outweighs the slight drop in tensile strength.

Numerous studies have been conducted to investigate the mechanical properties of LPBF-manufactured Ti-Al-4V, and one such analysis is that of authors [96], where they investigated the values of yield strength (YS), ultimate tensile strength (UTS) and elongation for different types of microstructures. Their results are presented in Figure 2.37 and show that the α' microstructure exhibits the highest YS and UTS but suffers from low elongation.

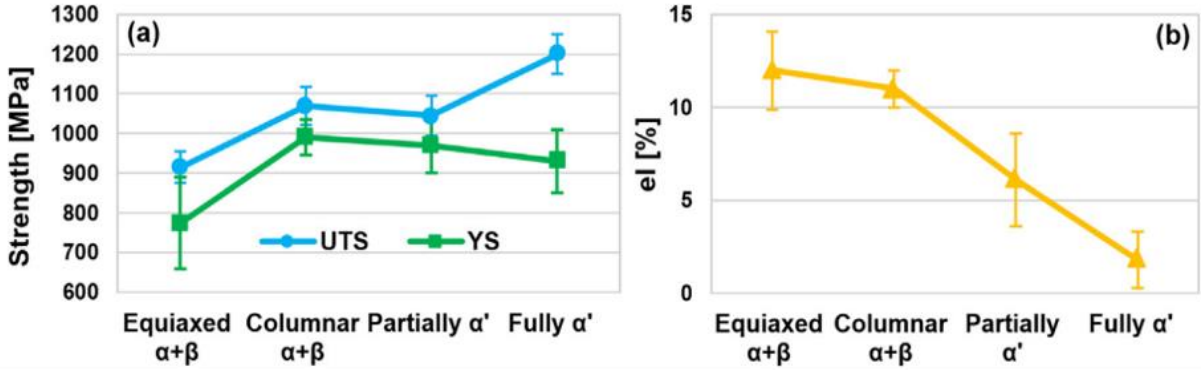

Figure 2.37: The influence of microstructure on tensile properties [96].

The α/α'-width is the most influential microstructural feature in Ti-6Al-4V, and the relationship between the α/α'-width and the tensile strength can be described by the Hall-Petch relation as illustrated in Figure 2.38, whereby a linear relationship was established

between the YS and the inverse square root of α or α' width [96]. The scatter in tensile properties was attributed to other factors such as specimen orientation, composition, porosity, powder characteristics, LPBF system, processing parameters, and scanning strategy. Some of the different heat-treatment procedures and mechanical properties of LPBF Ti-6Al-4V obtained from the literature are presented in Table 2.6

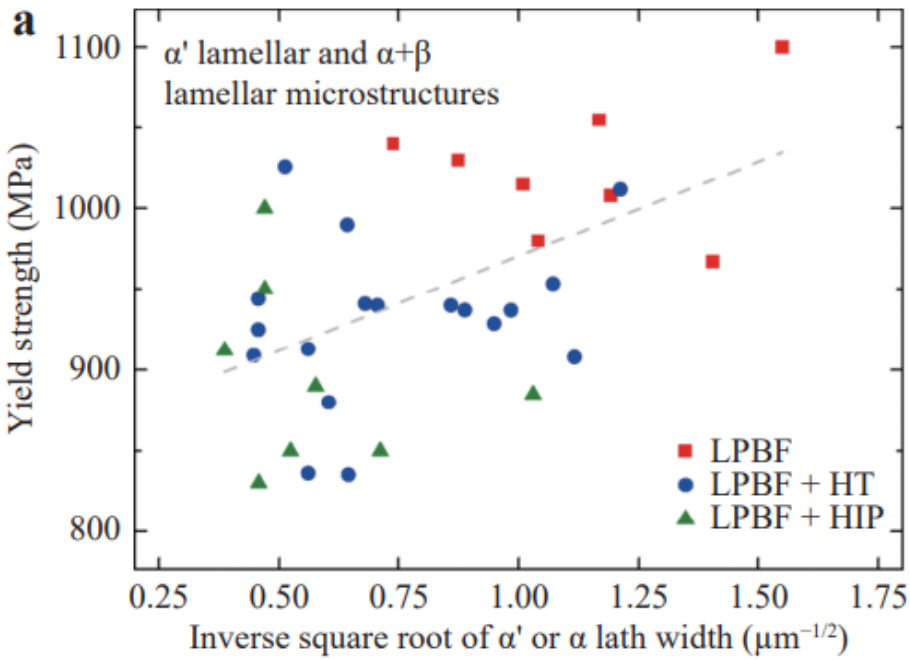

Figure 2.38: A Hall-Petch relation between yield strength and the width of α' or α laths in Ti-6Al-4V with a lamellar microstructure fabricated by LPBF [96].

Table 2.6: Review of microstructures and mechanical properties of LPBF Ti-6Al-4V after heat treatment [161]

Heat treatments	Procedure	Microstructure	Orientation	YS (MPa)	UTS (MPa)	Elongation (%)
	670 °C, 5 h, FC	Partially decomposed α' lamellar	Vertical	1015	1090	10
	700 °C, 2 h, FC	Partially decomposed α' lamellar	Vertical	1051	1115	11.3
	730 °C, 2 h, FC	Partially decomposed α' lamellar	Vertical	937 ± 9	1052 ± 11	9.6 ± 0.9

Annealing	800 °C, 2 h, FC	Partially decomposed α' lamellar	Vertical	-	1228 ± 32	8 ± 1.5
	800 °C, 6 h, FC	α+β lamella	Horizontal	937 ± 4	1041 ± 5	19 ± 1
	920 °C, 2 h, FC	α+β lamella	Vertical	850	933	15
	910 - 930 °C, 8 h, WQ + 750 °C, 4 h, FC	α+β bi-lamellar/bimodal	Vertical	~900	~950	~18
	Thermal cycling between 975 °C and 875 °C, 24 h, AC	α+β bi-modal	Vertical	849 ± 12	1004 ± 23	16 ± 1
Solution treatment	1050 °C, 2 h, FC	α+β lamella	Vertical	-	986 ± 45	13.8 ± 0.8
HIP	900 °C, 100 MPa, 2 h, FC	α+β lamella	Vertical	885	973	19
	920 °C, 100 MPa, 2 h, FC	α+β lamella	Vertical	850	960	14
	920 °C, 120 MPa, 2 h, FC	α+β lamella	Vertical	839	941	19
	930 °C, 100 MPa, 4 h, FC	α+β lamella	Horizontal	865 ± 19	936 ± 4	22 ± 2
	1050 °C, 100 MPa, 2 h, FC	α+β lamella		-	1007 ± 15	13.5 ± 0.7

2.9.3 Fatigue properties

The fatigue performance of LPBF Ti-6Al-4V has been widely studied, and it has been found that the surface roughness, manufacturing defects, residual stress, and microstructure affect the fatigue strength, with the surface roughness being the crucial factor [96], [103], [169]-[171]. The fatigue strength of as-built LPBF parts without surface treatment is worse than that of cast products. Measurement of fatigue strength is usually done by adopting the stress-life (S-N) or strain-life (ε-N) approaches. The fatigue limit and stress intensity factor before a crack propagates are two common parameters used to characterize fatigue performance. Figure 2.39 shows the experimental results from Bagehorn et al. [172] on the effect of various surface treatments on the fatigue strength. The comparable or even higher high-cycle-fatigue (HCF) strength in improved surface conditions is due to the finer microstructure than wrought or cast Ti-6Al-4V, which results

in short effective dislocation slip length and high resistance to crack initiation [172]. When the defects are present on the surface or subsurface, HIP cannot close such related defects and fails to improve the fatigue strength of samples with inherent surface quality.

The following observations are prominently based on fatigue data reported on LPBF Ti-6Al-4V [103], [169]-[174]:

1. Surface finishing is essential to achieve superior fatigue properties. For example, the fatigue limit of LPBF Ti-6Al-4V specimens with a surface roughness of Ra ≈ 13 μm was 210 MPa, compared to 500 MPa after polishing [175]. Shot peening and laser shock peening have also been proven effective in improving the fatigue limit by introducing a compressive residual stress layer [172].
2. The fatigue data of LPBF Ti-6Al-4V scatter broadly. Research has shown that LPBF Ti-6Al-4V can achieve fatigue strengths comparable to, or even better than, those of the mill-annealed Ti-6Al-4V. On the other hand, LPBF Ti-6Al-4V can be inferior to as-cast Ti-6Al-4V [173]-[175].
3. Anisotropic fatigue strength is observed in LPBF Ti-6Al4V due to the columnar prior β grain structures, non-uniform distribution of pores and lack-of-fusion defects, and other microstructural features [174]-[175].
4. HIP can improve fatigue strength and HCF performance and reduce data scatter because of much reduced internal porosity and the elimination of other defects. In general, LPBF HIPed Ti-6Al-4V samples with machined surfaces can show HCF performance comparable to, or better than, mill-annealed Ti-6Al-4V [96], [161].

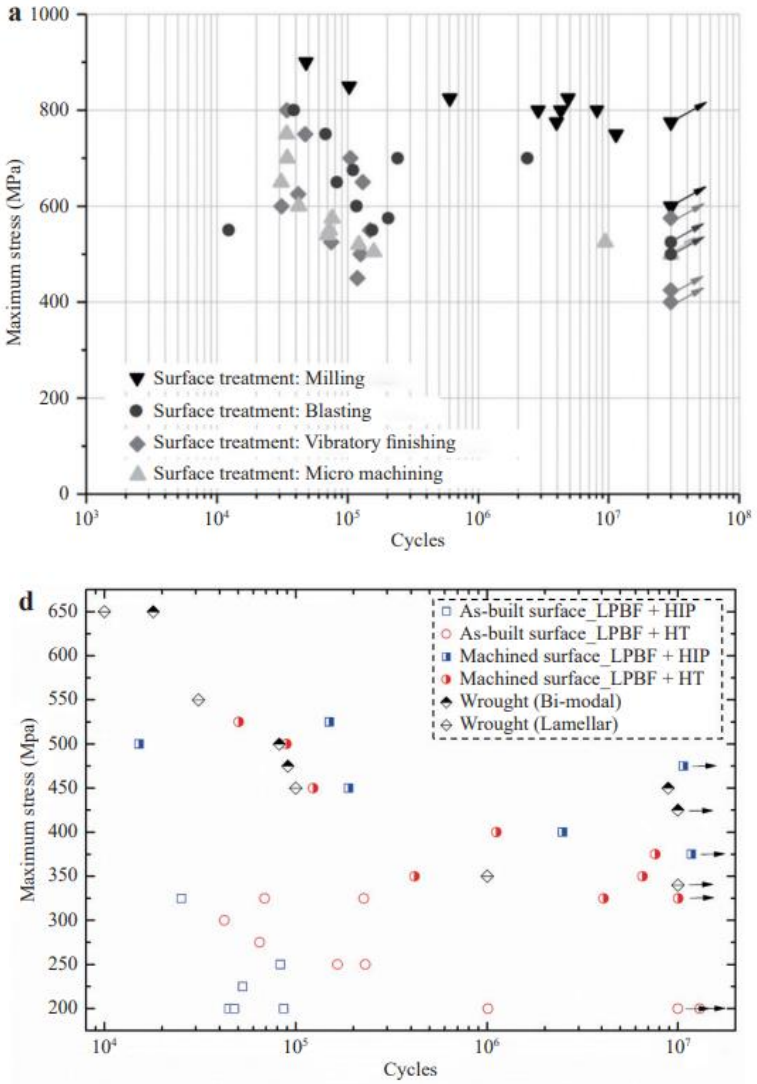

Figure 2.39: Effect of surface finishing on HCF strength of Ti-6Al-4V [172], [174].

2.10 Beam shaping in LPBF

With the aim of processing a larger volume of material instantly, the use of high-power laser sources has been proposed. Considering that the standard energy distribution profile of commercially available laser beams is Gaussian, a high local spot intensity in the centre of the beam facilitates the formation of keyhole porosity and spatter. In addition, the Gaussian profile is reported to result in a lack of fusion due to the low intensities at the edges of the beam. Therefore, a modification of the laser beam geometry was proposed to optimize the energy absorption while avoiding the formation of defects. Modern methods of beam shaping make it possible to use other beam shapes in addition to

Gaussian and top-hat profiles. The advantages of alternative beam profiles have been discussed in the literature with regard to welding. Research done to examine how the LPBF process can benefit from non-Gaussian laser beam profiles remains limited.

Single tracks were produced using a Gaussian profile, a top-hat profile, and donut profile, as well as varying laser power and scan speed on a CoCrMo powder [186]-[189]. Zhirnov eat al. [186] were able to achieve noticeably wider process windows using alternative beam profiles (top-hat and donut profile) instead of a Gaussian beam profile. Based on that, Metel et al. [187] showed that the process can be expanded with other beam profiles. For the top-hat profile, power and speed was increased by 14% with similar geometric parameters of the single tracks, and, by using donut profile, power and scan speed was increased by 43%. Okunova et al. [188],[189] also showed that the use of top-hat and donut-shape profiles can reduce spatter formation and the width of the denudation zone. The stability and productivity of the LPBF process was investigated by Wischeropp et al. [190] using a donut-shaped beam profile on AlSi10Mg powder. They were able to achieve larger melt pools with fewer defects (cracks, balling, and porosity), and thus a better process robustness. The potential to increase the build rates by using a top-hat profile was demonstrated by Schleifenbaum et al. [191] and Loh et al. [192] when processing steel. They achieved build rate of 5 mm^3/s with powder layer thicknesses of 100 µm [191] and build rates of 20 mm^3/s with powder layer thicknesses of 400 µm and relative densities of more than 99% [192].

Lantzsch et al. [193] used two alternative productivity scaling approaches, processing with defocused Gaussian and ring-mode laser profiles, to analyse melt pool formation, relative density and theoretical build rate for LPBF of Inconel 625 alloy. Analysis of the melt pool formation indicated a heat-conduction dominated processing regime within the entire process parameter range for both, defocused Gaussian and ring-mode beam profiles. Both approaches yielded theoretical build rates that were 110-150 % higher than the reference LPBF process while maintaining relative densities ≥ 99.9%. Bayol and Pallier [194] also studied the ability of laser beam shaping in addressing productivity and

quality challenges in LPBF using Inconel 939 powder. They used a multi-plane light conversion to develop a reconfigurable beam shaper that can create three different beam profiles: an ellipse, a ring and a round top-hat, and the latter two we found to produce parts with homogeneous properties across the entire working plane.

This shows that the use of non-Gaussian beam profiles has a high potential to positively influence the process. Most of the beam shaping methods established today in LPBF result in fixed symmetrical beam profiles such as top-hat or ring-shaped profiles. This limits the quality of solutions for an optimal beam profile optimised to a desired thermal profile. Therefore, in the field of LPBF, novel technologies to generate non-symmetric beam profiles are currently also developed and their applications are investigated [195].

2.11 Chapter summary

Laser powder bed fusion offers its capability to manufacture parts with complicated design features for various industrial applications. It uses a laser source to melt metal powder in a layer-by-layer process. In this chapter, several aspects of LPBF technology were reviewed and discussed. The typical physical phenomena taking place during laser-powder interaction were briefly discussed. These physical phenomena are important in LPBF as they govern the melting mechanisms and influence the quality of the melt track and the part manufactured. The general characteristics of parts manufactured by LPBF were also reviewed and briefly discussed. The most common attributes such as porosity, surface roughness, residual stress development, and microstructure texture associated with LPBF were discussed. It was found that proper selection of process parameters can help to reduce the occurrence of defects during the manufacturing process. It is necessary to recognise and conduct proper inspection of defects and mechanical properties before parts are placed in operation. As such, the literature review also addresses some of the common methods used to detect defects in LPBF. Post processing of LPBF parts is often applied to enhance the quality and mechanical properties of the parts. The most common post processing techniques applied to LPBF parts were also reviewed and discussed. It was found that post heat treatments can be applied to transform the heavily textured

microstructure obtained in the as-built condition to enhance the mechanical properties. Surface finishing operations can also enhance the quality and fatigue properties of the parts made by LPBF.

Aiming to improve the LPBF productivity, recent research progress on laser beam shaping as a potential method to increase productivity were reviewed and briefly discussed. It was found that there is a significant effect of laser beam profile on the LPBF process, and that non-Gaussian beam profiles offers several advantages over standard Gaussian beam profile. However, the effect of the beam profile on other important characteristics such as microstructure, surface roughness and, ultimately, the mechanical properties have not been thoroughly investigated. Accordingly, this research study aims to investigate the effects of high power LPBF using a non-Gaussian beam profile with enlarged spot diameter on the productivity and stability of the process and compared with counterparts made with regular commercially available setup. The microstructure and mechanical properties of the parts made using high powers with non-Gaussian beam profile will be investigated in this study. Because of the high surface roughness expected with the use of high powers and larger beam spot size, the influence of post processing on the surface evolution and fatigue properties will also be investigate.

Chapter 3
Material and methods

3.1 Introduction

This chapter describes the experimental work undertaken to study the effect of high-laser-power LPBF processing of Ti-6Al-4V alloy. The study commenced by characterizing the powder material. This was followed by developing processing parameters at high laser powers using experimental LPBF equipment developed in-house equipped with a 5-kW fibre laser by producing and analyzing single tracks and single layers produced at different process parameter combinations. Process parameters were then narrowed down to manufacture multi-layer test specimens to establish an optimal processing window for percentage porosity. The next step focused on investigating the effect of process parameter upscaling on the residual stress and surface roughness measured at the top surface, and the characterization of bulk porosity using the X-ray computed tomography technique. The samples were also analyzed to investigate the effect of high-power and low-power processing parameter upscaling on the microstructure, specifically on the size of the prior β-grains and its effect on α-colony size after heat treatment. The last part of the experimental work focused on investigating the vertical side surface roughness of samples manufactured using the high-laser-power experimental system, and the effect of centrifugal barrel finishing (CBF) on the surface roughness and mechanical properties. The material properties investigated were tensile properties and axial fatigue performance of the high-power-manufactured Ti-6Al-4V. An overview of the research methodology in the form of a flow chart is presented in Figure 3.1, with the primary aim of investigating and identifying peculiarities of high-power LPBF processing to improve productivity.

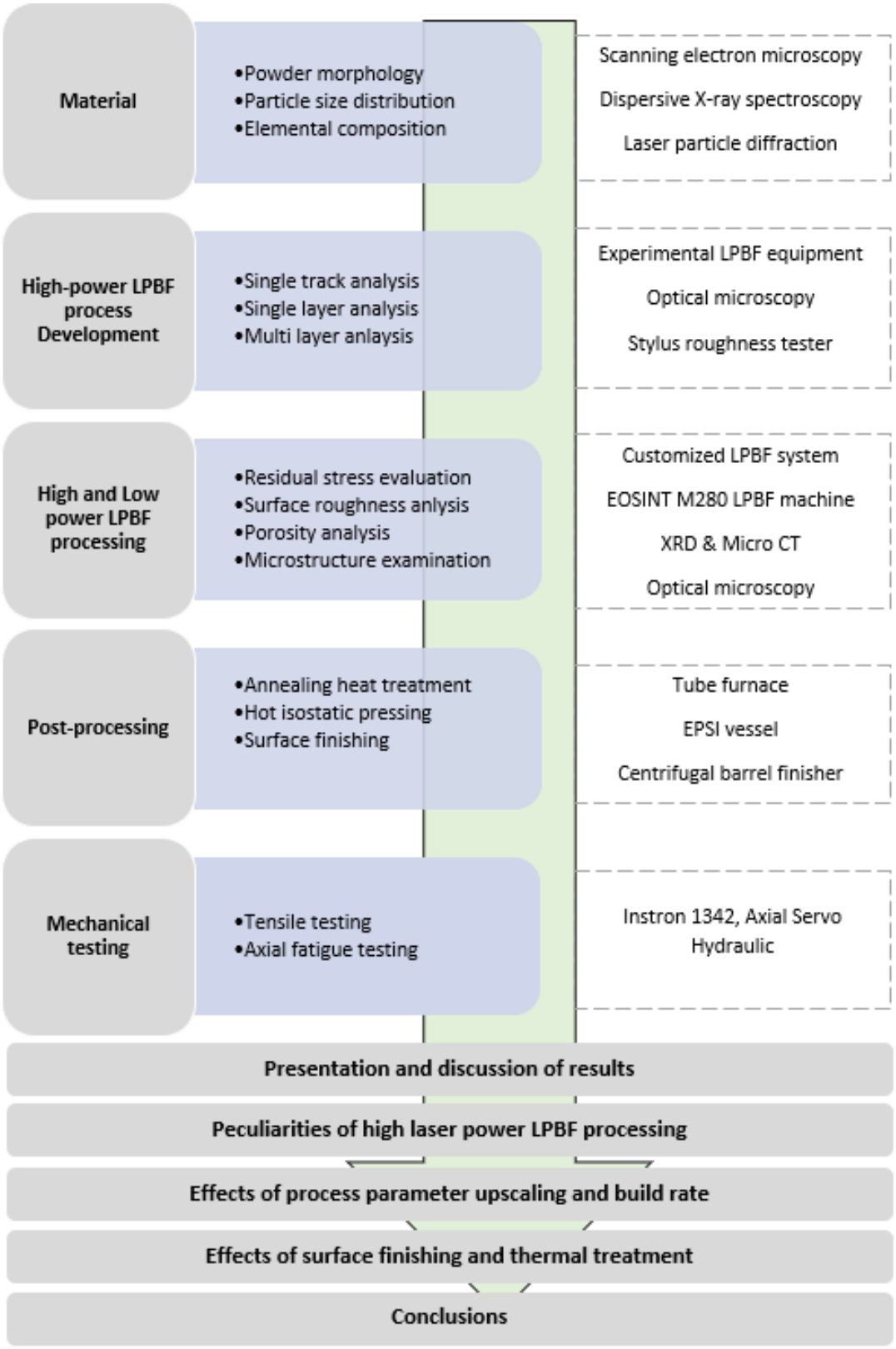

Figure 3.1: Overview of the experimental approach adopted, showing the major phases of the study.

3.2 Material

Titanium Ti-6Al-4V grade 5 powder supplied by TLS Technik (Germany) was used in this research, with the chemical specification shown in Table 3.1. The powder was gas atomized, and most of the particles were spherical in shape with smooth surfaces. Scanning electron microscopy with JOEL JSM-6010Plus/LAM revealed spherical particles with minor satellite particles attached to the sides, as shown in Figure 3.2. The 10th, 50th, and 90th percentiles of the equivalent diameters of the particle size distribution were D_{10} = 24 µm, D50 = 40 µm, and D_{90} = 56 µm, respectively. Figure 3.3 shows the particle size distribution of the powder.

Table 3.1: Technical chemical specification of the Ti-6Al-4V powder used

Element	**Wt. %**
Al	5.5–6.75
V	3.5–4.5
C	0.02
Fe	0.4
N2 max.	0.03
H max.	0.004
O2 max.	0.13
Ti	Bal.
All other impurities	≤ 0.4

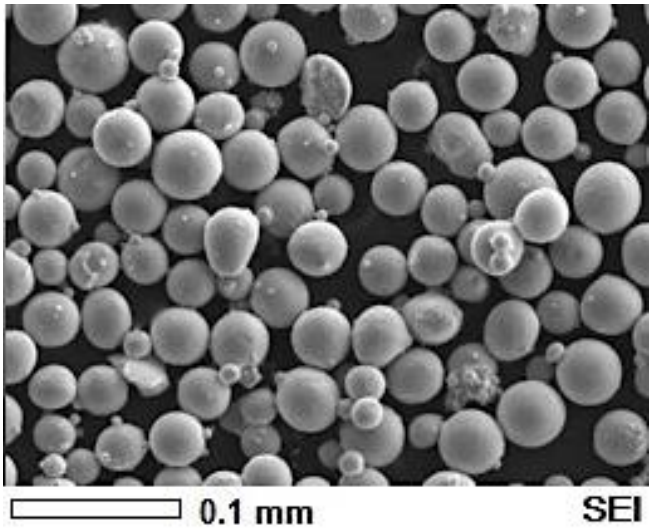

Figure 3.2 Surface morphology of the powder.

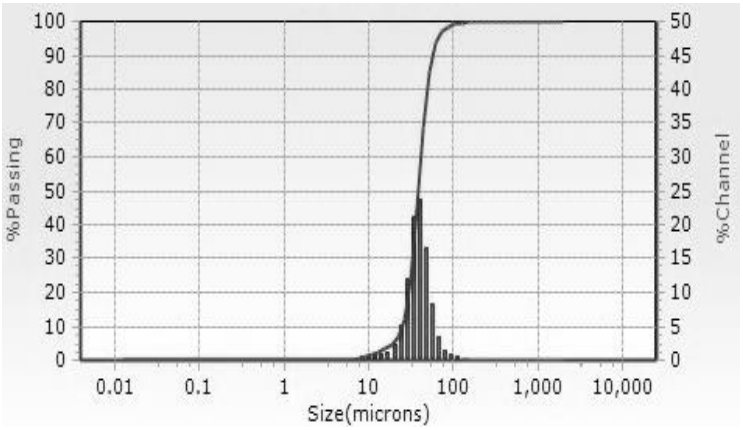

Figure 3.3: Particle size distribution of the power.

3.3 LPBF systems

3.3.1 Experimental LPBF equipment

The experimental equipment used in this research is shown in Figure 3.4. It is located at CSIR National Laser Centre in Pretoria. This system is equipped with a multimode 5 kW Ytterbium fibre laser and has a build volume of 400 mm diameter x 400 mm height. The laser is operated under continuous mode at a wavelength of 1071 nm. Processing occurs under an inert atmosphere; therefore, reactive powders like titanium and aluminium can be processed. It produces an inert atmosphere by purging the system with argon gas until the oxygen level drops below 1000 ppm before processing. The atmosphere within the chamber is circulated and filtered to remove airborne powder particles and soot that form

and interferes with the laser beam delivery during processing (see Appendix XVI). The machine was used to conduct experiments at laser powers above 500 W.

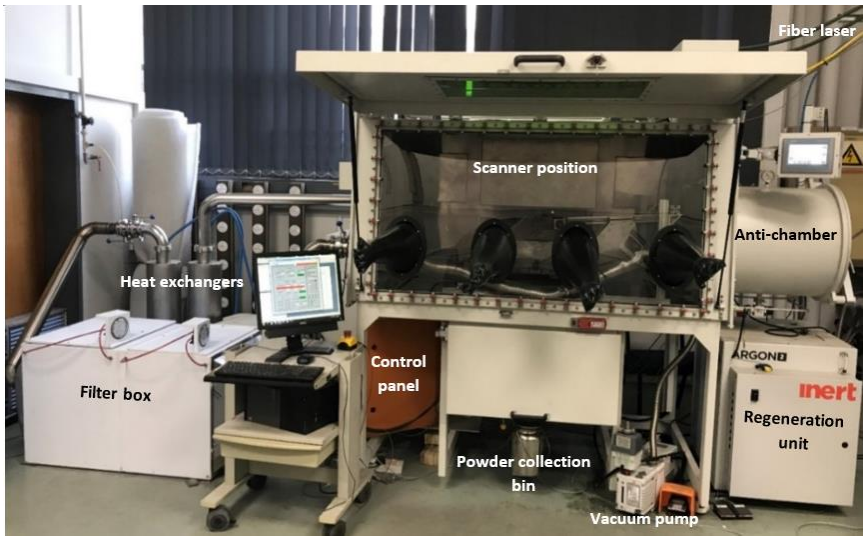

Figure 3.4: Layout of the high-power experimental system.

Single tracks, 20 mm in length, were scanned on top of a titanium baseplate made from Ti-6Al-4V. The substrate was first deposited with a 50 µm layer of the Ti-6Al-4V powder to investigate the effect of laser power and interaction time on the morphology of single tracks. The powder was deposited manually using a steel blade and shim stocks, as shown in Figure 3.5. Single layers were also scanned using the same approach to investigate the surface morphology and roughness of the synthesized layers. Each layer scanned had a cross-sectional area of 10 x 10 mm^2. Samples in the form of 10 mm x 10 mm x 10 mm cubes were manufactured to investigate the effect of process parameters on porosity. The layer thickness delivered during manufacturing was approximately 50 µm, and the scanning strategy used was a bi-directional (zig-zag) scan without contours, as shown in Figure 3.6. The specific designs of experiments are described in detail in Chapters 4 and 5.

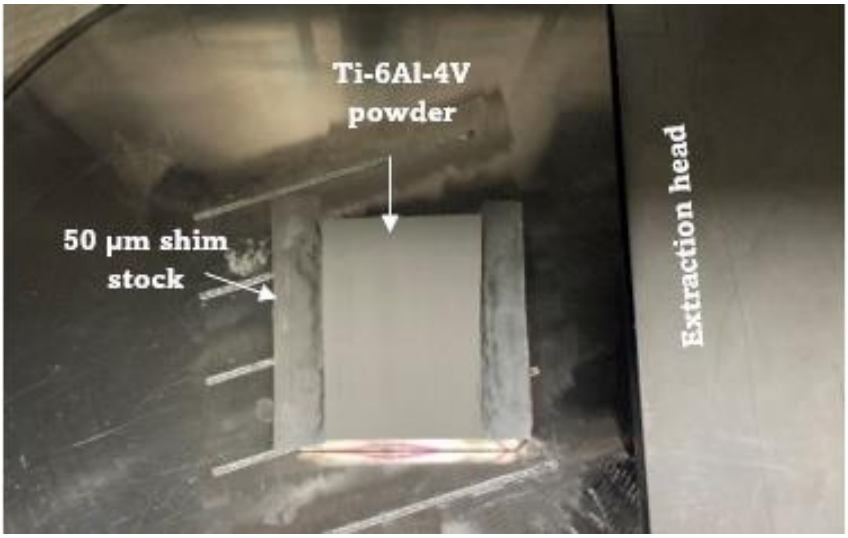

Figure 3.5: Layout of single tracks and single layer experiments.

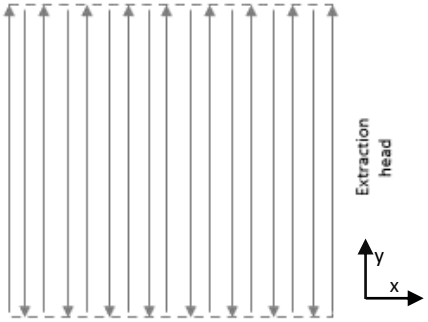

Figure 3.6: Illustration of the scanning strategy used.

3.3.2 EOSINT M280 machine

The EOSINT M280 machine used is located at Central University of Technology's Centre for Rapid Prototyping and Manufacturing in Bloemfontein, shown in Figure 3.7. It uses a single mode 400 W Ytterbium fibre with a focus diameter of 84 µm and has a build volume of 250 mm x 250 mm x 325 mm. The laser is also operated under continuous mode at a wavelength of 1075 nm. The machine is also operated in an inert atmosphere purging the build chamber with argon gas. This machine was used to conduct experiments at laser powers of 85 W, 170 W, and 340 W, respectively, to study the effect of process parameters on porosity, surface roughness, and residual stress. Test specimens in the form of 10 mm x 10 mm x 10 mm cubes were built directly on the Ti-6Al-4V baseplate without supports. The laser power and scanning speed were varied, as described in Chapter 5. The layer

thickness, hatch spacing, and scanning strategy were kept fixed, as shown in Table 3.2, and the samples were built without contours.

Figure 3.7: EOS M280 machine used.

Table 3.2: Scanning strategy parameters

Layer thickness	30 µm
Hatch spacing	70 µm
Scanning strategy	Zig-zag scanning using stripes with a size of 45 mm

3.4 Characterization facilities

3.4.1 Scanning electron microscope

A scanning electron microscope, JOEL JSM-6010Plus/LAM, shown in Figure 3.8, was used to obtain high-resolution images of the powder morphology, to analyze the single layers processed at high laser powers, and to study the fracture surfaces of the tensile and fatigue specimens. Additionally, this instrument can detect secondary electrons, allowing dispersive X-ray spectroscopy (EDX) to be performed to obtain the elemental composition of the powder material.

Figure 3.8: JOEL JSM-6010Plus/LAM scanning electron microscope.

3.4.2 Optical microscope

Optical microscopy, with an Olympus BX51M, shown in Figure 3.9, was used to characterize the surface morphology and cross-sections of the single tracks, to measure porosity following the image analysis technique, and to evaluate the microstructure of the test specimens manufactured. This microscope is equipped with UMPlanFL 5x, 10x, 20x, 50x, and 100x objectives and Stream Essentials software, which allows measurements of the single tracks and microstructural features. Porosity levels were determined by adjusting the brightness threshold, and porosity fractions were calculated automatically based on the contrast between dark porosity and bright solid material at a fixed 100x magnification.

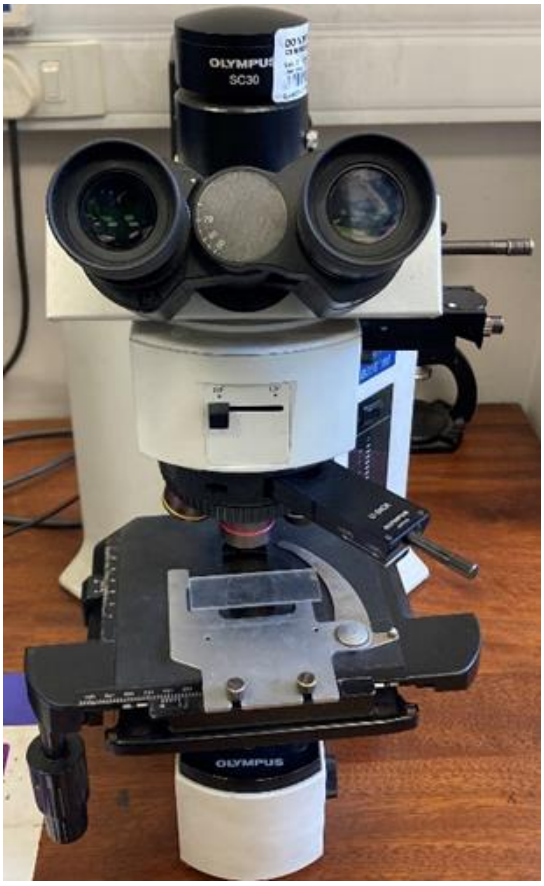

Figure 3.9: Olympus BX51M optical microscope.

3.4.3 X-ray diffractometer

Residual stress measurements were conducted using a ProtoXRD machine at Nelson Mandela University in Port Elizabeth (Figure 3.10). This instrument is equipped with two detectors used to determine the lattice deformations of the Ti-α using a CuK_{α} radiation source. Scans were performed around a {213} Bragg diffraction peak (i.e. $2\theta \sim 139.69°$) at 9 tilting angles ψ between -44.16° +44.16°. The residual stresses were determined using the $\sin^2 \psi$ method considering plane strain conditions using X-ray elastic constants shown in Table 3.3. Due to the high cost of characterization using this facility, only one sample per parameter was characterised.

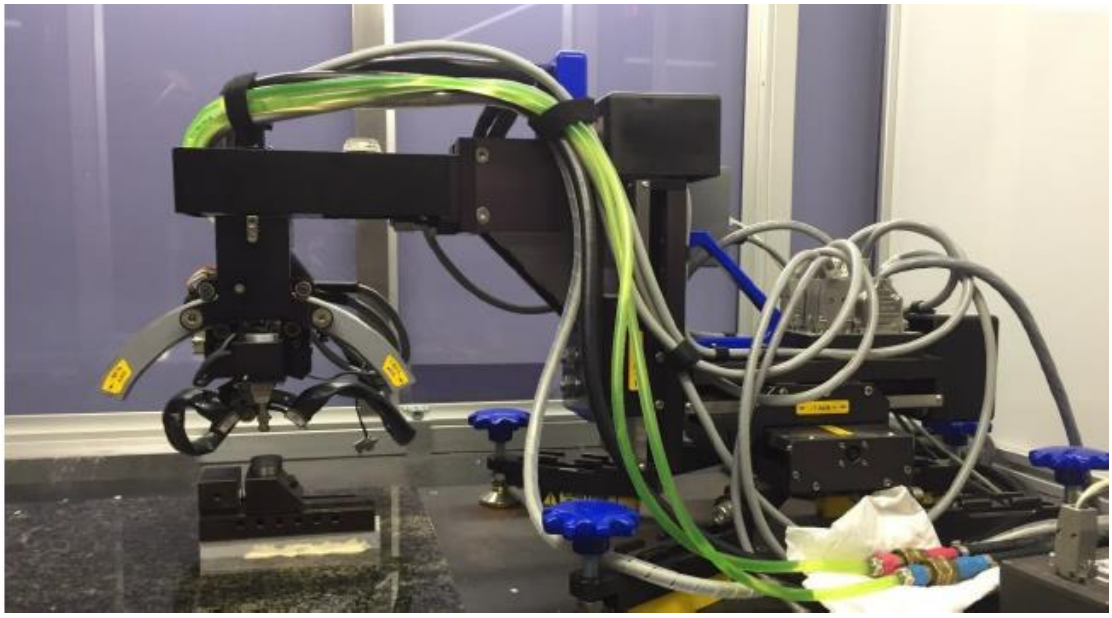

Figure 3.10: ProtoXRD diffractometer.

Table 3.3: Parameters used for X-ray measurements

Wavelength	**1.5418 Å**
Collimator	3 mm
Voltage	25 kV
Current	4 mA
Aperture	2 mm x 5 mm, rectangular
Diffraction peak	Ti {213}
Bragg angle, 2θ	139.69°
ψ-tilt	–44.16° to 44.16°
½ S_2	11.89 x 10^{-6} MPa^{-1}
-S_1	2.83 x 10^{-6} MPa^{-1}

3.4.4 Micro-computed tomography

X-ray tomography was performed using a General Electric Vtomex L240 system, shown in Figure 3.11, to characterize the areal top surface roughness and porosity in selected test specimens using 180 kV and 80 µA, with a 0.5 mm copper filter. Voxel size was set to 15 µm, and images were recorded in 3000 steps in a full 360-degree rotation of the sample. At each step position, the first image is discarded, and the next image is acquired for improved data quality compared to regular scans. Data were visualized and analysis performed in Volume Graphics VGSTUDIO MAX 3.4, according to methods applied in

prior works by du Plessis et al. [176]. The data was first de-noised using a default adaptive Gauss filter applied twice. The defect analysis module was employed with the VGDefX algorithm, using a minimum of 27 voxels and a probability of 2, set to remove small false pore identifications. For the surface roughness evaluation, a 3 x 3 mm region of interest was selected in the middle of the top surface, and a best-fit plane was selected. A mesh geometry element was created for this plane, and a nominal comparison from the actual surface to the plane-mesh provided a surface topographical evaluation from which the roughness can be measured. Due to the high cost of characterization using this facility, only one sample per parameter was characterised

Figure 3.11: General Electric Vtomex L240 system used in this study.

3.4.5 Stylus-type surface roughness tester

The vertical surface roughness of the samples was measured using a stylus-type portable surface roughness tester, Elcometer 7062 MarSurf PS1, shown in Figure 3.12. The instrument was first calibrated using a standard sample with known surface roughness before taking measurements on the samples in accordance with ISO 4287 international standard. The technical specification of the instrument is shown in Table 3.4.

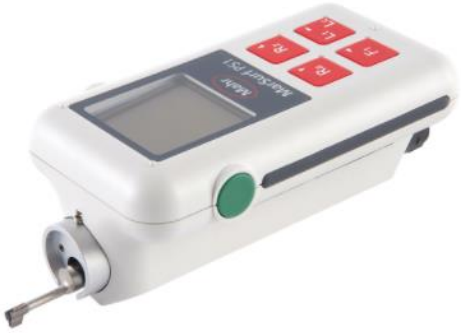

Figure 3.12: MarSurf PS1 portable roughness tester.

Table 3.4: MarSurf PS1 technical specification.

Measuring range	350 µm, 180 µm, 90 µm (changes automatically)
Probe	Inductive skidded stylus pick-up, 2 µm stylus tip, measuring force approximately 0.7mN
Travel length	1.75mm, 5.6mm, 17.5mm; automatic

3.4.6 Tensile and fatigue testing machine

Tensile testing of the vertically manufactured specimens was performed on a 50 kN Instron 1342 mechanical testing machine, shown in Figure 3.13, according to the ASTM E8/E8M international standard. An extensometer was used during the first part of the test to capture the YS at 0.2% offset. The specimens were loaded at a rate of 0.004 mm/s. The same machine was also used to perform tension-tension fatigue testing under the test criteria given in Table 3.5. For each pair of specimens, the maximum stress loading regime from which the semi-log S-N curves were derived was set between 675 MPa and 450 MPa.

Table 3.5: Tension-tension fatigue test criteria

Test standards	**ASTM E466-15 and ISO 1099 standards**
R-ratio	0.1
Control mode	Stress control mode
Frequency	15 Hz
Temperature	20 ± 2 °C
Run out	2 x 10^6

Figure 3.13: Instron 1342 mechanical testing machine used in this study.

3.5 Other facilities

3.5.1 Tube furnace

Standard post-annealing heat treatment of the tensile and fatigue specimens was carried out in a Carbolite STF 16/18 tube furnace, shown in Figure 3.14, under an argon atmosphere. This furnace has a 50 mm tube diameter with a length of 150 mm and can reach a maximum temperature of up to 1600 °C. It is incorporated with low thermal mass ceramic fibre insulation to improve the heat-up rates. The furnace temperature was adjusted using input from a built-in thermocouple and a programmed temperature controller (i.e. 950 °C).

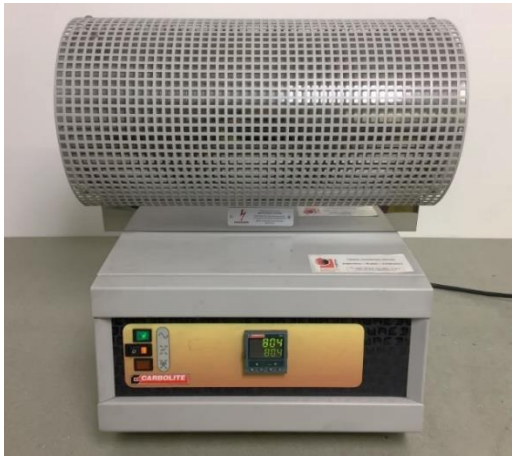

Figure 3.14: Carbolite STF 16/18 tube furnace.

3.5.2 EPSI HIP furnace

HIP of the tensile and fatigue specimens was performed in an EPSI HIP vessel shown in Figure 3.15, with a maximum operating temperature of up to 1450 °C and pressure of up to 200 MPa. This equipment consists of a furnace with molybdenum heating elements, a heat shield, a water-cooled pressure vessel, and a gas compressor system. A computer system continuously controls and monitors the temperature and pressure inside the HIP furnace. Temperature control was within ± 3°C throughout the working zone. Temperature and pressure were ramped up at rates of 5°C/min and 0.6 MPa/min, respectively.

Figure 3.15: EPSI HIP furnace.

3.5.3 Centrifugal barrel finisher

An industrial barrel finishing machine, shown in Figure 3.16, CB320-CBF from INOVATEC Machinery, was used to polish the specimens. The machine mainly consists of the driving device of the electromagnetic braking chief motor 4, the revolving disc 1 performing the planet transmission, the rolling vessels 2, the belt pulley system 6 driving

the revolving disc, the planet transmitting system driving the vessel to spin, the speed reduction unit 5 controlling the vessels in spinning and unloading, and the other operation systems and safety system. The polishing media used was an angle cut 10 mm x 10 mm ceramic media composed of alumina and silica.

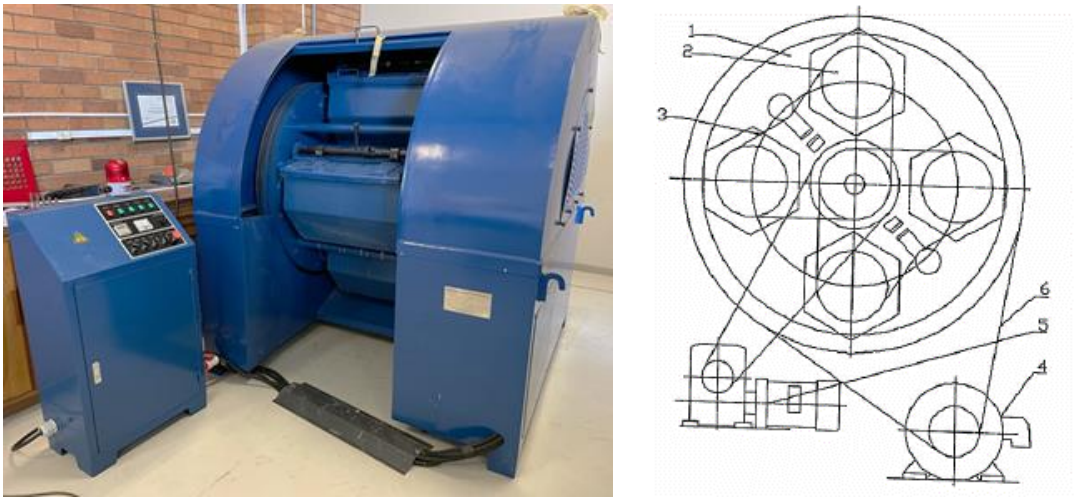

Figure 3.16: Image and schematic of barrel finishing machine used in this research.

3.5.4 Automatic grinding and polishing machine

Metallographic sample preparation was performed using an automatic grinding and polishing machine shown in Figure 3.17, Struers TegraPol31, as per the ASTM E3-11 standard guide for the preparation of metallographic specimens.

Figure 3.17: Struers TegraPol31 automatic grinding and polishing machine.

Chapter 4
Process development for high-power laser powder bed fusion of Ti-6Al-4V

4.1 Introduction

This chapter presents the results and discussions on the development of process parameters using the high-power LPBF system. The experiments commenced with the synthesis and analysis of single tracks produced at different laser powers and interaction times. The surface morphology and geometrical characteristics of the single tracks were analyzed by optical microscopy following standard sample preparation techniques. Upon that, single layers were produced to investigate the surface morphology and surface roughness using the scanning electron microscope and stylus-type surface roughness. These single layers were produced at laser powers and interaction times that yield both continuous and irregular tracks to evaluate the quality of the single layers as the percentage overlap was varied. This approach was adopted to investigate whether single layers of low roughness can be produced at high laser powers and shorter interaction time (high scanning speed) by increasing the percentage overlap. The shorter interaction times are desired as the primary goal of the study was to improve the build rate. Cubic samples were also manufactured to characterize porosity using the image analysis technique. The next section presents the experimental designs that were used in this study. This research does not disclose parameters such as scanning speed, hatch spacing, and beam spot size due to confidentiality restrictions. However, the laser power, interaction time, and percentage overlap are revealed to describe the parameters used in the study. In all the experiments, the layer thickness was fixed at 50 micrometers, and the scanning strategy used to produce single layers and multi-layers was line scanning using antiparallel tracks without contours.

4.2 Experimental designs

4.2.1 Single tracks

Table 4.1 below shows the parameters used to produce the single tracks. The maximum laser power was limited to 2000 W since higher laser powers produce excessive spatters that can cause damage to the lens protective window. The interaction time was derived from the scan speed and beam spot size, as shown by Equation 4.1. For each parameter, two identical tracks were produced and characterized.

$$\text{Interaction time} = \frac{Ø_s}{v} \qquad 4.1$$

where $Ø_s$ is the diameter of the beam spot, v is the scan speed.

Table 4.1: Parameters used to produce single tracks.

Power (W)	**600**	**1200**	**2000**
Interaction time (ms)	1.00	0.75	0.30
	0.75	0.50	0.15
	0.50	0.33	0.10
	0.33	0.25	0.075
	0.25	0.20	0.070
	0.20	0.17	0.060
	0.17	0.14	0.050
	0.14	0.12	0.040

4.2.2 Single layers

Single layers were produced using the parameters shown in Table 4.2. The parameters were chosen to investigate the effect of percentage overlap (see Equation 4.2) on the surface quality of single layers produced using continuous and irregular tracks at shorter interaction times in pursuit of high build rates.

$$\text{Overlap} = \left[1 - \frac{h}{Ø_s}\right] \qquad 4.2$$

$$\text{Build rate} = \left[\frac{l \times Ø_s^2 \times (1 - overlap)}{t_{int}}\right] \qquad 4.3$$

where h is the hatch spacing, $Ø_s$ is the diameter of the beam spot.

Table 4.2: Parameters used to produce single layers.

Power (W)	Interaction time (ms)	Overlap (%)	Power (W)	Interaction time (ms)	Overlap (%)
600	0.33	30	2000	0.075	30
600	0.33	40	2000	0.075	40
600	0.33	50	2000	0.075	50
600	0.33	60	2000	0.075	60
600	0.25	30	2000	0.070	30
600	0.25	40	2000	0.070	40
600	0.25	50	2000	0.070	50
600	0.25	60	2000	0.070	60

4.2.3 Multi-layers

Multi-layers in the form of 10 mm x 10 mm x 10 mm cubes were produced to characterize porosity using the parameters shown in Table 4.3. Porosity measurements were taken from the cross-sectional images collected. For each sample, five images were taken at different locations, as shown in Figure 4.1, to calculate the average porosity. The build rate is an estimation of the manufactured volume per unit time and was calculated using Equation 4.3.

Table 4.3: Parameters used to produce multi-layers/cubes

Power (W)	Interaction time (ms)	Overlap (%)	Build rate (mm^3/s)
600	0.33	50	6.8
600	0.33	60	5.4
600	0.25	50	9.0
600	0.25	60	7.2
2000	0.075	50	30.0
2000	0.075	60	24.0
2000	0.070	50	33.8
2000	0.070	60	27.0

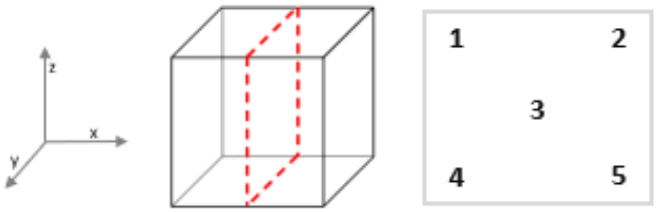

Figure 4.1: Cutting plane and positions on the cubes where images were taken.

4.3 Results and discussion

4.3.1 Single tracks

Analysis of single tracks before manufacturing 2D layers is an important step in LBPF. This step presents the opportunity to narrow down the number of experiments as potentially poor parameters can be identified early by analyzing the surface morphology and cross-sectional views of the single tracks produced. Figure 4.2 below presents the four main surface morphologies observed, summarized in Figure 4.3 for the different parameter combinations. The surface morphologies observed were continuous tracks with keyhole mode, continuous tracks with conduction mode, humping effect, and balling effect, represented as Type 1 to Type 4 in Figure 4.2.

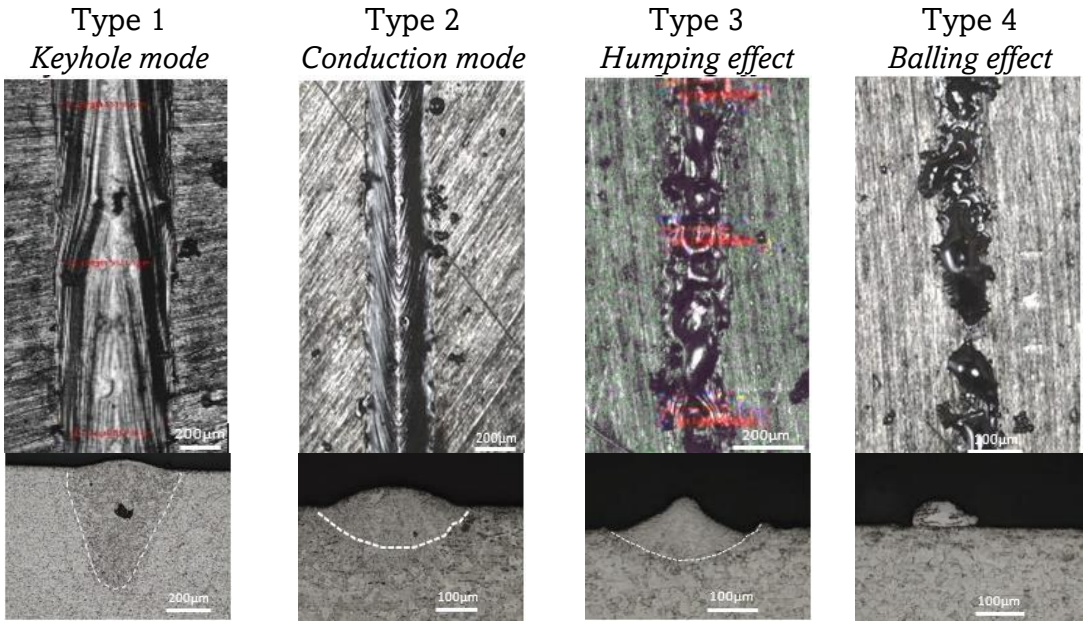

Figure 4.2: Different types of surface morphologies observed and the corresponding cross-sectional views of the single tracks.

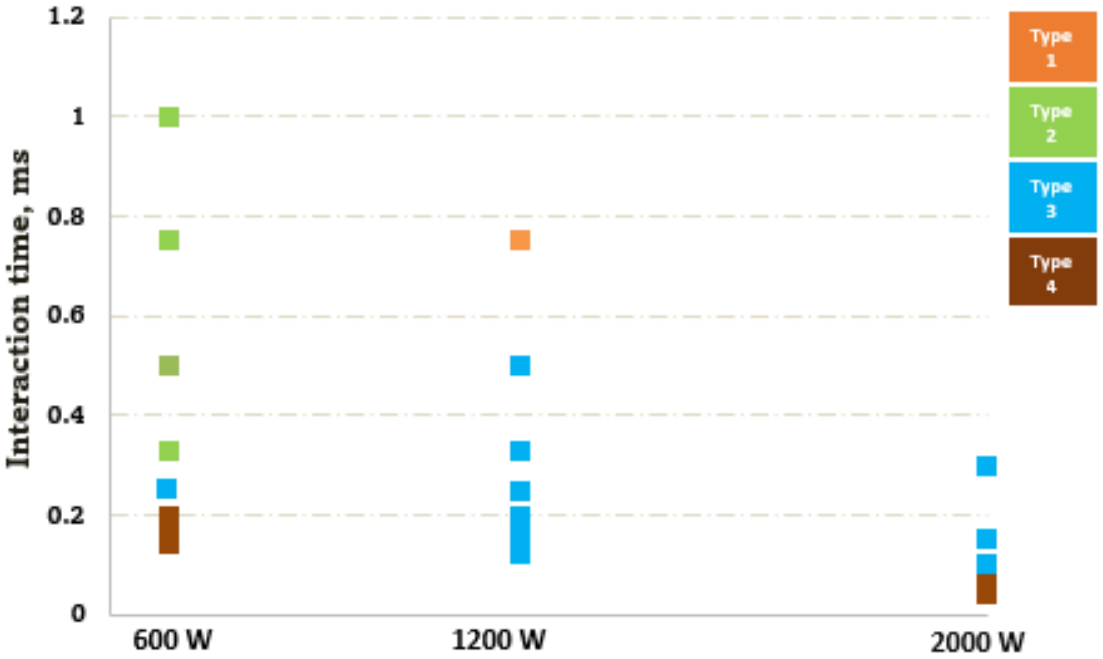

Figure 4.3: Summary of the different types of single-track morphologies formed.

The melting mode and shape of the molten pool in LPBF are dictated by the laser power density and the laser-matter interaction time, mainly controlled by the laser power, beam spot size, and scanning speed. The shape of the molten pool formed in the conduction mode is usually semi-circular, and the depth of the molten pool is about equal to its half-width. The keyhole mode causes the material to evaporate from the laser irradiation area, leading to the formation of a deep and narrow molten pool [177]-[179].

Continuous tracks with a conductive melting mode were observed at 600 W between 0.33 ms to 1 ms interaction time, and the humping and balling effect was observed at shorter interaction times below 0.33 ms. Doubling the laser power to 1200 W provoked keyhole mode when the interaction time was 0.75 ms, and the humping effect at interaction times varied between 0.5 ms to 0.12 ms. At 2000 W, two types of molten pools were formed, dominated by the humping and balling effect [177]-[180]. The variation of geometrical characteristics of the single tracks is shown in Figure 4.4.

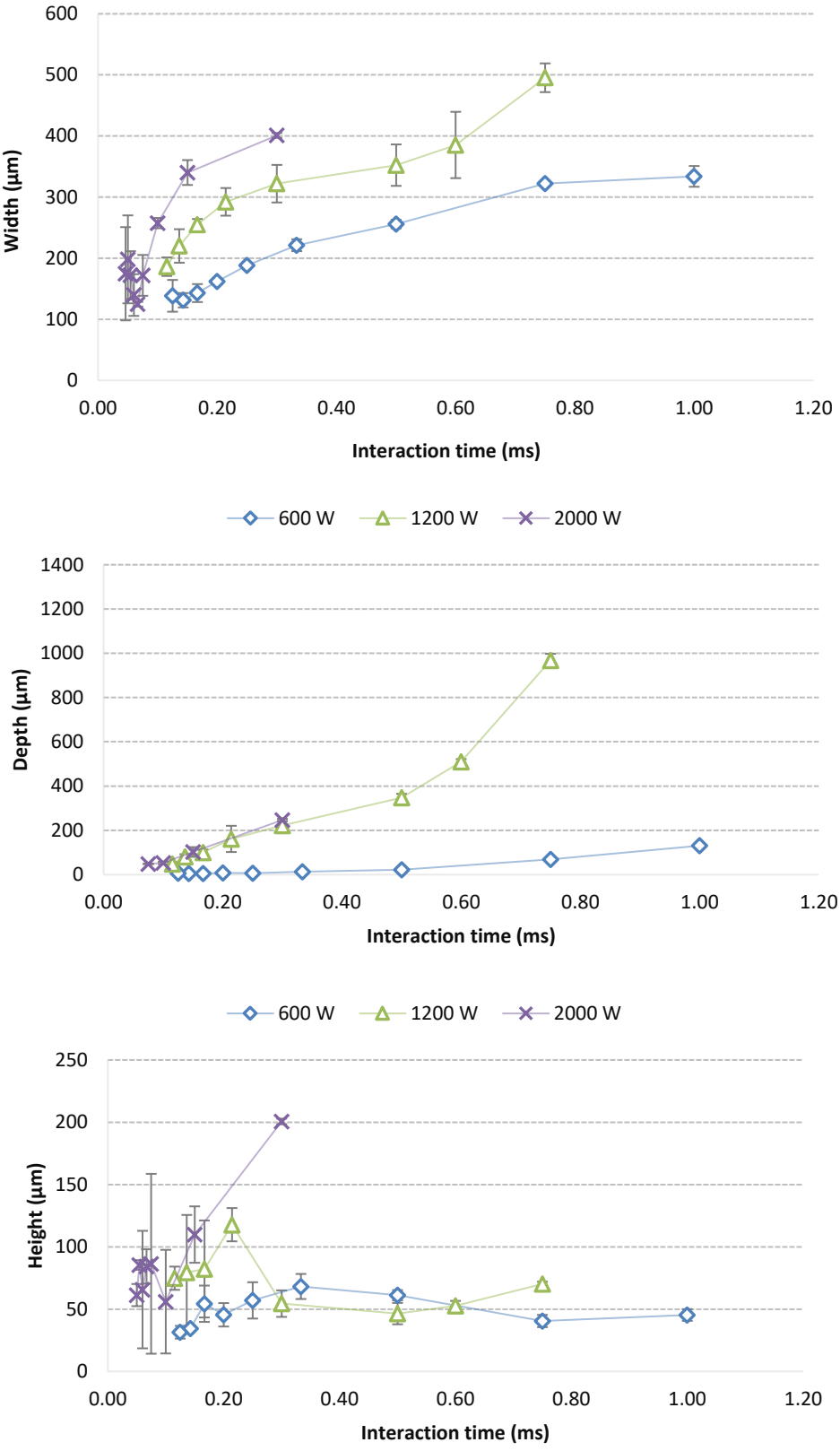

Figure 4.4: Variation of geometrical characteristics of the single tracks.

The width of the track increased with increasing interaction time, indicative of an increased molten pool size since more material is evolved in the melting process. Similarly, the depth of the track increased with the interaction time, and keyhole mode (i.e. depth > half-width) was formed at a laser power of 1200 W and interaction time of 0.75 ms. The height of the tracks varied greatly, possibly due to the inhomogeneity of the deposited layer and strong melt pool hydrodynamics, which promoted the humping and balling effect, especially at shorter interaction times (i.e. higher scanning speed).

The keyhole mode is known to promote the formation of internal porosity that can be detrimental to the mechanical properties of the finished part, and it is formed at higher laser power densities and shorter interaction times [177]-[178]. The humping and balling effect generally forms a layer with a rough and complex morphology. When the next layer of powder is deposited on the previous rough layer, non-homogeneities in the deposited layer may lead to different thermo-physical conditions at the scanning, thus producing parts with interlayer defects [177]-[179]. However, the possibility of using a high percentage overlap to influence the quality of layers formed using high laser power and shorter interaction time is not yet explored. As such, it was decided to investigate the effect of increasing the percentage overlap on the quality of single layers produced using both continuous tracks formed at 600 W and irregular tracks with a humping effect formed at 2000 W in pursuit of high build rates.

4.3.2 Single layers

The importance of analyzing single layers in LPBF cannot be over-emphasized since the LPBF is a layer-by-layer manufacturing process. The surface morphology and surface roughness of the layer influence the final product properties. Single layers were produced by varying the laser power, interaction time, and percentage overlap to study the surface morphology and surface roughness of the layers formed. The chosen parameters stem from the single-track results and the desire to produce parts at higher build rates by increasing the scanning speed (i.e., decreasing interaction time). Figure 4.5 shows the different surface morphologies formed under different parameter combinations.

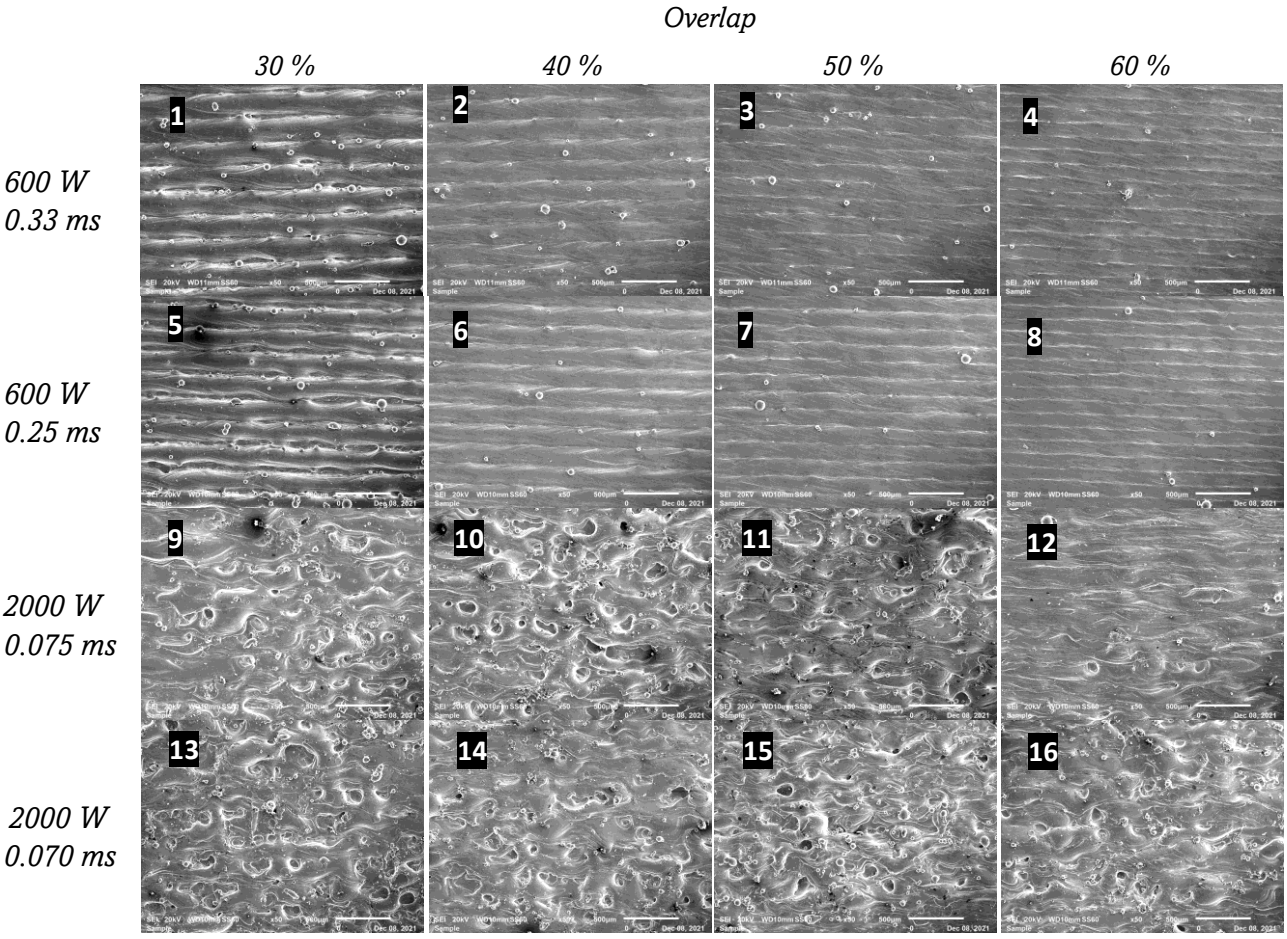

Figure 4.5: Different surface morphologies of the single layers formed with respective sample numbers.

Single layers formed at 600 W were mostly smooth with few spatters on the surface, except at 30% overlap, where the individual tracks can be clearly seen, with more spatters on the surface. When the overlap was increased, the distance between adjacent tracks and valleys on the surface was reduced, thus forming a single layer with a lower roughness. Reducing the interaction time decreases the track width and increases the gap between adjacent tracks, as seen in samples 1 and 5. At 2000 W, most of the single layers formed revealed a complex morphology with high surface roughness. Many voids and spatter particles were also present on the surface. However, sample 12 (image 12 in Figure 4.5), formed at 60% overlap, was flattened compared to the single layers formed at 2000 W, with an average surface roughness of R_a ~ 9 µm. Figure 4.6 shows the effect of

percentage overlap on the average surface roughness of the single layer manufactured at a given laser power and interaction time.

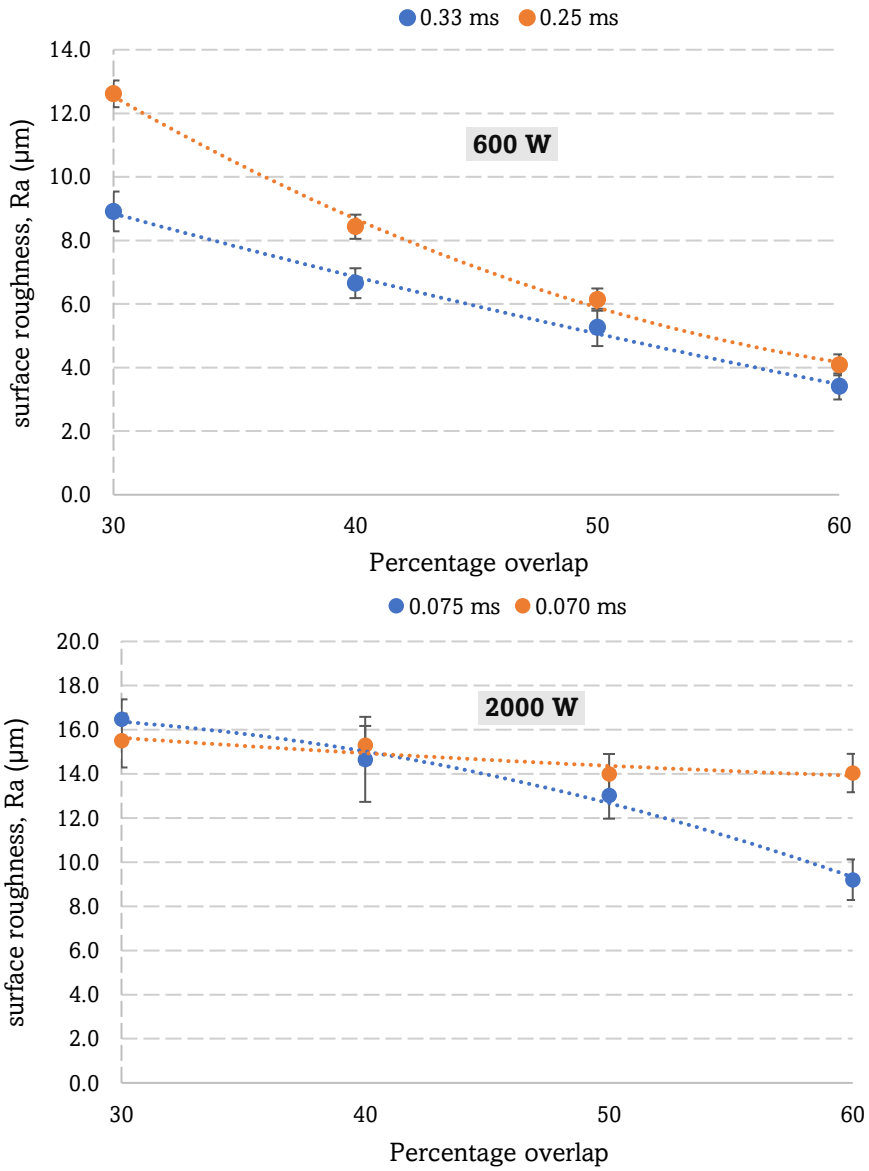

Figure 4.6: Effect of percentage overlap on the single layer surface roughness.

Generally, the parameters that form continuous tracks are chosen for porosity optimization in LPBF [181]-[182]. To the authors' knowledge, no study has been conducted to investigate the effect of high percentage overlap on the surface roughness of single layers produced using shorter interaction times. These results show that the surface roughness of the layer formed can be reduced by increasing the overlap, which results in increased remelting. Even at high laser power and shorter interaction time, a

regime dominated by the humping effect, increasing the overlap reduced the voids on the surface and the roughness of the layer formed as observed on the single layers produced at 2000 W and 0.075 ms (image 9 to 12 in Figure 4.5).

Xia et al. [183] have shown that for a given laser power and interaction time, increasing the percentage overlap tends to result in a significant thermal accumulation, leading to higher peak temperatures and sufficient liquid spreading to wet and melt the surrounding powder particles. A higher working temperature was also favourable to spreading the melt to the previous track, which benefited the formation of a sufficient metallurgical bonding between the neighbouring tracks and alleviated the fluctuation in surface roughness.

This coincided with the results in this study (Figure 4.7), where sufficient liquid spreading allowed the melt to flow into the surrounding gaps to close the pores on the surface, thus reducing the surface roughness. However, a further decrease in the interaction time to 0.070 ms at 2000 W did not yield a significant difference between the surface roughness of the single layers produced (samples 13 to 16 in Figure 4.5), and this is because the energy input per unit area decreases when the interaction time is decreased. This will result in lower peak temperatures which will increase the viscosity of the molten pool, thus resulting in insufficient melt flow and a high surface roughness.

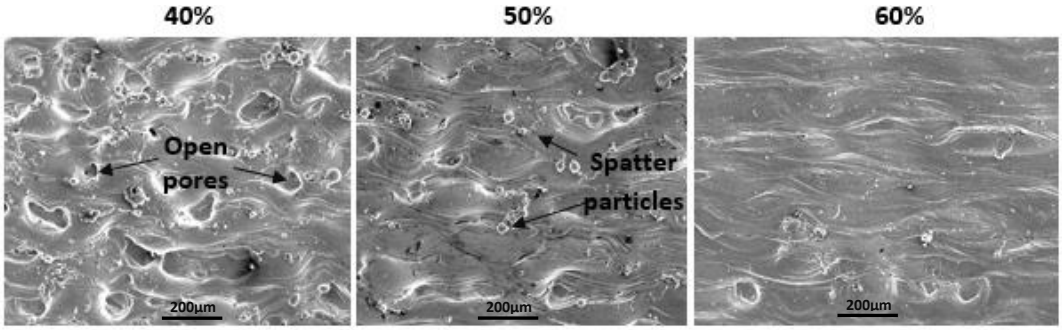

Figure 4.7: Closer view of single layers formed at 2000 W 0.075 ms, at different percentage overlap.

4.3.3 Multi-layers

The successful building of parts in LPBF relies on a balance between process parameters, scanning strategy, powder morphology, flow characteristics, amount of spatter generated, and many other factors [50], [110] [180], [183]-[185]. Porosity represents the most common defect observed in LPBF parts and can form for various reasons. Defects can

form systematically if inadequate combinations of process parameters are selected for manufacturing and can consist of keyhole porosity, gas porosity, and lack of fusion. Such defects are uniformly distributed throughout the material. Defects can also form stochastically in LPBF because of irregularities in the spreading of powder, irregularities in the powder packing, and process by-products like spatter particles. As such, the incidence and distribution of stochastic defects cannot be anticipated as their formation is not driven by user-defined parameters. Figure 4.8 and Figure 4.9 show the optical micrographs of each sample analyzed. The two main types of pores observed were incomplete melting-induced porosity and lack of fusion with unmelted particles randomly distributed in the material. Figure 4.10 shows a closer view of these types of defects.

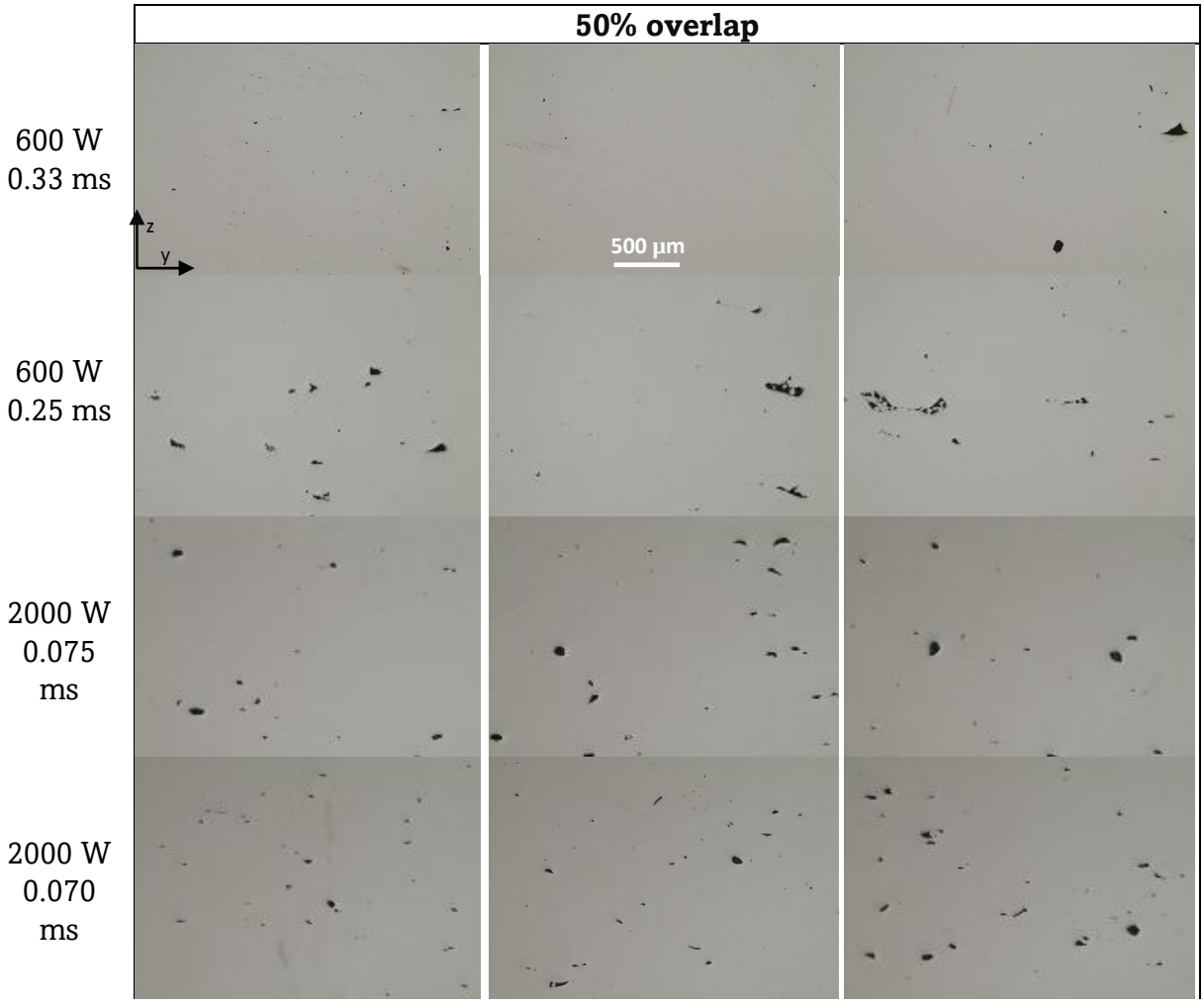

Figure 4.8: Optical micrographs of the cross-sectioned specimens manufactured at 50% overlap

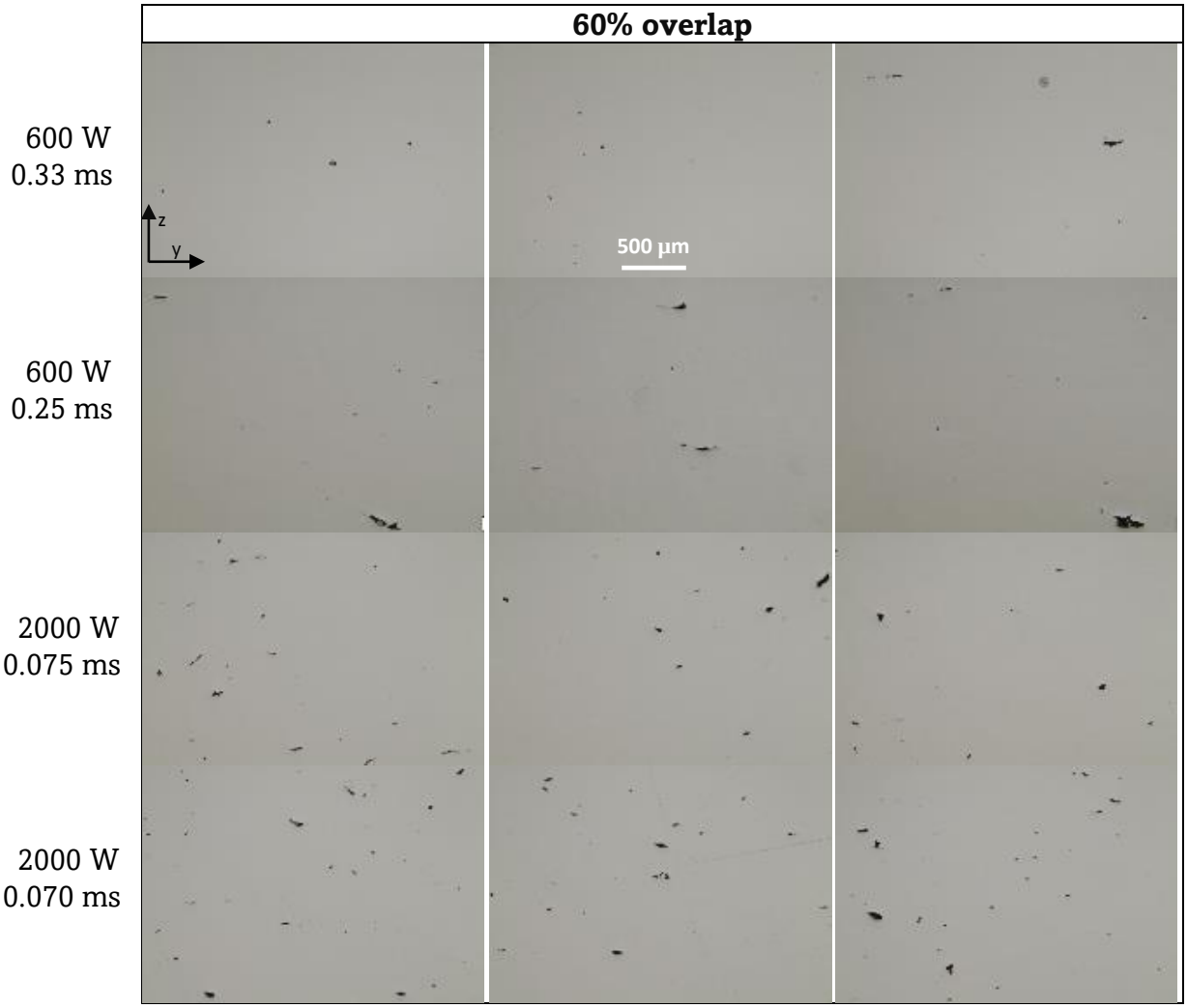

Figure 4.9: Optical micrographs along the centre of the cross-sectioned specimens manufactured at 60% overlap.

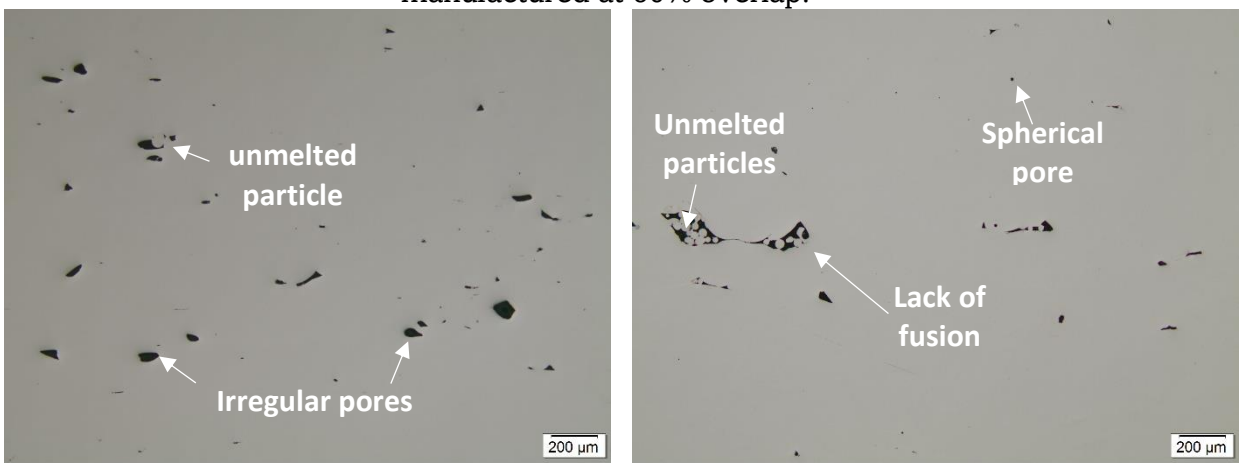

Figure 4.10: (a) Incomplete melting-induced porosity observed in the sample manufactured at 2000 W, 0.070 ms, 50 % overlap, and (b) lack of fusion with unmelted particles observed in the sample manufactured at 600 W, 0.25 ms, 50% overlap.

Figure 4.11 presents a plot of porosity measured on the samples manufactured against process parameters. At constant laser power, the porosity decreased with an increasing percentage of overlap and increased with decreasing interaction time. This is because increasing the percentage overlap reduces the gap between the adjacent tracks and increases the number of times each point in the part is melted, which promotes a reduction of porosity. The samples manufactured at 600 W and 0.33 ms had the lowest porosity, which can also be attributed to the more stable molten pool and continuous tracks formed. Decreasing the interaction time increased porosity since the laser beam spent less time on the irradiated area, thus resulting in insufficient melting of the powder in some areas. A similar trend was also observed for the samples manufactured at 2000 W, with a slightly higher percentage of porosity possibly exaggerated by the unstable molten pool and spatter particles redeposited on the synthesized layer (see Figure 4.12). Larger spatter particles can affect the homogeneity of the layer delivered and the top surface roughness, consequently increasing porosity in the part. Figure 4.13 illustrates the introduced pores caused by larger spatter particles.

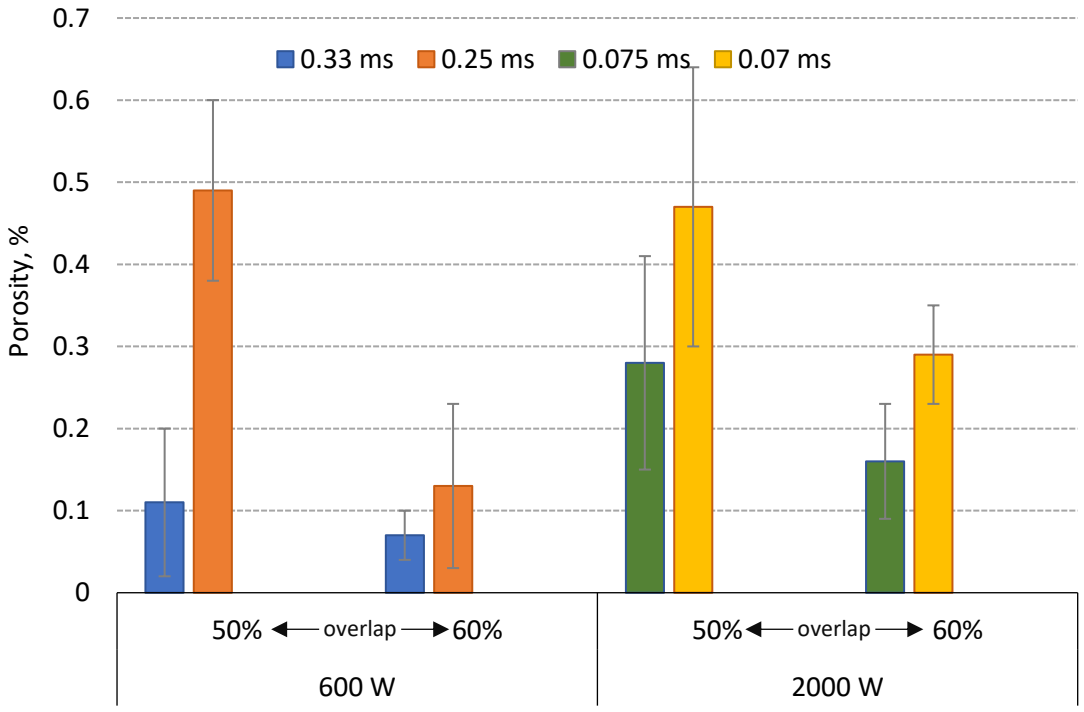

Figure 4.11: Variation of porosity with the process parameters.

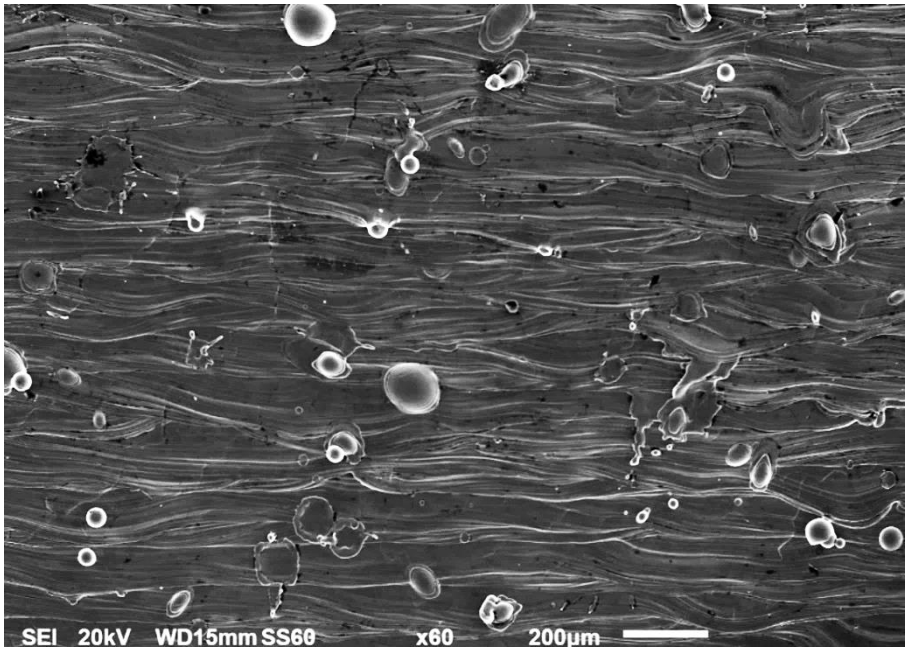

Figure 4.12: Spatter particles observed at the top surface of the sample manufactured at 2000 W.

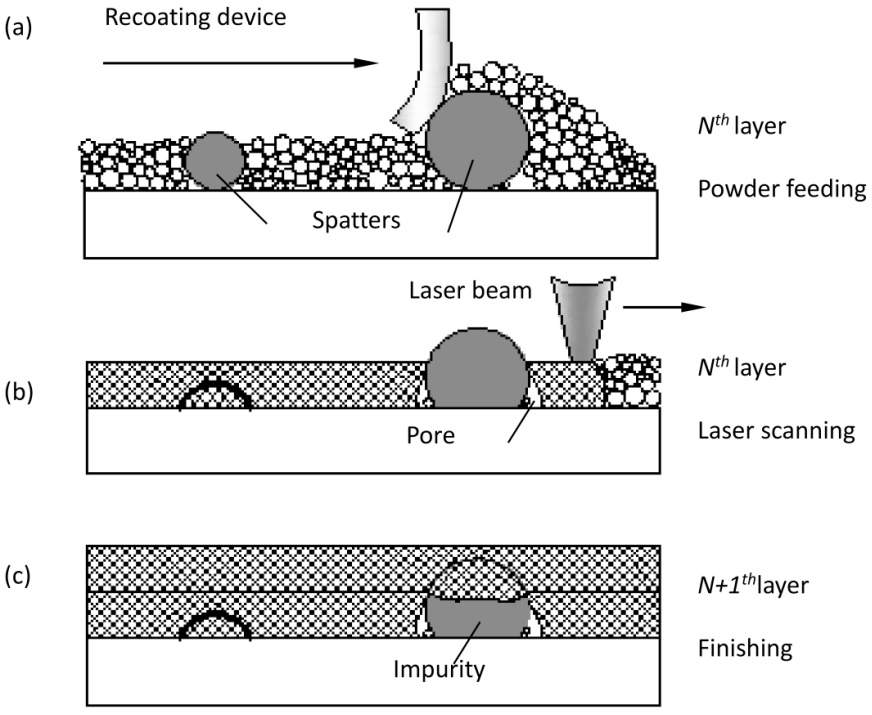

Figure 4.13: Schematic illustration of the effect of spatter on porosity in LPBF [196] .

The build rate is an estimation of the manufactured volume per unit time using values independent of a machine and can be used as a reference value of the productivity of the LPBF process. It is calculated as shown in Equation 4.3. The layer thickness and interaction time are usually limited by the available laser power, while the overlap is limited by beam spot size. In this case, the layer thickness was kept fixed at approximately 50 µm, and only the overlap and interaction time were varied to influence the build rate. Due to restrictions on proprietary information, values for hatch spacing and scan speed have not been disclosed. The achievable build rate for density/porosity is also limited by the laser power used since it affects the heat input.

Figure 4.14 shows the variation of porosity and surface roughness with the build rate. The average porosity and the top surface roughness increased with increasing the build rate. However, parts with an average porosity of ≤ 0.2% can be produced at both laser powers, with a maximum build rate of 7.2 mm^3/s and 24 mm^3/s at 600 W and 2000 W, respectively.

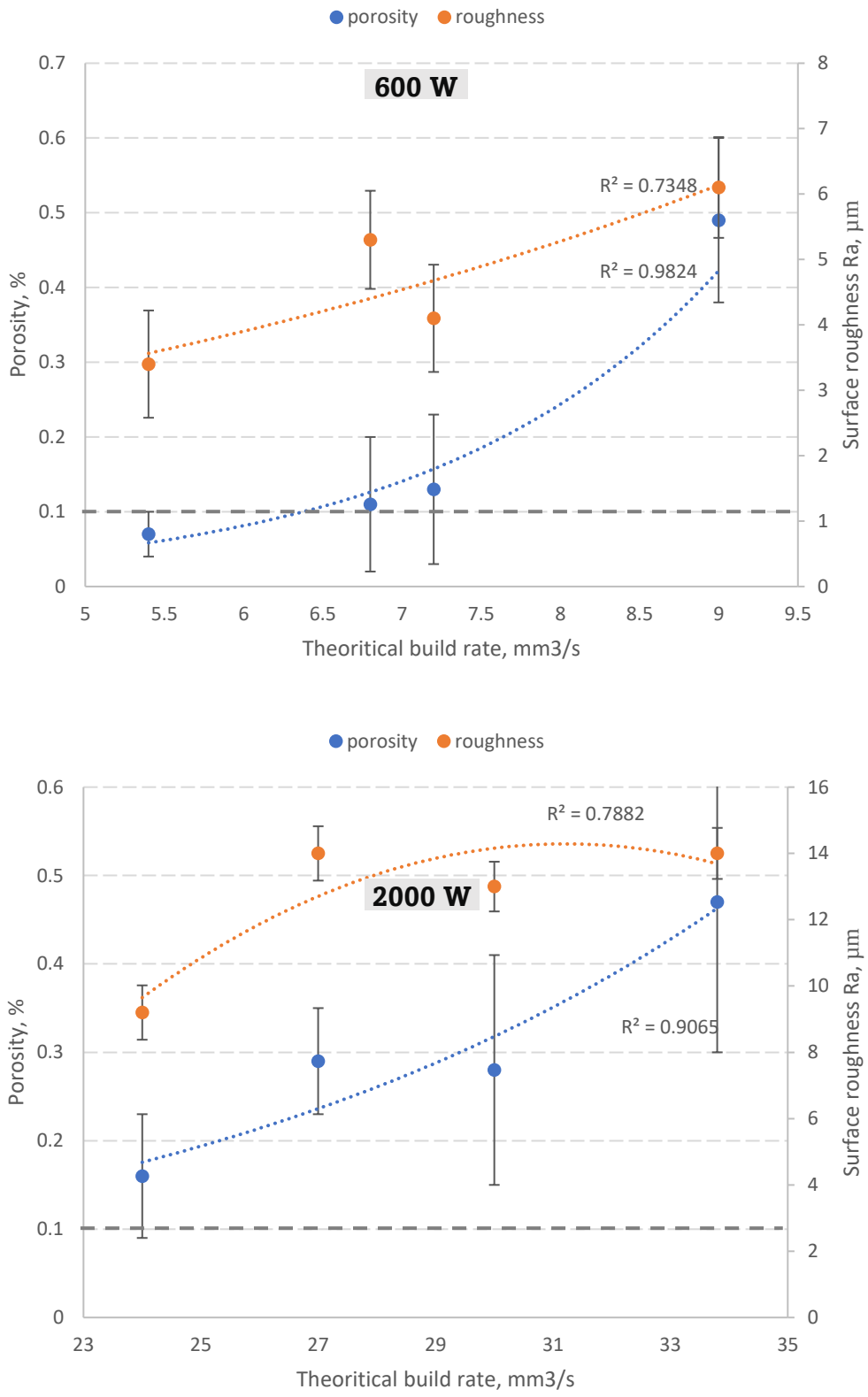

Figure 4.14: Effect of build rate on porosity and surface roughness.

4.4 Summary and conclusions

The focus of this investigation was to develop process parameters to obtain low porosity in the test coupons in pursuit of high build rates. The investigation commenced with an analysis of single tracks formed using different laser powers and interaction time, followed by the analysis of single layers. Cubes were also manufactured to investigate porosity in the samples using the image analysis technique. It was shown that single tracks formed under different parameters exhibit different morphologies, where longer interaction time can provoke keyhole mode, while shorter interaction times provoke humping and balling effect. Continuous tracks showing conduction mode were formed at 600 W when the interaction time was between 0.33 ms to 1 ms. Increasing the laser power to 1200 W formed single tracks showing keyhole mode and humping effect. Further increase in laser power to 2000 W provoked humping and balling effects. Analysis of single layers formed showed that continuous tracks produced homogeneous layers when the overlap was varied between 40% to 60%, while the humping effect produced layers with complex morphology and high surface roughness. However, increasing the percentage overlap decreased the surface roughness of the single layers formed at 2000 W and 0.075 ms. Multi-layers also showed that porosity in the sample decreased when the percentage overlap was increased but increased when the interaction time was decreased. Accordingly, the surface roughness and porosity increased with increasing the build rate at a fixed laser power. Overall, the maximum achievable build rate for porosity of <0.1 % was 5.4 mm^3/s at a laser power of 600 W. It was not possible to achieve porosity below 0.1 % at a laser power of 2000 W and higher build rates.

Chapter 5
Comparison of Ti-6Al-4V samples manufactured using high- and low-power laser powder bed fusion systems

5.1 Introduction

The structural integrity and mechanical performance of parts manufactured by LPBF are mainly affected by the stresses that develop and remain during the manufacturing process, the surface roughness formed, the pores/defects inside the part and the microstructure that is developed. The process parameters are the most influential variables on these output factors, which include, for example, laser power, scan speed, hatch spacing, layer thickness, scanning strategy, and powder rheological properties. These factors were reviewed and discussed in detail in Chapter 2 of the literature review. Increasing the productivity of LPBF systems is an urgent and important task. However, increasing the build rate based on higher laser power and a corresponding increase in the scanning speed at a constant beam spot size has limited scope due to the increased intensity at the processing zone and melt pool instabilities [197]-[199]. LPBF combining a large beam spot size and high laser power has been envisaged for productivity improvement. For example, Schleifenbaum et al. [200] showed that increasing the build rate to 8 mm^3/s was possible by increasing the laser power and beam diameter. Montero-Sistiaga et al. [201] were also able to increase the productivity by 2.5 times for 316L stainless steel manufacturing with a 1 kW laser compared to a classical LPBF process. Metelkova et al. [202] showed that a large beam defocusing (up to 260 μm) combined with high laser power (400–800 W) could increase the theoretical build rate up to 18 mm^3/s. The previous chapter also showed that high build rates could be achieved when a proper balance is struck between the interaction time, percentage overlap, and laser power. This adoption of process parameters is expected to influence the thermal cycles resulting from a large beam spot size and high laser powers, which can affect the stresses and microstructures that develop. Accordingly, this chapter is focused on investigating the influence of high laser powers using a customized LPBF system on

residual stress, surface roughness, bulk porosity, and microstructure formed; and comparing it to a classical low-power LPBF system.

5.2 Experimental designs

5.2.1 High-power LPBF

The high-power LPBF system was used to manufacture samples, 10 mm x 10 mm x 10mm, at different laser powers and build rates. From the previous experiments, it was not possible to achieve porosity below 0.1% at a laser power of 2000 W. As a result, it was decided to alter the process parameters to reduce porosity by building at somewhat slower build rates. Although the goal of this study is to maximise productivity, it must be noted that productivity cannot be considered in isolation without considering the quality. Generally, a trade-off between quality and productivity is vital for minimizing the building cost while keeping the quality at desired level. As such, higher percentage overlaps were used at high laser of 2000 W. Table 5.1 shows the modified process parameters used to manufacture the samples.

Table 5.1: Parameters used to manufacture samples using the high-power system

Sample no	Power (W)	Interaction time (ms)	Overlap (%)	Energy density (J/mm^3)	Build rate (mm^3/s)
1H	600	0.625	50	166.7	3.6
2H	600	0.500	50	133.3	4.5
3H	600	0.417	50	111.1	5.4
4H	750	0.500	50	166.7	4.5
5H	750	0.400	50	133.3	5.6
6H	750	0.333	50	111.1	6.8
7H	2000	0.075	80	166.7	12.0
8H	2000	0.075	75	133.3	15.0
9H	2000	0.075	70	111.1	18.0

5.2.2 Low-power LPBF

The EOSINT M280 machine was used to manufacture samples at low powers ranging from 85 W to 340 W, as shown in Table 5.2. These parameters where chosen based on

previous data obtained on the analysis of Ti6Al4V single tracks produced on the EOSINT M280 machine [177].

Table 5.2: Parameters used to manufacture the samples using the EOSINT M280

Sample no	Power (W)	Interaction time (ms)	Overlap (%)	Energy density (J/mm³)	Build rate (mm³/s)
1L	85	0.267	12	134.9	0.6
2L	85	0.200	12	101.2	0.8
3L	85	0.133	12	67.5	1.3
4L	170	0.100	12	101.2	1.7
5L	170	0.080	12	81.0	2.1
6L	170	0.067	12	67.5	2.5
7L	340	0.067	12	134.9	2.5
8L	340	0.050	12	101.2	3.4
9L	340	0.040	12	81.0	4.2

5.3 Results and discussion

5.3.1 Top surface roughness

The top surface roughness is an important parameter in LPBF since it directly influences the outcome of the manufacturing process. It affects the quality of subsequent layers deposited during the layer-by-layer manufacturing process, which can influence the formation of defects in the parts, and ultimately affect the mechanical properties. Generally, a high surface roughness promotes uneven layer deposition of subsequent layers and can trigger the formation of defects. The choice of process parameters, the quality of powder material, and the powder deposition system can all influence surface roughness [203]-[206]. This section investigates the influence of process parameters on the top surface roughness of the samples manufactured. The area surface roughness measurements obtained using micro-CT, as described in Chapter 3.4.4, are summarized in Figure 5.1 for the samples manufactured using high-power and low-power systems.

Figure 5.1 shows that the bulk of the samples produced had surface roughness ranging between 6.5–18 µm, with only a small number of samples having a surface roughness of more than 25 µm. It should be noted that Figure 5.1 was designed to provide an overview of the surface roughness assessment findings rather than to compare the samples directly.

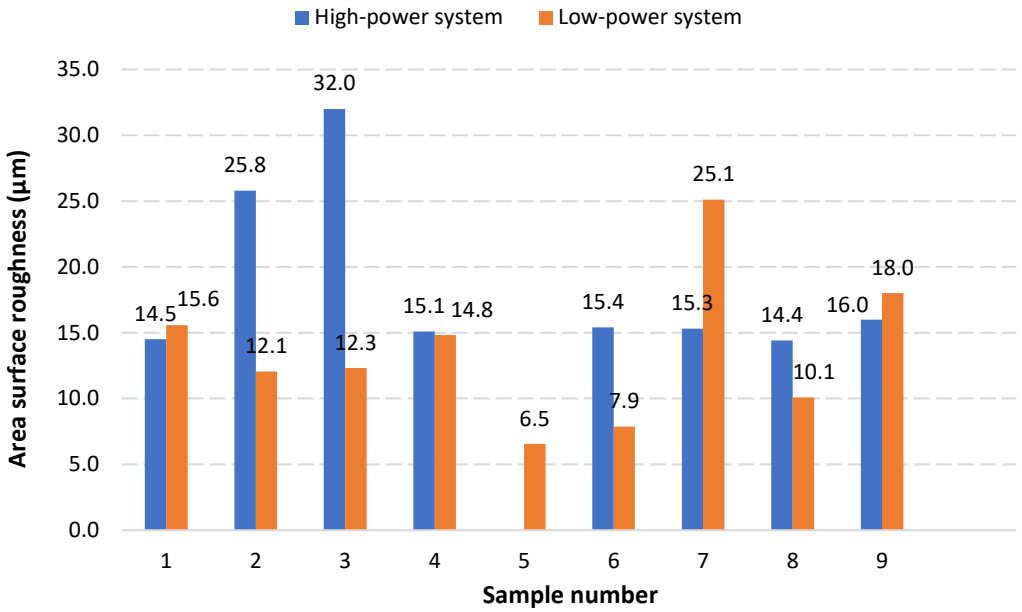

Figure 5.1: Summary of surface roughness measurements obtained.

The areal surface roughness is plotted in Figure 5.2 for different process parameters used to manufacture the samples using the high-power system. It is seen that at 600 W, the surface roughness decreased from 32 µm to 14.5 µm when the interaction time was increased from 0.417 ms to 0.625 ms. At 750 W, the surface roughness produced was almost identical for the two interaction times. The influence of percentage overlap, at 2000 W, on the surface roughness produced was also found to be insignificant when the overlap was changed between 70-80%. The lowest surface roughness of 14.5 µm was obtained at 600 W and 2000 W, at an interaction time and percentage overlap of 0.625 ms and 75% overlap, respectively.

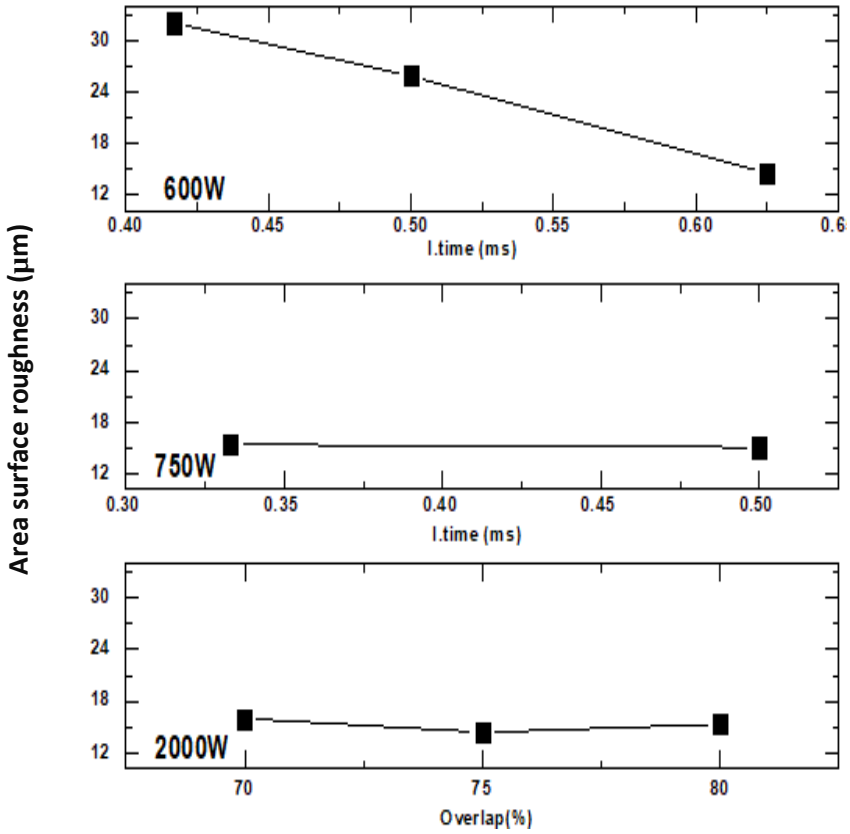

Figure 5.2: Variation of surface roughness with process parameters used to manufacture the samples using the high-power system.

The surface roughness can develop for several reasons, the most common of which is the periodic humps representing adjacent tracks on the top surface. The formation of these humps is controlled by the amount of heat input and solidification time available [203]-[206]. High energy would melt the powder and form a large enough melt pool to ensure melt flow and wetting of adjacent tracks, thus good overlap with previously formed tracks. Therefore, to have a high enough heat input, either by increasing the interaction time, increasing the laser power, or a combination of both is needed. Figure 5.3 shows the surface morphology of the samples manufactured at 600 W as the interaction time increases. At the lowest interaction time, the periodic humps representing the scan lines are evident and protruding from the surface, thus resulting in high surface roughness. There is also the added effect of satellite powders sintering to the top surface which can influence the quality of the subsequent powder layer and adds to the surface roughness. However, it can be observed that the solidified melt pool tracks are smoothed out as the

interaction time increases. At 2000 W and higher overlap, the solidified melt pool tracks were completely smoothed to a point where the tracks were no longer recognizable, as shown in Figure 5.4 (see Appendix I for all samples manufactured with the high-power system).

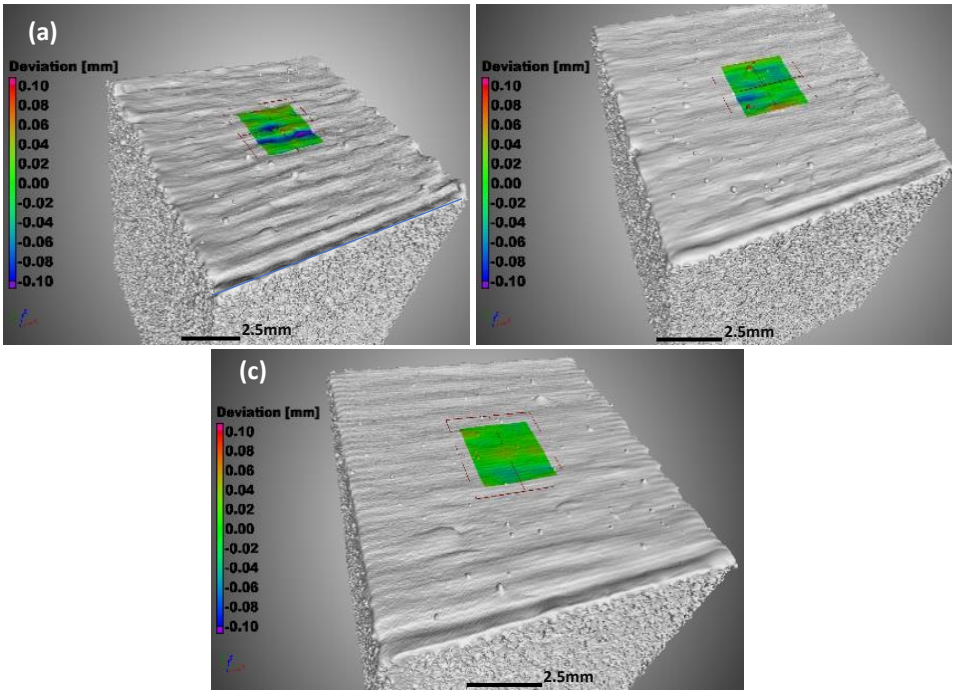

Figure 5.3: Surface morphology of samples manufactured at 600 W at different interaction times, (a) 0.417 ms, (b) 0.500 ms, and (c) 0.625 ms.

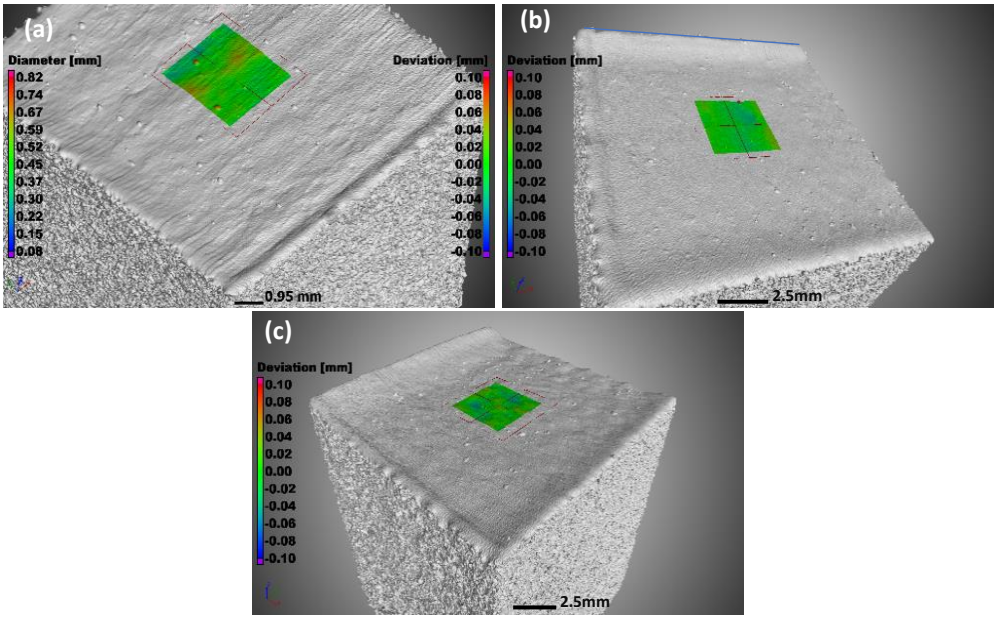

Figure 5.4 Surface morphology of samples manufactured at 2000 W at different percent overlap, (a) 70%, (b) 75%, and (c) 80%.

Figure 5.5 shows the relation between the surface roughness and interaction time, for the samples manufactured using the low-power system. The relationship, where the laser power was kept constant, is such that the surface roughness decreased with an increase in the interaction time, and then increased as the interaction time continued to increase. However, at 85 W laser power, the surface roughness was almost the same when the interaction time was increased from 0.13 ms to 0.200 ms, then increased slightly as the interaction time increased further. It is also seen that the highest laser power (340 W) produced the worst surface roughness on either side of the minima. The lowest surface roughness of 6.5 μm was obtained at a laser power of 170 W and an interaction time of 0.080 ms. Overall, these results show that both the laser power and interaction time significantly influence surface roughness. When the interaction time is low at a low laser power, there is insufficient heat input to ensure sufficient melt flow and wetting of the adjacent tracks; thus, the surface roughness will be high due to the balling phenomenon. On the other hand, excessive interaction time and heat input can induce oscillations and the Marangoni effect in the melt pool [206], thereby creating an unstable molten pool, which will increase the surface roughness. These examples are shown in Figure 5.6, where the surface roughness was found to be high on either side of the minima due to balling or an unstable molten pool formed.

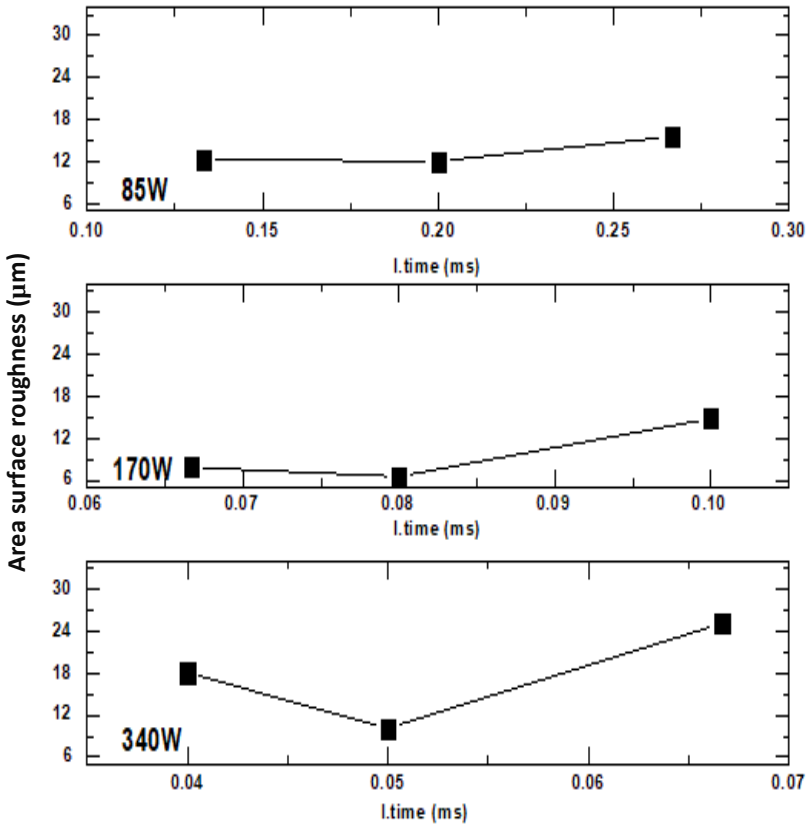

Figure 5.5: Variation of surface roughness with process parameters used to manufacture the samples using the low-power system.

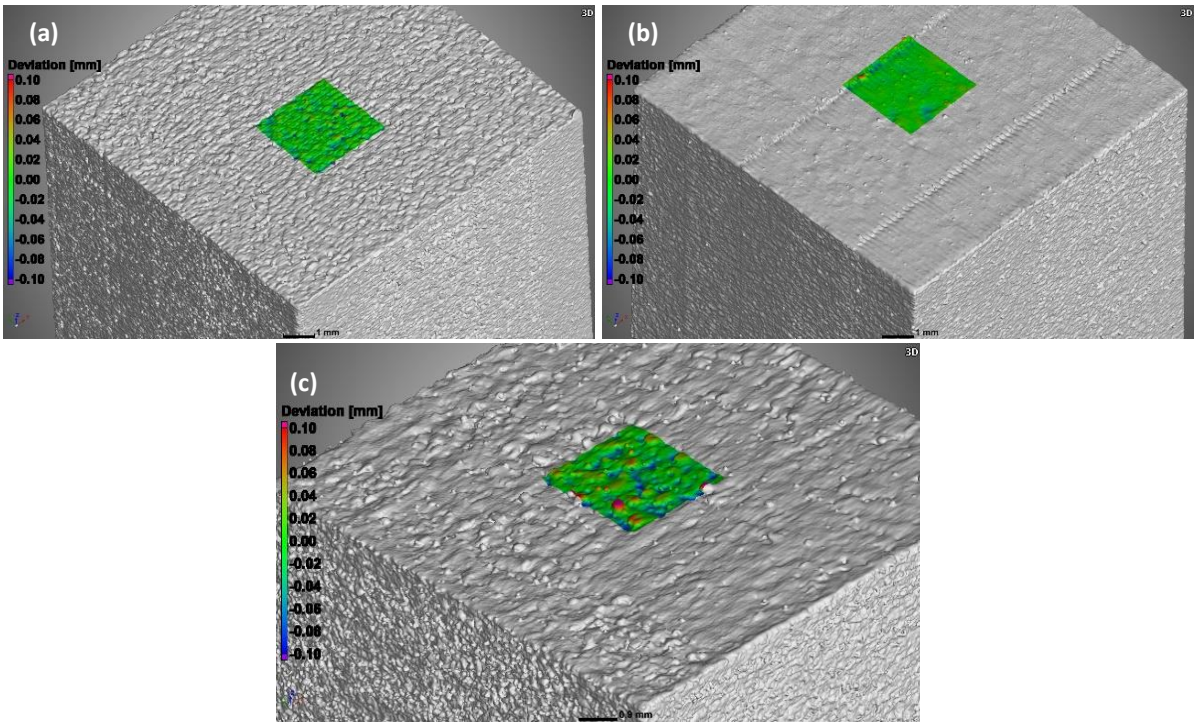

Figure 5.6: Surface morphology of samples manufactured at 340 W at different interaction times, (a) 0.04 ms, (b) 0.0500 ms, and (c) 0.067 ms (see Appendix II).

5.3.2 Porosity

The porosity associated with the different process parameters used was evaluated using X-ray micro-computed tomography. The results, summarized in Figure 5.7, show that the porosity for most of the samples was below 0.1%. Sample 3H, from the high-power system, was the only one with a porosity higher than 0.1%, while samples 7L and 9L were the worst for the low-power system, with porosity higher than 0.5%. The influence of process parameters used to manufacture the samples using the high-power system on porosity is plotted in Figure 5.8. It can be seen that porosity, at 600 W and 750 W, decreases with increasing the interaction time and then stays almost the same with a further increase in the interaction time. On the other hand, changing the overlap percent at 2000 W did not yield a significant difference in porosity, as the values obtained were quite low when the overlap changed from 70 to 80%. The highest porosity recorded was 0.17% (sample 3H) at a laser power and interaction time of 600 W and 0.417 ms, respectively. It is noted that sample 3H also had the highest surface roughness, which possibly contributed to high porosity within the bulk of the sample.

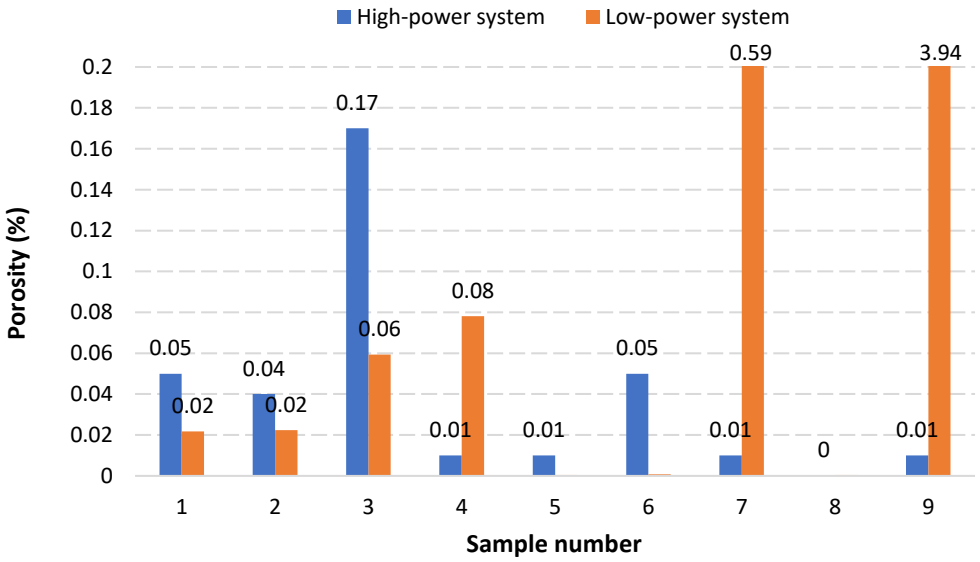

Figure 5.7: Summary of porosity measurement results.

Two main types of pores were dominant in the current investigation. First was the lack-of-fusion (LOF) pores which occur due to insufficient laser energy input. Usually, the formed melt pool that results in LOF pores is not large enough to ensure good overlap with the layer below or adjacent solidified tracks. These pores are distinguished by their

large non-circular shape with some sharp edges and were found to be dominant in the samples manufactured with the high-power system. They were found using the values of pore diameter and sphericity. The criteria selected were pores greater than 0.1 mm in diameter and less than 0.6 in sphericity [207]-[209].

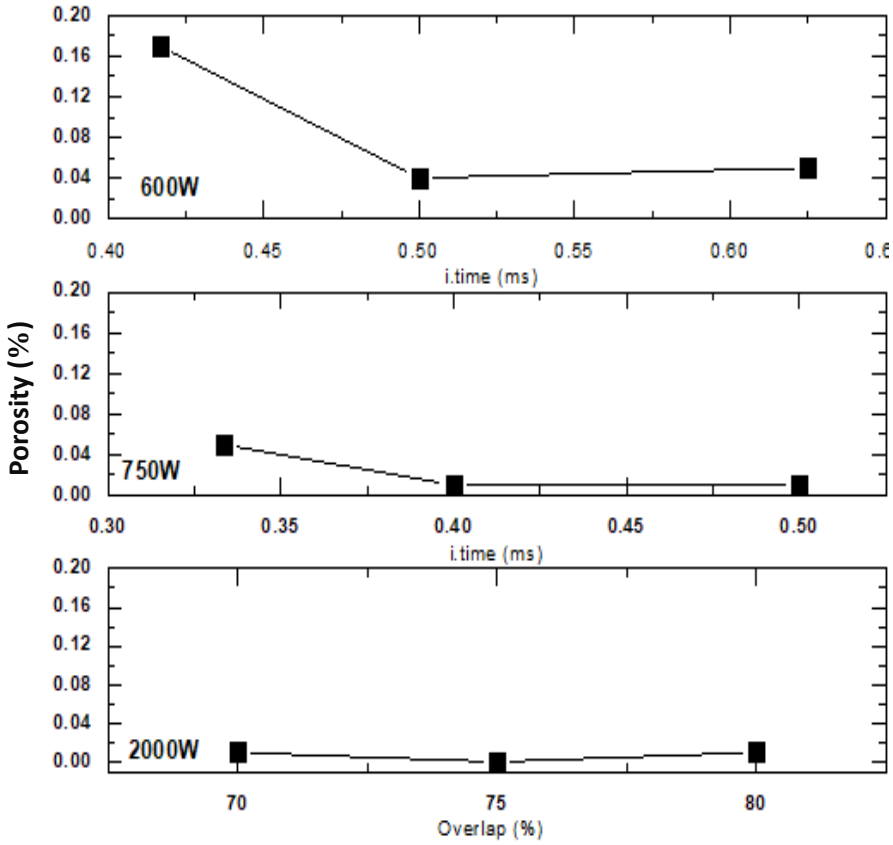

Figure 5.8: Variation of porosity with process parameters used to manufacture the samples using the high-power system.

Figure 5.9 shows the distribution and sphericity of pores in the samples manufactured using the high-power system (see Appendix III and V for separate graphs). It was found that most of the pores were indeed irregular in shape and ranged between 0.1 mm to 0.5 mm in size, with sample 3H having the highest count of pores. LOF defects can also form stochastically because of the irregular spreading of powder, and as such, their distribution cannot be anticipated as their formation is not driven by user-defined parameters. The high-power system used in this study is not a fully developed machine and occasionally suffers from powder delivery discrepancies, which can trigger the formation of stochastic

defects. This can clearly be seen in the images presented in Figure 5.10, where in some cases, the pores were localized, closer to the base of the sample. This could indicate that the layer delivery was not good enough at the beginning of the build and gradually improved as the samples were built up.

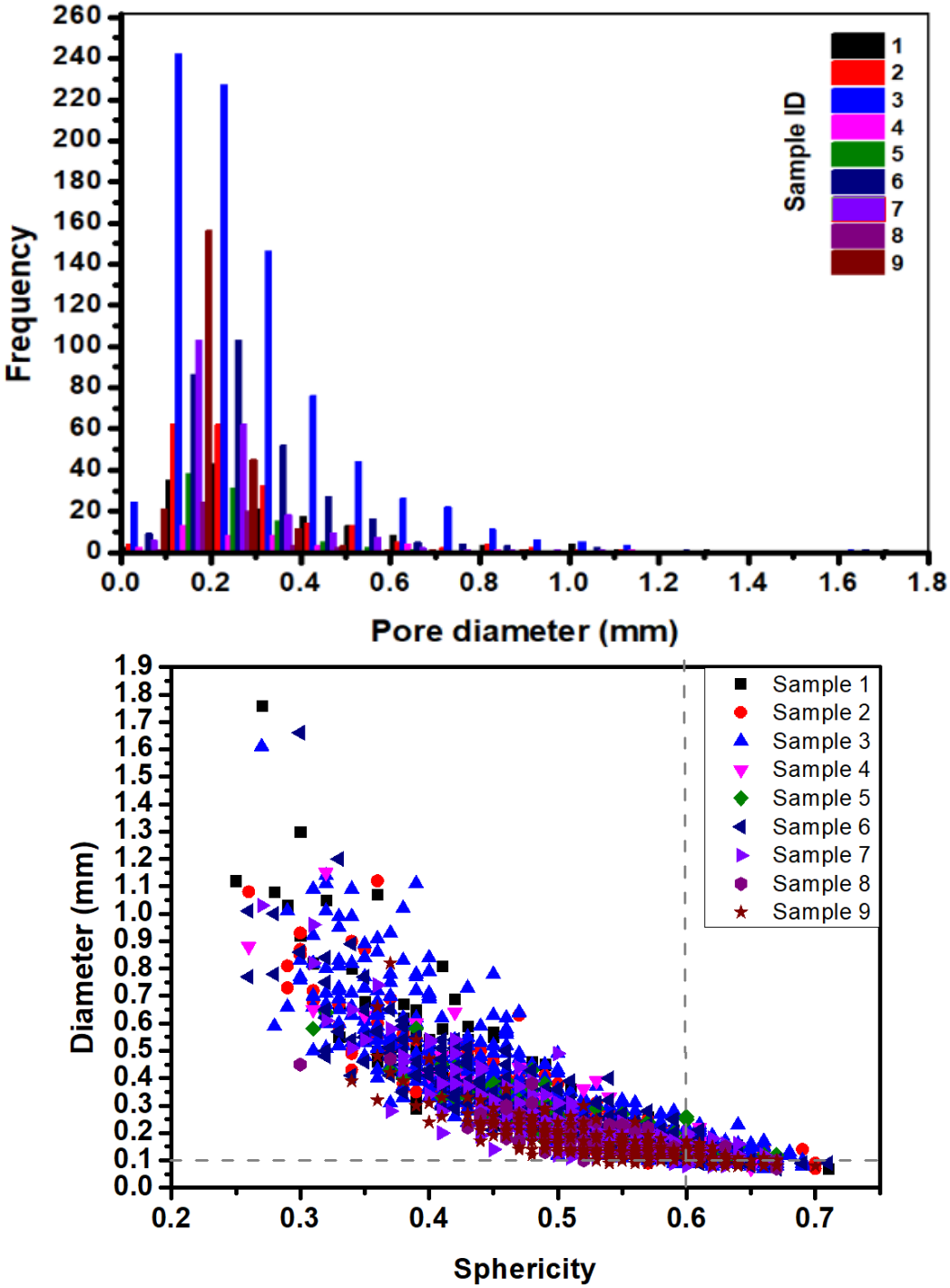

Figure 5.9: Characteristics of pores for high-power samples.

Figure 5.11-Figure 5.14 show the influence of process parameters on porosity for the samples manufactured using the low-power system. At 85 W and 170 W, porosity was lower than 0.1% for all the interaction times. However, porosity can be seen to be decreasing when the interaction time was increased at a laser power of 85 W, while at 170 W, porosity increased with increasing the interaction time. These show that the influence of interaction time on porosity also depends on the laser power. At low laser power (85 W) and low interaction time, the energy input is insufficient to melt the powder completely, and as such, porosity develops mainly due to the LOF defects. The second type of pores is formed when the energy input is very high, such as at high laser power and high interaction time and triggers the formation of porosity mainly due to keyhole [194,196]. Excessive energy input causes excessive penetration of the previous layer, which, after solidification, leaves a pore near the bottom of the melt pool [208], [210]. The result is relatively large pores (> 100 μm) that are usually elongated in the vertical direction [208]- [211]. Hence, porosity increased when the interaction time was increased at a laser power of 170 W.

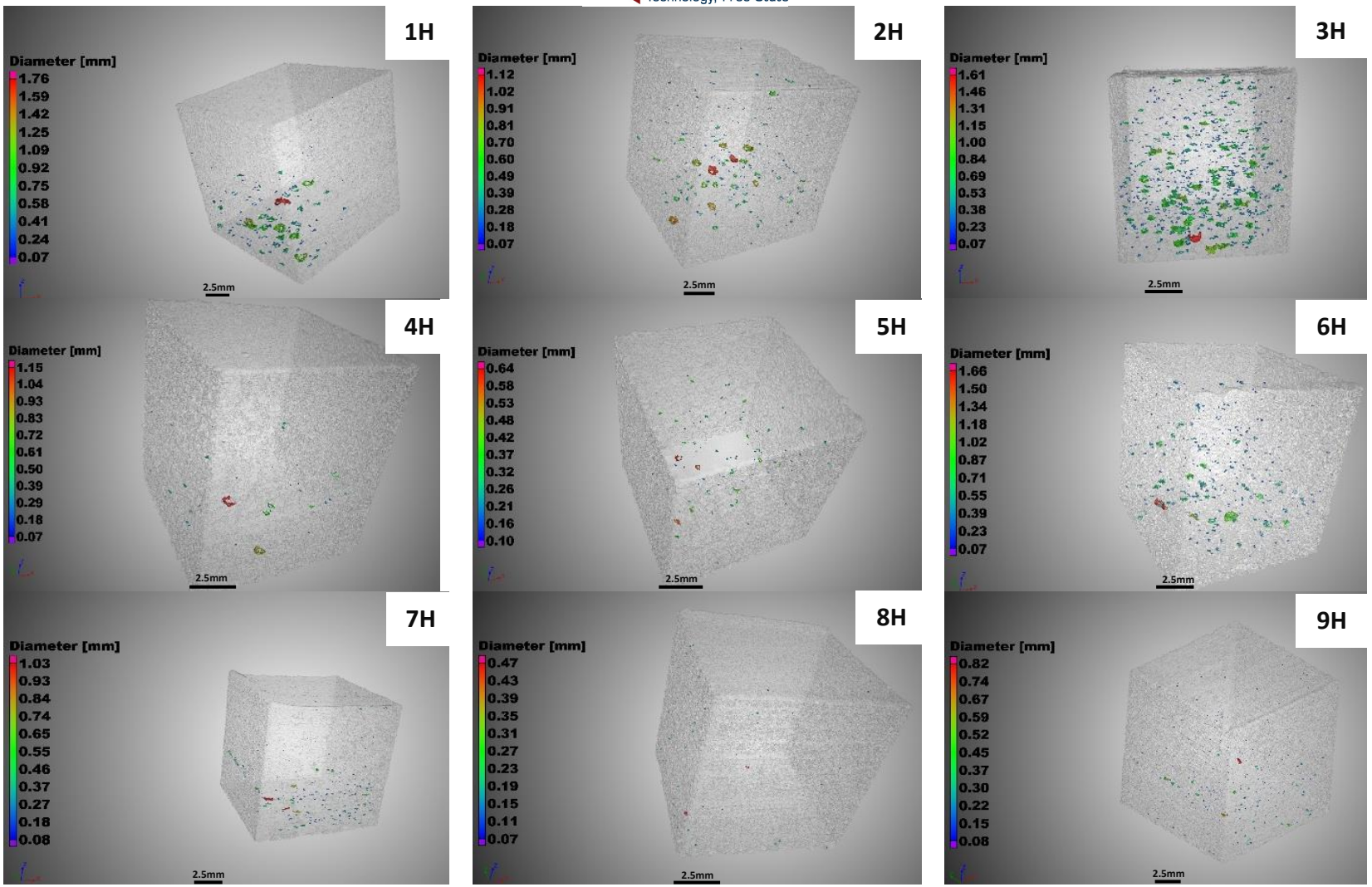

Figure 5.10: 3D micro-CT images of the samples manufactured using the high-power system.

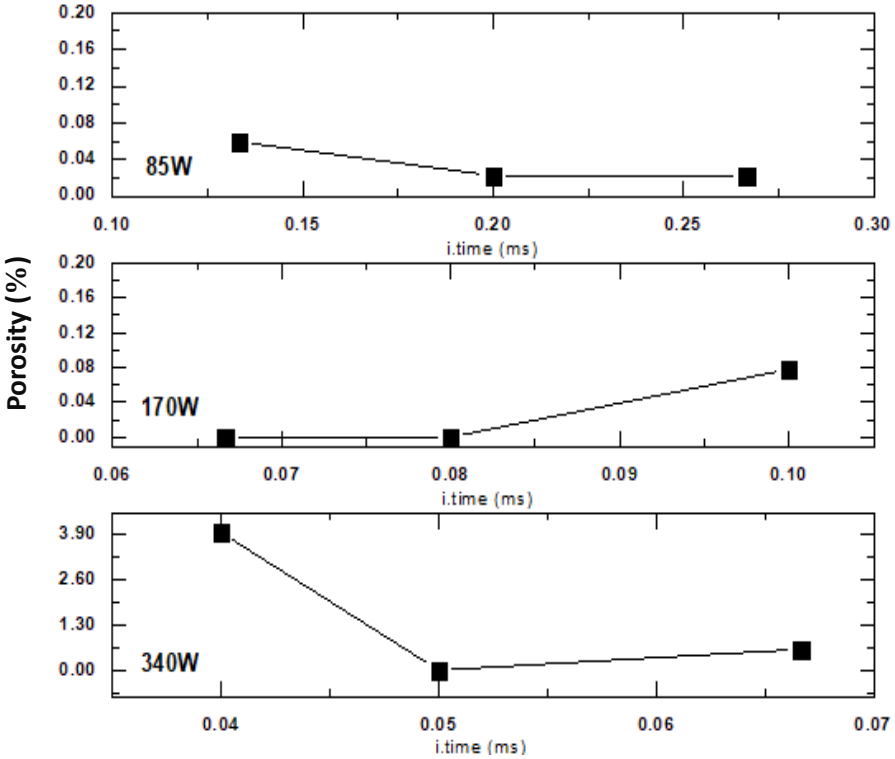

Figure 5.11: Variation of porosity with process parameters used to manufacture the samples using the low-power system.

Figure 5.12 shows the distribution and sphericity of pores in the samples manufactured using the low-power system (see Appendix IV and VI for separate graphs). It was found that most of the pores were irregular in shape and ranged between 0.1 mm to 0.4 mm in size, with samples 7L and 9L, manufactured at 340 W, having the highest count of pores. These high porosity levels are formed due to a mismatch between the laser power and interaction time at 340 W (see Figure 5.14, samples 7L and 9L). When the interaction time is low, the energy input is insufficient to melt the powder completely. As such, porosity develops mainly due to a lack of fusion (sample 9L). Conversely, when the interaction is very high (sample 7L), the energy input becomes excessive, and porosity develops mainly due to keyhole.

Lastly, it is noted that the influence of surface roughness on porosity cannot be overlooked. The increased surface roughness could cause inhomogeneous powder spreading and distribution, thus causing inconsistent melt flow and melt pool in subsequent layers [206]. The presence of discontinuities on the top surface can be very harmful to porosity development in bulk materials. In the current investigation, the

influence of surface roughness on porosity was almost insignificant when the surface roughness was below 30 µm, as shown in Figure 5.13.

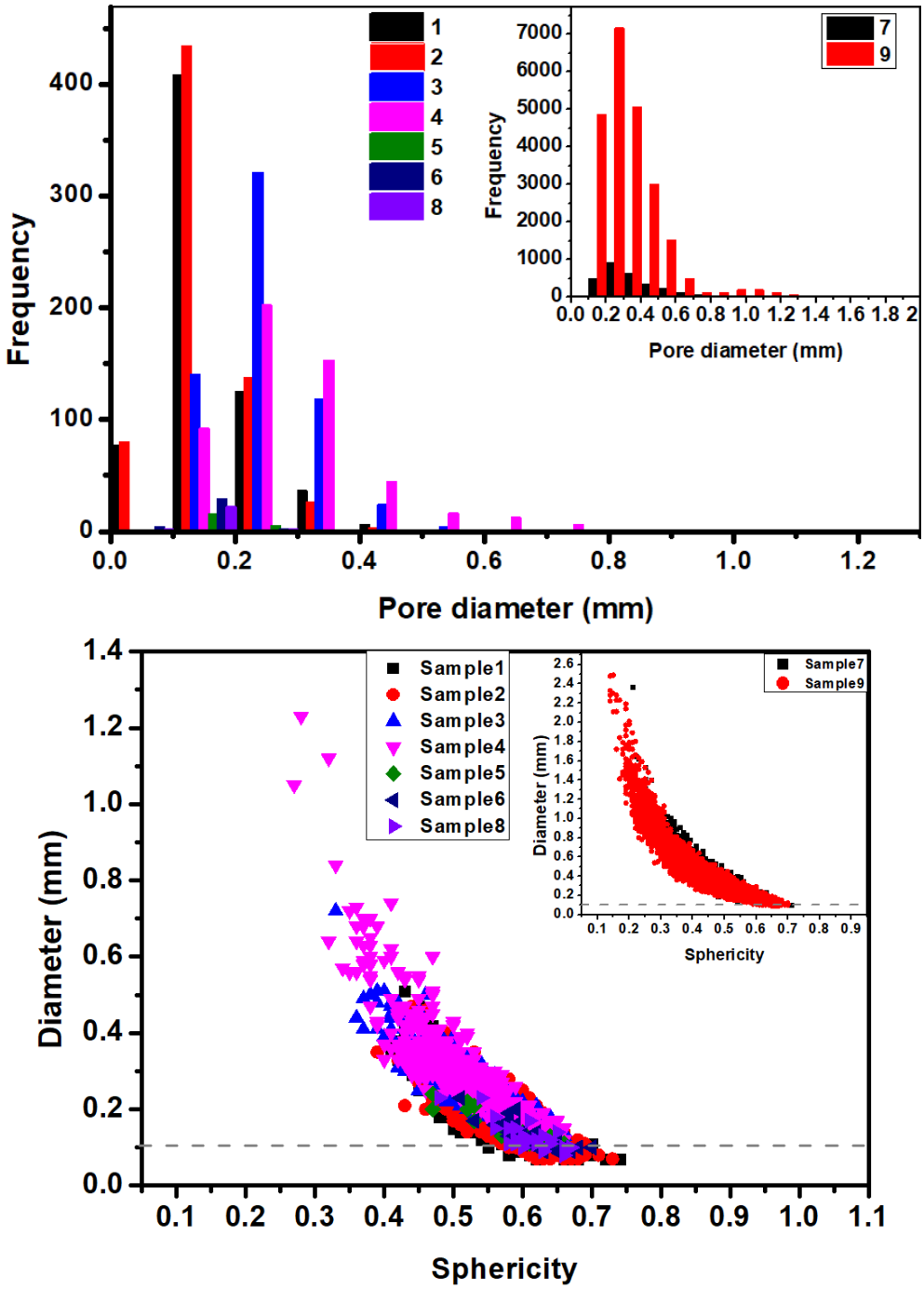

Figure 5.12: Characteristics of pores for samples manufactured using the low-power system.

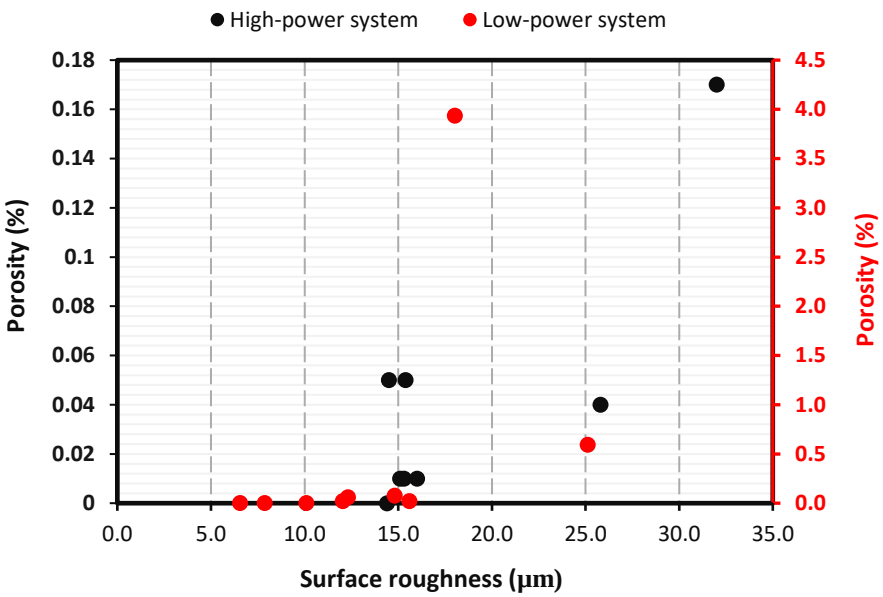

Figure 5.13: Influence of surface roughness on porosity.

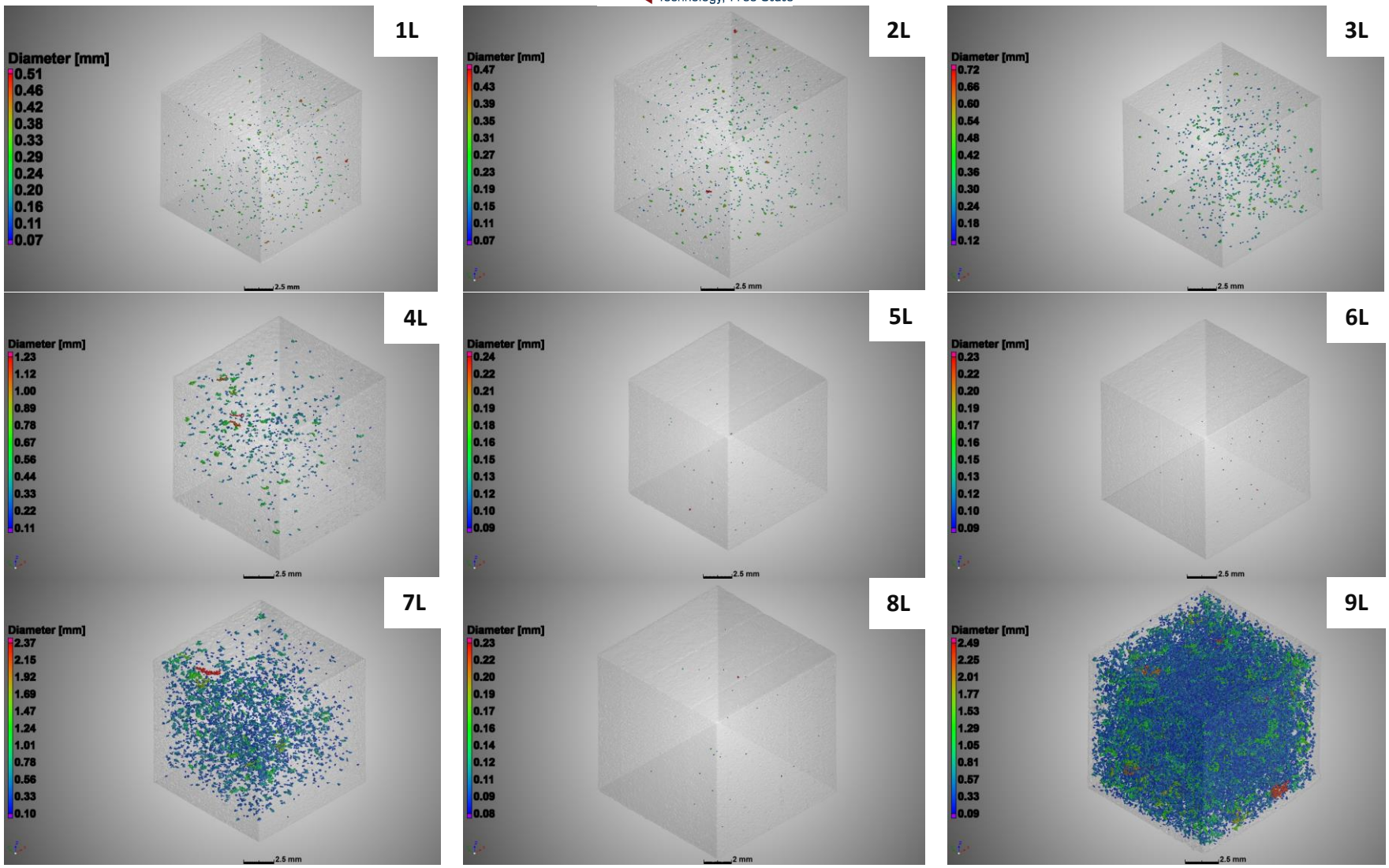

Figure 5.14: 3D micro-CT images of the samples manufactured using the low-power system.

5.3.3 Residual stress on the top surface

Surface residual stress was measured at the center of the top surface at three angles (0°, 45°, 90°) from which the maximum principal residual stress was determined. The 90° angle represents the direction parallel to the scan tracks. The residual stress on the top surface was found to be tensile in nature, as shown in Figure 5.15. This is because the shrinkage of the top layers was restricted by the underlying layers during solidification and cooling, as described by the temperature gradient mechanism [60]. The highest residual stresses (1138 MPa and 999 MPa) were found in samples 4L and 7L manufactured using the low-power system. For the high-power system, the residual stress varied between 445 MPa and a maximum of 720 MPa as the process parameters were changed.

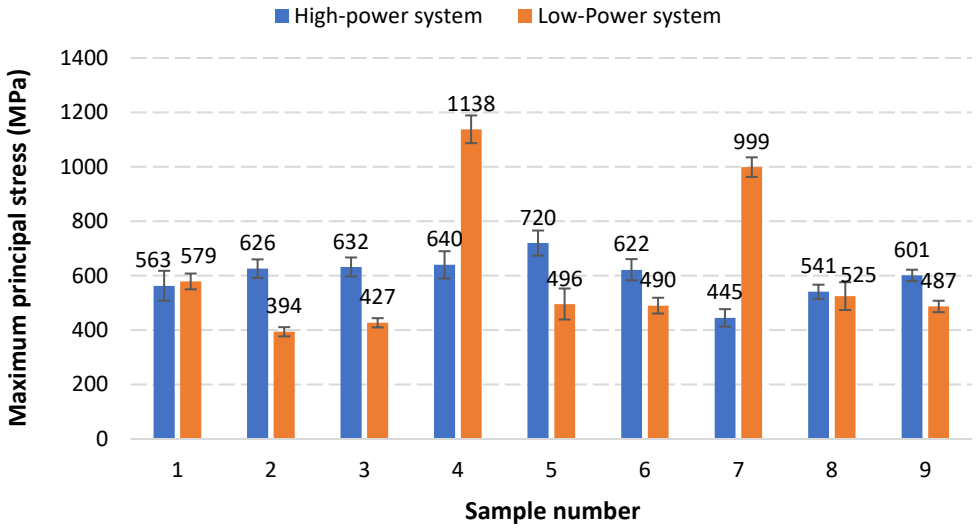

Figure 5.15 Summary of principal residual stress measurements obtained.

Residual stress during LPBF is mainly thermal stress, and therefore, the stress at one point is related to its corresponding thermal history, which is also influenced by the process parameters. In other studies [60]-[61], it was summarized that increasing the cross-sectional area of the melt pool either by decreasing the scan speed (equivalent to increasing the interaction time) or increasing the laser power leads to a reduction in cooling rate, more uniform shrinkage of the metal in and around the melt pool, and thus lower residual stress. This was consistent with the results obtained at a laser power of 600 W, as shown in Figure 5.15, although the difference between the residual stress values was quite small (<100 MPa). The relationship is somewhat different at 750 W, where

residual stress slightly increased with increasing the interaction time and then decreased with a further increase in interaction (Figure 5.16). However, the overall trend is that residual stress decreased slightly as the interaction time was increased. The effect of overlap on residual stress can be seen on the samples manufactured at a laser power of 2000 W, where residual stress decreased with increasing the percent overlap (equivalent to decreasing the hatch distance). This decrease in residual stress can be attributed to the increased remelting of the neighbouring tracks as the overlap increases. At high overlap, the heat accumulation effect becomes relatively marked and thus increases the initial temperature of the solidified layers. Accordingly, the thermal gradients of the remelted zones become much lower, effectively reducing the corresponding residual stress [61]. Generally, residual stresses are high in the scan direction since the tracks shrink along the scanning direction during solidification and cooling [60], [212]-[213]. This was also consistent with the results shown in Figure 5.17. Interesting to note is that the residual stresses developed at a laser power of 2000 W and higher percent overlap (sample 7H) were less anisotropic, as shown by the dotted circle.

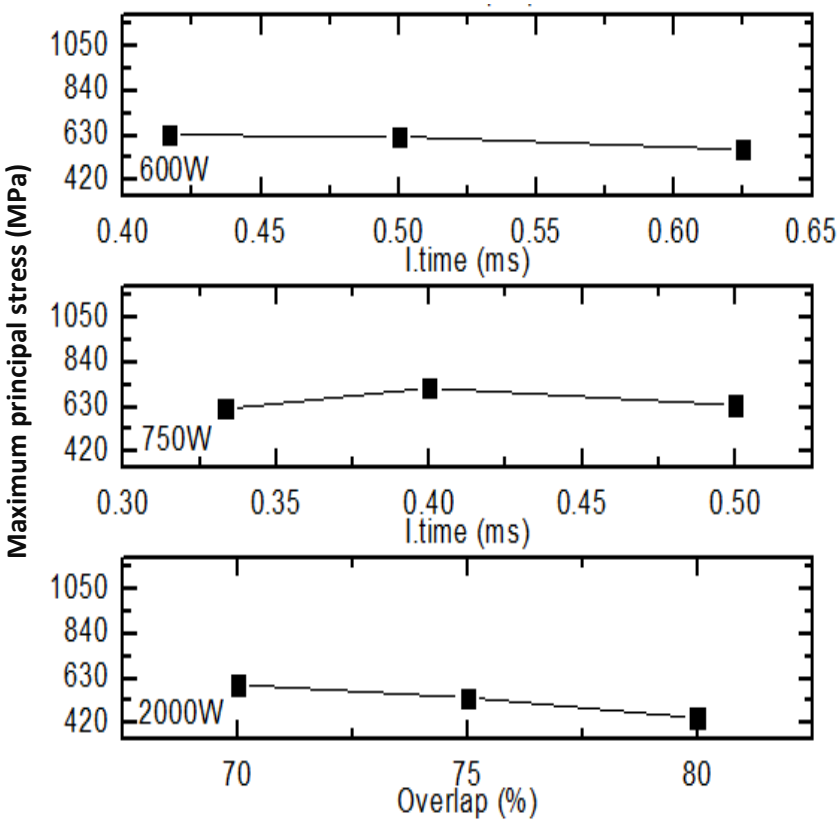

Figure 5.16: Influence of interaction time on residual stress for samples manufactured using the high-power system.

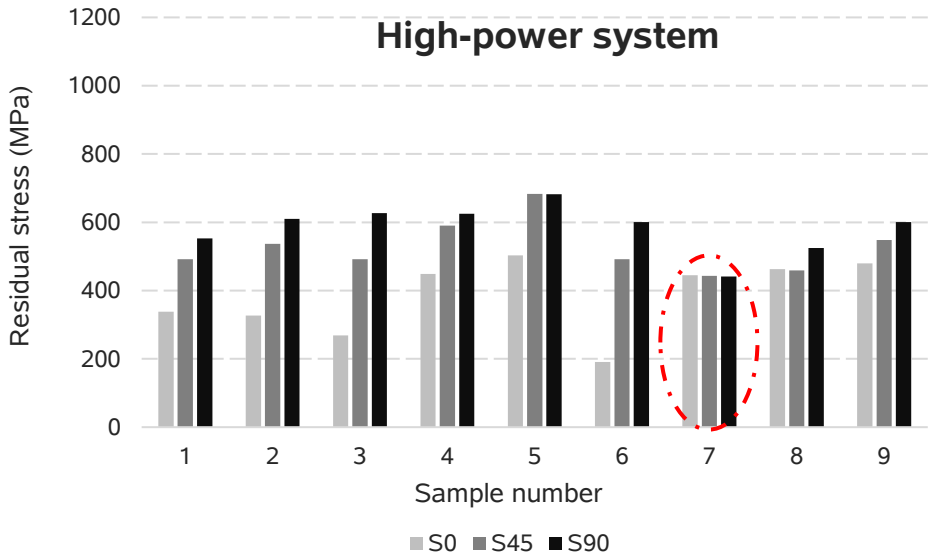

Figure 5.17: Directional stresses measured at the top surface of samples manufactured using the high-power system. Red-dashed area shows isotropic residual stresses measured on sample 7 manufactured at 2000 W.

The relationship between residual stress and process parameters differed in the samples manufactured using the low-power system, as shown in Figure 5.18. At first, residual stress did not change a lot as the interaction time was increased, and then increased with a further increase in the interaction time, especially at a laser power of 170 W and 340 W. This contradicts the results found on the samples manufactured using the high-power system; and shows that the effect of process parameters on residual stress is not monotonous. The complex relationship between residual stress and process parameters could be the reason for the contradictory parametric effects reported in the literature. Fast scanning (i.e. low interaction time) will provide insufficient melting and poor density at a given laser power, whereas slow scanning will produce overheating and keyholing. Thermal gradients, cooling rates, and build time are other variables that influence how residual stress develops.

The shape of the laser beam profile can also influence the shape of the molten pool and temperature gradients [214]-[215] and thus affect residual stress as well. When a gaussian beam is used, it is expected that high laser power and interaction time will contribute to steep temperature gradients due to keyholing [216]-[218], which could lead to the development of high thermal stress and consequently increase residual stress on the top surface. As seen in Figure 5.18, the increase in residual stress could indicate keyholing generated at higher energy input, which becomes prevalent at high laser powers and high

interaction time. Residual stresses were also high in the direction parallel to the scan tracks (90°), as shown in Figure 5.19. It is noted that high porosity in the sample can also lead to stress relaxation and lowering of residual stress. The sample manufactured at a laser power of 340 W and interaction time of 0.04 ms also had the highest porosity (3.94%) and possibly contributed to the lower residual stress measured.

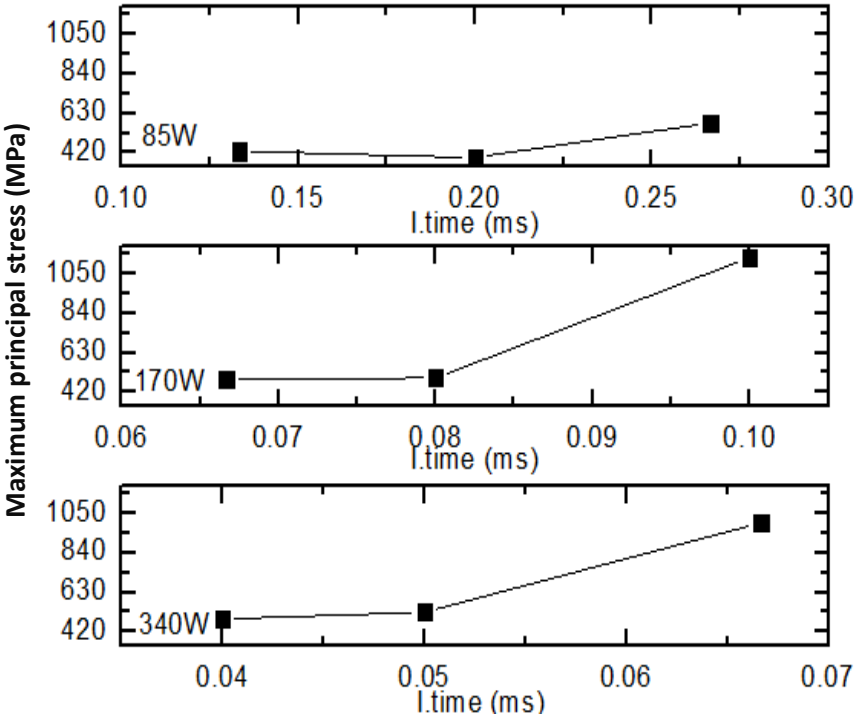

Figure 5.18: Influence of interaction time on residual stress for samples manufactured using the low-power system.

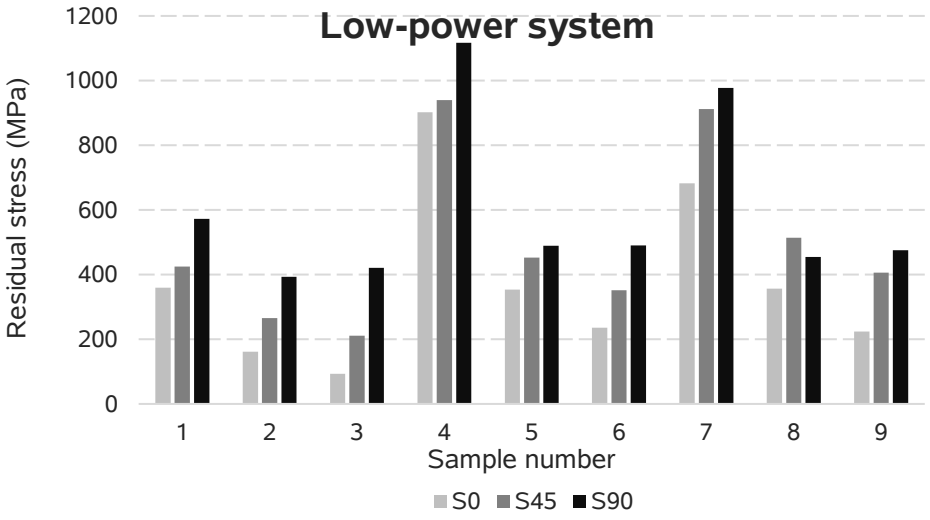

Figure 5.19: Directional stresses measured at the top surface of samples manufactured using the low-power system.

5.3.4 Influence of energy density

The energy density, ratio of laser power to the product of scanning, layer thickness, and hatch distance is commonly used by many researchers as design parameter for the process. It is used to predict the minimum energy required to avoid LOF defects and to describe parameters that lead to a stable process and dense parts [219]-[225]. However, this parameter does not consider other important factors such as the scan strategy, the interaction time between the laser and material, the laser beam diameter and its offset at the surface of the melt, and other essential material properties [226]-[229]. As a result, the same energy density can lead to LOF porosity, stable process, or keyhole, depending on the actual process parameters used. Figure 5.20 shows the influence of energy density on the response variables investigated in this study (porosity, surface roughness, and residual stress). When the energy density is varied by changing the process parameters simultaneously, there is no distinct relationship between the energy density and any of the response variables.

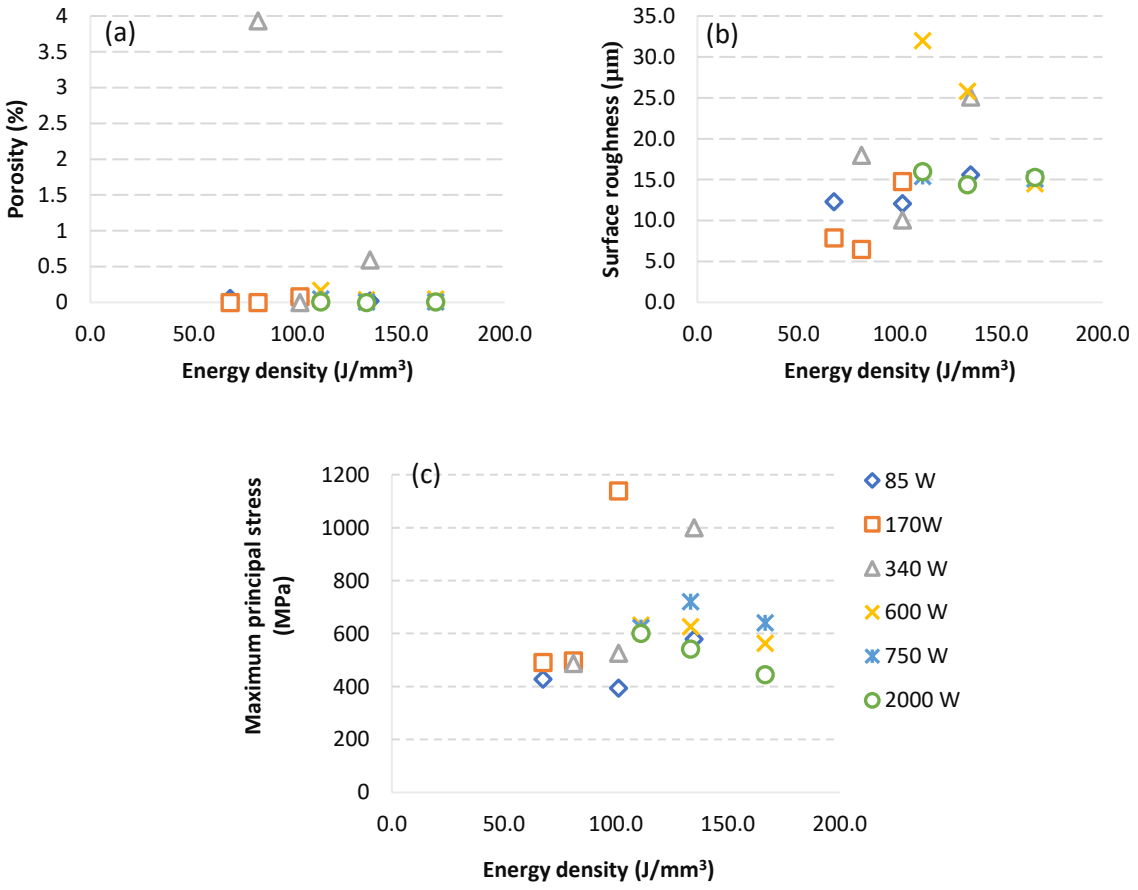

Figure 5.20: Influence of energy density on (a) surface roughness, (b) porosity, and (c) residual stress magnitude.

The same energy density can produce different results depending on the actual parameters used, as shown by other researchers in recent years on different materials [221]-[224], [230]-[232] which was in agreement with the results in this study. For example, at a laser power of 170 W and energy density of 81.0 J/mm^3, porosity was below 0.1%, thus indicating that there was sufficient energy supplied to avoid lack-of-fusion defects. However, the same energy density at 340 W increased porosity (3.94 %) due to a mismatch between the laser power and interaction, thus resulting in LOF defects. Table 5.3 shows other cases where different results were obtained at the same energy density. Figure 5.21 shows mico-CT images of the samples representing the worst-case scenarios where the same energy density produced different results.

Table 5.3: Variation of response variables at the same energy density levels

Laser power (W)	Interaction time (ms)	Sample number	Energy density (J/mm^3)	Bulk porosity (%)	Surface roughness (µm)	Maximum residual stress (MPa)
600	0.625	1H	**166.7**	0.05	14.5	563
750	0.500	4H		0.01	15.1	640
2000	0.075	7H		0.01	15.3	445
600	0.500	2H	**133.3**	0.04	25.8	626
750	0.400	5H		0.01	21.9	720
2000	0.075	8H		0.00	15.3	445
600	0.417	3H	**111.1**	0.17	32.0	632
750	0.333	6H		0.05	15.4	622
2000	0.075	9H		0.01	16.0	601
85	0.267	1L	**134.9**	0.022	15.6	579
340	0.067	7L		0.594	25.1	999
85	0.200	2L	**101.2**	0.022	12.1	394
170	0.100	4L		0.078	14.8	1138
340	0.050	8L		0.001	10.1	525
85	0.133	3L	**67.5**	0.059	12.3	427
170	0.067	6L		0.001	7.9	490
170	0.080	5L	**81.0**	0.001	6.5	496
340	0.040	9L		3.935	18.0	487

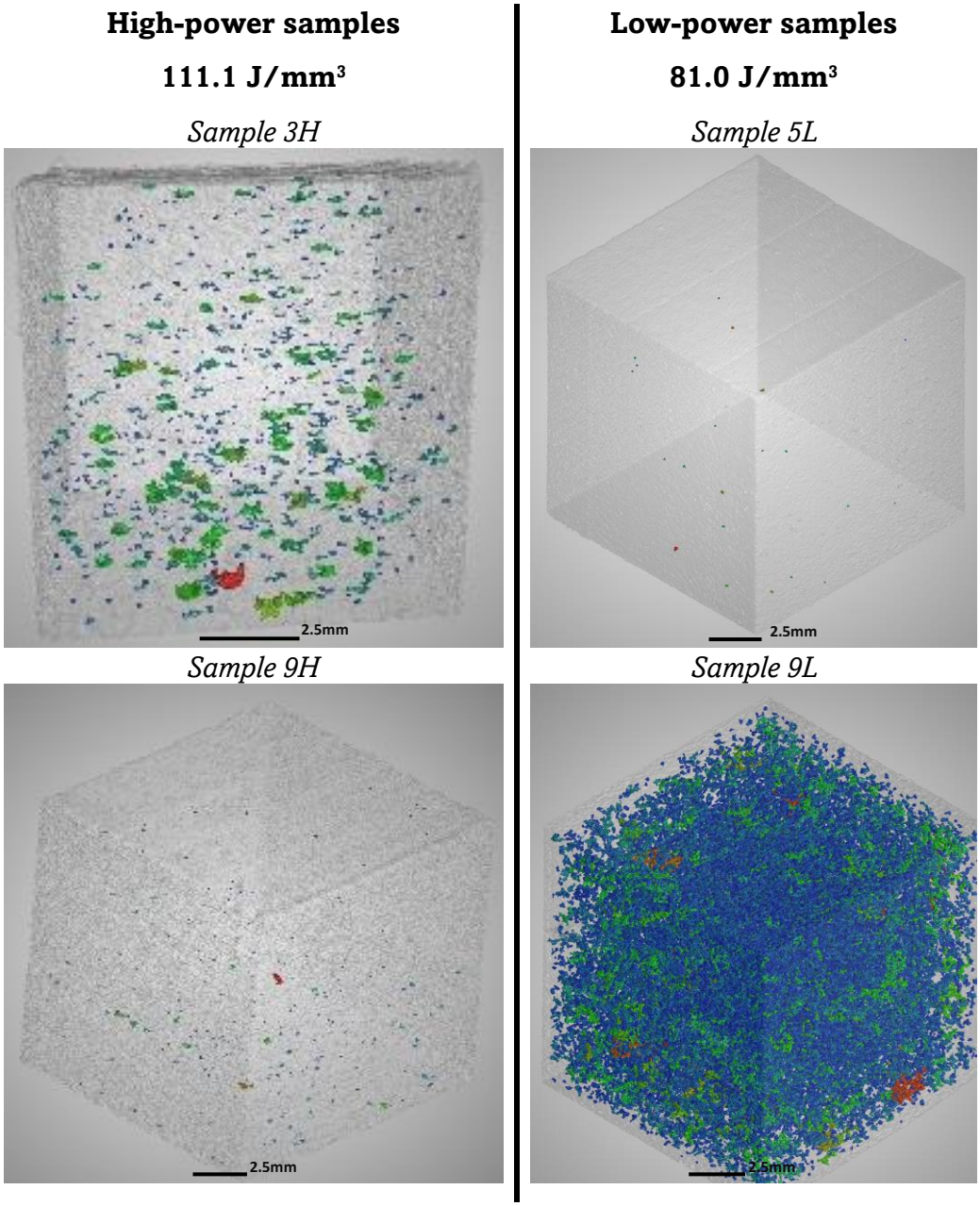

Figure 5.21: Micro-CT images show scenarios where the same energy density produced different results.

5.3.5 Influence on productivity

The primary goal of this investigation was to determine the maximum achievable build rates for the high-power and low-power LPBF systems used in this study. The amount of time required to melt and solidify the material usually limits the productivity of LPBF systems. The amount of material that the process can melt in a given amount of time, in this case, the build rate, was used to evaluate productivity. High scan speeds, long hatch distances, and thick layers are typically associated with the process parameters with the

fastest build rates [35], [233]-[236]. In the context of the current investigation, this is equivalent to decreasing the interaction time and percent overlap. Since the productivity of the LPBF process is primarily linked to the build rate, the influence of build rate on the response variable, and porosity, were also evaluated to determine the maximum achievable build rates.

Figure 5.22 shows the variation of porosity over different build rates. From the results, one can see that there was no distinct relationship between porosity and build rate. This was in good agreement with the results obtained by Wishcheropp et al. [215] using different beam profiles on aluminium alloys. This is because the build rate alone is not good enough to describe the behaviour of the process, as it does not account for the laser power and other essential material properties that affect the melting process. It is merely a parameter that can be used to measure the productivity of the process. Therefore, the maximum achievable build rate depends on the interaction between the actual process parameters, ensuring a stable process and producing highly dense parts. Accordingly, the maximum achievable build rates in the current investigation were 18 mm^3/s for the high-power system and 3.4 mm^3/s for the low-power system. Micro-CT images of these samples are shown in Figure 5.23.

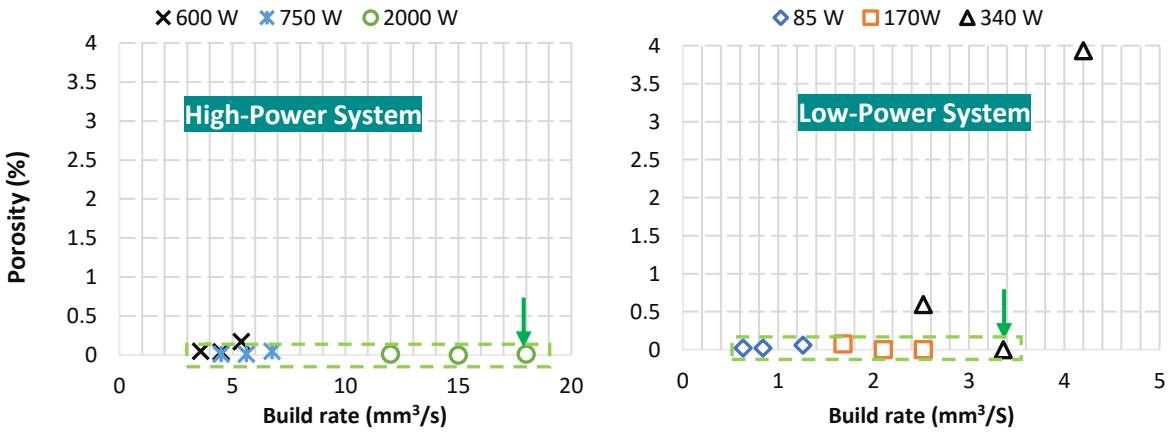

Figure 5.22: Comparison of porosity levels in the samples produced at different build rates. Green-dashed rectangle shows the optimal process window in terms of porosity <0.1%, while the green arrows show the maximum achievable build rates.

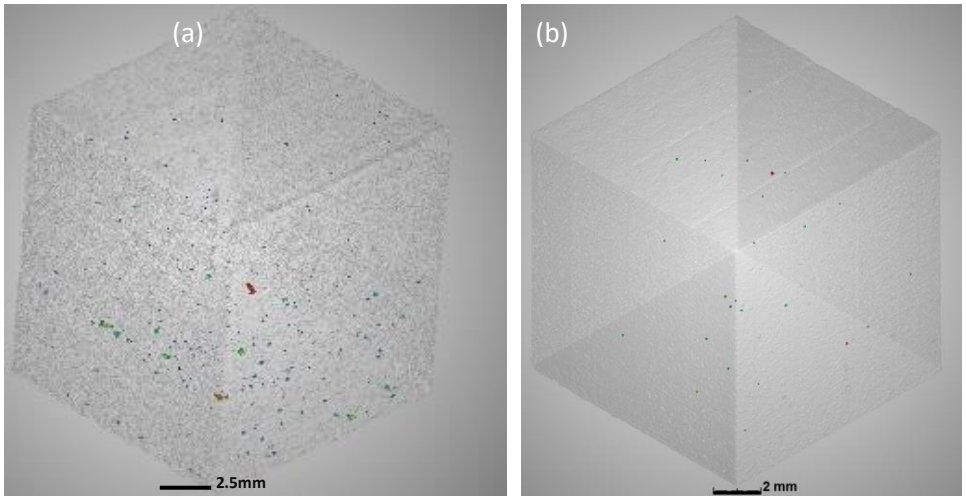

Figure 5.23: Micro-CT images of samples manufactured at maximum achievable build rates: (a) 18 mm^3/s high-power system, 3.4 mm^3/s low-power system.

5.3.6 Microstructure: prior-beta grain size

The microstructure evolution of Ti-6Al-4V primarily depends on the cooling rate. The typical microstructure formed in the as-built condition consists of columnar prior-beta grains that grow epitaxially across several layers. The transformation of Ti-6Al-4V into needle-like martensite (α') occurs at high cooling rates greater than 410 °C/s while lamellar Widmanstätten (α) forms at intermediate cooling rates between 20 and 410 °C/s [168]. Generally, the LPBF process has high cooling rates that exceed the critical cooling rate, which favours the transformation to martensite α'.

Figure 5.24 shows the microstructures of samples manufactured at maximum achievable build rates along the build direction (see Appendix VII and VIII for all samples). The microstructure showed a dominant presence of martensitic α' needles that formed due to the fast-cooling rates. The prior-beta grains were also found to span a few layers parallel to the build direction. A comparative plot of the prior-beta grain width is presented in Figure 5.25. Here it can be seen that material from the high-power system has a larger prior beta-grain size than the material built using the low-power system.

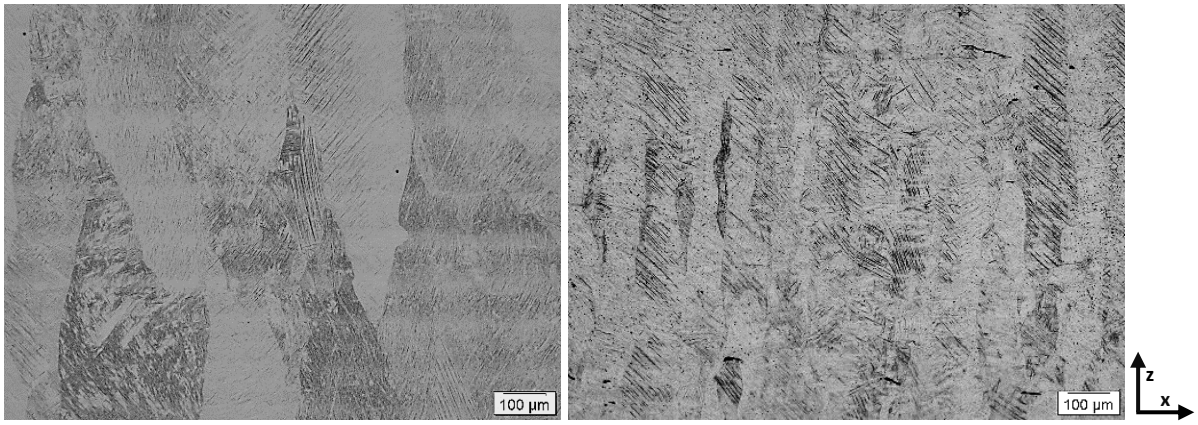

Figure 5.24: Optical micrographs of samples manufactured at (a) 2000 W, 18 mm^3/s and (b) 340 W, 3.4 mm^3/s, Z is a build direction.

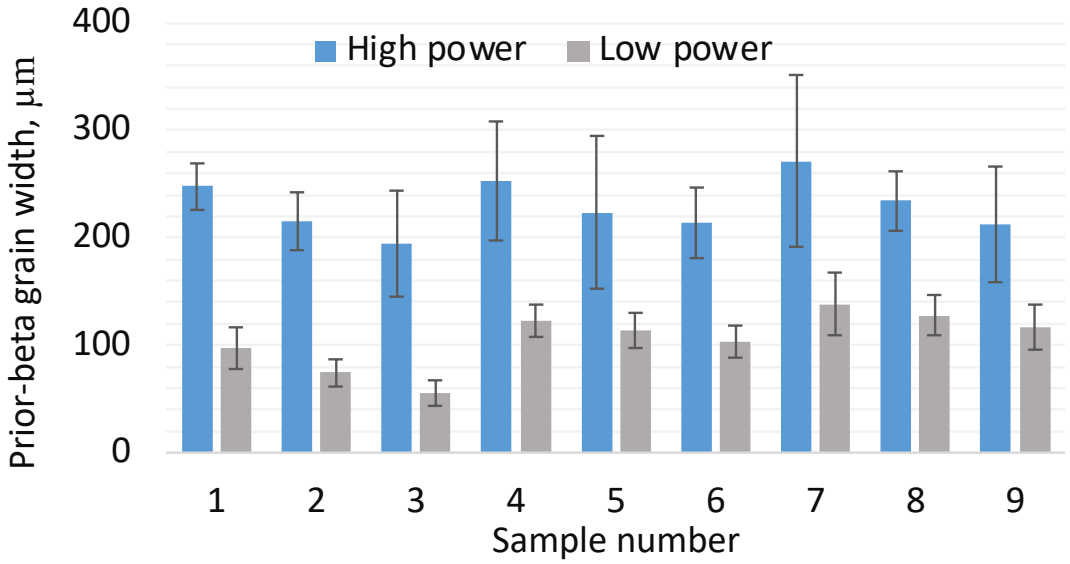

Figure 5.25: Prior-beta grain width measurements for samples manufactured using the high-power and low-power systems.

The size of prior-beta grains is an important microstructural feature that can influence the mechanical properties of Ti-6Al-4V, as this can affect the α-colony size and texture, as well as texture heterogeneity in the final product [161]. It is mainly determined by the time the material is exposed to temperatures above the beta (β) transus temperature. Longer time and increased temperature above β transus temperature lead to increased beta-grain size [161]-[163]. It is possible that the material built at high laser powers endured a longer time above the β transus temperature, and the melt pool size may also have influenced the prior-beta grain size. Similarly, when the interaction time or overlap

rate is high, the material is expected to endure a longer time above the β transus temperature and thus lead to an increased prior-beta grain size. Figure 5.26 shows the effect of interaction time and overlap on the prior-beta grain size.

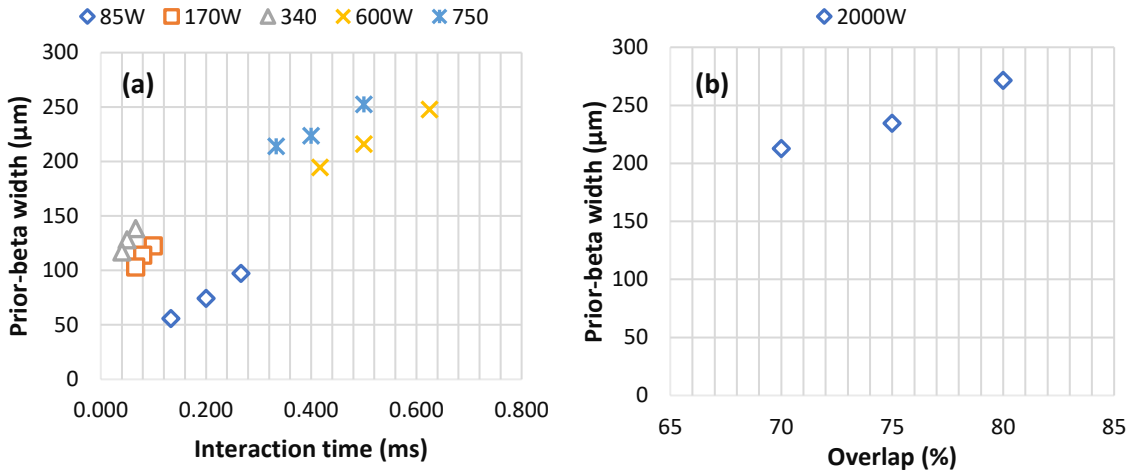

Figure 5.26: Influence of interaction time (a) and overlap (b) on the prior beta grain size.

5.4 Summary and conclusion

The purpose of this investigation was to characterize and compare the samples manufactured at high- and low-laser powers using two independent systems operating at different parameter regimes to improve productivity. Advanced characterization techniques such as X-ray computed tomography and X-ray diffraction were used to investigate the top surface roughness, bulk porosity in samples, and residual stress on the centre of the top surface. The microstructure in the as-built condition was also investigated using light optical microscopy to measure the size of prior beta grains. The influence of process parameters on the response variables was presented and discussed. Therefore, the most important findings can be summarized as follows:

1. The top surface roughness of the samples manufactured using the high-power system ranged between 14.4 to 32.0 µm and 6.5 to 25.1 µm for the samples manufactured using the low-power system.
2. The influence of process parameters on the surface roughness and porosity depends on the balance between the interaction time and laser power. At low interaction time and low power, the surface roughness and porosity increased due to balling effect, while at high interaction time and high laser power, the surface roughness and porosity increased due to unstable molten pool and keyhole effect.

3. The bulk porosity in the samples manufactured using the high-power system ranged between 0 to 0.17% and 0 to 3.94% for the samples manufactured using the low-power system.
4. Changing the percentage overlap at high laser power (2000 W) did not have a significant effect on the surface roughness (14.4 to 16.0 μm) and porosity (<0.1%).
5. The maximum residual stresses measured on the top surface were tensile and varied between 445 to 720 MPa at high laser powers and 394 to 1138 MPa at low laser powers. Residual stresses were found to be higher along the scan direction.
6. Increasing the percentage overlap at high laser power (2000 W) led to a reduction in residual stress (601 to 445 MPa).
7. There was no clear relationship between the energy density and any of the response variables. This shows that the energy density is not a good parameter to describe the behaviour of the LPBF process.
8. The maximum achievable build rates for porosity were 18 mm^3/s for the high-power system and 3.4 mm^3/s for the low-power system.
9. The size of prior-beta grains was larger for the samples manufactured using the high-power system.
10. The size of prior-beta grains increased when the interaction time, laser power, and overlap were increased.

Chapter 6
Effect of post-processing on the surface roughness and mechanical properties of Ti-6Al-4V manufactured with high laser power system

6.1 Introduction

The use of high-powered laser systems in AM presents a unique opportunity to improve the build rate and productivity of the process. However, the larger beam spot size produced parts with a higher surface roughness in the as-built condition. Such roughness can be as high as ~25 µm Ra and can negatively affect the mechanical properties and the resolution of parts manufactured. Post-processing is therefore required to improve the surface integrity of LPBF parts as it affects the mechanical properties, especially the fatigue strength of the material. The material strength and corrosion resistance were also proved sensitive to the surface quality, as shown in the literature review. Some common surface improvement techniques were also reviewed and discussed in detail in Chapter 2. Some of these techniques come with the disadvantages of being skilled-operator dependent, labour-intensive, and requiring heavy investment in facilities which may be a limitation for other entities. Centrifugal barrel finish (CBF) provides an alternative method with low equipment cost and versatility and can apply uniform finish even on complex geometries. The finishing operation is automatic and almost independent of the component's shape complexity, and the part does not need to be fixed. This chapter investigates the evolution of the vertical surface morphology of Ti-6Al-4V test parts processed by CBF and its effect on mechanical properties.

6.2 Experimental designs

6.2.1 Surface finishing

Ti-6Al-4V cylindrical test coupons manufactured using optimal parameters (laser power of 2000 W, interaction time of 0.075 ms, and build rate of 18 mm^3/s) were used to investigate the vertical surface morphology under different parameters during CBF. Two main parameters, rotational speed and polishing time were chosen for this investigation and were varied, as shown in Table 6.1, to establish the combination that results in low

surface roughness. The vertical surface roughness of each sample was measured using a stylus portable roughness tester in accordance with ISO 4287 international standard. Each sample was measured at least eight times to obtain average surface roughness. The samples were further characterized using a scanning electron microscope (SEM) to reveal the surface morphology.

Table 6.1: Surface polishing experimental conditions and sample ID

Rotational speed (rmp)	**Polishing time (hr.)**	**Sample ID**
45	1	A
45	2	B
45	3	C
45	4	D
45	5	E
85	1	F
85	2	G
85	3	H
85	4	I
85	5	J

6.2.2 Post-heat treatment and mechanical testing

Standard post-annealing and HIP heat treatments (Table 6.2) were applied on vertical tensile and fatigue testing specimens using the conditions in Table 6.1 to investigate the combined effect of surface finishing and heat treatment on mechanical properties. Annealing and HIP heat treatments were carried out under an argon atmosphere using a Carbolite tube furnace and EPSI HIP vessel shown in Chapter 3. Room temperature tensile tests and high-cycle tension-tension fatigue tests were conducted using an Instron 1342 servo-hydraulic testing machine. Figure 6.1 shows some of the tensile samples that were manufactured and tested.

Table 6.2: Heat treatment and surface conditions used in this study

Batch number	Heat treatment condition	Surface condition	Number of samples
1	Annealing (950 °C, 2 hours, furnace cooling)	As-built	12
2	Annealing (950 °C, 2 hours, furnace cooling)	Polished	12
3	Hot isostatic pressing (950 °C, 100 MPa, 2 hours, furnace cooling)	Polished	12

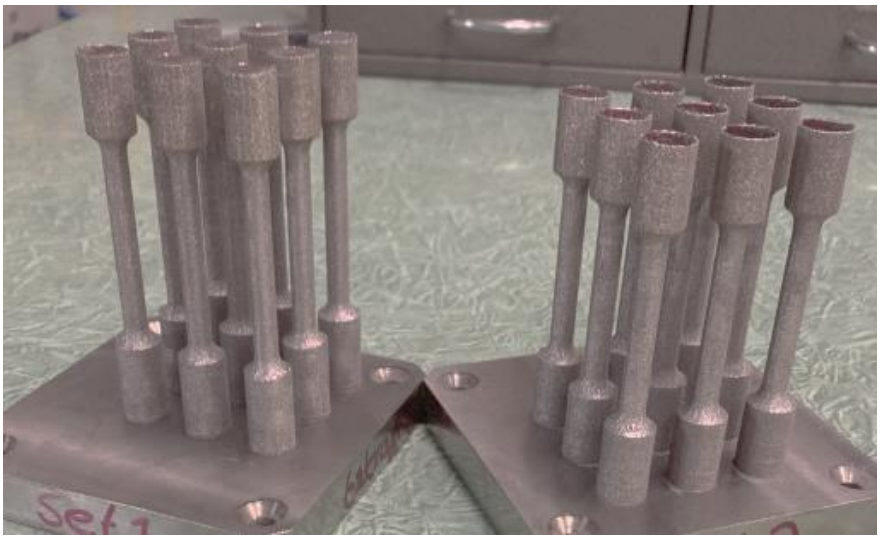

Figure 6.1: Image showing some of the test pieces manufactured.

6.3 Results and discussion

6.3.1 Surface finishing

The SEM images of the test pieces polished at different CBF parameters are presented in Figure 6.2. In the as-built condition, the surface was dominated by partially melted particles, resulting in high surface roughness. It is expected that during barrel finishing, the impacting media to the surface of the samples would result in the removal of some of the partially melted particles and roughness peaks due to plastic deformation and/or fracture of materials making repeated contact with the abrasive media. After the barrel finishing at a speed of 45 rpm, only a few of these particles are removed after the first hour and remain almost the same with increased processing time. At 85 rpm, the cutting

action is faster, and most of the partially melted particles are removed from the surface, with some roughness peaks deformed and flattened, but some valleys are still visible and open to the surface. The combination of rotational speed and time had a stronger effect on the surface roughness, and this was mainly because the speed affects the cutting force while longer polishing time increases the contact area, which in turn helps to lower the surface roughness [236].

One of the traits of post-treated surfaces is the disappearance of the peaks while valleys remain, which is due to the nature of the abrasive process. Increasing the processing time efficiently reduces the number of valleys exposed to the surface. Surface roughness measurements confirm the microscopic observations in Figure 6.3. The Ra value was reduced by up to 27% at 45 rpm and up to 90% at 85 rpm after 5 hours of processing. Figure 6.4 shows the cross-sectional views of the surface region of the as-built sample and samples polished at 45 rpm and 85 rpm, respectively. Although the surface quality at 85 rpm after 5 hours was significantly improved, the polishing process struggled to completely remove the troughs and peaks believed to be associated with the subsurface partially melted particles and laser contouring defects, resulting in residual cavities on the surface like the ones shown in Figure 6.4c.

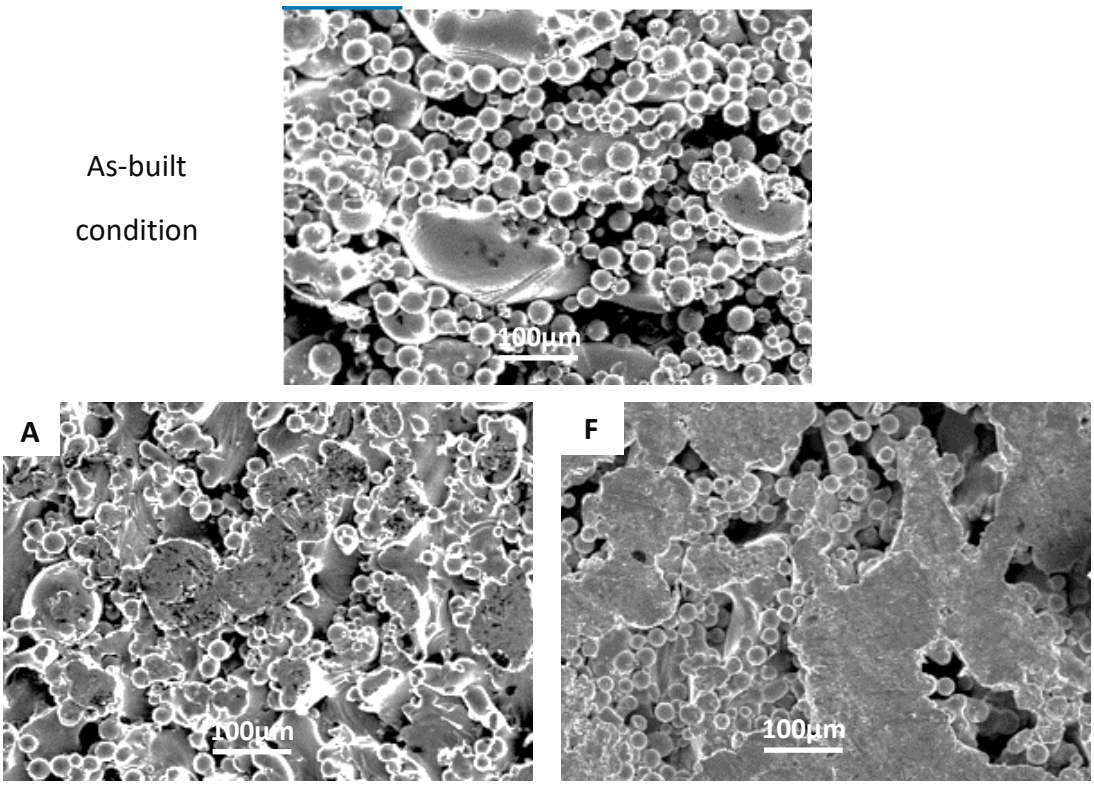

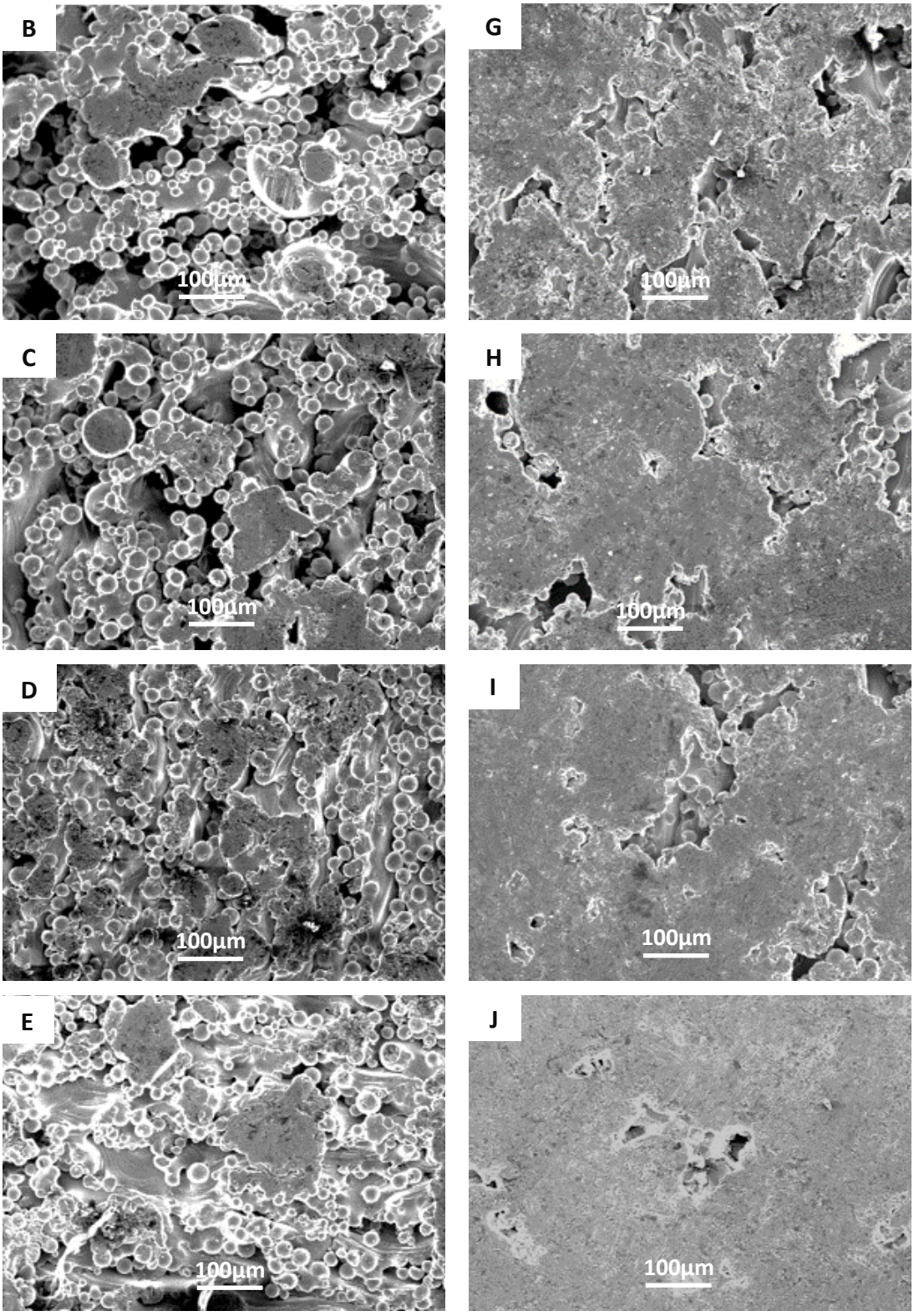

Figure 6.2: SEM micrographs showing the surface morphology of the samples processed (see Table 6.1 for sample ID).

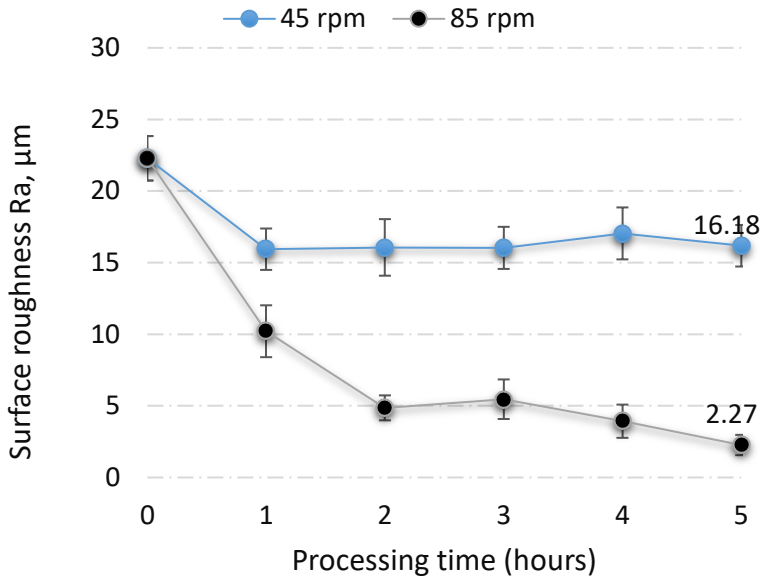

Figure 6.3: Surface roughness values as a function of polishing speed and time.

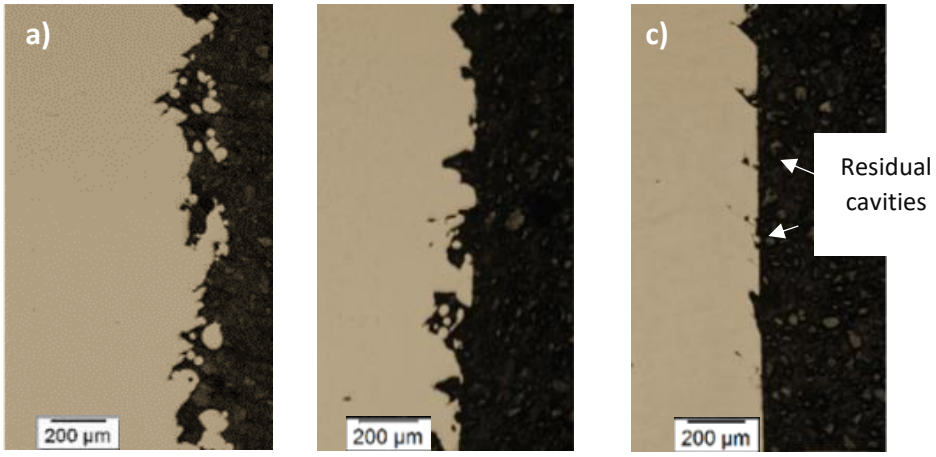

Figure 6.4: Cross-sectional views of (a) as-built sample, (b) sample processed at 45 rpm for 5 hours, and (c) sample processed at 85 rpm for 5 hours.

6.3.2 Tensile properties

Tensile tests were performed to evaluate the performance of the specimens following post-processing. Table 6.3 shows the tensile results visually represented in Figure 6.5 (see Appendix IX for the stress-strain graphs). The specimens that had only been annealed and tested with the inherent surface roughness (Batch 1) displayed low tensile properties in YS, UTS, and elongation. The measured YS and UTS of annealed and polished specimens (Batch 2) were above the minimum requirements of ASTM F2924-14, but the elongation was still less than the minimum criteria of 6.0%. The final batch of HIPed and

polished specimens had an average elongation of 6%, while the YS and UTS were lowered somewhat but remained over the minimal criteria.

Table 6.3: Summary of tensile results obtained

Specimens	Tensile stress at yield (Offset 0.2%) (MPa)	Modulus of (Chord 200–600 MPa) (Gpa)	UTS (MPa)	Elongation (%)	Reduction of area (%)
Batch 1 average ±S.D. CV	842.2 ± 31.1 0.0369	112.4 ± 4.0 0.0357	883.5 ± 5.4 0.006	1.6 ± 0.4 0.248	5.9 ± 1.6 0.265
Batch 2 average±S.D. CV	937.4 ± 1.2 0.021	113.5 ± 1.4 0.001	973.5 ± 7.3 0.012	5.7±0.2 0.0075	9.1±3.1 0.037
Batch 3 average±S.D. CV	824.5 ± 16.3 0.0197	117.3 ± 1.8 0.0134	931.7 ± 13.7 0.0147	6.2 ± 1.1 0.184	11.1 ± 5.9 0.529

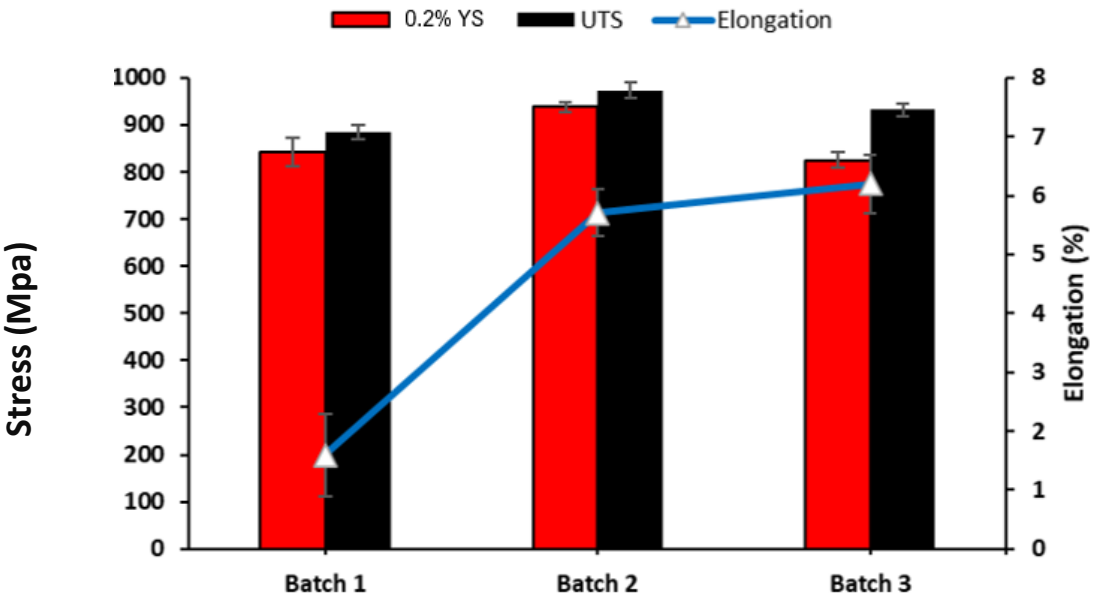

Figure 6.5: Graphical representation of the tensile results obtained.

After the tensile test, the fracture surfaces of the broken test pieces were analyzed under the SEM. It was found that most of the samples had interlayer defects on the fracture surface dominated by LOF, open pores, and unmelted particles, while the fractured area showed ductile-type fracture characterized by dimples (see Figure 6.6). Large pores

occupied by unmelted particles were also observed in some areas closer to the surface (see Figure 6.6c). The central area was clearly distinguishable from the shear lips on the periphery. To establish whether these defects were localized or distributed throughout the specimen, the gripping area of the tensile specimens was sectioned and analyzed under the optical microscope. This area of the specimens did not reveal any evidence of LOF defects, as shown in Figure 6.7, thus indicating that the defects present in the samples were rather localized. Powder delivery is an important step in the LPBF process and is closely linked to the quality of the parts. Defects in the powder bed often translate into defects in the manufactured parts due to the detrimental effects on the physical interaction between the laser beam and the powder bed. Unfortunately, the high-power experimental system used in this study occasionally suffers from powder delivery inconsistencies, i.e. incomplete powder spreading, which possibly contributed to the observed LOF defects.

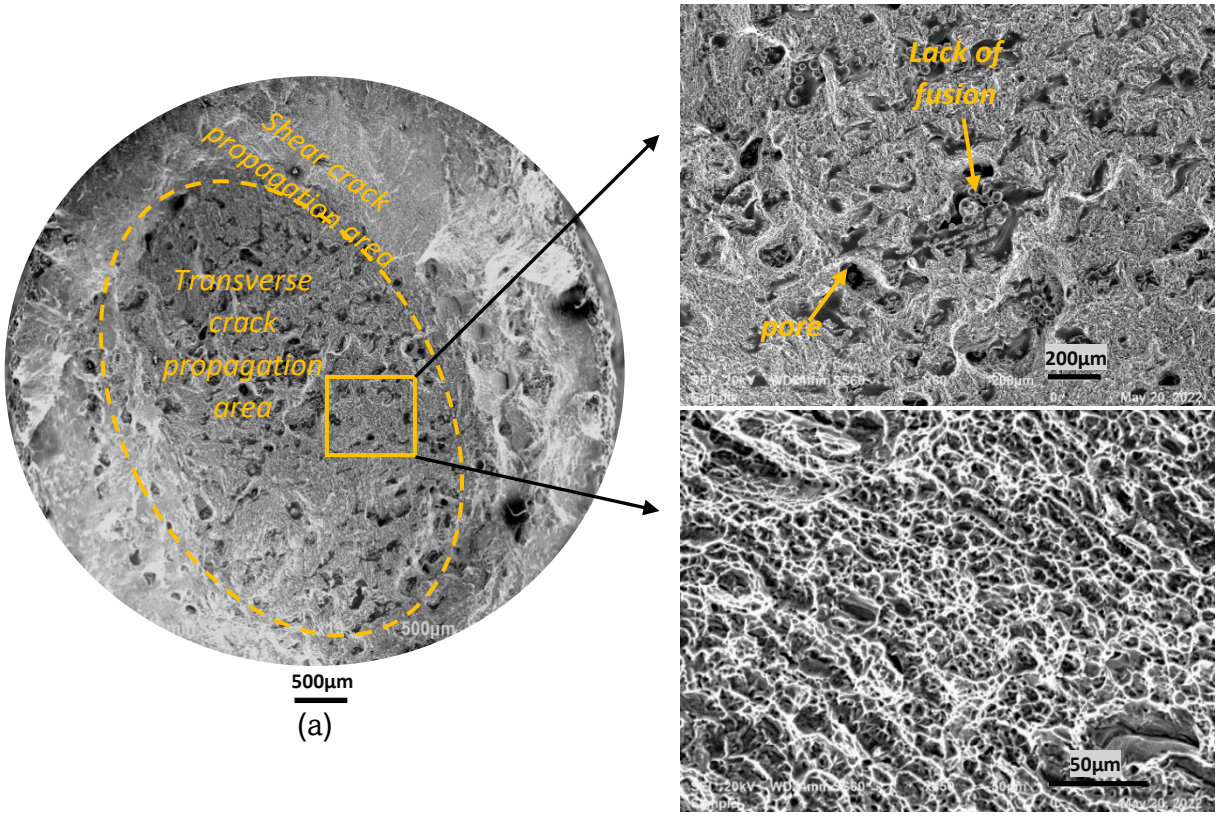

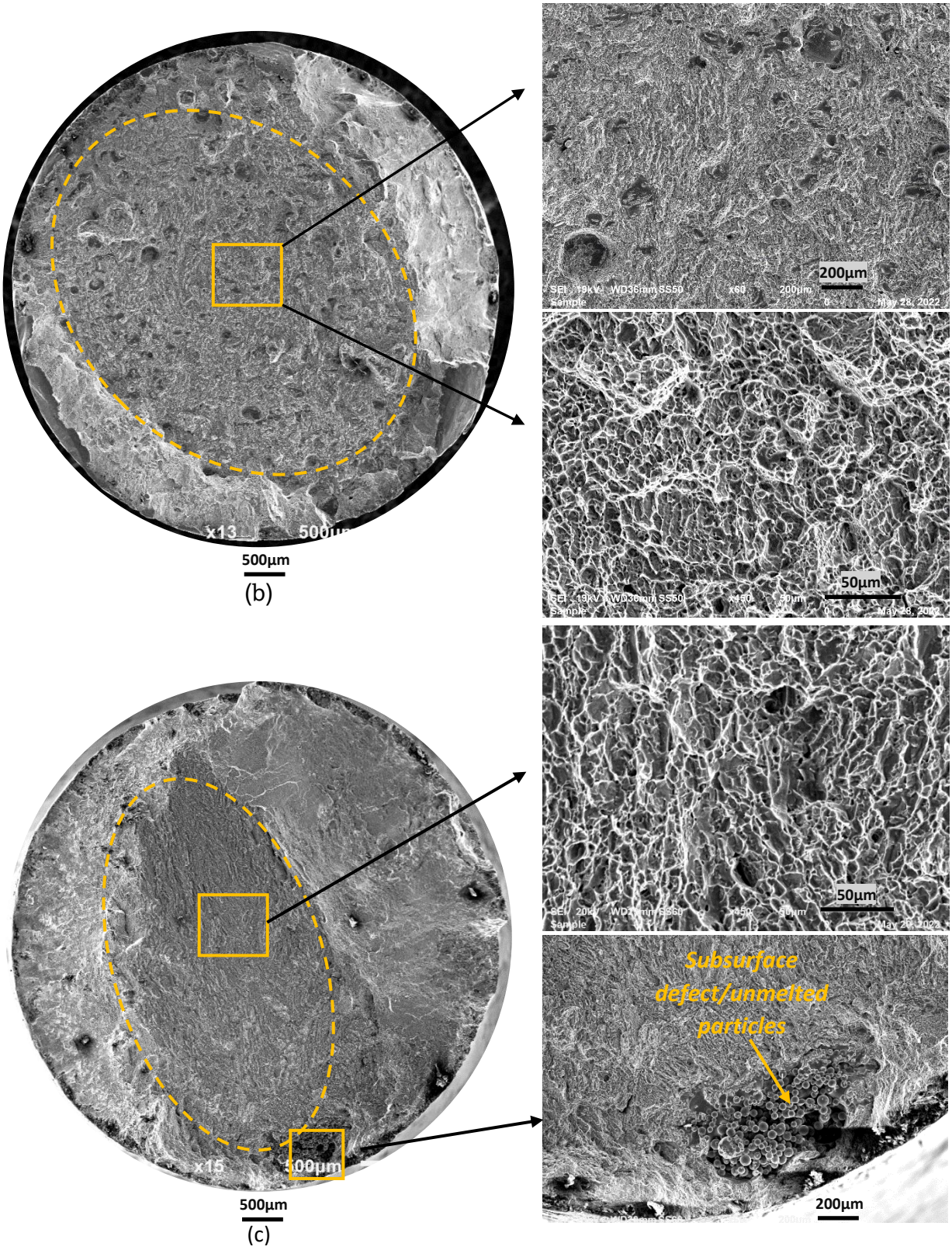

Figure 6.6: Fracture surfaces of tensile specimens: (a) annealed/not polished, (b) annealed/polished, and (c) HIPed/polished.

The elongation at fracture is generally more sensitive to porosity than strength. The detrimental nature of pores is typically explained through (i) a reduction in the true load-bearing area, (ii) the facilitation of pore coalescence leading to premature failure, (iii) increased stress concentration points, (iv) acting as initiation sites for microcracking, and (iv) providing a preferential path for crack propagation. These issues are frequently reported to be worse for vertically built samples due to the orientation of LOF pores and/or interlayer pores. It is known that as the porosity/defect population decreases, tensile behaviour generally improves. However, the type, rather than amount, of pores may matter more, as LOF pores are frequently reported to be far more detrimental to tensile properties. Because of how the primary axis of LOF pores is positioned relative to the tensile axis, as shown in Figure 6.8, LOF pores are particularly harmful to vertically built samples. As observed in Figure 6.8, the actual load-bearing cross-sectional area is much smaller, and the pore is also stretched apart perpendicularly to its major axis in tension which can lead to crack initiation. The cracks quickly coalesce and fracture prematurely with minimal necking. This inability to neck might also be why LOF defects affected elongation more than strength.

HIP is often proposed to close the pores after LPBF manufacturing [92]. The main issue with HIP is that pore closure is only effective when a high temperature is used and has been shown to coarsen the microstructure. To facilitate deformation, a temperature of 950°C was det during HIP treatment, which is higher than the phase transition temperature (882°C) of Ti6Al4V. From literature, it has been reported that standard HIP treatment results in coarsening of grain boundary α and nucleation of coarse intra granular α laths, which results in a decrease in yield and ultimate strength tensile from a Hall-Petch effect [92]-[97]. Additionally, the dislocation densities and twin crystals, which are strengthening factors, were also reported to reduce significantly after HIP treatment [98]. While reducing strengthening factors, plastic deformation becomes much easier, thus leading to an increase in elongation at the expense of strength. Figure 6.7 clearly shows that the microstructure of the HIPed sample was coarser compared to the other samples, and consequently resulted in reduced strength. Although the YS and UTS were somewhat lowered after HIP, they remained above the minimal criteria. Therefore, the reduction in strength after HIP can be attributed to structure coarsening and the reduction of dislocation densities and twin crystals, consequently resulting in better elongation.

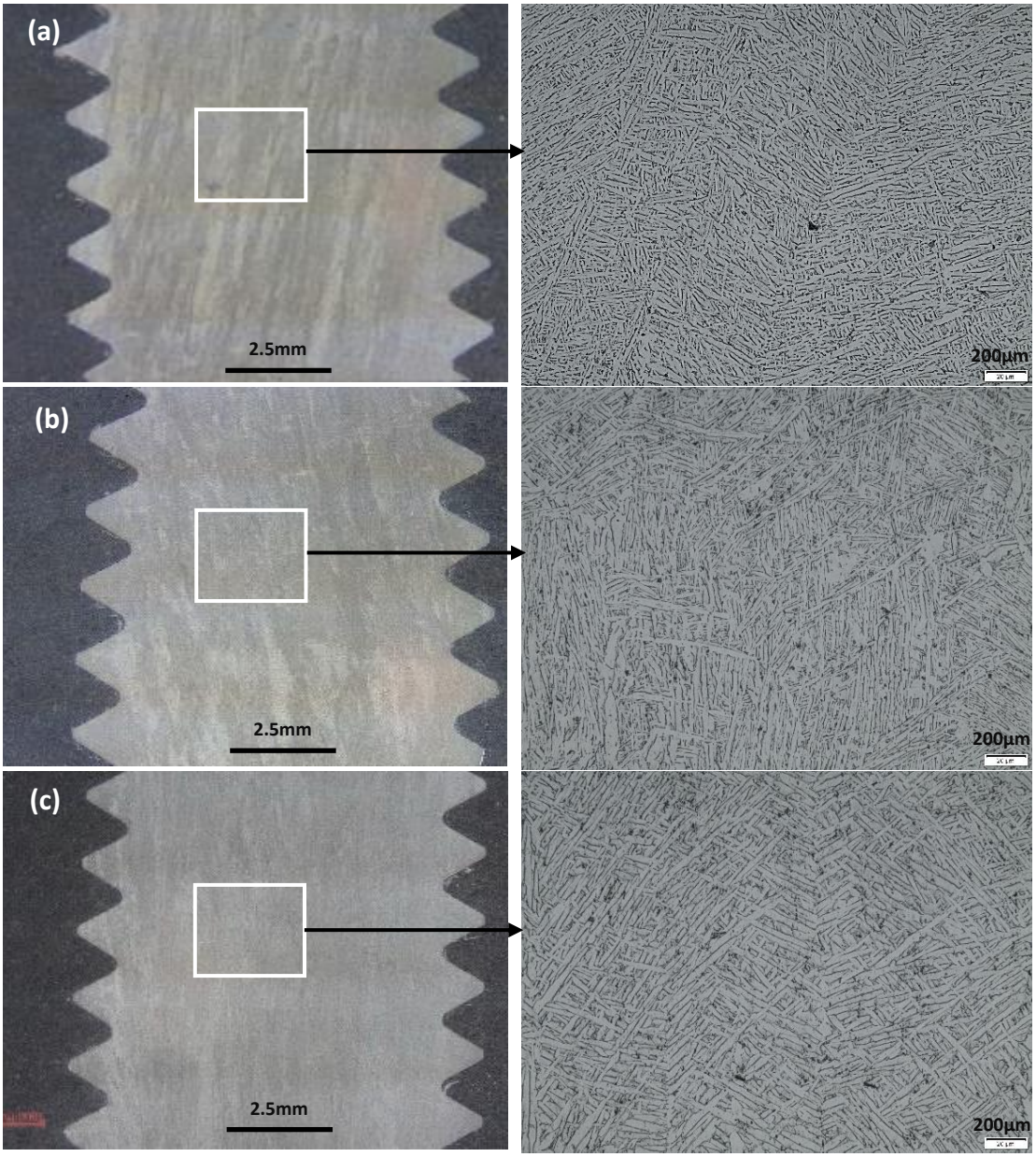

Figure 6.7: Optical micrographs and the microstructures of the broken test pieces in the gripping area: (a) annealed/not polished sample, (b) annealed/polished sample, and (c) HIPed/polished sample.

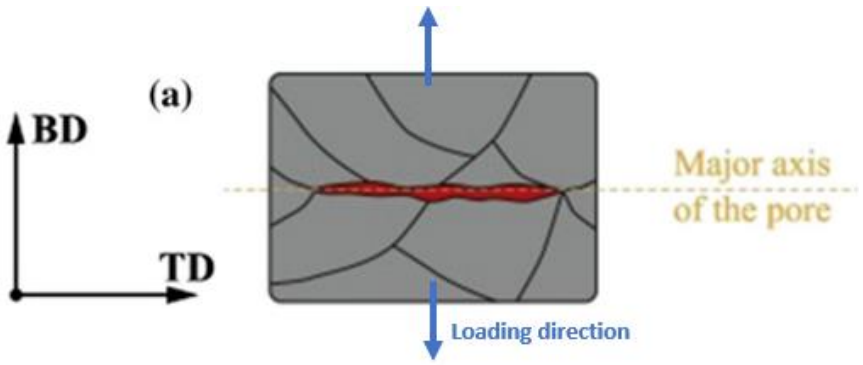

Figure 6.8: Schematic illustration of LOF defects' coalescence during tensile loading [237].

6.3.3 Fatigue performance

The tension-tension fatigue behaviour of the material has been investigated in the present study for samples with as-built and polished surfaces. Post-annealing heat treatment and HIP were also applied in the order shown in Table 6.2. Table 6.4 shows the fatigue stresses and the corresponding number of load cycles to failure of all the specimens. The data is shown graphically on a semi-log S-N curve of maximum stress against the number of life cycles in Figure 6.9.

Table 6.4: Tension-tension fatigue results obtained in this study

Batch number	Maximum stress σ_{max} (MPa)	Stress range $\Delta\sigma$ (MPa)	Stress amplitude σ_a (MPa)	Fatigue life Nf (cycles)
1	660	594	297	2149
	495	445.5	222.8	4781
	330	297	148.5	5927
	281	252.9	126.5	34478
	239	215.1	107.6	45394
	206	185.4	92.7	85610
2	660	594	297	3080
	495	445.5	222.8	5420
	330	297	148.5	17888
	281	252.9	126.5	41674
	239	215.1	107.6	65073
	206	185.4	92.7	140248
3	660	594	297	6252
	495	445.5	222.8	14245
	330	297	148.5	78167
	281	252.9	126.5	266195
	239	215.1	107.6	241962
	206	185.4	92.7	run-out

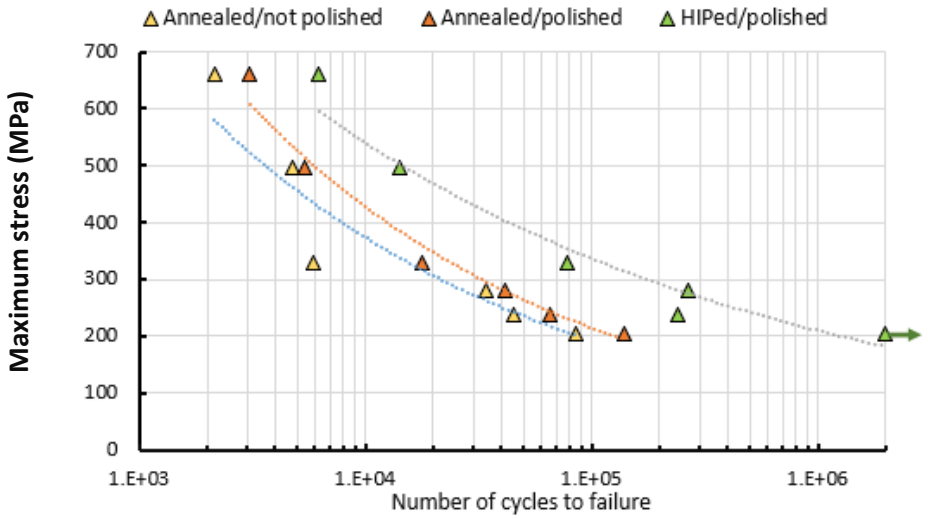

Figure 6.9: S-N curve showing fatigue performance of the specimens.

The fatigue properties of LPBF parts depend on the manufacturing process and post-processing procedures, and the fatigue life can be reduced due to, for example, the rough as-built surface, geometrical notches, or material defects inside the material. All these features lead to an increased local stress concentration which promotes fatigue crack initiation. Moreover, the fatigue properties of AM materials with rough as-built surfaces can be dominated by surface roughness rather than by internal defects.

Fatigue specimens with rough as-built surfaces generally have lower fatigue life. However, in the current investigation, it was found that the difference between the fatigue life of specimens with as-built surfaces (Batch 1) and specimens with polished surfaces (Batch 2) was insignificant. This could be explained by the presence of multiple LOF defects in the samples, see Figure 6.10. Even though the cracks start from the rough surface, LOF defects reduce the true load-bearing area of the fatigue specimen and thereby reduce the apparent fatigue strength.

HIP improves fatigue life of LPBF parts by eliminating internal pores and voids. Figure 6.9 shows a noticeable tendency of improved fatigue life for specimens that underwent HIP and polishing (Batch 3). LOF defects were reduced by HIP treatment, but not completely removed, especially closer to the surface as shown in Figure 6.10. Therefore, the results obtained with Batch 3 samples can mainly be attributed to the reduction of internal defects after HIP, which increase the effective cross-sectional area for crack propagation thus leading to an improvement in fatigue strength.

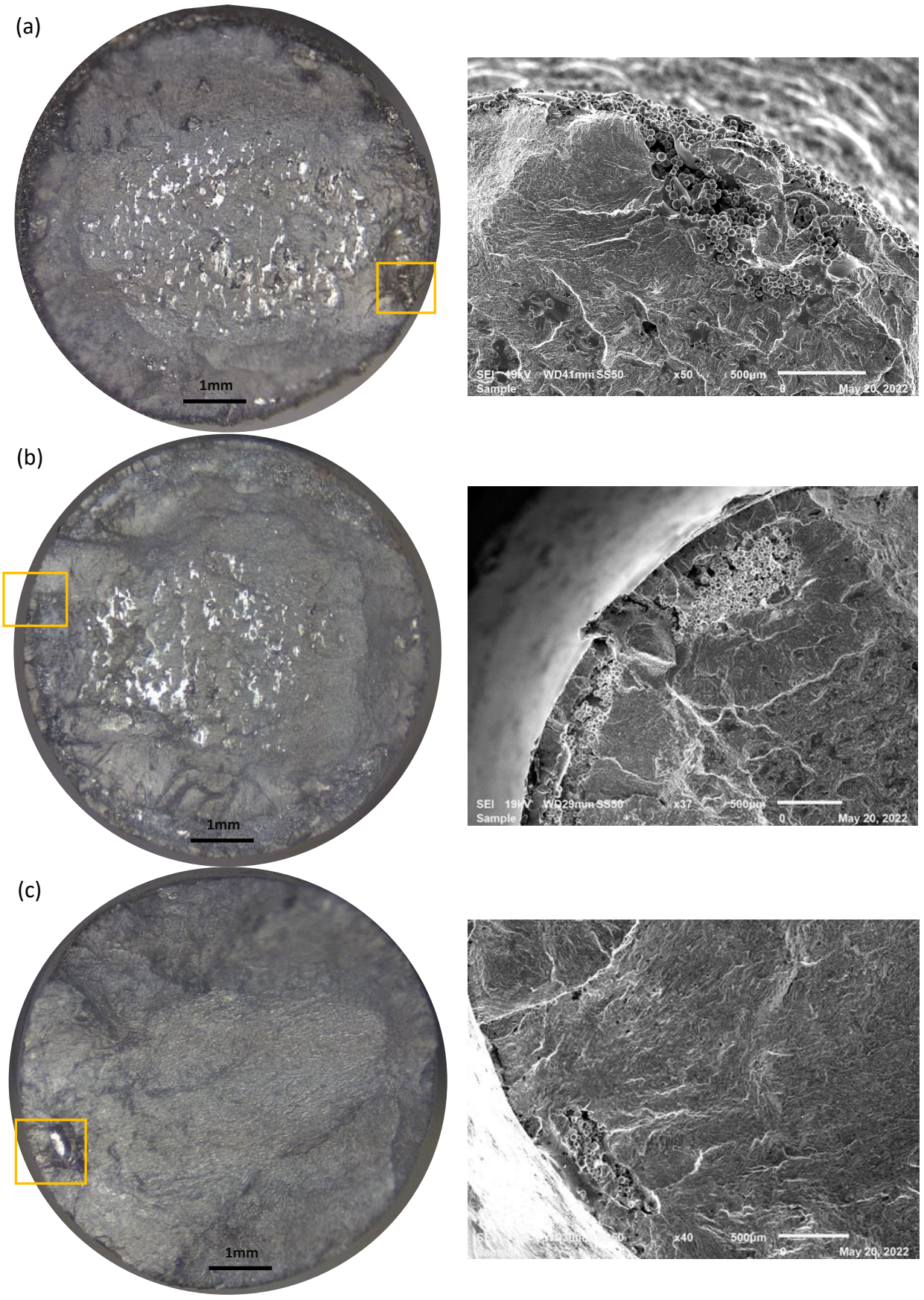

Figure 6.10: Examples of crack initiation sites observed near the surfaces of specimens from (a) Batch 1, (b) Batch 2, and (c) Batch 3 (see Appendix X and XI for other samples).

Three specimens, one from each batch, were selected for analysis using micro-CT to investigate the distribution of pores in the specimens. Figure 6.11 and Figure 6.12 shows the micro-CT images of the specimens and graphical representation of pore size distribution, respectively. It can be seen that most of the pores were located closer to the surface, and the specimens that were not HIPed had a high count of pores ranging from 0.1 mm to 0.6 mm.

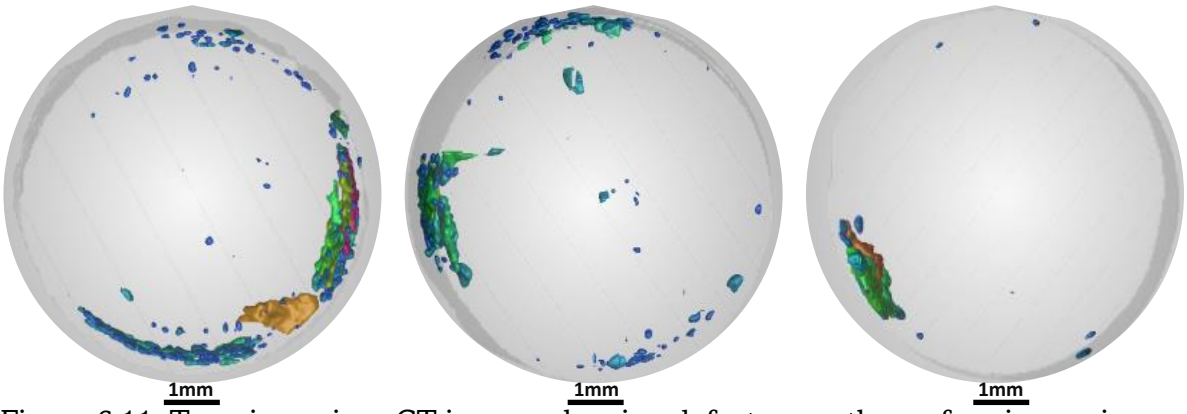

Figure 6.11: Top view micro-CT images showing defects near the surface in specimens from (a) Batch 1, (b) Batch 2, and (c) Batch 3.

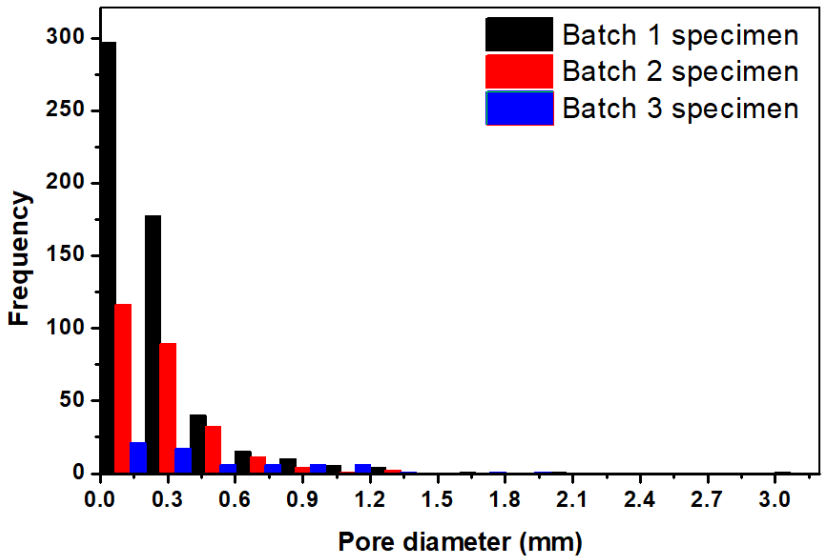

Figure 6.12: Pore size distribution in the specimens.

It is widely known that the fatigue life of materials is more sensitive to the surface condition. The shape and size of internal defects can be equally detrimental to the fatigue strength since they reduce the true load-bearing cross-sectional area and act as stress raisers. In the current study, LOF defects inside the material were found to be the dominating factor in the fatigue strength of specimens that were not HIPed, regardless of

the surface condition (Batch 1 compared to Batch 2). Even though HIP and surface polishing slightly improved the fatigue life of the specimens by reducing internal LOF and surface defects, the pores embedded closer to the surface were not completely removed. Consequently, the fatigue strength of HIPed specimens was severely affected by the presence of near-surface pores that could not be removed by barrel polishing. These pores were also aligned vertically on one side of the specimen, as shown in Figure 6.13. The origin of LOF pores in the contour is unclear but could be attributed to a lack of sufficient bead overlap between the starting and end point of the circular contour.

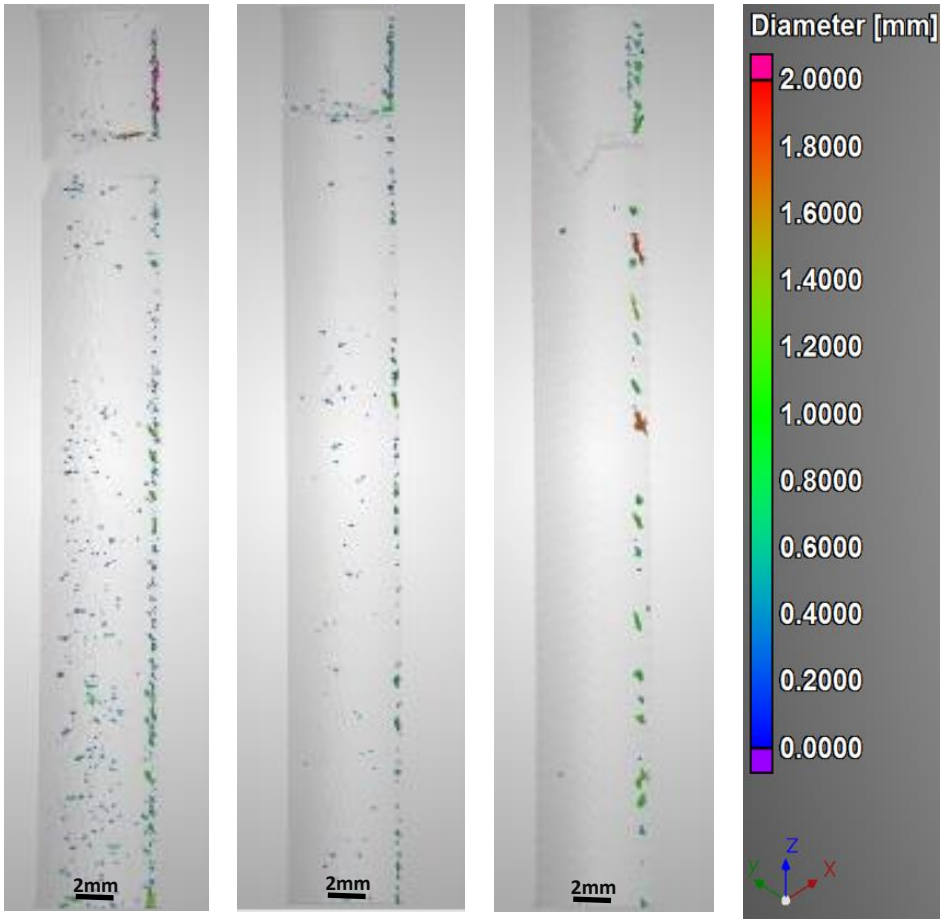

Figure 6.13: Side view micro-CT images of fractured specimens from (a) Batch 1, (b) Batch 2, and (c) Batch 3 (see Appendix XIII to XV).

6.4 Summary and conclusion

The focus of this chapter was to investigate the effect of CBS finishing and post-heat treatment on the surface roughness and mechanical properties of Ti-6Al-4V samples manufactured at high laser power and high build rate. The surface roughness of the samples in the as-built condition was high due to partially melted particles sticking to the surface, thus resulting in an average surface roughness of 22 µm Ra. CBF was used to

investigate the effect of polishing speed and time on the surface morphology and surface roughness. The lowest surface roughness obtained was 2.27 µm Ra when the polishing speed was set at 85 rpm for 5 hours, thus yielding a 90% reduction in the surface roughness. These parameters were then used to polish tensile and fatigue specimens manufactured to evaluate the mechanical properties. The tensile properties of the specimens with the as-built and polished surface were found to have low ductility mainly due to LOF defects that were present in the samples. After HIP, the ductility was slightly improved to obtain an average elongation of 6%. Even though HIP reduced the LOF defects in the samples, residual pores were still present inside and closer to the surface of the samples. It was also observed that the defects present in the samples were localized in specific areas, possibly due to machine instabilities, such as powder dosing and recoating errors. Dimples on the fracture surface were also observed, indicating that the failure mode occurred by ductile fracture. LOF defects were also observed on the fracture surfaces of the fatigue specimens, especially the ones that were not HIPed. As such, the fatigue properties of specimens without HIP were low regardless of the surface condition. Even though HIP and surface polishing slightly improved the fatigue life of the specimens by reducing internal LOF and surface defects, the pores embedded closer to the surface were not completely removed. Consequently, the fatigue strength of HIPed specimens was also affected by the presence of near-surface pores that could not be removed by barrel polishing. Analysis with micro-CT revealed an array of pores aligned vertically on one side of the specimens. The origin of these pores in the contour is unclear at this stage but could be attributed to a lack of sufficient bead overlap between the starting and end point of the circular contour. Overall, this investigation has revealed that surface finishing by CBF can substantially reduce the surface roughness of parts manufactured at high power and high build rate. However, the presence of stochastic LOF defects and near-surface defects in the samples were critical to the achievable mechanical properties. Stochastic defects, as opposed to process-induced defects, usually form due to secondary factors unrelated to the process parameters. As such, it can be concluded that the formation of defects observed in the current study was not induced by the process parameters but possibly formed due to machine-related errors.

Chapter 7
Conclusions and future outlook

The use of high-powered lasers in LPBF presents an opportunity to improve productivity without significantly increasing equipment costs. This is because instead of using a multi-beam system, a single laser equipped with a larger beam spot size can be used to increase the melt pool size, thus allowing the melt of a large area of powder to reduce the scanning time, which in turn will increase the build rate and productivity. However, random porosity, poor surface quality, high residual stresses, and inconsistent mechanical properties are some of the challenges in LPBF, and this can be made worse by the increased intensity at the processing zone when the laser power is increased without increasing the beam spot size. The purpose of this study was to investigate high-power laser powder bed fusion of Ti-6Al-4V alloy as a way of improving LPBF productivity. Based on the results obtained, the following key conclusions can be drawn in accordance with the study objectives:

Objective 1 – To identify the process parameter window for low porosity and high build rate

1. Single tracks processed at different parameter combinations revealed four characteristic morphologies, namely continuous tracks with keyhole mode, continuous tracks with conduction mode, humping effect, and balling effect.
2. High laser power and longer interaction time favoured keyhole mode, while shorter interaction times provoked humping and balling effects.
3. High power and shorter interaction times produced single layers with complex morphologies and high surface roughness.
4. Increasing the percentage overlap effectively reduced the surface roughness of the single layer processed at high laser powers and shorter interaction, i.e. 2000 W and 0.075 ms.
5. High laser power and shorter interaction accompanied by an increased overlap rate resulted in low porosity below 0.1%.

6. The maximum achievable build rates were 18 mm^3/s at 2000 W for the high-power system and 3.4 mm^3/s at 340 W for the low-power system.

Objective 2 – To characterize the top surface roughness, residual stress, and microstructure

1. The top surface roughness of the samples manufactured using the high-power system ranged between 14.4 to 32.0 µm and 6.5 to 25.1 µm for the low-power system.
2. The influence of process parameters on surface roughness depends on the combination of laser power and interaction time. At low power and low interaction time, the surface roughness increased due to balling effect, while at high power and high interaction time, the surface roughness increased due to the unstable molten pool formed at excessive heat input.
3. The maximum residual stresses measured on the top surface were tensile and varied between 445 to 720 MPa at high laser powers and 394 to 1138 MPa at low laser powers. Residual stresses were found to be higher along the scan direction.
4. High laser powers produced microstructures with large prior-beta grains.
5. The size of prior-beta grains increased when the interaction time, laser power, and overlap were increased.

Objective 3 – To investigate the effect of post-processing on the surface roughness and mechanical properties

1. The vertical surface roughness in the as-built condition was high, Ra ~ 22µm, and was dominated by partially sintered particles.
2. CBF at 85 rpm for 5 hours reduced the vertical roughness by 90%, with some small cavities remaining on the surface.
3. The tensile and fatigue properties obtained were affected by the presence of localized and interlayer defects believed to be related to powder delivery and contouring errors.
4. HIPing of the samples, followed by barrel finishing, improved the tensile properties to obtain the minimum requirements.

5. The fatigue strengths obtained were relatively low due to the presence of near-surface and interlayer defects. However, the results indicate that surface finishing and HIPing can improve fatigue strength.

Summary and recommendations

This study has demonstrated the feasibility of improving productivity by using high laser power and shorter interaction time to gain a high build rate. It was shown that almost fully dense test coupons could be manufactured at a high build rate of 18 mm^3/s, exhibiting low top surface roughness and residual stress below the YS, while the microstructure exhibited coarser prior-beta grains. The vertical surface roughness of the parts was found to be higher due to the presence of partially melted powder particles attached to the surface. Surface finishing by CBF was investigated to improve the surface quality, and it was shown that the surface roughness could be reduced by 90%, with some small cavities remaining on the surface. The application of HIPing helped to improve the tensile properties and fatigue strength. However, the presence of localized subsurface and interlayer defects drastically affected the fatigue strength. These defects are believed to be related to powder delivery and contouring errors. As such, the following recommendations are made:

1. Investigate factors that prompt layer delivery defects and the development of a quality control framework to prevent process conditions that lead to interlayer or stochastic defects.
2. Optimize contouring parameters/strategy to reduce surface defects.
3. Robust mechanical testing of defect-free specimens for verification.
4. Quantify the effect of a high build rate on part resolution and dimensional accuracy.

References

[1] T. Wohlers, I. Campbell, O. Diegel, R. Huff, J. Kowen, Wohlers Report 2020: 3D printing and additive manufacturing global state of the industry, Wohlers Associates (2020).

[2] J.-P. Kruth, G. Levy, F. Klocke, T. Childs, Consolidation phenomena in laser and powder-bed based layered manufacturing, CIRP annals 56 (2007) 730-759.

[3] M. Mani, B.M. Lane, M.A. Donmez, S.C. Feng, S.P. Moylan, A review on measurement science needs for real-time control of additive manufacturing metal powder bed fusion processes, Int J Prod Res 55 (2017) 1400-1418.

[4] V. Bhavar, P. Kattire, V. Patil, S. Khot, K. Gujar, R. Singh, A review on powder bed fusion technology of metal additive manufacturing, Additive Manufacturing Handbook (2017) 251-253.

[5] I. Yadroitsev, I. Yadroitsava, A. du Plessis, Basics of laser powder bed fusion, in: Fundamentals of laser powder bed fusion of metals, Elsevier, 2021, pp. 15-38.

[6] A. Simchi, F. Petzoldt, H. Pohl, Direct metal laser sintering: Material considerations and mechanisms of particle: Rand tooling of powdered metal parts, Int J Powder Metall 37 (2001) 49-61.

[7] J.-P. Kruth, L. Froyen, M. Rombouts, J. Van Vaerenbergh, P. Mercells, New ferro powder for selective laser sintering of dense parts, CIRP annals 52 (2003) 139-142.

[8] H.H. Zhu, L. Lu, J. Fuh, Influence of binder's liquid volume fraction on direct laser sintering of metallic powder, Mater Sci Eng A 371 (2004) 170-177.

[9] M. Agarwala, D. Bourell, J. Beaman, H. Marcus, J. Barlow, Post-processing of selective laser sintered metal parts, Rapid Protyp J (1995).

[10] S. Das, M. Wohlert, J.J. Beaman, D.L. Bourell, Processing of titanium net shapes by SLS/HIP, Mater Des 20 (1999) 115-121.

[11] S. Kumar, J. Kruth, Effect of bronze infiltration into laser sintered metallic parts, Mater Des 28 (2007) 400-407.

[12]D.D. Gu, D D, W. Meiners, K. Wissenbach, R. Poprawe. Laser additive manufacturing of metallic components: materials, processes and mechanisms. International Materials Reviews (2012) 57(3), 133–164.

[13] D. Bourell, J.P. Kruth, M. Leu, G. Levy, D. Rosen, A.M. Beese, A. Clare, Materials for additive manufacturing, CIRP annals 66 (2017) 659-681.

[14] P. Rangaswamy, T.M. Holden, R.B. Rogge, M.L. Griffith, Residual stresses in components formed by the laser engineered net shaping (LENS®) process, J Strain Anal Eng Des 38 (2003) 519-527.

[15] B. Dutta, S. Palaniswamy, J. Choi, L.J. Song, J. Mazumder, Direct metal deposition, Adv Mater Processes (2011) 33.

[16] D. Gu, Laser additive manufacturing of high-performance materials, Springer, 2015.

[17] M. Das, V.K. Balla, T.S. Kumar, I. Manna, Fabrication of biomedical implants using laser engineered net shaping (LENS™), Trans Indian Ceram Soc 72 (2013) 169-174.

[18] V. Matilainen, H. Piili, A. Salminen, O. Nyrhilä, Preliminary investigation of keyhole phenomena during single layer fabrication in laser additive manufacturing of stainless steel, Phys Procedia 78 (2015) 377-387.

[19] N. Contuzzi, S.L. Campanelli, A.D. Ludovico, 3D finite element analysis in the selective laser melting process, Int J Simul Model 10 (2011) 113-121.

[20] N. Guo, M.C. Leu, Additive manufacturing: technology, applications and research needs, Front Mech Eng 8 (2013) 215-243.

[21] H. Fayazfar, M. Salarian, A. Rogalsky, D. Sarker, P. Russo, V. Paserin, E. Toyserkani, A critical review of powder-based additive manufacturing of ferrous alloys: Process parameters, microstructure and mechanical properties, Mater Des 144 (2018) 98-128.

[22] N.B. Dahotre, S. Harimkar, Laser fabrication and machining of materials, Springer Science & Business Media, 2008.

[23] L. Facchini, Microstructure and mechanical properties of biomedical alloys produced by rapid manufacturing techniques, Doctoral dissertation, University of Trento (2010).

[24] J. Ciurana, L. Hernandez, J. Delgado, Energy density analysis on single tracks formed by selective laser melting with CoCrMo powder material, J Adv Manuf Technol 68 (2013) 1103-1110.

[25] I. Yadroitsev, P. Krakhmalev, I. Yadroitsava, Hierarchical design principles of selective laser melting for high quality metallic objects, Addit Manuf 7 (2015) 45-56.

[26] S. Das, Physical aspects of process control in selective laser sintering of metals, Adv Eng Mater 5 (2003) 701-711.

[27] P.G.E. Jerrard, Selective laser melting of advanced metal alloys for aerospace applications, Doctoral dissertation, University of Exeter (2011).

[28] I. Yadroitsau, Direct manufacturing of 3D objects by selective laser melting of metal powders, Doctoral dissertation, Saint-Etienne (2008).

[29] I.G. Gibson, Additive manufacturing technologies 3D printing, rapid prototyping, and direct digital manufacturing, Johnson Matthey Technol Rev 59 (2015) 193-198.

[30] S.A. Khairallah, A.T. Anderson, A. Rubenchik, W.E. King, Laser powder-bed fusion additive manufacturing: Physics of complex melt flow and formation mechanisms of pores, spatter, and denudation zones, Acta Mater 108 (2016) 36-45.

[31] T.J. Lienert, S.S. Babu, V.L. Acoff, N.Y. Zhou, E. DeGuire, S. Lampman, E. Marquard, B. Musgrove, B. Riley, ASM Handbook 6 (2011), ASM International, Materials Park, OH, 2011.

[32] I. Yadroitsev, I. Yadroitsava, P. Bertrand, I. Smurov, Factor analysis of selective laser melting process parameters and geometrical characteristics of synthesized single tracks, Rapid Prototyp J (2012).

[33] I. Yadroitsev, A. Gusarov, I. Yadroitsava, I. Smurov, Single track formation in selective laser melting of metal powders, J Mater Process Technol 210 (2010) 1624-1631.

[34] R. Li, J. Liu, Y. Shi, L. Wang, W. Jiang, Balling behavior of stainless steel and nickel powder during selective laser melting process, J Adv Manuf Technol 59 (2012) 1025-1035.

[35] X. Shi, S. Ma, C. Liu, C. Chen, Q. Wu, X. Chen, J. Lu, Performance of high layer thickness in selective laser melting of Ti-6Al-4V, J Mater 9 (2016) 975.

[36] R.J. Hebert, Metallurgical aspects of powder bed metal additive manufacturing, J Mater Sci 51 (2016) 1165-1175.

[37] J. Kruth, M. Badrossamay, E. Yasa, J. Deckers, L. Thijs, J. Van Humbeeck, Part and material properties in selective laser melting of metals, In proc. ISEM XVI (2010) 3-14.

[38] R. Morgan, C.J. Sutcliffe, W. O'Neill, Density analysis of direct metal laser re-melted 316L stainless steel cubic primitives, J Mater Sci 39 (2004) 1195-1205.

[39] D. Gu, Y. Hagedorn, W. Meiners, G. Meng, R.J.S. Batista, K. Wissenbach, R. Poprawe, Densification behavior, microstructure evolution, and wear performance of selective laser melting processed commercially pure titanium, Acta Mater 60 (2012) 3849-3860.

[40] J.A. Slotwinski, E.J. Garboczi, Porosity of additive manufacturing parts for process monitoring, In proc AIP 1581 (2014) 1197-1204.

[41] S.M. Yusuf, Y. Chen, R. Boardman, S. Yang, N. Gao, Investigation on porosity and microhardness of 316L stainless steel fabricated by selective laser melting, Metals 7 (2017) 64.

[42] I. Yadroitsev, I. Yadroitsava, A. du Plessis, E. MacDonald, Fundamentals of laser powder bed fusion of metals, Elsevier (2021).

[43] A.M. Mancisidor, F. Garciandia, M. San Sebastian, P. Álvarez, J. Díaz, I. Unanue, Reduction of the residual porosity in parts manufactured by selective laser melting using skywriting and high focus offset strategies, Phys Procedia 83 (2016) 864-873.

[44] S. Leuders, M. Thöne, A. Riemer, T. Niendorf, T. Tröster, H.A. Richard, H.J. Maier, On the mechanical behaviour of titanium alloy TiAl6V4 manufactured by selective laser melting: Fatigue resistance and crack growth performance, Int J Fatigue 48 (2013) 300-307.

[45] I. Rosenthal, E. Tiferet, M. Ganor, A. Stern, Post-processing of AM-SLM AlSi10Mg specimens: Mechanical properties and fracture behaviour, Annals of "Dunerea de Jos" University of Galati, Fascicle XII welding Equipment and Technology 26 (2015) 33-38.

[46] W. Tillmann, C. Schaak, J. Nellesen, M. Schaper, M.U. Aydinöz, K. Hoyer, Hot isostatic pressing of IN718 components manufactured by selective laser melting, Addit Manuf 13 (2017) 93-102.

[47] B. AlMangour, D. Grzesiak, J. Yang, Selective laser melting of TiB2/316L stainless steel composites: The roles of powder preparation and hot isostatic pressing post-treatment, Powder Technol 309 (2017) 37-48.

[48] A. Sola, A. Nouri, Microstructural porosity in additive manufacturing: The formation and detection of pores in metal parts fabricated by powder bed fusion, Adv Manuf Process 1 (2019) e10021.

[49] T. DebRoy, H.L. Wei, J.S. Zuback, T. Mukherjee, J.W. Elmer, J.O. Milewski, A.M. Beese, A.D. Wilson-Heid, A. De, W. Zhang, Additive manufacturing of metallic components–process, structure and properties, Prog Mater Sci 92 (2018) 112-224.

[50] D. Wang, S. Wu, F. Fu, S. Mai, Y. Yang, Y. Liu, C. Song, Mechanisms and characteristics of spatter generation in SLM processing and its effect on the properties, Mater Des 117 (2017) 121-130.

[51] A.B. Anwar, Q. Pham, Study of the spatter distribution on the powder bed during selective laser melting, Addit Manuf 22 (2018) 86-97.

[52] V. Gunenthiram, P. Peyre, M. Schneider, M. Dal, F. Coste, I. Koutiri, R. Fabbro, Experimental analysis of spatter generation and melt-pool behavior during the powder bed laser beam melting process, J Mater Process Technol 251 (2018) 376-386.

[53] C. de Andrade Schwerz, Detection and classification of internal flaws in laser powder bed fusion: application of in-situ monitority for quality control of Hastelloy X Builds, Doctoral dissertation, Chalmers Teknisa Hogskola Sweden (2021).

[54] I. Yadroitsev, P. Krakhmalev, I. Yadroitsava, A. du Plessis, Qualification of Ti-6Al-4V ELI alloy produced by laser powder bed fusion for biomedical applications, JOM 70 (2018) 372-377.

[55] Y. Harada, Y. Ishida, D. Miura, S. Watanabe, H. Aoki, T. Miyasaka, A. Shinya, Mechanical properties of selective laser sintering pure titanium and Ti-6Al-4V, and its anisotropy, Mater 13 (2020) 5081.

[56] M. Kahlin, H. Ansell, D. Basu, A. Kerwin, L. Newton, B. Smith, J.J. Moverare, Improved fatigue strength of additively manufactured Ti-6Al-4V by surface post processing, Int J Fatigue 134 (2020) 105497.

[57] J. Pegues, M. Roach, R.S. Williamson, N. Shamsaei, Surface roughness effects on the fatigue strength of additively manufactured Ti-6Al-4V, Int J Fatigue 116 (2018) 543-552.

[58] J. Zhang, A. Chaudhari, H. Wang, Surface quality and material removal in magnetic abrasive finishing of selective laser melted 316L stainless steel, JMP45 (2019) 710-719.

[59] Y. Sun, R. Bailey, A. Moroz, Surface finish and properties enhancement of selective laser melted 316L stainless steel by surface mechanical attrition treatment, Surf Coat Technol 378 (2019) 124993.

[60] M. Shiomi, K. Osakada, K. Nakamura, T. Yamashita, F. Abe, Residual stress within metallic model made by selective laser melting process, CIRP annals 53 (2004) 195-198.

[61] L. Mugwagwa, I. Yadroitsava, N.W. Makoana, I. Yadroitsev, Residual stress in laser powder bed fusion, in: Anonymous, Fundamentals of laser powder bed fusion of metals, Elsevier,2021, pp. 245-276.

[62] M.F. Sadali, M.Z. Hassan, F. Ahmad, H. Yahaya, Z.A. Rasid, Influence of selective laser melting scanning speed parameter on the surface morphology, surface roughness, and micropores for manufactured Ti-6Al-4V parts, J Mater Res 35 (2020) 2025-2035.

[63] D. Wang, Y. Liu, Y. Yang, D. Xiao, Theoretical and experimental study on surface roughness of 316L stainless steel metal parts obtained through selective laser melting, Rapid Prototyp J (2016).

[64] P. Mercelis, J. Kruth, Residual stresses in selective laser sintering and selective laser melting, Rapid Prototyp J (2006).

[65] A. Basak, S. Das, Epitaxy and microstructure evolution in metal additive manufacturing, Annu Rev Mater Res 46 (2016) 125-149.

[66] W.J. Sames, F.A. List, S. Pannala, R.R. Dehoff, S.S. Babu, The metallurgy and processing science of metal additive manufacturing, Int Mater Rev 61 (2016) 315-360.

[67] L. Thijs, F. Verhaeghe, T. Craeghs, J. Van Humbeeck, J. Kruth, A study of the microstructural evolution during selective laser melting of Ti-6Al-4V, Acta Materia 58 (2010) 3303-3312.

[68] M.G. Moletsane, I. Yadroitsava, I. Yadroitsev, P. Krakhmalev, N. Kazantseva, A. du Plessis, Tensile properties and microstructure of direct metal laser-sintered Ti-6Al-4V (ELI) alloy, SAJIE 27 (2016) 110-121.

[69] T.H. Becker, C. Scheffer, M. Beck, Microstructure and mechanical properties of direct metal laser sintered Ti-6Al-4V d article, SAJIE 26 (2015) 1-10.

[70] S. Sarkar, C.S. Kumar, A.K. Nath, Effect of different heat treatments on mechanical properties of laser sintered additive manufactured parts, J Manuf Sci Eng139 (2017).

[71] S. Gorsse, C. Hutchinson, M. Gouné, R. Banerjee. Additive manufacturing of metals: a brief review of the characteristic microstructures and properties of steels, Ti-6Al-4V and high-entropy alloys. Science and Technology of Advanced Materials (2017) 18(1):584-610.

[72] A. Gratton, Comparison of mechanical, metallurgical properties of 17-4PH stainless steel between direct metal laser sintering (DMLS) and traditional manufacturing methods, NCUR (2012).

[73] J. Delgado, J. Ciurana, C.A. Rodríguez, Influence of process parameters on part quality and mechanical properties for DMLS and SLM with iron-based materials, J Adv Manuf Technol 60 (2012) 601-610.

[74] P. Hanzl, M. Zetek, T. Bakša, T. Kroupa, The influence of processing parameters on the mechanical properties of SLM parts, Procedia Eng 100 (2015) 1405-1413.

[75] G. Kasperovich, J. Hausmann, Improvement of fatigue resistance and ductility of TiAl6V4 processed by selective laser melting, J Mater Process Technol 220 (2015) 202-214.

[76] W. Xu, M. Brandt, S. Sun, J. Elambasseril, Q. Liu, K. Latham, K. Xia, M. Qian, Additive manufacturing of strong and ductile Ti-6Al-4V by selective laser melting via in situ martensite decomposition, Acta Materia 85 (2015) 74-84.

[77] E. Brandl, C. Leyens, F. Palm, Mechanical properties of additive manufactured Ti-6Al-4V using wire and powder-based processes, In IOP conference series: Mater Sci and Eng 26 (2011) 012004.

[78] P. Edwards, M. Ramulu, Fatigue performance evaluation of selective laser melted Ti-6Al-4V, Mater Sci Eng A 598 (2014) 327-337.

[79] H. Gong, K. Rafi, T. Starr, B. Stucker, Effect of defects on fatigue tests of as-build Ti-6Al-4V parts fabricated by selective laser melting, Int SFF symposium University of Texas (2012).

[80] B. Van Hooreweder, D. Moens, R. Boonen, J. Kruth, P. Sas, Analysis of fracture toughness and crack propagation of Ti-6Al-4V produced by selective laser melting, Adv Eng Mater 14 (2012) 92-97.

[81] M. Seifi, M. Dahar, R. Aman, O. Harrysson, J. Beuth, J.J. Lewandowski, Evaluation of orientation dependence of fracture toughness and fatigue crack propagation behavior of as-deposited ARCAM EBM Ti-6Al-4V, JOM 67 (2015) 597-607.

[82] V. Cain, L. Thijs, J. Van Humbeeck, B. Van Hooreweder, R. Knutsen, Crack propagation and fracture toughness of Ti-6Al-4V alloy produced by selective laser melting, Addit Manuf 5 (2015) 68-76.

[83] F.R. Kaschel, R.K. Vijayaraghavan, A. Shmeliov, E.K. McCarthy, M. Canavan, P.J. McNally, D.P. Dowling, V. Nicolosi, M. Celikin, Mechanism of stress relaxation and phase

transformation in additively manufactured Ti-6Al-4V via in situ high temperature XRD and TEM analyses, Acta Materia 188 (2020) 720-732.

[84] E. Uhlmann, R. Kersting, T.B. Klein, M.F. Cruz, A.V. Borille, Additive manufacturing of titanium alloy for aircraft components, Procedia CIRP 35 (2015) 55-60.

[85] T. Mishurova, S. Cabeza, K. Artzt, J. Haubrich, M. Klaus, C. Genzel, G. Requena, G. Bruno, An assessment of subsurface residual stress analysis in SLM Ti-6Al-4V, Mater 10 (2017) 348.

[86] I. Yadroitsava, S. Grewar, D. Hattingh, I. Yadroitsev, Residual stress in SLM Ti-6Al-4V alloy specimens, In Mater Sci Forum 828 (2015) 305-310.

[87] P.O. Omoniyi, E.T. Akinlabi, R.M. Mahamood, Heat treatments of Ti-6Al-4V alloys for industrial applications: An overview, In IOP Conference Series: Mater Sci and Eng 1107 (2021) 012094.

[88] B. Vrancken, L. Thijs, J. Kruth, J. Van Humbeeck, Heat treatment of Ti-6Al-4V produced by selective laser melting: Microstructure and mechanical properties, J Alloys Compounds 541 (2012) 177-185.

[89] X. Zhang, G. Fang, S. Leeflang, A.J. Böttger, A.A. Zadpoor, J. Zhou, Effect of subtransus heat treatment on the microstructure and mechanical properties of additively manufactured Ti-6Al-4V alloy, J. Alloys Compounds 735 (2018) 1562-1575.

[90] C. Li, J.W. Won, S. Choi, J. Choe, S. Lee, C.H. Park, J. Yeom, J.K. Hong, Simultaneous achievement of equiaxed grain structure and weak texture in pure titanium via selective laser melting and subsequent heat treatment, J Alloys Compounds 803 (2019) 407-412.

[91] P. Lekoadi, M. Tlotleng, K. Annan, N. Maledi, B. Masina, Evaluation of heat treatment parameters on microstructure and hardness properties of high-speed selective laser melted Ti-6Al-4V, Metals 11 (2021) 255.

[92] E. Liverani, A.H. Lutey, A. Ascari, A. Fortunato, The effects of hot isostatic pressing (HIP) and solubilization heat treatment on the density, mechanical properties, and microstructure of austenitic stainless-steel parts produced by selective laser melting (SLM), Int Adv Manuf Technol 107 (2020) 109-122.

[93] H.V. Atkinson, S. Davies, Fundamental aspects of hot isostatic pressing: an overview, Metall Mater Trans A 31 (2000) 2981-3000.

[94] M. Wu, P. Lai, The positive effect of hot isostatic pressing on improving the anisotropies of bending and impact properties in selective laser melted Ti-6Al-4V alloy, Mater Sci Eng A 658 (2016) 429-438.

[95] N. Eshawish, S. Malinov, W. Sha, P. Walls, Microstructure and mechanical properties of Ti-6Al-4V manufactured by selective laser melting after stress relieving, hot isostatic pressing treatment, and post-heat treatment, J Mater Eng Perform 30 (2021) 5290-5296.

[96] S. Cao, Y. Zou, C.V.S. Lim, X. Wu. Review of laser powder bed fusion (LPBF) fabricated Ti-6Al-4V: process, post-process treatment, microstructure, and property, Light:Adv Manuf 2 (2021) 313-332.

[97]A. Du Plessis, E. Macdonald. Hot isostatic pressing in metal additive manufacturing: X-ray tomography reveals details of pore closure, Additive Manufacturing 34 (2020), 101191.

[98] L. Liu, H. Zheng, C. Deng. Influence of HIP Treatment on Mechanical Properties of Ti6Al4V Scaffolds Prepared by L-PBF Process Metals, 9 (2019) 1267.

[99] N. Mohammadian, S. Turenne, V. Brailovski, Surface finish control of additively manufactured Inconel 625 components using combined chemical-abrasive flow polishing, J Mater Process Technol 252 (2018) 728-738.

[100] Q. Zhang, B. Duan, Z. Zhang, J. Wang, C. Si, Effect of ultrasonic shot peening on microstructure evolution and corrosion resistance of selective laser melted Ti-6Al-4V alloy, J Mater Sci Technol 11 (2021) 1090-1099.

[101] H. Zhang, R. Chiang, H. Qin, Z. Ren, X. Hou, D. Lin, G.L. Doll, V.K. Vasudevan, Y. Dong, C. Ye, The effects of ultrasonic nanocrystal surface modification on the fatigue performance of 3D-printed Ti64, Int. J. Fatigue 103 (2017) 136-146.

[102] E. Uhlmann, C. Fleck, G. Gerlitzky, F. Faltin, Dynamical fatigue behavior of additive manufactured products for a fundamental life cycle approach, Procedia CIRP 61 (2017) 588-593.

[103] B. Fotovvati, N. Namdari, A. Dehghanghadikolaei, Fatigue performance of selective laser melted Ti-6Al-4V components: state of the art, MRX 6 (2018) 012002.

[104] P. Lott, H. Schleifenbaum, W. Meiners, K. Wissenbach, C. Hinke, J. Bültmann, Design of an optical system for the in-situ process monitoring of selective laser melting (SLM), Phys Procedia 12 (2011) 683-690.

[105] M. Doubenskaia, M. Pavlov, S. Grigoriev, E. Tikhonova, I. Smurov, Comprehensive optical monitoring of selective laser melting, J Laser Micro Nannoeng 7 (2012) 236.

[106] F. Bayle, M. Doubenskaia, Selective laser melting process monitoring with high-speed infra-red camera and pyrometer, In Fundamentals of laser micro and nanotechnologies 6985 (2008) 698505.

[107] S. Berumen, F. Bechmann, S. Lindner, J.-P. Kruth, T. Craeghs, Quality control of laser- and powder bed-based Additive Manufacturing (AM) technologies, Physics Procedia, 5(Part B) (2010) 617- 22

[108] T. Purtonen, A. Kalliosaari, A. Salminen, Monitoring and adaptive control of laser processes, Phys Procedia 56 (2014) 1218-1231.

[109] S.K. Everton, M. Hirsch, P. Stravroulakis, R.K. Leach, A.T. Clare, Review of in-situ process monitoring and in-situ metrology for metal additive manufacturing, Mater Des 95 (2016) 431-445.

[110] S. Clijsters, T. Craeghs, S. Buls, K. Kempen, J. Kruth, In-situ quality control of the selective laser melting process using a high-speed, real-time melt pool monitoring system, Int Adv Manuf Technol 75 (2014) 1089-1101.

[111] T. Furumoto, M.R. Alkahari, T. Ueda, M.S.A. Aziz, A. Hosokawa, Monitoring of laser consolidation process of metal powder with high-speed video camera, Physics Procedia 39 (2012) 760-766.

[112] M. Pavlov, M. Doubenskaia, I. Smurov, Pyrometric analysis of thermal processes in SLM technology, Phys Procedia 5 (2010) 523-531.

[113] H. Krauss, T. Zeugner, M.F. Zaeh, Layerwise monitoring of the selective laser melting process by thermography, Phys Procedia 56 (2014) 64-71.

[114] T. Craeghs, S. Clijsters, E. Yasa, J. Kruth, Online quality control of selective laser melting, In Int SFF sysmposium University of Texas (2011).

[115] C.S. Lough, X. Wang, C.C. Smith, R.G. Landers, D.A. Bristow, J.A. Drallmeier, B. Brown, E.C. Kinzel, Correlation of SWIR imaging with LPBF 304L stainless steel part properties, Addit Manuf 35 (2020) 101359.

[116] C. Bruna-Rosso, A.G. Demir, B. Previtali, Selective laser melting finite element modeling: Validation with high-speed imaging and lack of fusion defects prediction, Mater Des 156 (2018) 143-153.

[117] E. Westphal, H. Seitz, A machine learning method for defect detection and visualization in selective laser sintering based on convolutional neural networks, Addit Manuf 41 (2021) 101965.

[118] B. Wu, X. Ji, J. Zhou, H. Yang, D. Peng, Z. Wang, Y. Wu, Y. Yin, In-situ monitoring methods for selective laser melting additive manufacturing process based on images—A review, China Foundry 18 (2021) 265-285.

[119] S.A. Shevchik, C. Kenel, C. Leinenbach, K. Wasmer, Acoustic emission for in situ quality monitoring in additive manufacturing using spectral convolutional neural networks, Addit Manuf 21 (2018) 598-604.

[120] H. Taheri, L.W. Koester, T.A. Bigelow, E.J. Faierson, L.J. Bond, In-situ additive manufacturing process monitoring with an acoustic technique: clustering performance evaluation using K-means algorithm, J Manuf Sci Eng 141 (4) (2019) 041011.

[121] L. Koester, H. Taheri, L.J. Bond, D. Barnard, J. Gray, Additive manufacturing metrology: State of the art and needs assessment, In AIP conference proc 1706 (2016) 130001.

[122] A.A. Hassen, M.M. Kirka, Additive Manufacturing: The rise of a technology and the need for quality control and inspection techniques, Mater. Eval. 76 (2018) 438-453.

[123] N.P. Aleshin, T. Grigor'ev, N.A. Shchipakov, M.A. Prilutskii, V.V. Murashov, Applying nondestructive testing to quality control of additive manufactured parts, Russ J Nondestruct Test 52 (2016) 600-609.

[124] P. Wang, H. Zhou, L. Zhang, H. Chen, X. Zhu, H. Lei, D. Fang, In situ X-ray micro-computed tomography study of the damage evolution of prefabricated through-holes in SLM-printed AlSi10Mg alloy under tension, J Alloys Compounds 821 (2020) 153576.

[125] H. Gong, V.K. Nadimpalli, K. Rafi, T. Starr, B. Stucker, Micro-CT evaluation of defects in Ti-6Al-4V parts fabricated by metal additive manufacturing 7 (2019) 44.

[126] S. Shrestha, T. Starr, K. Chou, Porosity analysis in metal additive manufacturing by micro-CT, Technol J 52019 (2018) V002T02A059.

[127] G. Pyka, G. Kerckhofs, J. Schrooten, M. Wevers, The effect of spatial micro-CT image resolution and surface complexity on the morphological 3D analysis of open porous structures, Mater Charact 87 (2014) 104-115.

[128] A. du Plessis, P. Sperling, A. Beerlink, L. Tshabalala, S. Hoosain, N. Mathe, S.G. le Roux, Standard method for microCT-based additive manufacturing quality control 1: Porosity analysis, MethodsX 5 (2018) 1102-1110.

[129] E.I. Todorov, Measurement of electromagnetic properties of powder and solid metal materials for additive manufacturing, NDT E Int10169 (2017) 1016907.

[130] B.M. Sharratt, Non-destructive techniques and technologies for qualification of additive manufactured parts and processes, Sharret Research and Consulting Inc: Victoria, BC USA (2015).

[131] G.S. Schajer, Practical residual stress measurement methods, John Wiley & Sons, 2013.

[132] F.A. Kandil, J.D. Lord, A.T. Fry, P.V. Grant, A review of residual stress measurement methods-a guide to technique selection. NLP Report MAT(A)04 (2001).

[133] P.S. Prevey, X-ray diffraction residual stress techniques, ASM Handbook 10 (1986) 380-392.

[134] M.E. Fitzpatrick, A.T. Fry, P. Holdway, F.A. Kandil, J. Shackleton, L. Suominen, Determination of residual stresses by X-ray diffraction, NPL issue 2 (2005).

[135] P.J. Withers, H. Bhadeshia, Residual stress. Part 1–measurement techniques, Mater Sci Technol 17 (2001) 355-365.

[136] M.T. Hutchings, P.J. Withers, T.M. Holden, T. Lorentzen, Introduction to the characterization of residual stress by neutron diffraction, CRC Press (2005).

[137] M.E. Fitzpatrick, A. Lodini, Analysis of residual stress by diffraction using neutron and synchrotron radiation, CRC Press (2003).

[138] A.J. Allen, M.T. Hutchings, C.G. Windsor, C. Andreani, Neutron diffraction methods for the study of residual stress fields, Adv Phys 34 (1985) 445-473.

[139] P. Yadav, K.K. Saxena, Effect of heat-treatment on microstructure and mechanical properties of Ti alloys: An overview, In Proc Mater Today 26 (2020) 2546-2557.

[140] M. Takeyama, S. Kobayashi, Physical metallurgy for wrought gamma titanium aluminides: Microstructure control through phase transformations, Intermetallics 13 (2005) 993-999.

[141] R. Wanhill, S. Barter, Metallurgy and microstructure, in: Anonymous, Fatigue of beta processed and beta heat-treated titanium alloys, Springer, 2012, pp. 5-10.

[142] S. Liu, Y.C. Shin, Additive manufacturing of Ti-6Al-4V alloy: A review, Mater Des 164 (2019) 107552.

[143] S.L. Semiatin, T.R. Bieler, Effect of texture and slip mode on the anisotropy of plastic flow and flow softening during hot working of Ti-6Al-4V, Mater Trans A 32 (2001) 1787-1799.

[144] A. Ducato, L. Fratini, M. La Cascia, G. Mazzola, An automated visual inspection system for the classification of the phases of Ti-6Al-4V titanium alloy, Springer Berlin Heidelberg, Berlin, Heidelberg, 2013 362–369.

[145] T. Ahmed, H.J. Rack, Phase transformations during cooling in α + β titanium alloys, Mater. Sci. Eng. A 243 (1) (1998) 206–211.

[146] A.A. Antonysamy, Microstructure, texture and mechanical property evolution during additive manufacturing of Ti-6Al-4V alloy for aerospace applications, Doctoral dissertation The University of Manchester (2012).

[147] ASTM, F2924-14, Standard Specification for Additive Manufacturing Titanium-6 Aluminum-4 Vanadium with Powder Bed Fusion (2014).

[148] ASTM, Standard Specification for Titanium–6Aluminum–4Vanadium Alloy Castings for Surgical Implants (UNS R56406): F1108-14 [S] (2014).

[149] American Society for Testing and Materials, (ASTM), ASTM F136—13 Standard Specification for Wrought Titanium-6Aluminum-4Vanadium ELI (Extra Low Interstitial) Alloy for Surgical Implant Applications (UNS R56401) (2013) 6-10.

[150] Y.-L. Lee, J. Pan, R. Hathaway, Fatigue Testing and Analysis: Theory and Practice. Elsevier, 2011, 416 p.

[151] Additive Manufacturing Fatigue and Fracture. NIST, 2020. Avaliable online: https://www.nist.gov/programs-projects/additive-manufacturing-fatigue-and-fracture

[152] M. Bernabei, L. Allegrucci, M. Amura. Fatigue failures of aeronautical items: Trainer aircraft canopy lever reverse, rescue helicopter main rotor blade and fighter-bomber aircraft ground-attack main wheel. In: Handbook of materials failure analysis: with case studies from the aerospace and automotive industries. Ed.: A. S. H. Makhlouf, M.Aliofkhazraei, Elsevier, (2016) 87-116.

[153] L.B. Malefane, W.B. du Preez, M. Maringa, High cycle fatigue properties of as-built Ti6AL4V (ELI) produced by direct metal laser sintering, S. Afr. J. Ind. Eng, 28 3 Pretoria (2017) 188-199

[154] M. Simonelli, Y.Y. Tse, C. Tuck, On the texture formation of selective laser melted Ti-6Al-4V, Mater Trans A 45 (2014) 2863-2872.

[155] M. Simonelli, Microstructure evolution and mechanical properties of selective laser melted Ti-6Al-4V, Doctoral dissertation, Loughborough University (2014).

[156] D. Gu, Y. Hagedorn, W. Meiners, G. Meng, R.J.S. Batista, K. Wissenbach, R. Poprawe, Densification behavior, microstructure evolution, and wear performance of selective laser melting processed commercially pure titanium, Acta Materia 60 (2012) 3849-3860.

[157] Z. Zhou, Y. Liu, X. Liu, Q. Zhan, K. Wang, Microstructure evolution and mechanical properties of in-situ Ti-6Al-4V–TiB composites manufactured by selective laser melting, Composite Part B: Eng 207 (2021) 108567.

[158] Z. Liang, Z. Sun, W. Zhang, S. Wu, H. Chang, The effect of heat treatment on microstructure evolution and tensile properties of selective laser melted Ti-6Al-4V alloy, J. Alloys Compounds 782 (2019) 1041-1048.

[159] X. Zhang, C.J. Yocom, B. Mao, Y. Liao, Microstructure evolution during selective laser melting of metallic materials: A review, J Laser Appl 31 (2019) 031201.

[160] S. Suwas, D. Kumar, Microstructure–texture–mechanical property relationship in alloys produced by additive manufacturing following selective laser melting (SLM) technique, INAE 5 (2020) 1-10.

[161] P. Barriobero-Vila, J. Gussone, J. Haubrich, S. Sandlöbes, J.C. Da Silva, P. Cloetens, N. Schell, G. Requena, Inducing stable α β microstructures during selective laser melting of Ti-6Al-4V using intensified intrinsic heat treatments, Mater 10 (2017) 268.

[162] H. Ali, L. Ma, H. Ghadbeigi, K. Mumtaz, In-situ residual stress reduction, martensitic decomposition and mechanical properties enhancement through high temperature powder bed pre-heating of selective laser melted Ti-6Al-4V, Mater Sci Eng 695 (2017) 211-220.

[163] W. Xu, E.W. Lui, A. Pateras, M. Qian, M. Brandt, In situ tailoring microstructure in additively manufactured Ti-6Al-4V for superior mechanical performance, Acta Materia 125 (2017) 390-400.

[164] L. Papadakis, D. Chantzis, K. Salonitis, On the energy efficiency of pre-heating methods in SLM/SLS processes, Int J Adv Manuf Technol 95 (2018) 1325-1338.

[165] A. Zafari, M.R. Barati, K. Xia, Controlling martensitic decomposition during selective laser melting to achieve best ductility in high strength Ti-6Al-4V, Mater Sci Eng 744 (2019) 445-455.

[166] G.M. Ter Haar, T.H. Becker, Low temperature stress relief and martensitic decomposition in selective laser melting produced Ti-6Al-4V, MDPC 3 (2021) e138.

[167] A. Khorasani, I. Gibson, U.S. Awan, A. Ghaderi, The effect of SLM process parameters on density, hardness, tensile strength and surface quality of Ti-6Al-4V, Addit Manuf 25 (2019) 176-186.

[168] M.J. Donachie, Titanium: a technical guide, ASM International, 2000.

[169] B. Vayssette, N. Saintier, C. Brugger, M. Elmay, E. Pessard, Surface roughness of Ti-6Al-4V parts obtained by SLM and EBM: Effect on the high cycle fatigue life, Procedia Eng 213 (2018) 89-97.

[170] D. Agius, K.I. Kourousis, C. Wallbrink, A review of the as-built SLM Ti-6Al-4V mechanical properties towards achieving fatigue resistant designs, Metals 8 (2018) 75.

[171] J. Günther, S. Leuders, P. Koppa, T. Tröster, S. Henkel, H. Biermann, T. Niendorf, On the effect of internal channels and surface roughness on the high-cycle fatigue performance of Ti-6Al-4V processed by SLM, Mater Des 143 (2018) 1-11.

[172] S. Bagehorn, J. Wehr, H.J. Maier, Application of mechanical surface finishing processes for roughness reduction and fatigue improvement of additively manufactured Ti-6Al-4V parts, Int J Fatigue 102 (2017) 135-142.

[173] V. Chastand, P. Quaegebeur, W. Maia, E. Charkaluk, Comparative study of fatigue properties of Ti-6Al-4V specimens built by electron beam melting (EBM) and selective laser melting (SLM), Mater Charact 143 (2018) 76-81.

[174] Z. Chen, S. Cao, X. Wu, C.H. Davies, Surface roughness and fatigue properties of selective laser melted Ti-6Al-4V alloy, in: Additive manufacturing for the aerospace industry, Elsevier, 2019, pp. 283-299.

[175] E. Wycisk, C. Emmelmann, S. Siddique, F. Walther, High cycle fatigue (HCF) performance of Ti-6Al-4V alloy processed by selective laser melting, Adv Mater Res 816 (2013) 134-139.

[176] A. du Plessis, P. Sperling, A. Beerlink, O. Kruger, L. Tshabalala, S. Hoosain, S.G. le Roux, Standard method for microCT-based additive manufacturing quality control 3: surface roughness, MethodsX 5 (2018) 1111-1116.

[177] I. Yadroitsava, J. Els, G. Booysen, I. Yadroitsev, Peculiarities of single-track formation from Ti-6Al-4V alloy at different laser power densities by selective laser melting, SAJIE 26 (2015) 86-95.

[178] C. Tenbrock, F.G. Fischer, K. Wissenbach, J.H. Schleifenbaum, P. Wagenblast, W. Meiners, J. Wagner, Influence of keyhole and conduction mode melting for top-hat shaped beam profiles in laser powder bed fusion, J Mater Process Technol 278 (2020) 116514.

[179] H. Ghasemi-Tabasi, J. Jhabvala, E. Boillat, T. Ivas, R. Drissi-Daoudi, R.E. Logé, An effective rule for translating optimal selective laser melting processing parameters from one material to another, Addit Manuf 36 (2020) 101496.

[180] C. Tang, K.Q. Le, C.H. Wong, Physics of humping formation in laser powder bed fusion, Int J Heat Mass Transfer 149 (2020) 119172.

[181] S.R. Narasimharaju, W. Liu, W. Zeng, T.L. See, P. Scott, X. Jiang, S. Lou, Surface texture characterization of metal selective laser melted part with varying surface inclinations, J Tribol 143 (2021) 051106.

[182] I. Yadroitsev, I. Smurov, Surface morphology in selective laser melting of metal powders, Phys Procedia 12 (2011) 264-270.

[183] M. Xia, D. Gu, G. Yu, D. Dai, H. Chen, Q. Shi, Influence of hatch spacing on heat and mass transfer, thermodynamics and laser processability during additive manufacturing of Inconel 718 alloy, Int J Mach Tools Manuf 109 (2016) 147-157.

[184] M. Hamidi Nasab, A. Giussani, D. Gastaldi, V. Tirelli, M. Vedani, Effect of surface and subsurface defects on fatigue behavior of AlSi10Mg alloy processed by laser powder bed fusion (L-PBF), Metals 9 (2019) 1063.

[185] L. Yang, L. Lo, S. Ding, T. Özel, Monitoring and detection of meltpool and spatter regions in laser powder bed fusion of super alloy Inconel 625, PIAM 5 (2020) 367-378.

[186] I.V. Zhirnov, P.A Podrabinnik, A.A. Okunkova,A.V.Gusarov. 2015. Laser beam profiling: experimental study of its influence on single-track formation by selective laser melting, Mech. Ind. Mech IND 16(2015) 709.

[187] A.S. Metel, M.M. Stebulyanin, S.V. Fedorov, A.A. Okunkova. Power density distribution for laser additive manufacturing (SLM): potential, fundamentals and advanced applications. Technologies 7(2018) 5.

[188] A. Okunkova, M. Volosova, P. Peretyagin, Y. Vladimirov, I. Zhirnov, A.V. Gusarov. Experimental approbation of selective laser melting of powders by the use of non-Gaussian power density distributions, Phys. Procedia 56 (2014) 48-57.

[189] A.A. Okunkova, P.Y. Peretyagin,P.A. Podrabinnik, I.V. Zhirnov, A.V. Gusarov. Development of laser beam modulation assets for the process productivity improvement of selective laser melting, Procedia IUTAM 23 (2017) 177-186.

[190] T.M. Wischeropp, H. Tarhini, C. Emmelmann. Influence of laser beam profile on the selective laser melting process of AlSi10Mg. J. Laser Appl. 32(2020) 022059.

[191] H. Schleifenbaum, W. Meiners, K. Wissenbach, C. Hinke. 2009, November. High power selective laser melting: A new approach for individualized series production. In International Congress on Applications of Lasers & Electro-Optics 1 (2009) 385-394.

[192] L.E. Loh, Z.H. Liu, D.Q. Zhang, M. Mapar, S.L. Sing,C.K. Chua, W.Y. Yeong. 2014. Selective Laser Melting of aluminium alloy using a uniform beam profile: The paper analyzes the results of laser scanning in Selective Laser Melting using a uniform laser beam. Vitual Phys. Prototyp. 9(2014) 11-16.

[193] T. Lantzsch, D. Heussen, N. Praetzsch, C. Haefner. 2022, March. Evaluation of productivity scaling approaches for laser powder bed fusion of nickel-base alloy 625. In High-Power Laser Materials Processing: Applications, Diagnostics, and Systems 11 (2022) 19-31 SPIE.

[194] J. Bayol, G. Pallier. 2022. Advances in laser powder bed fusion thanks to beam shaping: Beam shaper based on multi-plane light conversion enables new forms of material processing. PhotonicsViews, 19(2022) 52-55.

[195] J. Grünewald, V. Blickle, M. Allenberg-Rabe, P. Wagenblast, K. Wudy. Flexible and highly dynamic beam shaping for Laser-Based Powder Bed Fusion of metals. Procedia CIRP 111 (2022) 65-70.

[196] D. Wang, S. Wu, F. Fu, S. Mai, Y. Yang, Y. Liu, C. Song, Mechanisms and characteristics of spatter generation in SLM processing and its effect on the properties, Mater Des 117 (2017) 121-130.

[197] C. Qiu, C. Panwisawas, M. Ward, H.C. Basoalto, J.W. Brooks, M.M. Attallah, On the role of melt flow into the surface structure and porosity development during selective laser melting, Acta Materia 96 (2015) 72-79.

[198] M. Balbaa, S. Mekhiel, M. Elbestawi, J. McIsaac, On selective laser melting of Inconel 718: Densification, surface roughness, and residual stresses, Mater Des 193 (2020) 108818.

[199] M.C. Sow, T. De Terris, O. Castelnau, Z. Hamouche, F. Coste, R. Fabbro, P. Peyre, nfluence of beam diameter on Laser Powder Bed Fusion (L-PBF) process, Additive Manufacturing 36 (2018) 101532.

[200] H. Schleifenbaum, W. Meiners, K. Wissenback, C. Hinke, Individualized production by mean of high power Selective Laser melting, CIRP J. of Manuf. Sci. and Technol. 2 (2010) 161–169.

[201] M.L. Montero-Sistiaga, M.G. Martinez, K. Boschmans, J.P. Kruth, J.V. Humbeeck, K. Vanmeensel, Microstructure evolution of 316L produced by HP-SLM (high power selective laser melting, Addit. Manuf. 23 (2018) 402–410.

[202] J. Metelkova, Y. Kinds, K. Kempen, C. De Formanoir, A. Witvrouw, B. Van Hooreweder, On the influence of laser defocusing in selective laser melting of 316L, Addit. Manuf. 23 (2018) 161–169.

[203] M. Leary, Surface roughness optimisation for selective laser melting (SLM): accommodating relevant and irrelevant surfaces, in: Laser additive manufacturing, Elsevier, 2017, pp. 99-118.

[204] X. Shi, C. Yan, W. Feng, Y. Zhang, Z. Leng, Effect of high layer thickness on surface quality and defect behavior of Ti-6Al-4V fabricated by selective laser melting, Opt Laser Technol 132 (2020) 106471.

[205] A.H. Maamoun, Y.F. Xue, M.A. Elbestawi, S.C. Veldhuis, Effect of selective laser melting process parameters on the quality of al alloy parts: Powder characterization, density, surface roughness, and dimensional accuracy, Mater 11 (2018) 2343.

[206] A.M. Khorasani, I. Gibson, A.R. Ghaderi, Rheological characterization of process parameters influence on surface quality of Ti-6Al-4V parts manufactured by selective laser melting, Int J Adv Manuf Technol 97 (2018) 3761-3775.

[207] G. Kasperovich, J. Haubrich, J. Gussone, G. Requena, Correlation between porosity and processing parameters in TiAl6V4 produced by selective laser melting, Mater Des 105 (2016) 160-170.

[208] R. Snell, S. Tammas-Williams, L. Chechik, A. Lyle, E. Hernández-Nava, C. Boig, G. Panoutsos, I. Todd, Methods for rapid pore classification in metal additive manufacturing, JOM 72 (2020) 101-109.

[209] A. du Plessis, I. Yadroitsev, I. Yadroitsava, S.G. le Roux, X-ray microcomputed tomography in additive manufacturing: a review of the current technology and applications, 3D Print Addit Manuf 5 (2018) 227-247.

[210] Y. Huang, T.G. Fleming, S.J. Clark, S. Marussi, K. Fezzaa, J. Thiyagalingam, C.L.A. Leung, P.D. Lee, Keyhole fluctuation and pore formation mechanisms during laser powder bed fusion additive manufacturing, Nat Commun 13 (2022) 1-11.

[211] N. Nudelis, P. Mayr, A novel classification method for pores in laser powder bed fusion, Metals 11 (2021) 1912.

[212] H. Ali, H. Ghadbeigi, K. Mumtaz, Effect of scanning strategies on residual stress and mechanical properties of selective laser melted Ti-6Al-4V, Mater Sci Eng 712 (2018) 175-187.

[213] Y. Liu, Y. Yang, D. Wang, A study on the residual stress during selective laser melting (SLM) of metallic powder, Int J Adv Manuf Technol 87 (2016) 647-656.

[214] D. Wang, S. Wu, Y. Yang, W. Dou, S. Deng, Z. Wang, S. Li, The effect of a scanning strategy on the residual stress of 316L steel parts fabricated by selective laser melting (SLM), Mater 11 (2018) 1821.

[215] T.M. Wischeropp, H. Tarhini, C. Emmelmann, Influence of laser beam profile on the selective laser melting process of AlSi10Mg, J Laser Appl 32 (2020) 022059.

[216] A.S. Metel, M.M. Stebulyanin, S.V. Fedorov, A.A. Okunkova, Power density distribution for laser additive manufacturing (SLM): potential, fundamentals and advanced applications, Technologies 7 (2018) 5.

[217] J.P. Oliveira, A.D. LaLonde, J. Ma, Processing parameters in laser powder bed fusion metal additive manufacturing, Mater Des 193 (2020) 108762.

[218] M. Bayat, A. Thanki, S. Mohanty, A. Witvrouw, S. Yang, J. Thorborg, N.S. Tiedje, J.H. Hattel, Keyhole-induced porosities in laser-based powder bed fusion (L-PBF) of Ti-6Al-4V: High-fidelity modelling and experimental validation, Addit Manuf 30 (2019) 100835.

[219] J. Han, J. Yang, H. Yu, J. Yin, M. Gao, Z. Wang, X. Zeng, Microstructure and mechanical property of selective laser melted Ti-6Al-4V dependence on laser energy density, Rapid Prototyp J (2017).

[220] S. Pal, N. Gubeljak, R. Hudak, G. Lojen, V. Rajtukova, J. Predan, V. Kokol, I. Drstvensek, Tensile properties of selective laser melting products affected by building orientation and energy density, Mater Sci Eng 743 (2019) 637-647.

[221] Č Donik, J. Kraner, I. Paulin, M. Godec, Influence of the energy density for selective laser melting on the microstructure and mechanical properties of stainless steel, Metals 10 (2020) 919.

[222] H. Gu, H. Gong, D. Pal, K. Rafi, T. Starr, B. Stucker, Influences of energy density on porosity and microstructure of selective laser melted 17-4PH stainless steel, Int SFF symposium Texas (2013).

[223] C. Meier, R.W. Penny, Y. Zou, J.S. Gibbs, A.J. Hart, Thermophysical phenomena in metal additive manufacturing by selective laser melting: fundamentals, modeling, simulation, and experimentation, Annu Rev Heat Transf 20 (2017).

[224] H. Shipley, D. McDonnell, M. Culleton, R. Coull, R. Lupoi, G. O'Donnell, D. Trimble, Optimisation of process parameters to address fundamental challenges during selective laser melting of Ti-6Al-4V: A review, Int J Mach Tools Manuf 128 (2018) 1-20.

[225] L. Tonelli, A. Fortunato, L. Ceschini, CoCr alloy processed by selective laser melting (SLM): Effect of laser energy density on microstructure, surface morphology, and hardness, J Manuf Process 52 (2020) 106-119.

[226] L. Mugwagwa, Investigation and management of residual stresses in selective laser melting of maraging steel, Doctoral dissertation, Stellenbosch: Stellenbosch University (2019).

[227] U.S. Bertoli, A.J. Wolfer, M.J. Matthews, J.R. Delplanque, J.M. Schoenung, On the limitations of volumetric energy density as a design parameter for selective laser melting, Mater Des 113 (2017) 331-340.

[228] K.G. Prashanth, S. Scudino, T. Maity, J. Das, J. Eckert, Is the energy density a reliable parameter for materials synthesis by selective laser melting? 5 (2017) 386-390.

[229] T.M. Wischeropp, Advancement of selective laser melting by laser beam shaping, Springer, 2021.

[230] M. Guo, D. Gu, L. Xi, H. Zhang, J. Zhang, J. Yang, R. Wang, Selective laser melting additive manufacturing of pure tungsten: Role of volumetric energy density on densification, microstructure and mechanical properties, Int J Refract Hard Met 84 (2019) 105025.

[231] S. Greco, K. Gutzeit, H. Hotz, B. Kirsch, J.C. Aurich, Selective laser melting (SLM) of AISI 316L - impact of laser power, layer thickness, and hatch spacing on roughness, density, and microhardness at constant input energy density, Int J Adv Manuf Technol 108 (2020) 1551-1562.

[232] P. Ferro, R. Meneghello, G. Savio, F. Berto, A modified volumetric energy density-based approach for porosity assessment in additive manufacturing process design, Int J Adv Manuf Technol 110 (2020) 1911-1921.

[233] Z. Sun, X. Tan, S.B. Tor, W.Y. Yeong, Selective laser melting of stainless steel 316L with low porosity and high build rates, Mater Des 104 (2016) 197-204.

[234] A. Leicht, M. Fischer, U. Klement, L. Nyborg, E. Hryha, Increasing the productivity of laser powder bed fusion for stainless steel 316L through increased layer thickness, J Mater Eng Perform 30 (2021) 575-584.

[235] S. Wang, Y. Liu, W. Shi, B. Qi, J. Yang, F. Zhang, D. Han, Y. Ma, Research on high layer thickness fabricated of 316L by selective laser melting, Mater 10 (2017) 1055.

[236] M. Khorasani, I. Gibson, A. Ghasemi, M. Brandt, M. Leary, On the role of wet abrasive centrifugal barrel finishing on surface enhancement and material removal rate of LPBF stainless steel 316L, J Manuf Process 59 (2020) 523-534.

[237] W.H. Kan, L.N.S. Chiu, C.V.S. Lim, Y. Zhu, Y. Tian, D. Jiang, A. Huang, A critical review on the effects of process-induced porosity on the mechanical properties of alloys fabricated by laser powder bed fusion, J Mater Sci (2022) 1-48.

Appendices

Appendix I: Surface tomography of samples manufactured with the high-power system

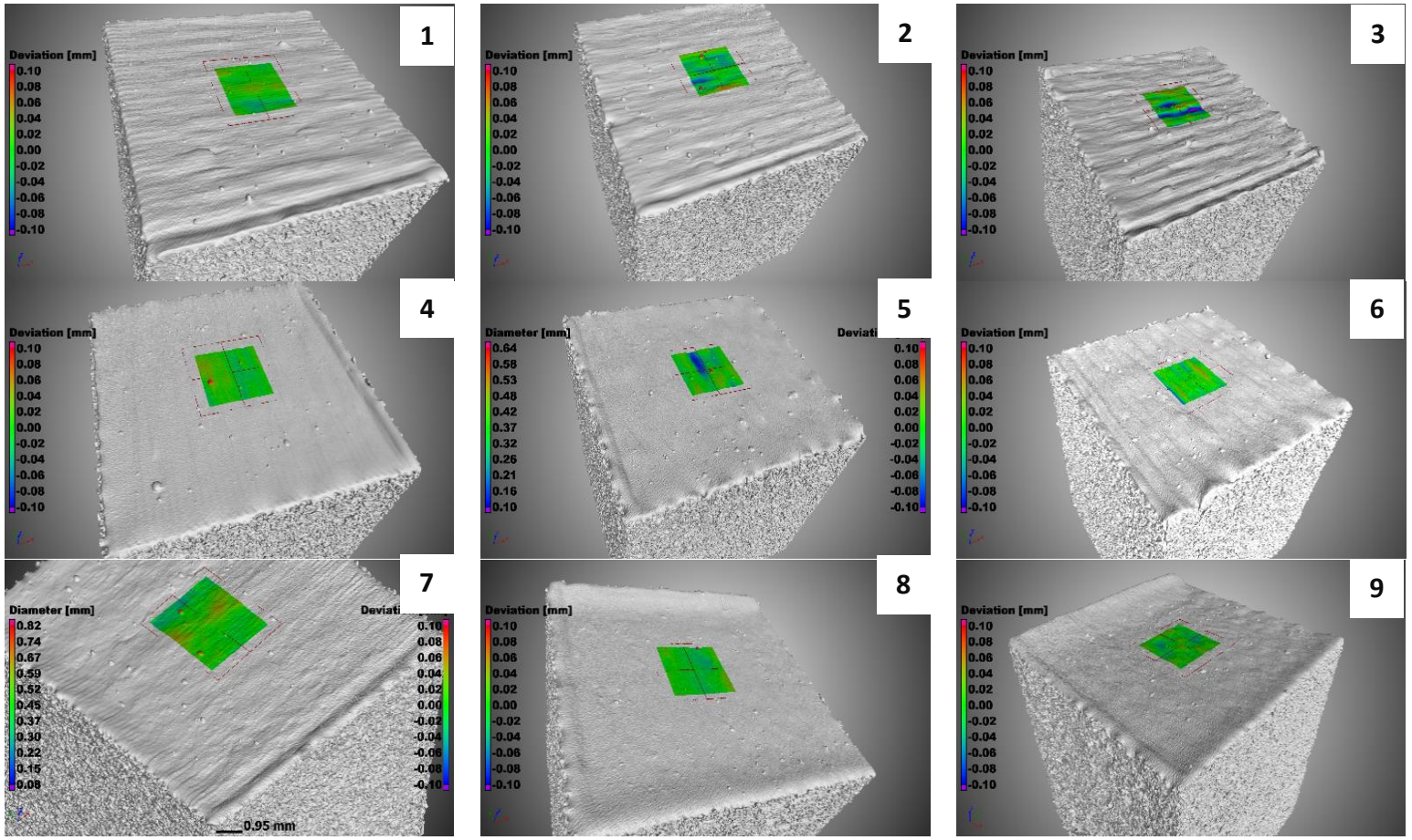

Appendix II: Surface tomography of samples manufactured with the EOS machine

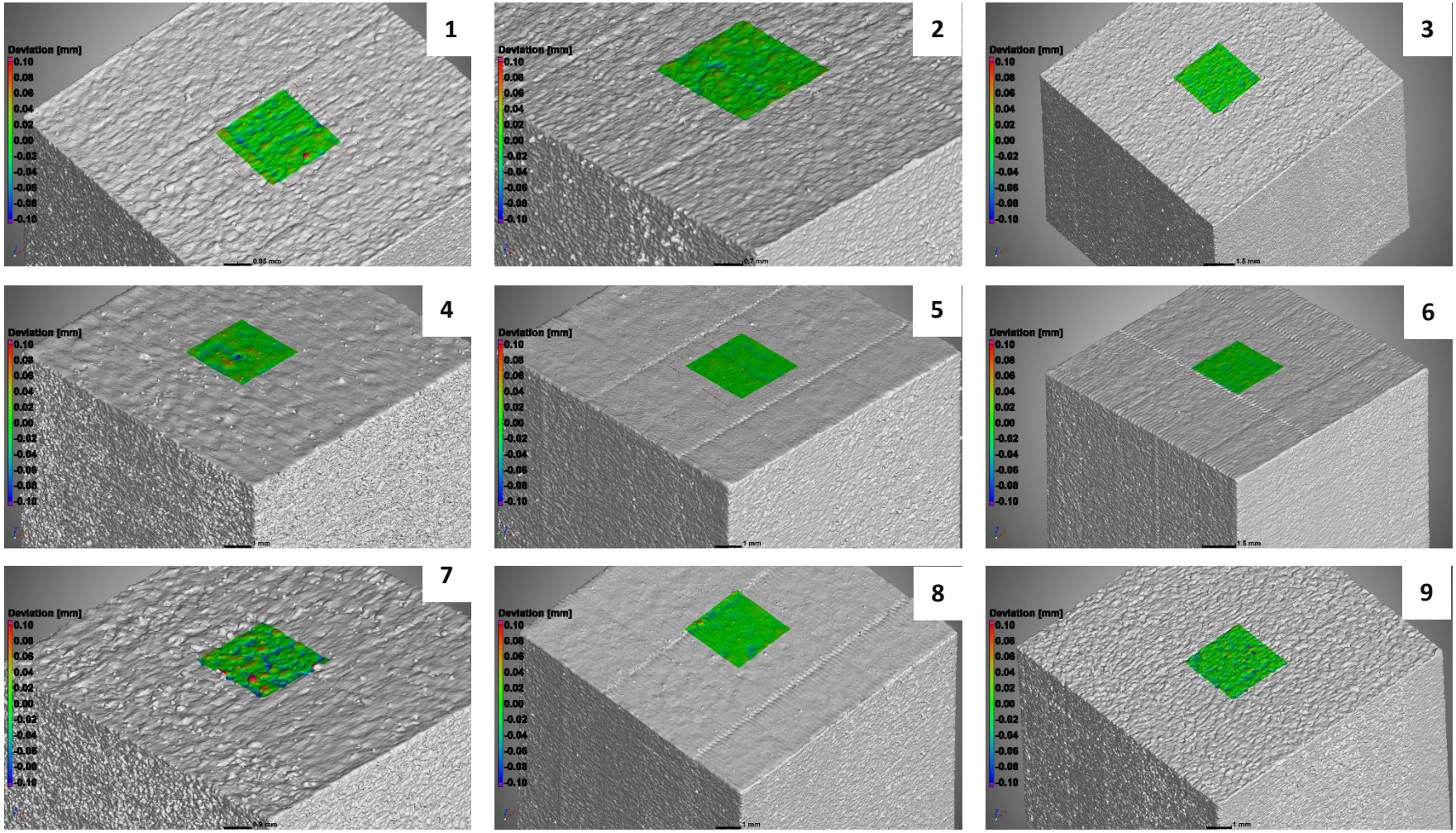

Appendix III: Pore size distribution in the samples manufactured with the high-power system

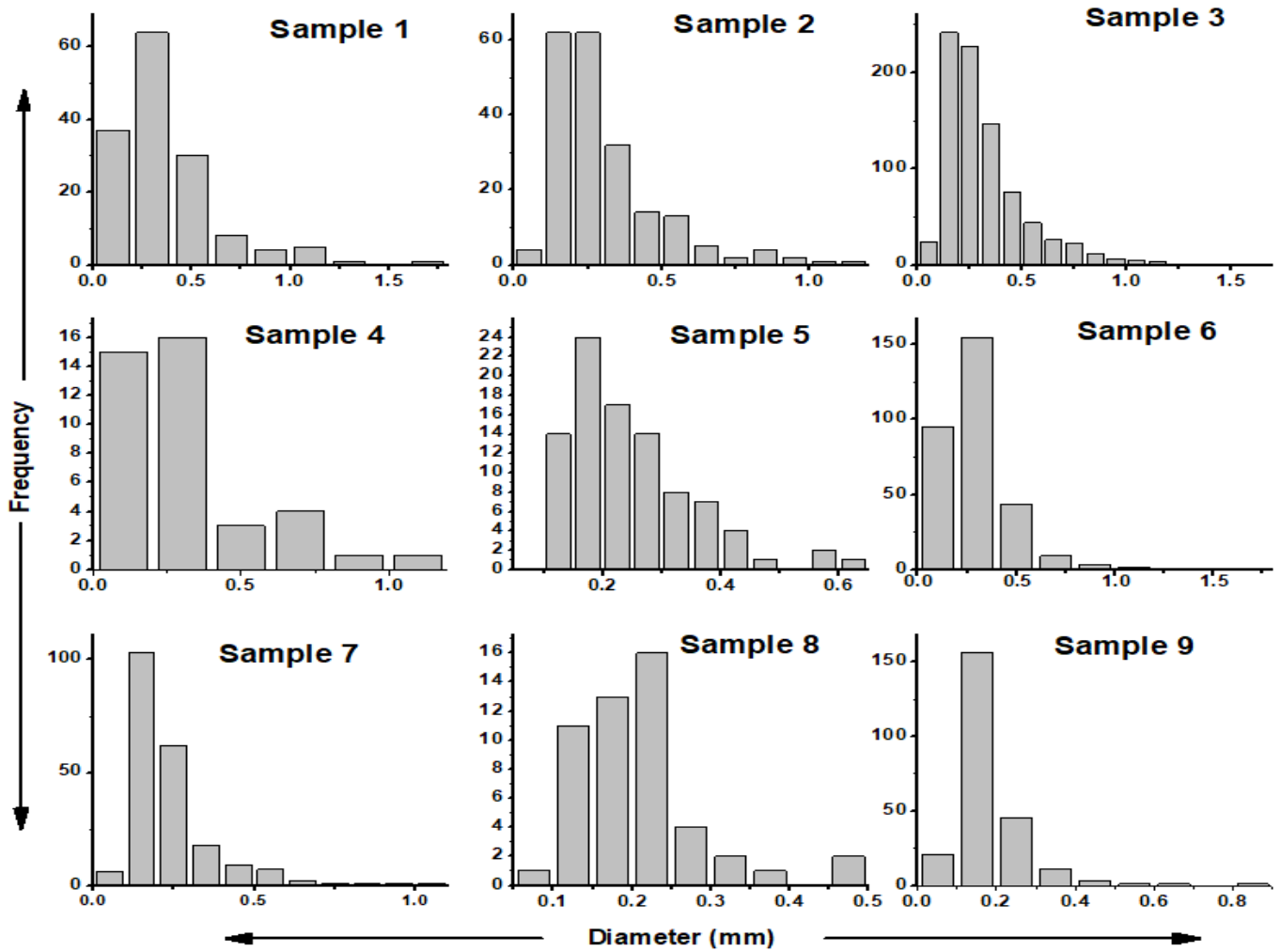

Appendix IV: Pore size distribution in the samples manufactured with the EOS machine

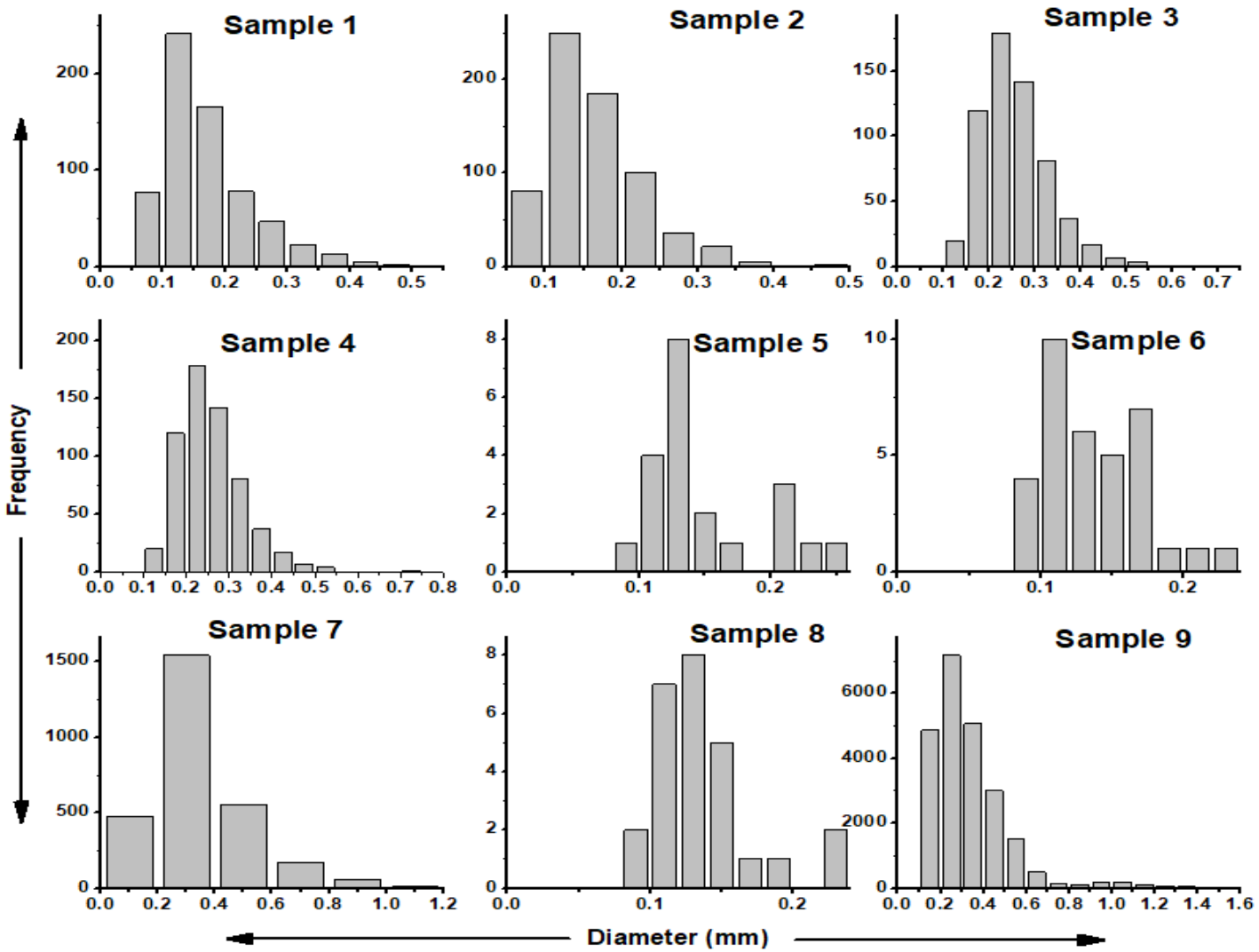

Central University of Technology, Free State

Appendix V: Diameter-Sphericity trend in the samples manufactured with the high-power system

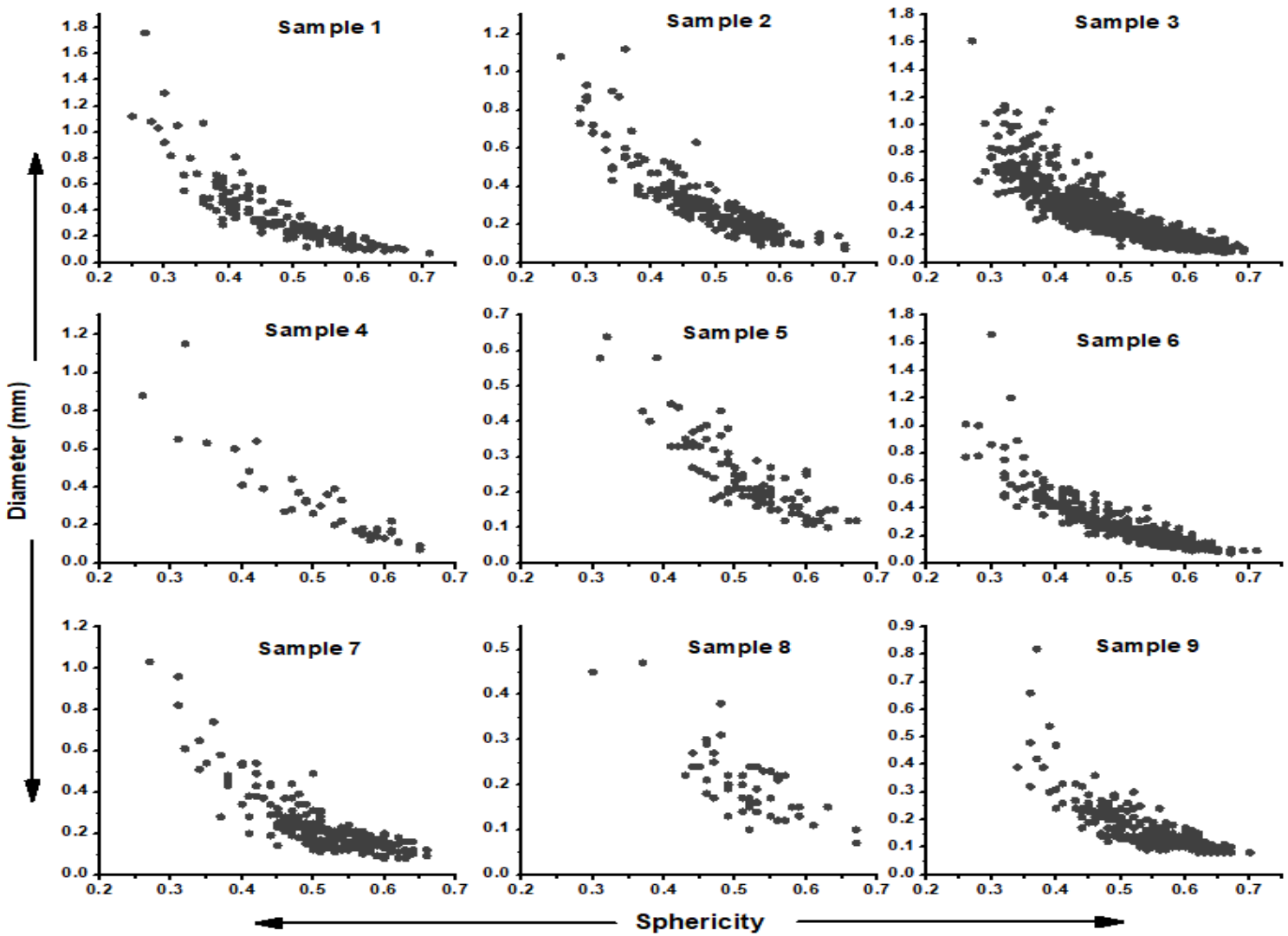

Central University of Technology, Free State

Appendix VI: Diameter-Sphericity trend in the samples manufactured with the EOS machine

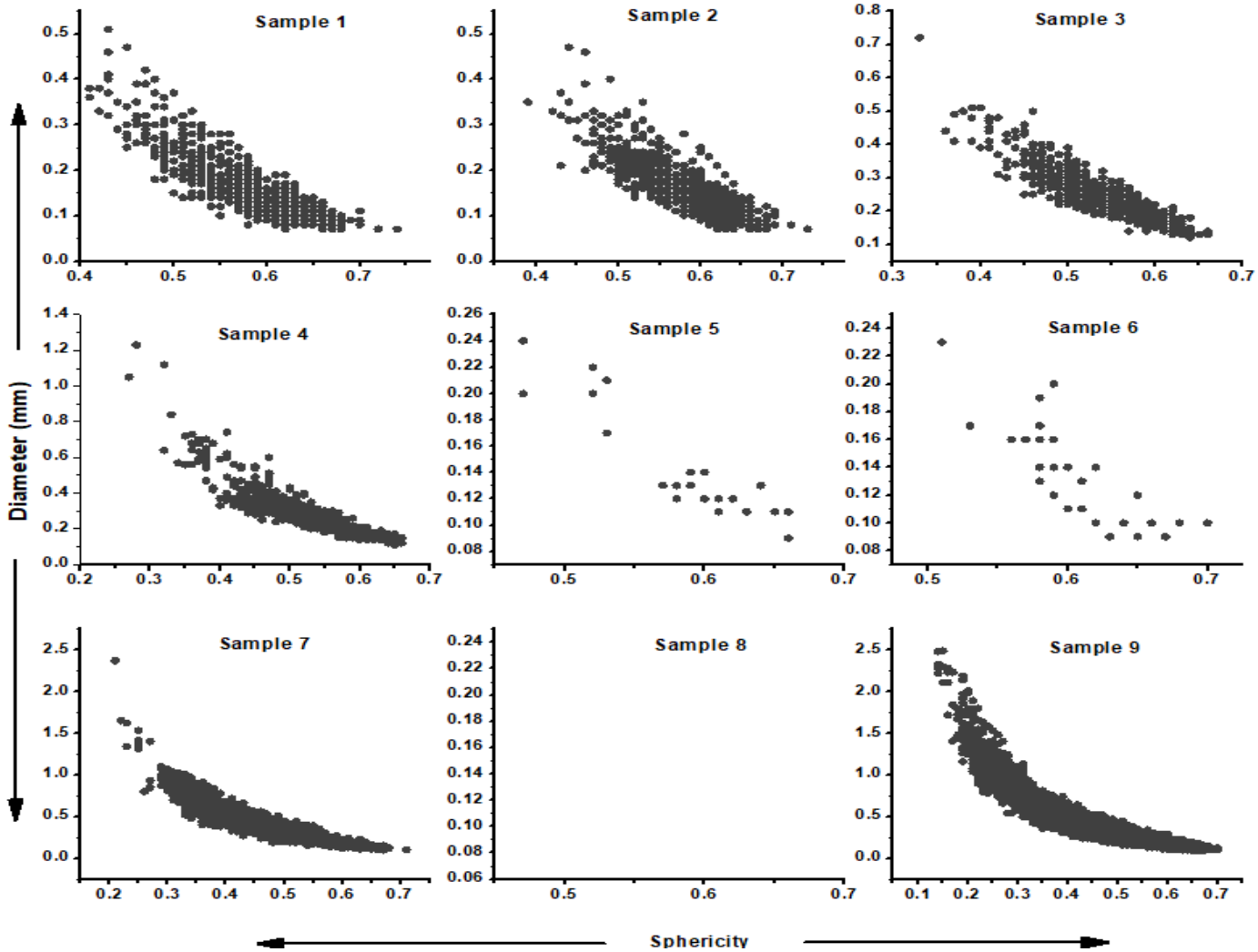

Central University of Technology, Free State

Appendix VII: As-built microstructures of samples manufactured with the high-power system

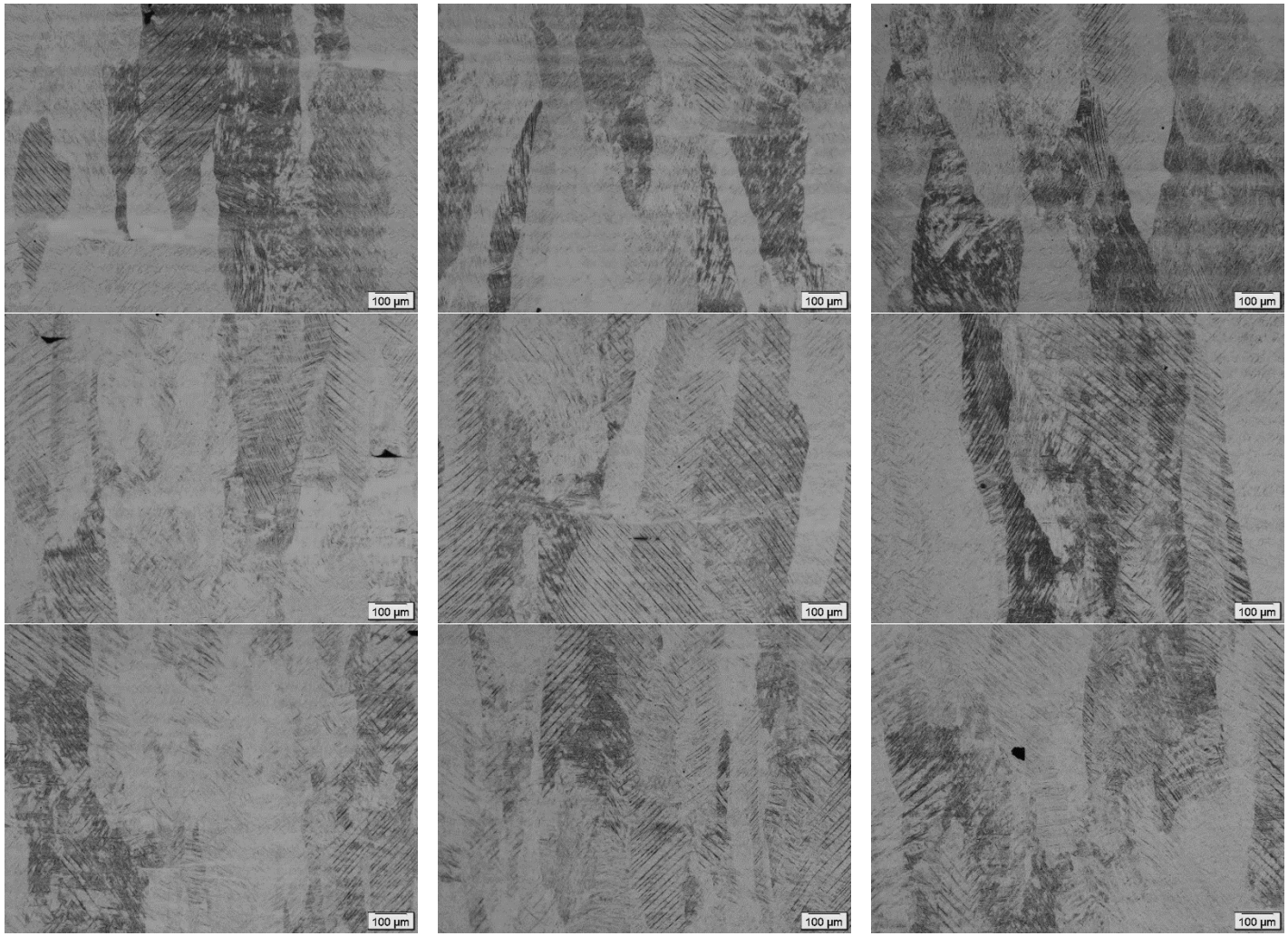

Central University of Technology, Free State

Appendix VIII: As-built microstructures of samples manufactured with the EOS machine

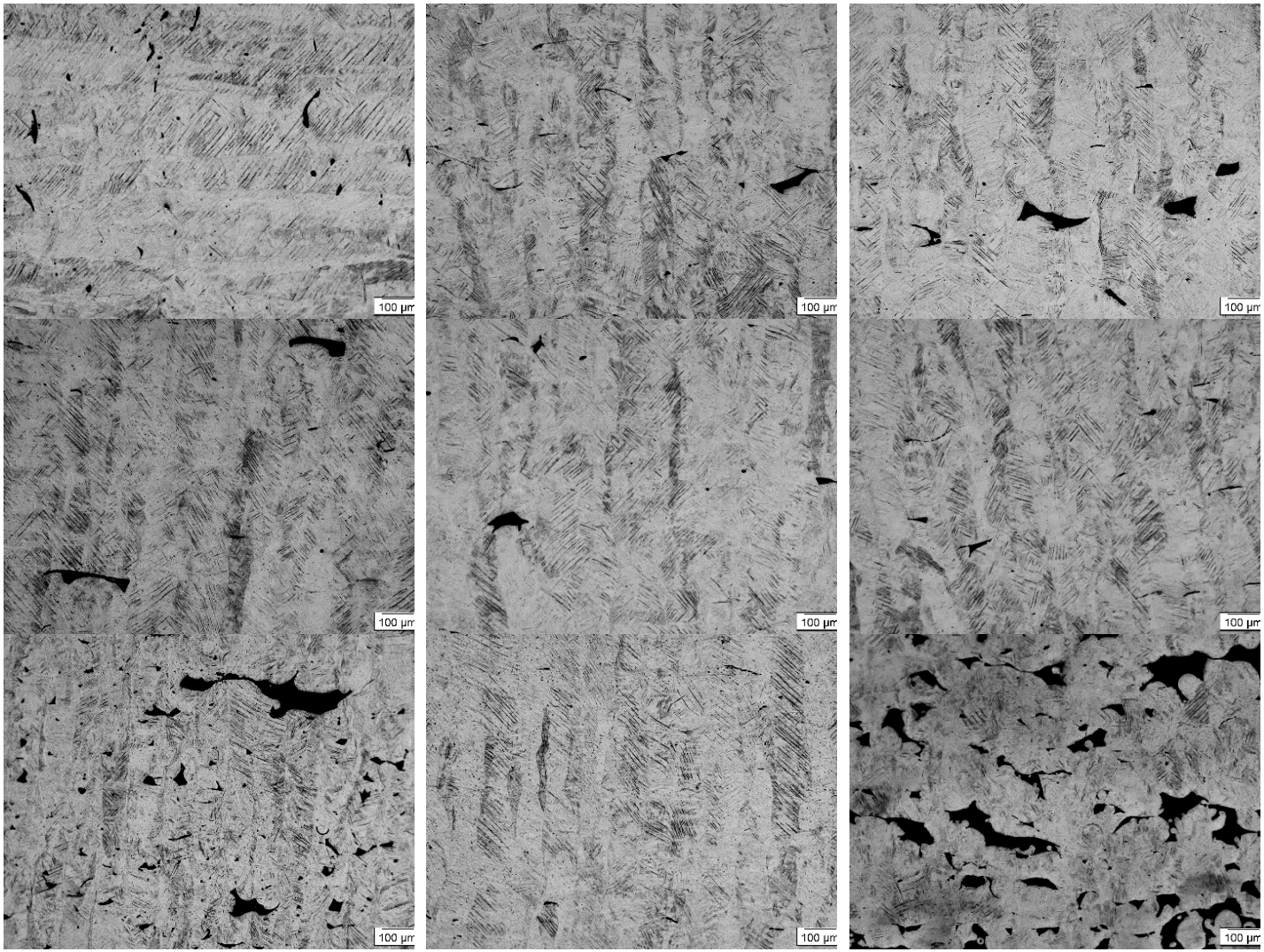

Appendix IX: Stress-Strain curves, Batch 1, 2, and 3, respectively

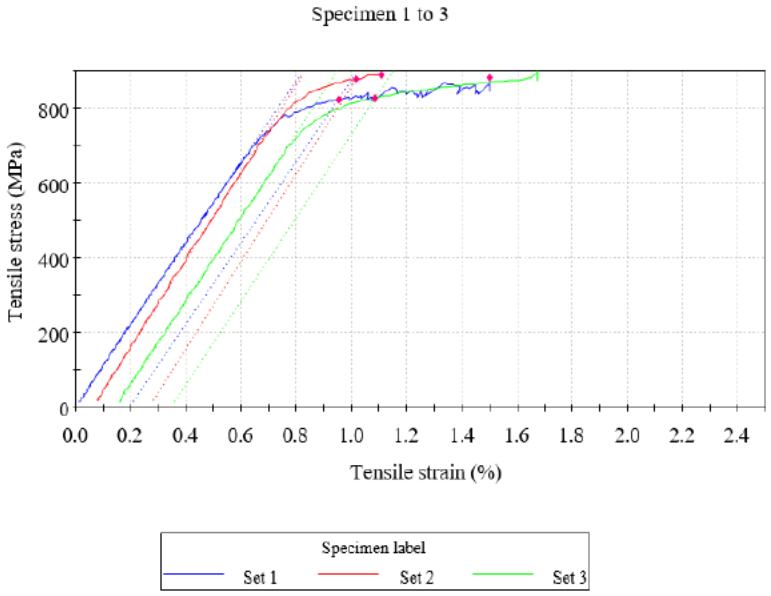

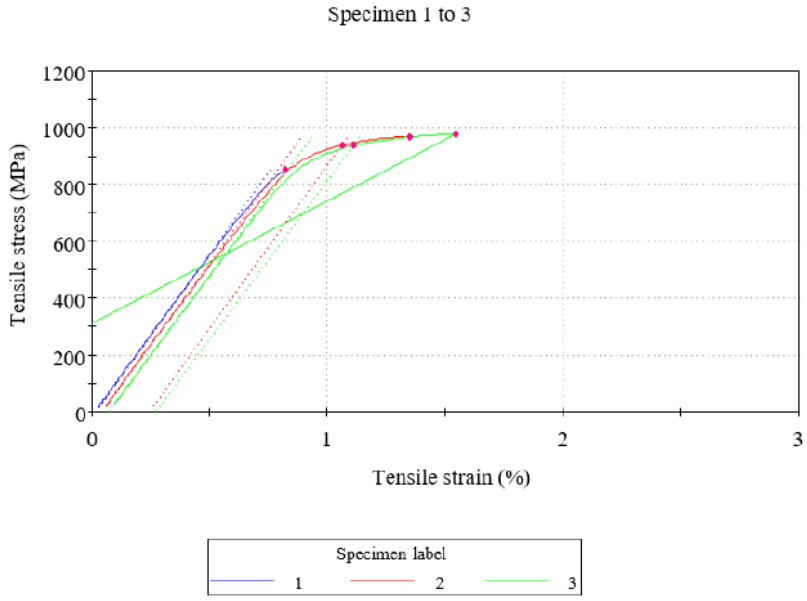

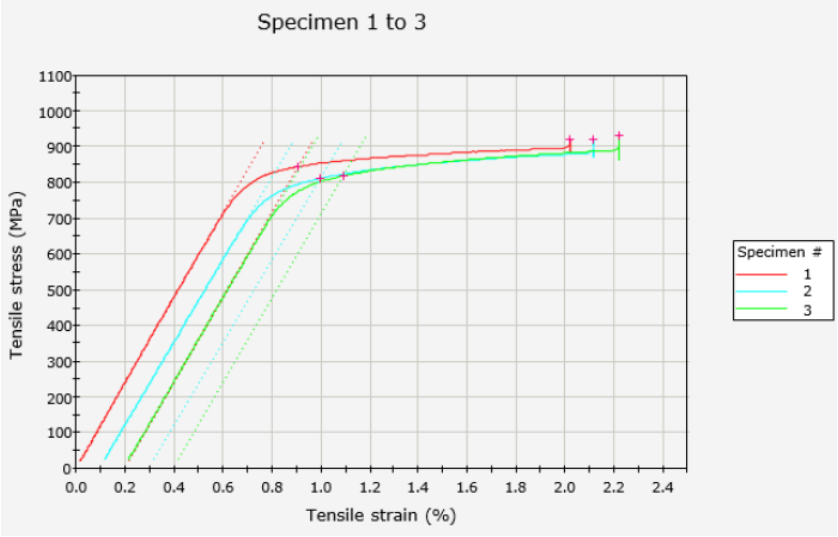

Central University of Technology, Free State

Appendix X: Fatigue fracture surface - Batch 1

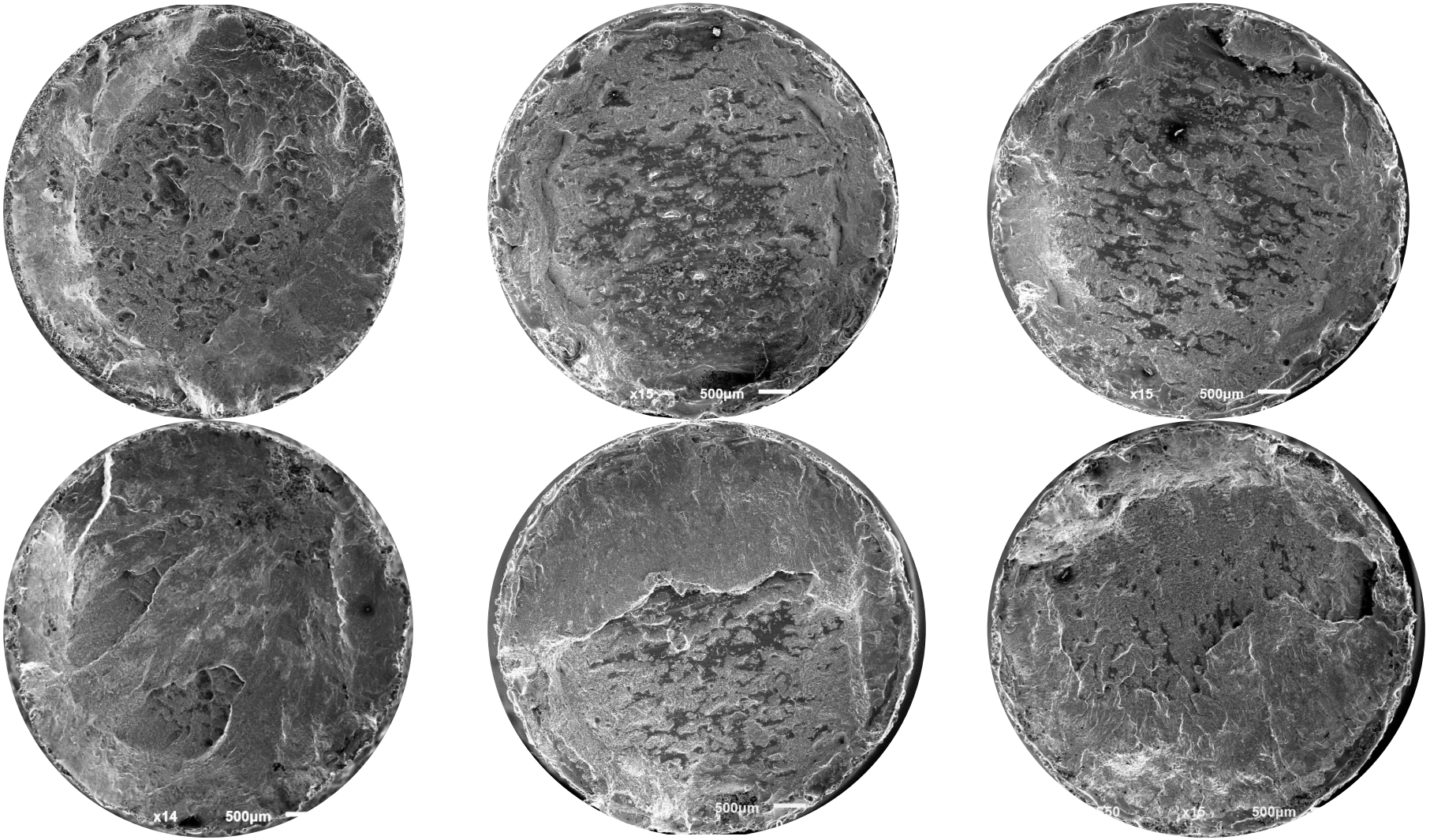

Central University of Technology, Free State

Appendix XI: Fatigue fracture surface - Batch 2

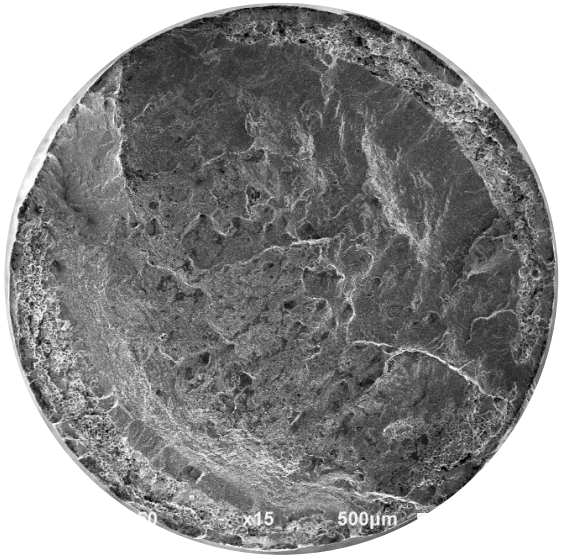

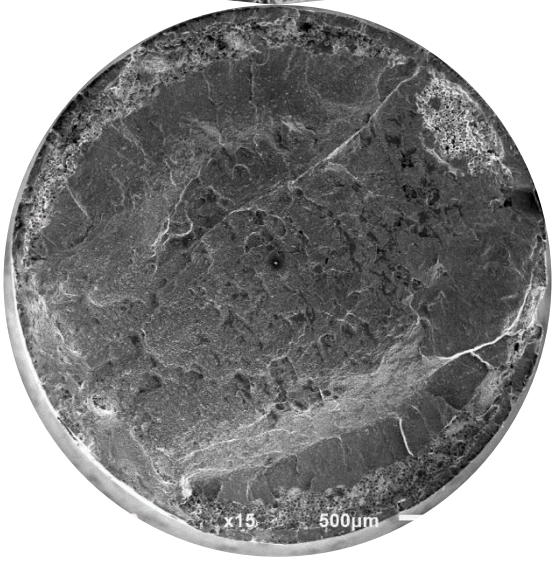

Central University of Technology, Free State

Appendix XII: Fatigue fracture surface - Batch 3

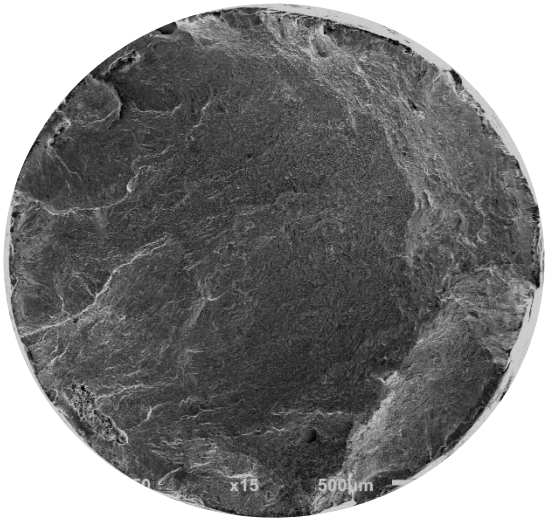

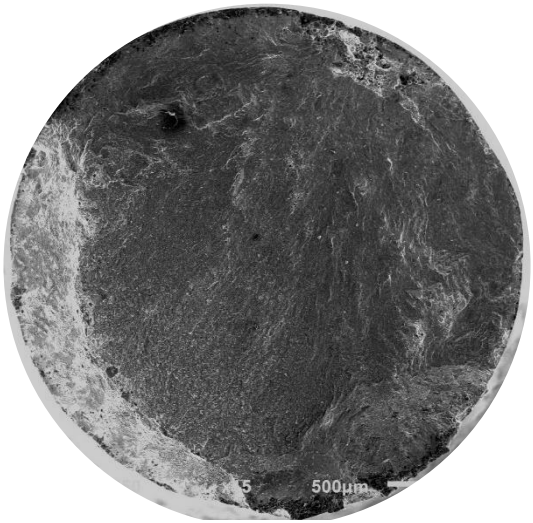

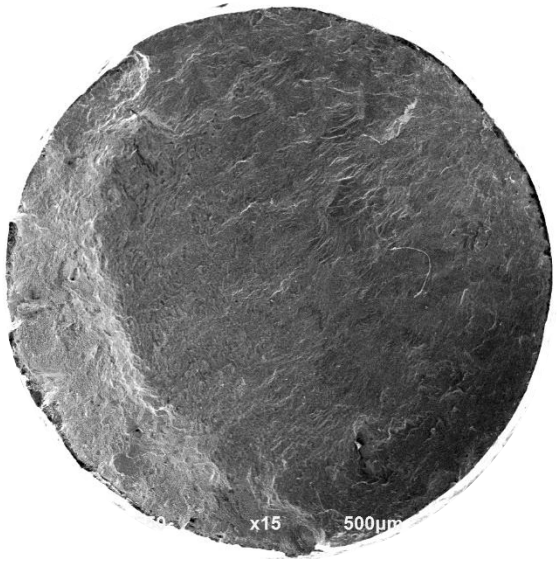

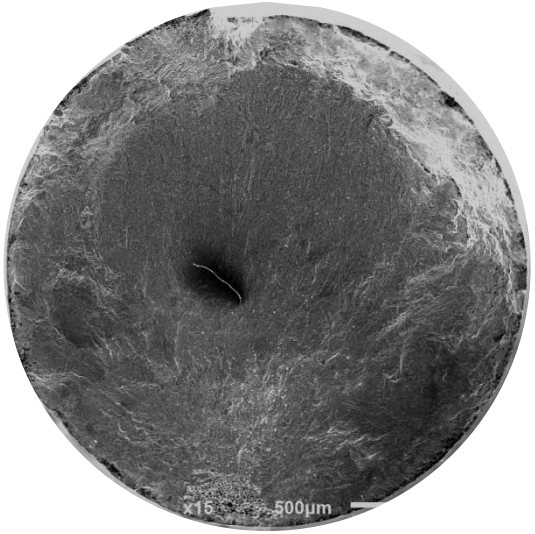

Appendix XIII: Micro-CT images of fractured specimen from Batch 1

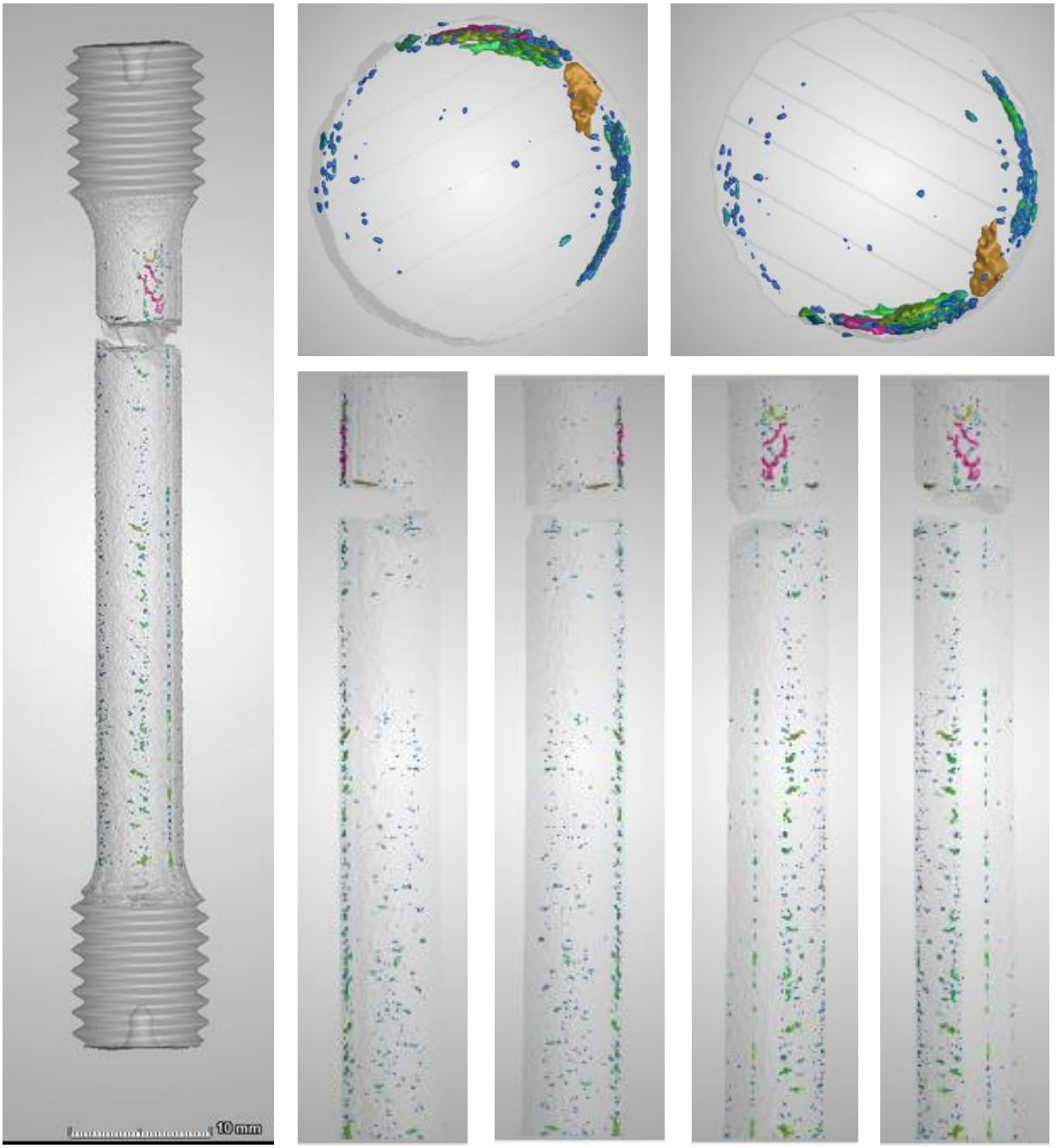

Appendix XIV: Micro-CT images of fractured specimen from Batch 2

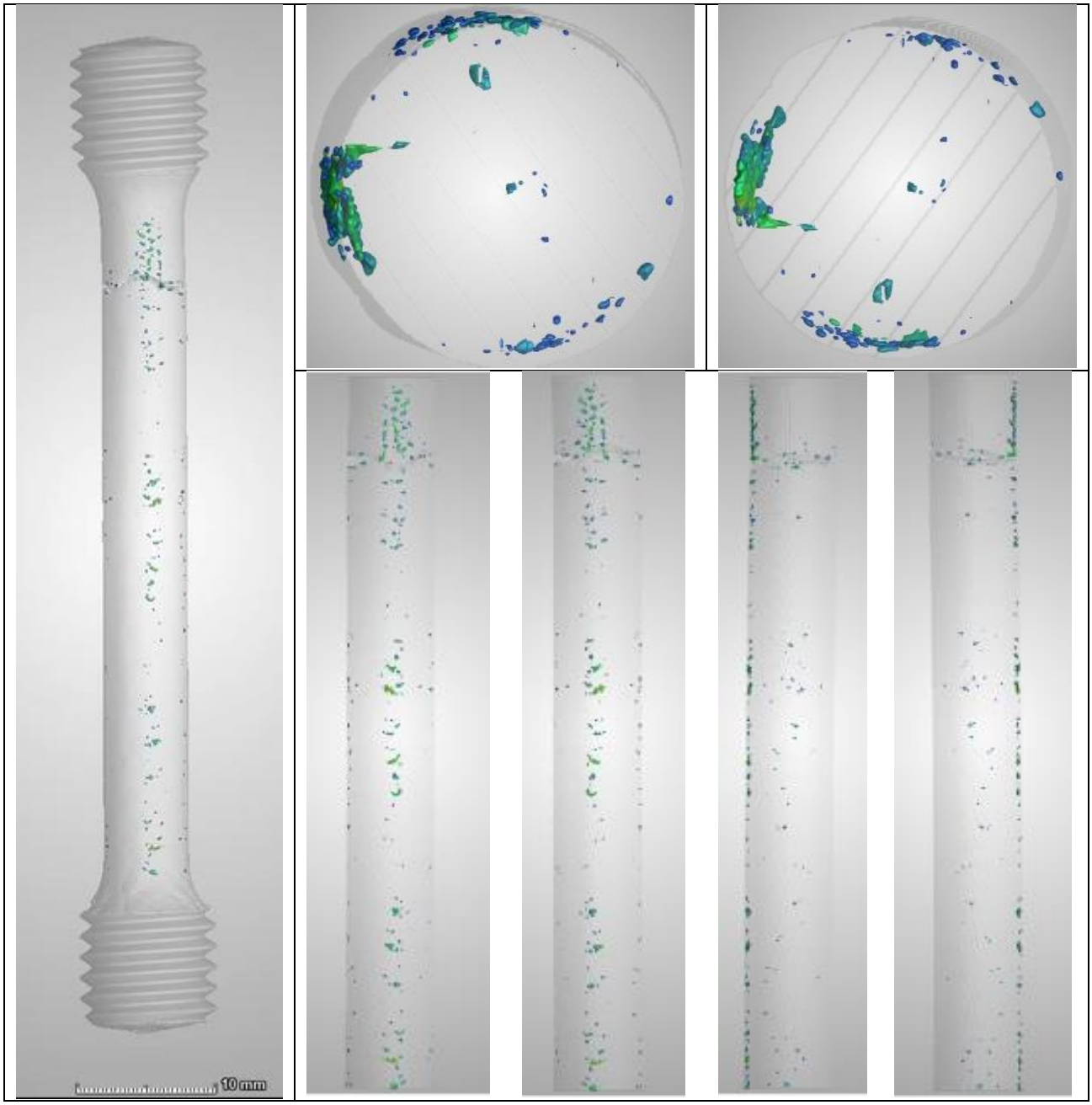

Appendix XV: Micro-CT images of fractured specimen from Batch 3

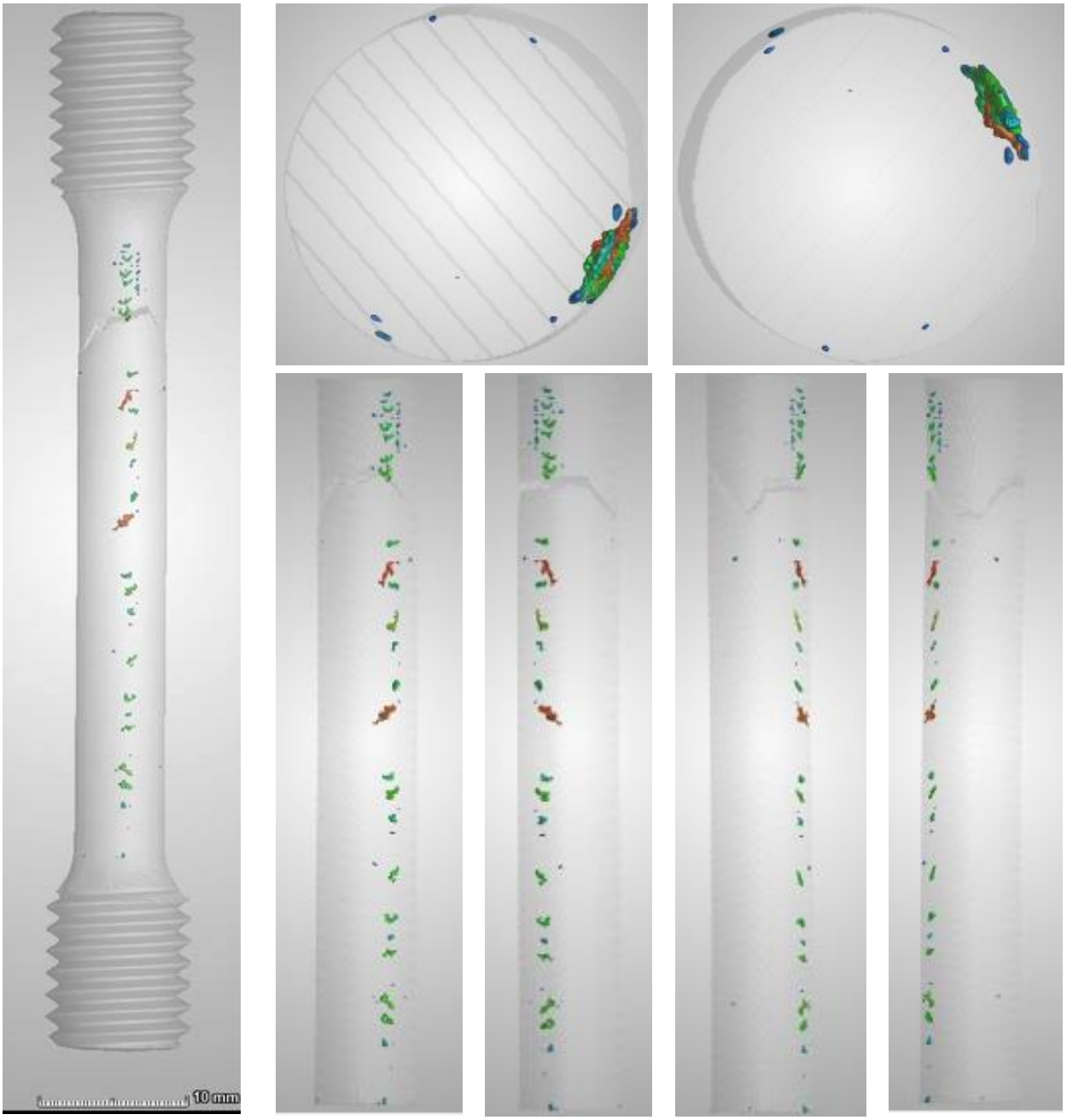

Appendix XVI: Gas flow configuration for the High-power system